

**SEMICONDUCTOR NANOWIRE NETWORKS
GROWN BY MOLECULAR BEAM EPITAXY**
VAPOR-LIQUID-SOLID AND SELECTIVE AREA GROWTH

by *Filip Krizek*

ACADEMIC ADVISORS:

Prof. Peter Krogstrup

AND

Prof. Charles M. Marcus

CENTER FOR QUANTUM DEVICES
AND
STATION Q COPENHAGEN

NIELS BOHR INSTITUTE
UNIVERSITY OF COPENHAGEN

UNIVERSITY OF
COPENHAGEN



THIS PHD THESIS HAS BEEN SUBMITTED TO THE PHD SCHOOL OF THE FACULTY OF
SCIENCE, UNIVERSITY OF COPENHAGEN ON 20TH OF JULY 2018

Abstract

This thesis presents results and advancements achieved in pursuit of high-yield in-situ growth of superconductor/semiconductor hybrid nanowire based networks. Such hybrid structures were proposed as a material platform suitable for realization of topological quantum computing based on Majorana Fermions. This specific application sets various requirements on the materials, namely strong spin-orbit coupling, large Landé g -factor, superconducting pairing, tunability of chemical potential and at last multi-terminal geometry with high-quality junctions between quasi-1D nanowires. That put together sets the overall goal of this work.

The thesis starts by investigation of early stages of vapor-liquid-solid growth of InAs nanowires. A new role of catalyst nanoparticles, that governs the NW growth on (001) substrates is uncovered. The understanding of the growth process in combination with atypical patterning of the growth substrate by gold particles, allows for formation of 'inclined' nanocrosses and more complex multiterminal nanowire networks.

The study continues with a description of two distinct vapor-liquid-solid mechanism based growth methods, that rely on in-situ kinking of growth direction of typical [0001] InAs nanowires. The described methods are used to grow two novel types of nanocrosses. That is enabled by specific patterning of the substrate, where gold catalysts are precisely aligned to the crystal orientation of the substrate.

The analysis of the crystal structure withing the inclined nanocrosses reveals that they form well defined polytypic wurtzite/zincblende/wurtzite junctions. Resistivity measurements through the nanowire intersections show that the zincblende inclusion affects its transparency to electron transport. We demonstrate that the inclusion can be used as an intrinsic quantum dot embedded into the junction of multi-terminal nanowire structures. In addition the overall crystal structure of the whole inclined nanocross can be modified by increase in growth temperature. That results in growth of complex but periodic polytypic structures. The two presented types of kinked nanocrosses form single crystalline junctions and no additional barriers that would affect electron transport were measured.

By implementing the described growth methods, new possibilities of scaling up the growth into larger nanowire networks are introduced together with in-situ shadow masking of hybrid semiconductor/superconductor nanowire heterostructures. The presented vapor-liquid-solid based growth strategies are still limited by challenging fabrication on larger

networks. In order to increase the scalability potential, new advances in the in-plane InAs nanowire network selective area growth are presented. It is shown that selective area growth offers full scalability, comparable to standard top-down methods. It is also demonstrated that electronic devices can be fabricated directly on the growth substrate and used in low temperature transport measurements.

The device performance is enhanced by implementation of a GaAs(Sb) buffer layer, which improves the nanowire/substrate interface quality by allowing for partial elastic relaxation of the InAs NW. The buffered nanowires show field effect mobility and spin orbit coupling comparable to typical vapor-liquid-solid structures. In addition the buffered networks show coherent transport in Aharonov-Bohm experiments. The characterization is concluded by demonstrating the compatibility of the selected area grown nanowires and networks with in-situ growth of radial superconductor/semiconductor heterostructures.

Dansk resume

Denne tese præsenterer resultater og fremskridt der er opnået i forbindelse med dyrkning af netværk bestående af hybride halvleder/superleder nanotråde. De hybride strukturer, der er baseret på epitaksial dyrkning af superleder/halvledere in-situ er foreslået som en materialeplatform til udarbejdelsen af en topologisk kvantecomputer baseret på Majorana fermioner. Denne specifikke applikation sætter en række krav til de ønskede materialer, navnlig en stærk spin-bane-kobling, en stærk Landé g-faktor, superledning, justerbarhed af det kemiske potentiale og en multi-terminal geometri med forbindelser imellem kvasi-endimensionelle nanotråde af høj kvalitet. Disse forudsætninger sætter målet for dette arbejde, som er in-situ dyrkning af netværk af halvleder-nanotråde vha. mole-kylær stråle epitaksi.

Først undersøges de tidlige stadier af damp-væske-faststof dyrkelsen af InAs nanotråde på (001) substrater, hvor en ny rolle af de brugte katolyse nano-partikler afdækkes. Forståelsen af dyrkningsprocessen kombineret med de atypiske mønstre udformet på dyrkningssubstratet tillader dyrkning af 'hældende' nano-kryds og mere komplekse multi-terminale netværk.

En anden damp-væske-faststof dyrkningsmekanisme baseret på in-situ ændring af dyrkningsretningen på gængse [0001] InAs nanotråde, er derefter brugt til at dyrke to nye typer af 'knækkede' nanokryds. Dette er muliggjort ved konsistent substratfabrikation og rationel mønstring af substratet, hvor placeringen af katalysepartiklerne specifikt er justeret til krystalorienteringen af substratet. Krystalstrukturanalysen viser at nanokryds dyrket på (001) substrater danner veldefinerede poly-typiske wurtzite/zinblendende/wurtzite skæringspunkter. Resistivitetmålinger over skæringspunktet mellem nano-trådene viser at opståelsen af zinblendende elementer påvirker gennemsigtigheden for elektrontransporten. På den anden side, er det vist at dette zinblendende element kan bruges som intrinsisk kvante-ø indlejret i skæringspunkterne i de multi-terminale nano-tråde.

I kontrast, danner de to præsenterede typer af 'knækkede' nanokryds enkelt-krystalforbindelser og udviser fuld transparens for elektrontransport. Dette viser også kompatibilitet imellem disse strukturer og standard fabrikationsprocesser. Muligheden for at opskalere netværksdyrkelsen er derefter introduceret sammen med nye muligheder inden for brugen af in-situ 'skygge-masker' til hybride halvleder/superleder nanotråds heterostrukturer. De præsenterede damp-væske-faststof dyrkningsstrategier er stadig begrænset af relativt lavt udbytte og udfordringer indenfor fabrikation på større netværk.

Til sidst er nye fremskridt indenfor dyrkelsen af InAs nanotråde i planet vha. selektiv-område-dyrkning præsenteret. Det er vist at denne metode ikke kun muliggør fuld skalerbarhed, der er sammenlignelig med gængse top-down metoder, men også udviser gode egenskaber under lav-temperatur målinger af devices fabrikeret direkte på dyrkningssubstratet. Deviceegenskaberne er forbedret ved at implementere et GaAs(Sb) buffer lag, der forbedrer kvaliteten af grænsefladen imellem substratet og nanotrådene, ved at tillade partiel elastisk relaksation af InAs nanotrådene. De bufferede nanotråde viser felleffekt mobilitet og spin-bane-kobling, der er sammenlignelig med nanotråde dyrket ved damp-væske-faststof metoden. Desuden viser de bufferede netværk lange koherenstider i Aharonov-Bohm eksperimenter. Karakteriseringen er afsluttet ved at vise kompatibiliteten af de selektivt-område dyrkede nanotråde og netværk med halvleder/superleder epitaksi. Samlet set viser resultaterne præsenteret i denne tese succesfulde dyrkninger af netværk af halvleder nanotråde ved brug af forskellige tilgange, og demonstrerer potentialet af de dyrkede strukturer til eksperimenter inden for kvantetransport.

Acknowledgements

At first, I would like to thank all the people who supported this project, but also supported me during the whole three years. The most gratitude goes to the advisor of the project Peter Krogstrup. Peter's ideas and experience with crystal growth and material science, together with his excitement for the topic and constant availability made this whole project possible. In addition, his expertise in crystal growth and ability to point very close to ideal growth parametric space without excessive testing, made the project progress very fast. A big thank you also belongs to Charles M. Marcus not only for giving me opportunity to do research at the Center for Quantum devices, but also for co-supervising the whole project.

I would like to thank Shivedra Upadhyay for constant interest in my work, sharing his expertise in fabrication and also for being a good friend. As big amount of gratitude goes to Joachim Sestoft, for help with the SAG related part of the project. It was great to work with him, despite of his compulsive inclination to Danish hygge lifestyle. The same goes for Saulis Vaitiekėnas and Dovydas Razmadze for their help during my fabrication learning phase.

I would like to thank Hadas Shtrikman and Philippe Caroff for their hospitality and openness during my visits to their laboratories. It was an important experience, that not only helped with my work, but also helped me to realize what I want to do after my time at Qdev.

I thank to all co-authors who contributed to this research, for their contributions and ideas. Especially to Jordi Arbiol, Sara Martí-Sánchez, Erik Johnson and Thomas Kanne for their great work and help with TEM analysis of the presented structures, without which the project would feel very incomplete.

A big gratitude goes to the Secretary team of the Center for Quantum Devices, because their help made it possible for me to fully focus on research. I would also like to thank Jesper Nygård, Lucas Casparis, Thomas S. Jespersen, Erik Johnson and Martin Aagesen for being open about their research and sharing ideas. Thank you, also goes to Claus. B Sørensen for keeping our MBE growth system running smoothly. I would also like to thank the whole material team for making things work and making work fun, that includes especially to Joachim Sestoft, Thomas Kanne and Tomáš Stankevič.

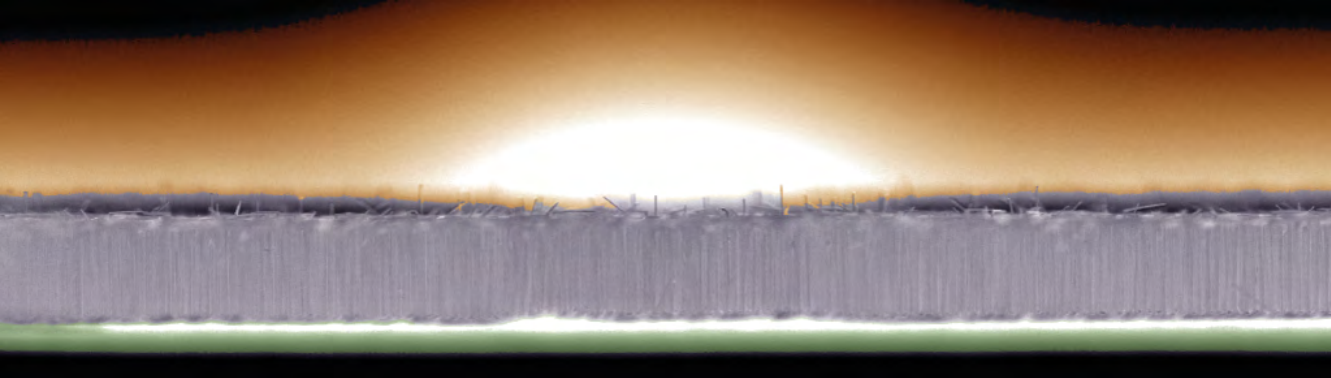
There are many people who deserve to be acknowledged for their help and contributions. Therefore, I would like to thank to the whole Center for Quantum Devices for support. That also includes the financial support from Microsoft.

I would mainly like to thank all my friends who I met during my PhD. studies for their support and ideas. Center for Quantum Devices is a big group, so I can not write down all the names of people who deserve it. Thanks for the good times, for the beer, for the entertainment, for making the lab a place where its often fun to come in the weekends and ultimately for not making me regret coming to Denmark. Any of you will always be welcome to come wherever I end up to be and get a special acknowledgement in person. Most likely a cheap Czech beer and a free sofa in Prague to sleep on.

At last, I would like to thank my soon to be wife Katarína for being at my side.

This research was done under the supervision of Peter Krogstrup and Charles M. Marcus with the financial support from Microsoft Research and ERC starting grant "HEMs-DAM" under the Horizon 2020 scheme, from August 15th 2015 to June 20th of 2018.

Released, August 2018



List of publications

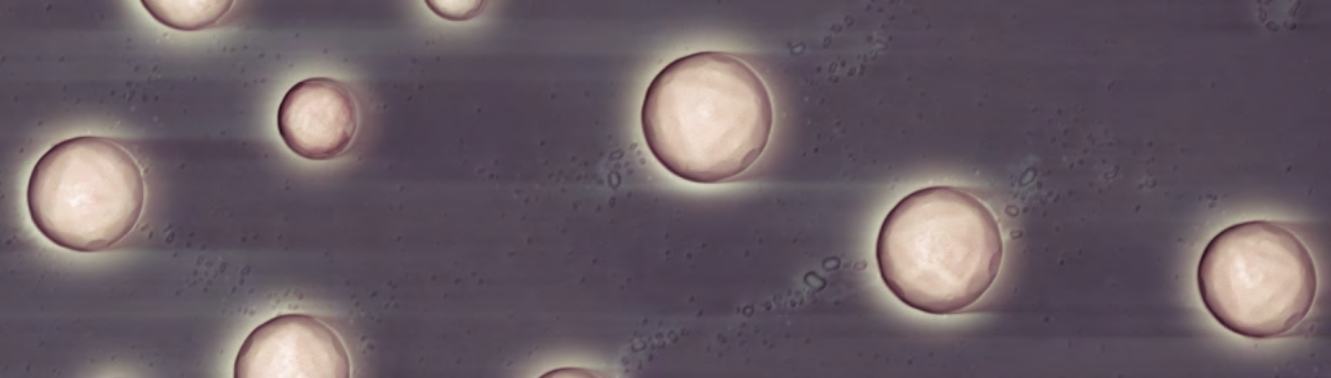
* These authors contributed equally.

These publications will be referred to in the text as Pub. 1, 2, etc.

- 1. Growth of InAs Wurtzite Nanocrosses from Hexagonal and Cubic Basis**
F. Krizek, T. Kanne, D. Razmadze, E. Johnson, J. Nygård, C. M. Marcus, P. Krogstrup
Nano Letters, (11), pp 6090-6096, (2017).
- 2. Au-assisted substrate-faceting for inclined nanowire growth**
J. Kang*, F. Krizek*, M. Załuska-Kotur, P. Krogstrup, P. Kacman, H. Beidenkopf, H. Shtrikman
Nano Letters, (18), pp 4115-4122, (2018).
- 3. Crystal phase quantum dots in InAs nanocrosses**
D. Carrad*, F. Krizek*, L. Stampfer, T. Kanne, R. Tanta, P. Krogstrup, T. S. Jespersen, J. Nygård
In preparation
- 4. Field effect enhancement in buffered quantum nanowire networks**
F. Krizek*, J. E. Sestoft*, P. Aseev*, S. Martí-Sánchez, S. Vaitiekėnas, L. Casparis, S. A. Khan, Y. Liu, T. Stankevič, A. M. Whiticar, A. Fursina, F. Boekhout, R. Koops, E. Uccelli, L. P. Kouwenhoven, C. M. Marcus, J. Arbiol, P. Krogstrup
Physical Review Materials, Accepted. (available as arXiv:1802.07808)

5. **Selective Area Grown Semiconductor-Superconductor Hybrids: A Basis for Topological Networks**

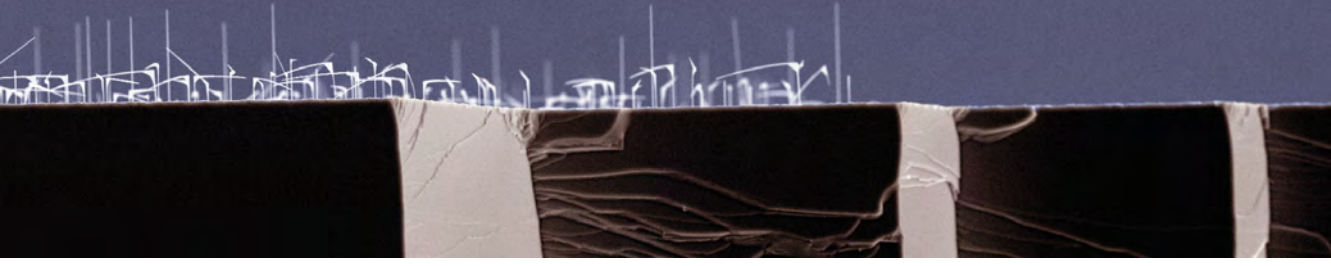
S. Vaitiekėnas, A. M. Whiticar, M. T. Deng, F. Krizek, J. E. Sestoft, C. J. Palmstrøm, S. Martí-Sánchez, J. Arbiol, P. Krogstrup, L. Casparis, C. M. Marcus
Arxiv pre-print, arXiv:1802.04210.



List of Abbreviations

2DEG	2-dimensional electron gas
AFM	atomic force microscopy
AB	Aharonov-Bohm effect
ALD	atomic layer deposition
BEP	beam equivalent pressure
buffered HF	ammonium fluoride buffered oxide etchant
CBE	chemical beam epitaxy
EBL	electron beam lithography
EDX	energy-dispersive x-ray spectroscopy
EELS	electron energy loss spectroscopy
ERS	equilibrium reference state
HAADF	high-angle annular dark-field
MBE	molecular beam epitaxy
MMA	methyl methacrylate
MOCVD	metal organic chemical vapor deposition
NW	nanowire
PECVD	plasma enhanced chemical vapor deposition
PMMA	polymethyl methacrylate

RHEED	reflection high-energy diffraction
RPM	rotation per minute
SAG	selected area growth
SEM	scanning electron microscope
STEM	scanning transmission electron microscopy
SU/SE	superconductor/semiconductor
TEM	transmission electron microscope
VLS	vapor-liquid-solid
WAL	weak antilocalization
WZ	wurtzite
ZB	zinc blende



Contents

- 1 Nanowire Networks 21**
- 1.1 Semiconductor nanowires in quantum computing 21**
- 1.2 Basics of Molecular Beam epitaxy 24**
- 1.2.1 Molecular Beam Epitaxy system 25
- 1.2.2 Beam fluxes, growth temperature and calibration 27
- 1.3 Thermodynamics, kinetics and nanocrystal growth 29**
- 1.3.1 Kinetics described by local thermodynamic equilibrium 29
- 1.3.2 Kinetic transitions 31
- 1.3.3 Surface energies and Wulff construction 32
- 1.3.4 Growth regimes in MBE 34
- 1.3.5 Nucleation 35
- 1.3.6 Diffusion in crystal growth - The adatom phase 36
- 1.4 Vapor-Liquid-Solid NW growth 38**
- 1.4.1 Polytypism in InAs crystals 41
- 1.4.2 Self-assembled, patterned and self catalyzed growth 43

1.4.3	Changing NW structure and growth direction	46
1.5	Selective Area Growth of nanowires	47
1.6	In-situ III-V Nanowire networks - an overview	49
1.7	Semiconductor/Superconductor hybrid NWs	51
2	VLS Nanowire Crosses	53
2.1	Methods	54
2.1.1	Patterned substrate preparation	55
2.1.2	NW growth on (001) substrates	56
2.1.3	NW growth on (111)B substrates	56
2.1.4	Structural characterization	57
2.1.5	Device fabrication	58
2.1.6	Resistivity measurements	58
2.2	Results and discussion	59
2.2.1	Catalyst role in inclined NW growth	59
2.2.2	Growth of inclined nanocrosses	66
2.2.3	Changing NW direction by catalyst manipulation	70
2.2.4	Growth of kinked-vertical and kinked-planar nanocrosses	73
2.2.5	Crystal structure within the nanocross junctions	76
2.2.6	Electron transport transparency of the junctions	81
2.2.7	Crystal phase quantum dots in inclined nanocrosses	83
2.2.8	Scaling of kinked nanocrosses into larger networks	85
2.2.9	Shadowing VLS superconductor/semiconductor hybrid NWs	86
2.3	Conclusion	87
2.4	Outlook	88
3	SAG Nanowire Networks	91
3.1	Methods	93
3.1.1	Oxide mask	93

3.1.2	Growth of non-buffered NWs	94
3.1.3	Growth of GaAs(Sb) buffered NWs	94
3.1.4	Superconductor in-situ deposition	94
3.1.5	Structural characterization	95
3.1.6	Device fabrication	96
3.1.7	Electronic Characterization	96
3.2	Results and discussion	101
3.2.1	Growth of single nanowires	101
3.2.2	Crystal symmetry and nanowire morphology	103
3.2.3	Growth of SAG networks	107
3.2.4	GaAs(Sb) buffered NWs	108
3.2.5	Crystal structure of buffered NWs	116
3.2.6	Interface to the transport channel	118
3.2.7	Field effect mobility	120
3.2.8	Electron coherence and magnetotransport	123
3.2.9	Superconductor/semiconductor hybrid nanowires	127
3.3	Conclusion	128
3.4	Outlook	129
4	Fabrication	131
4.1	Electron beam lithography in growth substrate preparation	131
4.1.1	Catalyst size and beam defocusing	132
4.1.2	Pattern alignment to substrate crystal axis	133
4.2	Fabrication of substrates with trenches	134
4.3	Oxide masked substrates	137
4.4	VLS Nanowire deposition	142
4.5	Device fabrication on VLS nanocrosses	144
4.6	Device fabrication on SAG NWs	148
4.7	Conclusion	150

5	Conclusion	151
	Appendices	153
A	Appendix Substrate fabrication recipes	153
A.1	Au pre-patterned (001) InAs and InP substrates with SiO_x mask	153
A.2	Au pre-patterned (111)B InAs substrates Al₂O_x mask	155
A.3	SAG substrate fabrication	157
B	Appendix Growth recipes	159
B.1	Growth recipe for inclined nanocrosses	159
B.2	Growth recipe for kinked nanocrosses	161
B.3	Growth recipe for SAG on InP wafers	162
B.4	Growth recipe for buffered SAG on GaAs wafers	163
C	Appendix Device fabrication	165



Introduction

Material development is a crucial aspect of many research fields in modern science. With the revolution in nanotechnology more and more novel nanomaterials are being developed on almost a daily basis, all around the world¹. One of the important subgroups of the nanomaterial family are nanocrystals. They have already paved their way into an immense amount of industrial applications. Especially semiconductor nanocrystals became of great importance in modern computing schemes².

As well described by Moore's law³, we seem to be approaching a limit of classical computing as we know it. The raw computational power that we can manage to squeeze onto a microchip is limited by a single transistor size. As the transistors get smaller and smaller the reliability of standard schemes is lost, because quantum mechanical effects start to govern the electron transport. As science thrives to overcome any limit it encounters, the idea of quantum computation was suggested as a solution⁴. Even though quantum computation may not replace classical computers, it has the potential to solve problems that are not accessible by present technology^{5,6}, i.e. computations in chemistry⁷ and cryptography⁸.

The quantum computation field is rapidly expanding and has already attracted attention of the big industry corporations, e.g. Microsoft, Google and IBM^{9,10}. Many different platforms are investigated on the path towards building a quantum computer, which can be for example based on photonics¹¹, superconducting qubits^{12,13} or spin qubits based on standard semiconductor technologies¹⁴. A more recent proposal¹⁵, suggests

the possibility to realize highly fault tolerant topological quantum computing based on Majorana fermions, which obey non-Abelian statistics¹⁶. For that purpose, semiconductor nanowires (NW) and NW networks became a promising material candidate¹⁷.

Regardless of the connection to quantum computing development, semiconductor NWs have received significant amount of attention from the scientific community since the pioneering work on vapor-liquid-solid (VLS) growth, presented by Wagner and Ellis¹⁸ in 1964. In this approach, nanocatalyst particles are used as collection centers for the precursor materials and mediate growth of thin elongated crystals. In parallel, selective area growth (SAG) of in-plane NWs was studied and also shown great promise in quasi 1-D structure growth^{19,20}. In the SAG approach material is deposited into lithographically predefined openings in amorphous masks on crystalline substrates. As the field evolved, so did the selection of materials available for NW synthesis, ranging from Si²¹ to ZnO²², II-VI semiconductors²³, III-V semiconductors² and more²⁴. In addition, the free-standing morphology was combined with growth of both radial and axial heterostructures and allowed for engineering of even more exceptional material properties²⁵. Moreover, the increased attention contributed to development of new growth methods and NWs were grown by variety of different techniques²⁶, including MBE (Molecular Beam Epitaxy), MOCVD (Metal Organic Chemical Vapor Deposition), CBE (Chemical Beam Epitaxy), MOVPE (Metal Organic Vapor Phase Epitaxy) or PECVD (Plasma Enhanced Chemical Vapor Deposition). The versatility of the methods pushed the field even further and NWs became a promising material in various applications²⁷ ranging from sensing²⁸, lasing²⁹ or solar energy conversion³⁰ to nanoelectronics³¹. The broad interest in semiconductor NWs drives the effort for attaining control over the synthesis and pushing the structures towards industrial applications.

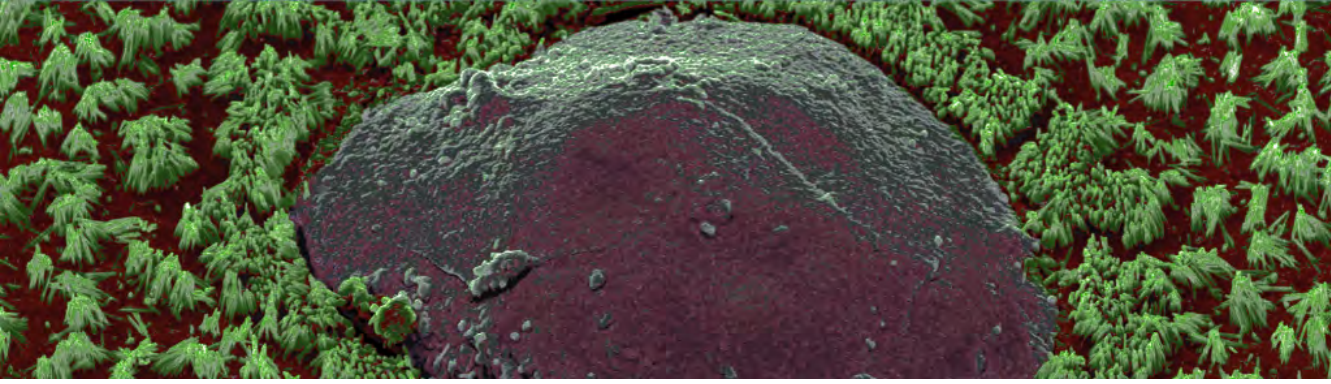
The presented work is motivated by a very specific aspect of the NW field, which are quantum transport experiments. Especially group III-V NWs have previously shown excellent transport properties in terms of mobility^{32,33}, spin orbit coupling³⁴⁻³⁶ and response to field effect chemical potential tuning. In addition, InAs and InSb NWs have recently shown potential in experiments that rely on superconductivity proximity effect^{17,37,38}. Combining all these features into 1-D nanowires offers the possibility to obtain the solid state realization of Majorana fermion quasi-particles³⁹⁻⁴¹. Another important step on the route towards topological quantum computation was proposed to be shift from single NW to multi-terminal device geometries⁴². At this stage of research, relevant experiments require constant development of new materials and improvements of material quality. The main purpose of this work was to develop NW based networks that satisfy the material requirements, previously set on the single NWs. In addition, the potential of presented structures reaches beyond this specific application and the results will hopefully inspire new experiments and developments within the NW community.

In **Chapter 1**, I will focus on a brief explanation of the material requirements set by Majorana based transport experiments and their role in the field of topological quantum computing. Most importantly, I address why is it interesting to develop high-yield and controlled growth of NW networks. The majority of the growth was done in a MBE system, which will be introduced together with the basic principles of operation. After, I will describe nanocrystal growth in the terms of thermodynamic and kinetic principles. The last parts of the introductory chapter are focused on the general mechanisms and aspects of VLS and SAG of NWs and basic description of their properties, with emphasis on NW networks.

Chapter 2 is focused on VLS growth and characterization of NW crosses. At first, I will discuss the role of catalyst nanoparticles in growth on non-standard substrate orientations. This is an important aspect in synthesis of 'inclined' nanocrosses which are discussed right after. The next part reports on in-situ changing of NW growth direction, which is demonstrated to be useful in growth of two different types of NW crosses, 'kinked vertical' and 'kinked planar'. The later sections of the chapter focus on the characterization of crystal structure and basic transport properties of the nanocrosses. Finally, potential applications of the structures are explored in terms of crystal phase quantum dot formation, scaling of the growth into larger networks and selective masking of in-situ semiconductor/superconductor hybrid structures.

In **Chapter 3**, I will present new results in SAG of InAs NW networks. The scalability of the SAG networks provides an important advantage over more commonly used VLS growth techniques, since it allows for wafer-scale parallel fabrication of electrical devices directly on the growth chip. Importantly, it is shown that using a GaAs(Sb) buffer layer for InAs SAG NW's improves their basic transport properties, e.g. mobility and gate tunability, and promotes elastic strain relaxation at the NW/substrate interface. Finally, the potential of the SAG NWs is extended by demonstrating coherent quantum transport on loop structures and hard superconducting gap in superconductor/semiconductor hybrid NWs.

Chapter 4 summarizes the non-standard fabrication steps, that were crucial for achieving the results and comments on some of the fabrication approaches that could be useful in further development of the presented structures.



1. Nanowire Networks

The first section of this chapter is dedicated to a general description of the Majorana braiding experiment and its role in quantum computing. That is important as it sets the specific material requirements and describes motivation for this project. The later sections are dedicated to crystal growth in MBE systems, which is specifically targeted at growth of nanostructures and NW networks.

1.1 Semiconductor nanowires in quantum computing

Low temperature transport properties of semiconductor NWs have been thoroughly investigated in various measurements⁴³ and often related to quantum dot experiments^{44–46} and spin orbit coupling characterization^{47–49}. Apart from their potential in standard qubit schemes³⁵, the 1-D nature of the NWs have opened the route for studying Majorana fermions in condensed matter systems³⁷.

In 1937, Italian physicist Ettore Majorana theoretically proposed that certain fermionic particles can be their own antiparticles⁵⁰, without violating the Dirac relativistic quantum mechanical formalism⁵¹. In the field of high-energy physics, the question whether there is a real elementary particle classified as Majorana, still remains to be answered. However, Majorana fermions were proposed to exist in the form of quasiparticle excitations in specifically designed condensed matter systems³⁹.

The property of Majorana quasi-particles in condensed matter systems relevant for computation is that they obey non-Abelian particle exchange statistics. Specifically, their ground state is degenerate and adiabatic exchange of the quasiparticles non-commutatively changes the state of the system from one ground state to another. That implies that information can be effectively encoded and manipulated throughout this operation⁵². Such exchange statistics would then provide a platform for a non-trivial topology, which protects the system from quantum decoherence, i.e. protects it against local perturbations. This stability of the quantum state is what makes Majorana fermions so attractive for quantum computation.

In his paper, Kitaev³⁹ has shown that a 1-D chain of electrons with a specific pairing has two ground states, which are degenerate in energy. These Majorana states are delocalized to the ends of the chain and have zero energy. One of the states is empty, while the other is occupied by an electron, which provides a basis for qubit operations^{42,52}. From the material perspective, making of such a chain requires a p-wave superconductor. To realize such a system Lutchyn et al. and Oreg et al. proposed a material basis in Refs.^{40,41}, while setting the following requirements:

- 1-D system
- Strong spin-orbit coupling
- Large Landé g-factor
- Superconductivity
- Tunable chemical potential
- External magnetic field

That makes group III-V NWs coupled to a semiconductor an excellent candidate. Intrinsically, they combine their quasi 1-D nature with strong spin-orbit coupling and high electron mobility together with a good response to field-effect gating, i.e. tunability of the chemical potential. In addition, it has been shown that while connected to superconductors via low disorder interface⁵³, a superconducting gap with low density of in-gap states can be induced into the semiconductor NW^{54,55}. Indeed, not long after the suggestion, first signature of Majorana fermions was observed in the proposed system, where InSb NW was proximitized by NbTiN contacts and the whole system was tuned into the topological regime by applying magnetic field perpendicular to the spin-orbit direction and by a set of electrostatic gates³⁷. Following this work, multiple reports of Majorana fermion signatures have shown promising results on both InSb and InAs NWs⁵⁶⁻⁵⁹.

A guideline for the Majorana braiding experiment⁵², which would provide the tool for encoding the quantum information into a system containing multiple Majorana zero modes and become a final proof of their non-Abelian nature, was given by Aasen et al. in Ref. [42]. As mentioned, Majorana zero modes are generated in pairs, delocalized to the opposing ends of the proximitized NW. When two modes are brought together, they

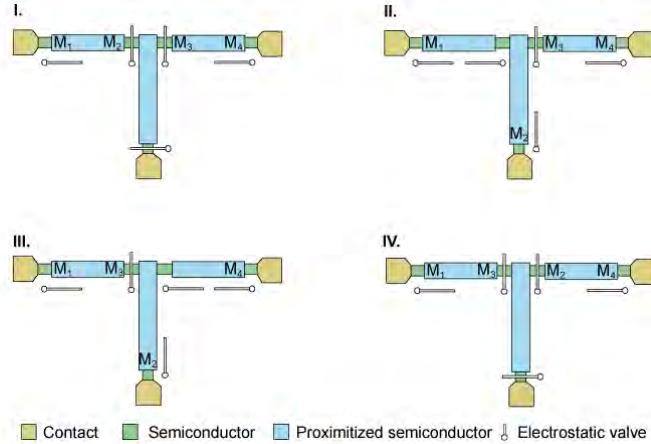


Figure 1.1: Schematics of a proposed braiding operation adapted from Ref. [42]. Here tuning the chemical potential of a SU/SE hybrid NW network by set of electrostatic gates (shown in steps I-IV.) is used to move the individual Majorana zero modes around the structure.

can either annihilate or combine into an electron with outcome defined by a specific set of fusion rules. If multiple modes are generated, manipulation of their respective pairing allows for tuning of the system into a well defined quantum state. The state is protected from fast decoherence by its topology and is described by the outcome of fusion of paired Majorana zero modes. This sets the basis for fault tolerant quantum computing.

The first proposed experiments rely on moving from single NW geometries to more complex NW networks^{52,60,61}. An example of a Majorana zero-mode manipulation is shown in Fig.1.1, where proximitized segments of a NW T-junction are tuned into the topological regime. This generates Majorana zero modes at each end of the segments (M_1 , M_2 , M_3 and M_4). The modes are then moved around by a combination of electrostatic gate operations. Subsequent sets of such operations can be used to initialize the qubit, braid in the information by manipulation of the Majorana states and finally read out the state of the system. Physical implementation is complicated and faces various difficulties. A basic building block could be for example a single hybrid superconductor/semiconductor (SU/SE) NW cross. The important requirements are therefore to produce high quality NW hybrids that can ultimately be effectively scaled up to large NW networks, since some proposals require complex geometries and braiding schemes⁶². Importantly, as will also be shown in this work, it is possible to grow such complex geometries by MBE, while maintaining the unique III-V material properties. Following sections describe the basics of MBE systems and related crystal growth processes.

1.2 Basics of Molecular Beam epitaxy

A wide variety of growth methods are implemented in order to grow low defect density and high purity semiconductor crystals. For bulk III-V semiconductor growth, Czochralski and Bridgeman methods and their variations are the most common ones⁶³. These methods are constantly improved and further developed⁶⁴. Such progress is also important for NW growth, because majority of high-quality thin film or nanostructure growth strongly relies on epitaxy to the substrate, where many bulk defects are easily inherited and growth results can be affected.

The majority of epitaxial thin film and nanocrystal growth methods rely on vapor mediated precursor transport. These methods can be divided into two types, depending on the character of the precursor which can be either in form of chemical vapors or molecular beams. The first type relies on chemical decomposition of the precursors on the substrate surface, like in chemical vapor deposition (CVD), MOCVD, MOVPE, metal organic MBE (MOMBE) etc. In the second case, atoms or molecules of pure precursors are used for direct growth without complex chemical reactions, like in MBE. Of course, many other methods or their variations can be used, e.g. PECVD or laser ablation, or combined together, e.g. hydrogen assisted MBE, CBE and many more.

The structures in this work were all grown using MBE for several reasons. One of the main advantages over the other methods is purity of the growth process. Since only the elements that are intended for direct incorporation into the grown structures are used, it is possible to achieve purity which is not attainable in systems that use alien chemicals for precursor. This is especially true for systems dedicated to be used for very specific material combinations. Another advantage is that the growth process itself is simplified due to the absence of the complex chemical reactions needed to dissociate the precursors in other methods. Such chemical reactions can complicate not only theoretical descriptions of the growth mechanisms, but also control over the growth itself, e.g. growth of doped structures. In addition the solid sources of pure material fluxes, in combination with in-situ growth monitoring by reflection high-energy electron diffraction (RHEED), allow for a straightforward control over growth rates and composition and also offer the possibility to achieve slow layer by layer growth. Main disadvantages include relatively slow growth rate, expensive maintenance, duration of loading and growth preparation. Another complication is that in the chemical based methods the dissociation of precursors can strongly enhance the selective growth parameter window on masked substrates, which can be difficult in MBE, as will be shown in chapter 3.

1.2.1 Molecular Beam Epitaxy system

The growth chamber of a MBE system is high purity environment, where the pressure can be as low as 10^{-12} Torr. Such high vacuum levels are usually maintained in systems that are dedicated to specific material combinations and growth of high mobility 2DEG materials⁶⁵. In this work, a Varian GEN II system was used for growth. Since the system is used for a wide range of materials (mainly Ga, In, As, Sb, Al, Au) and more importantly the majority of growth was carried on pre-processed substrates, it is typically idle at low end of 10^{-10} Torr. That can be related to the fact that the substrates are exposed to a wide variety of chemicals during processing, and therefore become source of impurities.

In order to maintain purity, the loading of samples into the growth chamber consists of various stages. The simplest case are non-processed wafers, which can be loaded directly as-received from the supplier. In contrast, pre-processed wafers require thorough cleaning in two steps. First, oxygen plasma is used to remove organic residues, e.g. resists used for lithography. Subsequently, an etch in diluted HF acid is used to remove most of remaining residues, while also stripping the native oxide. Typical MBE systems consist of a load lock chamber, a buffer chamber and a growth chamber. After loading the sample into load lock, the chamber is baked together with the samples and holders in order to desorb condensed water and other contaminants, while being pumped on by a turbo-molecular pump. Once the pressure reaches approximately 10^{-8} Torr a gate valve into the buffer chamber can be opened and the samples transferred. The low buffer chamber pressure is maintained by an ion pump, which can typically reach down to 10^{-11} Torr (low end of 10^{-10} in our system). In the buffer chamber, the sample holders are usually slowly heated one by one to temperatures given by the stability of the material and limits of the heating stage, in order to desorb additional impurities before transfer into the growth chamber. Both buffer chamber and the load-lock are often equipped with mass spectrometers, which allow to monitor composition of desorbed contaminants during heating. This is important especially for checking on the purity of fabrication processes, in order to minimize contamination.

A typical growth chamber arrangement is sketched in Fig.1.2. A rotational heated sample holder is connected to an ion gauge facing the opposite way, which allows for measurement of the direct flux coming from the effusion cells (beam equivalent pressure - BEP), before rotating and growing on the sample. The effusion cells are in principle high-vacuum compatible heating systems, which can be loaded with crucibles containing ultra-pure material. The cells can have either one or two stages of heating, where the first stage heats the material in the crucible and the second is located near the opening to the growth chamber. Maintaining the second heater on higher temperature prevents cooling from surrounding cryo panels and therefore possible material condensation at the cell edge

instead of inside the crucible. An important type of an effusion cell is a cracker cell. The cracker cell has an integrated valve used for flux control of high vapor pressure materials. In addition a secondary heater, the cracker, can be used in order to dissociate evaporated molecules, e.g. change the flux from As_4 into As_2 .

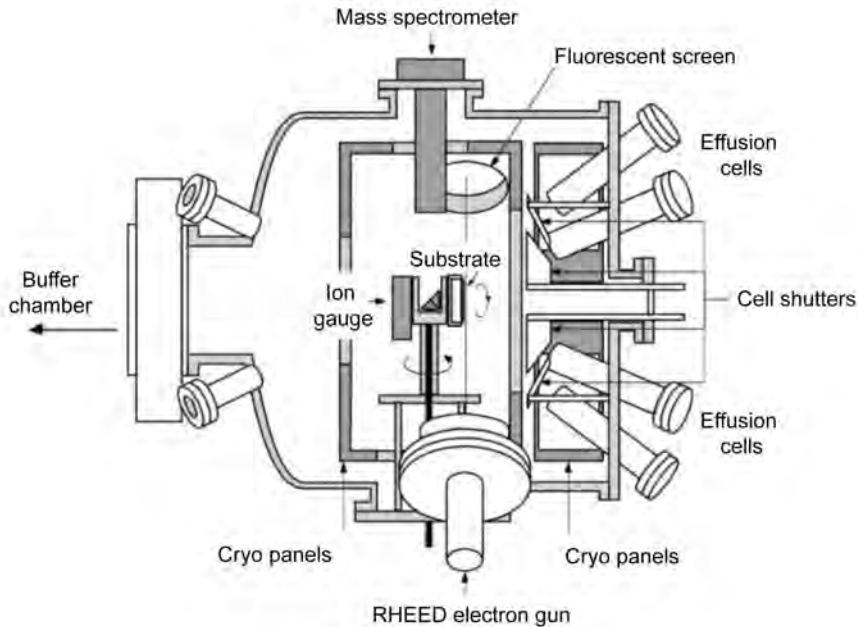


Figure 1.2: Schematics of a MBE system growth chamber, which is similar to the Varian GEN II chamber used in this work. The substrate is loaded from the buffer chamber and placed facing the effusion cells, which contain the high purity source materials. The beam flow can be turned on and off using the shutters and monitored by the ion gauge. The gauge is located on the rotational sample holder, on the opposite side of the substrate. A mass spectrometer and secondary ion gauge are used to monitor impurity levels and overall chamber pressure, respectively. The growth rate is monitored using RHEED which involves firing high energy electrons from the gun at the substrate and detecting them on a fluorescent screen, in form of diffraction patterns. The cryo panels that surround the growth chamber serve as cold traps and limit desorption of the trapped growth species and impurities. Adapted from Ref. [66].

An essential part of any MBE system is the RHEED electron gun, which provides a relatively simple tool for in-situ growth monitoring. The low angle of the incident electron beam and relatively low energy of the electrons allow to probe surface atomic arrangement by diffraction. It is possible not only to monitor layer by layer growth, but also to distinguish between different surface reconstructions or track surface roughness

by analyzing elongation of diffraction peaks displayed on fluorescent screen. Monitoring growth with RHEED allows one to extract the growth rate. The RHEED intensity changes during growth of a single mono layer, due to gradual change in the coverage of the surface, i.e. its roughness. Growth of several monolayers then results in periodic oscillations, where the period can be converted in thickness of deposited material as a function of time.

The whole chamber is typically surrounded by liquid nitrogen cooled cryo panels, which minimize any desorption of trapped impurities or growth species. In addition, a mass spectrometer can be installed for rough composition analysis and is very useful in determining causes of possible sources of leaks, contaminations etc. The high vacuum levels are maintained by cryo pumps. The heated holder is usually coupled to a thermometer which measures the temperature near the backside of the wafer. This type of measurement is not very reliable, since the temperature on the front side of the wafer can be affected by wafer roughness, material, thickness etc. Therefore, it is advantageous to have a heated view-port with a pyrometer, in order to measure the thermal emission directly from the substrate surface. The heating is necessary to desorb condensed growth species and maintain transparency of the view-port. We now turn our attention to the specific aspects of growth in MBE system.

1.2.2 Beam fluxes, growth temperature and calibration

The main parameters that can be used to control III-V semiconductor growth in MBE are growth temperature, beam fluxes, flux ratios (e.g. binary and ternary growth), type of growth molecules (e.g. As_2 , As_4 etc.), warm-up/cool-down procedure and native oxide desorption. Each of them should be carefully calibrated and has a significant impact on the crystal quality of grown structures.

The first step of III-V growth is desorption of the native oxide, in order to access the crystal structure of the substrate. This often requires heating of the sample far above the growth temperature. While heating III-V semiconductors, the surface tends to become unstable as group V atoms start to desorb (around 400°C for InAs). Therefore, the surface needs to be stabilized by sufficient flux of group V atoms, which is then maintained at elevated temperatures. The oxide desorption temperature can be effectively monitored by RHEED. As the substrate is heated, no Bragg peaks are visible due to the reflection from the amorphous oxide, but appear once the layer is desorbed. The oxide desorption temperature can then be related to table values. When the oxide is removed, RHEED also makes it possible to calibrate the growth temperature by monitoring the diffraction patterns of different surface reconstructions. Under specific conditions, the substrate surface reconstructs into various configurations, which have specific transition temperatures. Therefore, these 'real' surface temperatures can be probed and related to

the temperatures measured by the stage thermocouple and/or pyrometer.

The direct precursor beam pressures (BEP) are determined by the temperature set to the effusion cell and/or valve opening and can be measured in the form of pressure by the ion gauge connected to the sample stage. Unfortunately, the measured value is hard to transfer from system to system due to geometry, gauge type etc. Therefore, it is convenient to extract the atomic flux (in $\frac{n_{atoms}}{nm^2 \cdot s}$), which takes the specifics of the system into account. For group III calibration, the RHEED oscillation period can be used to measure growth-rate, since low vapor pressure of the materials typically make their desorption negligible. If the group V-III ratio is higher than one, the growth is considered as group III limited and increase of group V flux does not significantly change the growth rate. That means that all the group III atoms are considered to incorporate into the growing crystal and the real atomic flux of group III can be extracted, independently of group V flux. The measured monolayer (ML) per second growth rate is converted to $\frac{n_{atoms_{III}}}{nm^2 \cdot s}$, based on the material crystal structure and lattice constant.

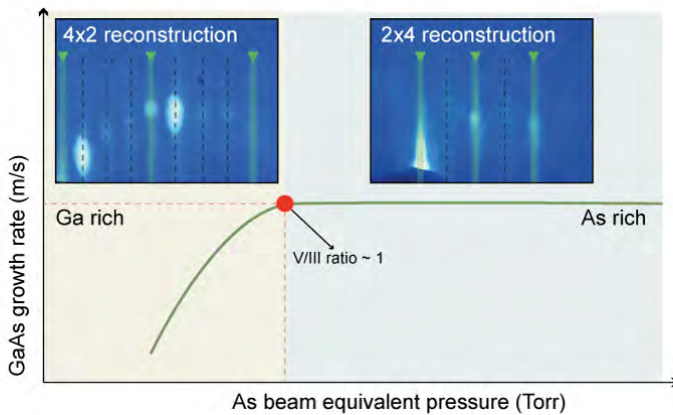


Figure 1.3: Typical dependence of GaAs growth rate on As beam equivalent pressure. The critical point (red) corresponds to change from As rich to Ga rich conditions. The insets show corresponding transition from 2x4 to 4x2 surface measured by RHEED along the [110] axis.

The situation can be more complicated for group V species, where temperature dependent desorption, affects the amount of atoms incorporated into the crystal. The simplest approach is illustrated in Fig. 1.3. Here, the growth of GaAs is initiated at high As flux and the growth rate is measured. After, the As flux is gradually reduced and the corresponding growth rates are measured. At a certain value of As BEP, the growth rate starts to decrease. This point also corresponds to transfer from As rich to Ga rich growth conditions and is defined by change of surface reconstruction from 2x4 to 4x2 (measurable

by RHEED along [110] direction). For a set temperature, the V/III ratio is defined as equal to one. Therefore, the real atomic flux corresponding to a certain BEP can be directly related to the calibrated group III atomic flux. The fluxes should be calibrated for different temperatures, due to the impact of temperature dependent group V desorption.

As mentioned above, a cracker type cell allows for control of As_2 and As_4 molecule ratio, by adjusting the cracker temperature. It was shown, that growth under As_4 increases the surface diffusion length of group III species⁶⁷. Therefore, selection of the As molecule type is important and may strongly affect the growth results^{68,69}. For example, using As_4 species in VLS growth increases the facet ad-atom diffusion length and reduces NW tapering⁷⁰. That is an important point, because thinking in terms of relative surface to surface diffusion length provides an important insight into nanocrystal growth.

Similarly to warm-up to oxide desorption temperature, the group V overpressure should be maintained during sample cooldown, in order to prevent surface decomposition and roughening. The cooldown rate and the stabilizing As flux can also have impact on the growth results. That is especially significant for SAG, where group III adatoms that are diffusing on the amorphous mask are exposed to the group V overpressure and can nucleate isolated crystallites.

1.3 Thermodynamics, kinetics and nanocrystal growth

Two general approaches – thermodynamic and kinetic – can be used for description of crystal growth. In essence thermodynamics determines the global statistical state and evolution of an equilibrium system. In contrast, kinetics works with rates and probabilities of the processes, often on the atomic scale. As for NW growth, aspects of both of the approaches need to be taken into account and their combination govern the observed phenomena since the system is usually far from equilibrium during growth⁷¹. As thermodynamics may still be used to describe the local properties of the system, the individual (especially surface related) processes that are often related to local energy barriers require kinetic description⁷². For the purpose of this work, it is important to make an overview of the processes and set the basic guidelines and terminology for description of the presented results.

1.3.1 Kinetics described by local thermodynamic equilibrium

The growth system is not in equilibrium during MBE growth, due to the ongoing energy transfer between the sources and the substrate. Therefore, an equilibrium reference state (ERS), was introduced by Krogstrup et al. in Ref. [72], which allows for the description

of this dynamic out of equilibrium system in terms of local thermodynamical parameters.

The local states of the system can then be described in the terms of Gibbs free energy, which then determines the chemical potential as $\mu_p = \frac{\partial G_p}{\partial N_p}$, where N_p is the number of atoms of specific atomic species in phase p . That means, that part of the system is considered to be in local equilibrium. The growth system consists of multiple co-existing phases: I) vapor phase, II) solid phase and III) adatom phase, as illustrated in Fig. 1.4 (a). Specifically, the vapor phase includes a mixture of beam flux and desorbed atoms and the adatom phase includes the diffusing species on the solid surface. In addition, liquid phase of an alloy between catalyst and the precursors is integral to VLS NW growth, as will be discussed in section 1.4. The natural choice of the reference for ERS is the bulk solid phase, where the chemical potential can be considered constant, due to the predetermined stoichiometry. Specification of the ERS then depends on parametric degrees of freedom and local equilibrium conditions set for the whole system.

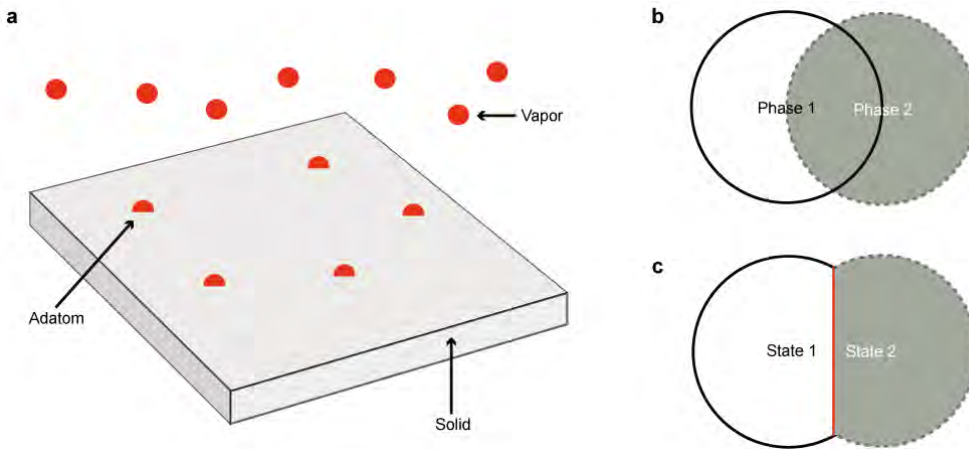


Figure 1.4: (a) Sketch of the three phases that are present in a basic MBE growth. (b) and (c) illustrate the idea behind combining the local thermodynamical parameters together with kinetic state transition approach.

The local Gibbs free energy and other thermodynamical parameters can be calculated from a local statistical ensemble, associated with a specific volume within a specific phase as illustrated in in Fig. 1.4 (b). Such local ensemble can be used to describe the local environment of the out of equilibrium system. At the same time it provides the necessary information to advance to atomistic description and importantly the state transition theory.

1.3.2 Kinetic transitions

A specific ERS state is now described by thermodynamical parameters given within the local statistical ensemble and related to the stable solid phase. Therefore, for two local overlapping states that occupy two different phases, it is advantageous to introduce a single Gibbs interface, as illustrated in Fig. 1.4 (c). The interface now separates two local states, within which the atoms are described by a specific set of parameters. This introduces a discontinuity of Gibbs free energy, which can be regarded as an energy barrier. From the atomistic point of view, a probability of a transition from state 1 to state 2 is given by $P_{1,2} \sim \exp\left(-\frac{G_{\text{barrier}} - G_{\text{state1}}}{k_b T}\right)$, where k_b is the Boltzman constan, T is the growth temperature and $G_{\text{barrier}} - G_{\text{state1}}$ is the difference of free energy Gibbs between the current state and height of the barrier. The idea behind such transition is illustrated in Fig. 1.5. This simple situation illustrates how the atomic fluxes can be determined using the state transition probability, given as

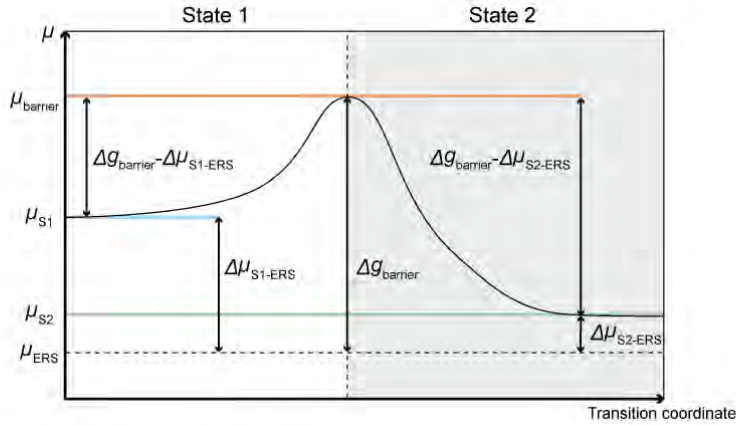


Figure 1.5: Illustration of the barrier and chemical potential relations associated with Gibbs interface between states S1 and S2. Here $\Delta g_{\text{barrier}}$ is the represents the normalized Gibbs energy of the barrier with respect to the chemical potential of the reference state μ_{ERS} . The chemical potentials μ_{S1} and μ_{S2} correspond to the states involved in the transition.

$$\Gamma_{S1 \rightarrow S2} = \text{constant} \cdot \bar{X} \cdot \exp\left(-\frac{\Delta g_{\text{barrier}} - \Delta \mu_{S1-ERS}}{k_B T}\right) \quad (1.1)$$

where the constant includes the specific properties of the system and \bar{X} includes atomic concentrations, i.e. the compositions within the states. The exponential includes the difference between the height of the barrier $\Delta g_{\text{barrier}}$ and chemical potential $\Delta \mu_{S1-ERS}$ of the initial state, with values taken with respect to the chemical potential of the ERS,

μ_{ERS} . That is in essence, the free energy difference between the state and the barrier, taken with respect to the local thermodynamics defining the transition. Then the flux of particles from state to state can be described as

$$\Delta\Gamma_{S1\rightarrow S2} = \Gamma_{S1\rightarrow S2} - \Gamma_{S2\rightarrow S1} \quad (1.2)$$

This simple relation sets the baseline for growth description within state transition theory. Importantly, the transition rates are related to atomic fluxes (i.e. currents) which can be used to determine the atomic concentrations within specific states. This further allows for the description of adatom densities, incorporation, desorption, diffusion and even nucleation in terms of atomic transition rates from one state to another. It is therefore possible to predict the behavior of an out of equilibrium system. This is done by studying local chemical potentials which are related to known values of fluxes, crystal surface orientations, material combinations, material vapor pressures, solubilities, sticking coefficients etc. In addition, systems that maintain a steady state, e.g. during VLS NW growth, are described mainly by stable transitions between different local phases. Therefore, it is possible to predict growth rates, stoichiometry, growth regimes etc., as was previously described by Krogstrup et. al in Ref. [72].

1.3.3 Surface energies and Wulff construction

Surface energies play an important role not only in nanostructure growth, as they dictate the specific shape and faceting of crystals^{73,74}. A specific facet corresponds to a plane terminated with cut through the bulk structure. The corresponding surface related lattice spacing and termination affect the chemical potential of given facet. Therefore, the surface orientation influences the growth related phenomena, e.g. growth rates, diffusion etc.⁷⁵, but also other processes as for example wet etch selectivity⁷⁶ and reactivity⁷⁷.

The Wulff construction is the common method for determination of equilibrium shape in crystalline nanostructures. The idea is illustrated by two examples in Fig. 1.6, where radial vectors (with magnitude corresponding to the surface energy in the given direction) are constructed from the center of the structure pointing to the local minima in free interfacial energy profile. This profile is set by the surface energy associated with a specific direction within the given crystal and significantly varies between different materials and compositions. By constructing tangent lines perpendicular to the radius vectors, a minimal area emerges within all the intersections. The border of this area reflects the preferential shape of a real crystal, which is volume independent.

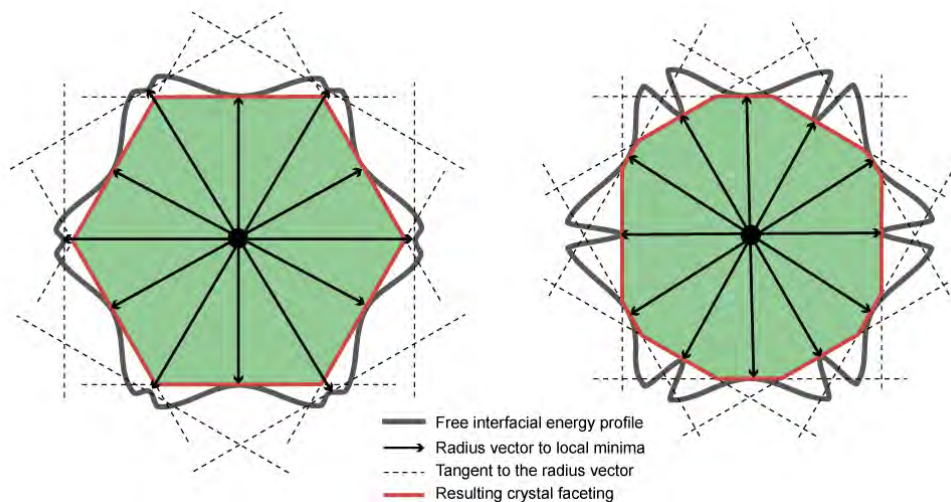


Figure 1.6: An example of two different Wulff shape constructions, where the crystal shape is determined by direction dependent surface energies.

This means that the specific shape of a crystal is strongly correlated to the substrate orientation. The surface energies can be controlled by change in the growth conditions⁷⁵, which therefore also affect the resulting crystal shape. In addition the independence of the volume can diminish if a spacial constriction is put onto the crystal, so that it can not freely expand to all directions. That is very important concept for SAG NWs, as will be demonstrated in chapter 3.

The minima in the surface energy are often associated with high symmetry orientations of the crystal. For example, the faceting of an InAs crystal growing along $\langle 111 \rangle$ direction tends to form $(11\bar{2})$ family facets, and therefore minimize the number of broken bonds. The situation can be different for other materials, e.g. InSb where the local cusps in surface energies are less pronounced, allowing for formation of additional facets and more round profile of the crystal. This allows for a simple first prediction of crystal faceting, by looking at the relevant stereographic projections. The free surface energies can be used to determine single crystal shape, but the situation complicates when an interface to a different crystal needs to be considered during heteroepitaxial growth. The lattice matching and strain accommodation play an important role and affect the crystal shape⁷⁸.

1.3.4 Growth regimes in MBE

Just as for the single crystal shape, the morphology of thin films during growth is governed by surface free energy ratios. During heteroepitaxial growth, the free energy of the interface between the crystal and the substrate needs to be considered⁷⁹. Ratio between three surface energies between crystal→vapor ($\gamma_{C\rightarrow V}$), crystal→substrate ($\gamma_{C\rightarrow S}$) and vapor→substrate ($\gamma_{V\rightarrow S}$) determines the shape of the grown crystal and bases the distinction of three different growth modes⁸⁰ as illustrated in Fig. 1.7.

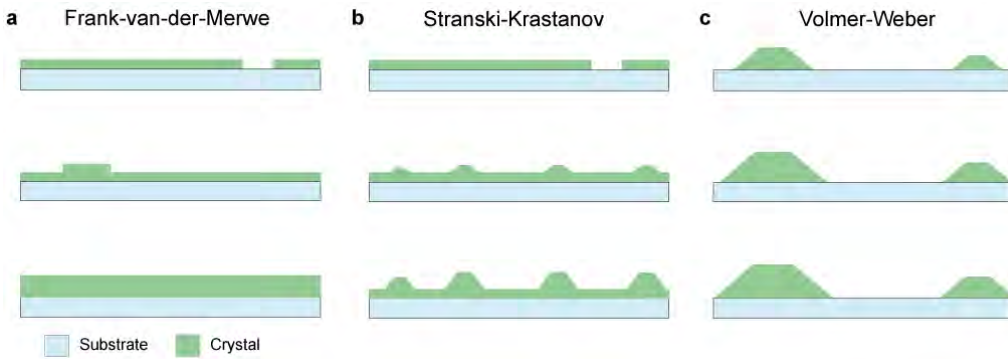


Figure 1.7: Illustration of the main thin film growth modes, typical for MBE, where (a) corresponds to Frank-van-der-Merve, (b) Stranski-Krastanov and (c) Volmer-Weber modes. The occurrence of a specific mode is defined by a specific free surface energy relations.

The Frank-van-der-Merve mode shown in Fig. 1.7 (a) is usually preferred for smooth thin film growth, since it is stable against dewetting and progresses layer by layer⁸¹. The Stranski-Krastanow mode first makes conformal layers, but the subsequent growth dewets upon them and form inhomogeneous islands with thicknesses of multiple monolayers, as illustrated in Fig. 1.7 (b). Homoepitaxial growth is initiated only after long growth, when the surface free energy of the substrate ceases to be important (i.e. the surface of the substrate stops influencing the free energy of the grown surface). A very roughened surface with disconnected domains of different sizes is characteristic for the Volmer-Weber mode (c). This type of crystallite formation in heteroepitaxial growth has shown great promise in growth of self-assembled quantum dots⁸².

It is important to note, that the growth becomes more complicated on inhomogeneous surfaces, where nucleation, diffusion and step flow are necessary to describe the complex growth processes. In addition, apart from the morphology, the surface composition also plays an important role. Even though this work is not focused on thin films, the growth regimes can be related to growth of buffered SAG NWs, as will be shown in chapter 3.

1.3.5 Nucleation

The grown surface can evolve in various ways: forming steps, terraces, kinks, adatom clusters etc. As suggested by Stranski⁸³, the specific evolution of a crystal during growth is associated with a local energy barrier. This barrier depends on how strongly are the atoms bound to the surface and therefore also on the amount of nearest neighboring sites that provide free bonds⁸⁴. This is described by the Kossel-Stranski model, where the desorption rate depends on the number of neighboring bonds, but the impingement rate is independent of local configurations. This approach can be used to describe growth of steps by movement of kink sites, which does not change the global surface free energy. As Kenneth points out in Ref. [85], application of this idea to a simple cubic crystal, contains the essence of why there is a strong anisotropy in growth rate of certain crystals and still serves as a basis for modern statistical growth modeling methods. Therefore, there is a clear connection between growth of thin films and the kinetic approach described above.

For growth on almost ideal atomically flat surface, the incorporation rate can be low due to absence of incorporation sites. In this case, further growth changes the global surface energy, as it changes the area and facet ratios of the surface. At the elevated temperatures of MBE growth, the phase above the flat surface can reach a certain level of supersaturation, which is needed for nucleation of a new solid layer. That provides the step necessary for further growth (in the form of highly probable incorporation sites). In essence, nucleation describes how cluster of atoms removed from one phase is transformed into a cluster of atoms in another phase. This can be described in terms of overcoming a barrier which needs to be surpassed in order to nucleate the new layer⁸⁵.

Within the nucleation theory, the free energy difference required for nucleation of a cluster of certain volume can be written in a simplified manner as $\Delta G_N = -V \cdot \Delta\mu_V + S \cdot \sigma$, where V is the volume of the nucleus, $\Delta\mu_V$ is the chemical potential associated with free energy required to add atoms to the solid phase per unit volume, S the surface area associated with the nucleation process and σ is the surface free energy per unit area. A derivative of this equation can be easily related to a critical size of a nucleus, which is necessary to initiate the nucleation process under given growth conditions and become the mediator of further growth⁸⁵.

The connection to the Kossel-Stranski model is that the nucleation process provides new sites, that allow for growth of new layers on flat surfaces via step flow. Therefore, the overall growth rate is related to another transition equation, which describes rate at which the critical size nuclei are formed and can be expressed within the kinetic formalism as

$$J = J_0 \cdot \exp\left(-\frac{\Delta G_{critical}}{kT}\right), \quad (1.3)$$

where $\Delta G_{critical}$ is the nucleation barrier associated with critical dimensions of the nucleus under given conditions. This is a very important mechanism for VLS NW growth, where the nucleation is mediated by the liquid phase, as will be described below. The interface of the solid NW top-facet is initially atomically flat and the growth progresses via step flow from a nucleus solidified from the supersaturated liquid phase⁸⁶. The last part of this section will be dedicated to the adatom phase and importance of diffusion in NW growth.

1.3.6 Diffusion in crystal growth - The adatom phase

The adatom phase consists of the atomic or molecular species, which exist within the interval in-between the impingement on the growth surface and subsequent desorption or incorporation. Diffusion describes motion and distribution of the particles during their lifetime on the substrate surface⁸⁵. Such motion can be described either from the macro or microscopic point of view. The macroscopic approach allows for description of particle fluxes, concentration profiles or driving forces, whereas the microscopic one provides the phenomenological coefficients and particle site to site jumping frequencies⁸⁷.

The ERS introduced above provides the local thermodynamical basis which allows for description of the driving forces and fluxes which drive the local diffusion mechanisms. For growth, the main driving force is associated with chemical potential gradients, i.e. particle concentrations in regions with lower chemical potential. This is described by the Fick's first law $\vec{J} = -D \cdot \nabla c$, where \vec{J} is the diffusion flux, c is concentration and D is the diffusion coefficient, which is set by the type of diffusion phenomenon. The time evolution of a simple diffusive system can be described with Fick's second law $\frac{\partial c}{\partial t} = -\vec{J}$, which is a form of a general continuity equation for conservation of diffusing species. This equation accounts for accumulation of the diffusing species and serves as a basic tool for description of many types of diffusion phenomena⁸⁷.

In crystal growth, the diffusion coefficient is coupled to the diffusion length $\lambda = \sqrt{D \cdot \tau}$ and the adatom lifetime which is defined by the desorption and adsorption components as $\tau = (\tau_{adatom \rightarrow solid}^{-1} + \tau_{adatom \rightarrow vapor}^{-1})^{-1}$. Both the diffusion constant and the adatom lifetime can be expressed within the means of the kinetic formalism described above⁷². For diffusivity we can in simplified form write

$$D_{adatom \rightarrow adatom} = \text{prefactor} \cdot \exp\left(-\frac{\Delta g_{adatom \rightarrow adatom} - \Delta \mu_{S1-ERS}}{k_B T}\right) \quad (1.4)$$

and similarly for the lifetime, which consists of two components

$$\tau_{\text{adatom} \rightarrow \text{solid}} = \text{prefactor} \cdot \exp\left(-\frac{\Delta g_{\text{adatom} \rightarrow \text{solid}} - \Delta \mu_{S1-ERS}}{k_B T}\right) \quad (1.5)$$

or

$$\tau_{\text{adatom} \rightarrow \text{vapor}} = \text{prefactor} \cdot \exp\left(-\frac{\Delta g_{\text{adatom} \rightarrow \text{vapor}} - \Delta \mu_{S1-ERS}}{k_B T}\right) \quad (1.6)$$

where Δg describes the barrier associated with the relevant phase transition. The prefactor depends on the details of the structure and growth conditions, e.g. impingement rates, incorporation rates, incorporation site distance, desorption rates etc. Since the surface chemical potential plays an essential role in determination of the barriers, diffusion is a strongly surface dependent process. It also often plays a crucial role in crystal growth, especially for MBE where the diffusion length can be very long⁸⁸.

The adatom phase concentrations can dramatically vary on specific facets and significantly influence growth results. In VLS growth, the adatoms contributing to supersaturation by diffusing into the liquid phase can affect the crystal morphology^{89,90} and their absence can even completely suppress the NW growth. Additionally, SAG NWs exhibit different faceting depending on the NW alignment with respect to the substrate. That sets the ratio between surfaces involved in growth. Therefore, the resulting NW morphology can be partially explained by differences in surface orientation dependent diffusion. With the formalism and arguments given in this section, we will now progress towards the description of VLS NW growth and relevant phenomena.

1.4 Vapor-Liquid-Solid NW growth

After the first report by Wagner and Ellis¹⁸, the VLS mechanism and its variations became the major method for synthesis of semiconductor NWs⁹¹. The basic principle is shown in Fig. 1.8. First a catalyst nanoparticle is placed on a crystalline substrate, (a). The (111)B substrate orientation is typical choice for VLS NW growth, since it has been shown that it is the preferential low energy orientation for NW nucleation⁹². After, the sample is heated up and the precursor fluxes are introduced. The melted liquid catalyst is supersaturated with the precursor atoms as shown in (b), and layer by layer growth is initiated resulting in formation of crystal, (c). Maintaining steady income of the precursor atoms subsequently results in formation of a NW like free-standing structure (d).

A more detailed explanation is necessary to understand the details of the solidification process. For an ideal solution, supersaturation is the change in chemical potential resulting from difference in real C and equilibrium C_0 concentrations and can be simply expressed as $\delta\mu = k_B T \ln(\frac{C}{C_0})$. From the perspective of the introduced kinetic formalism, the concentration C_0 corresponds to the ERS. The idea can be applied for description of a system, where a liquid catalytic nanoparticle is driven into supersaturation by a stable incoming flux of precursors, as shown in Fig.1.8 (e). The momentary state of the alloy of the catalyst and precursors follows the eutectic phase diagram of the materials. The figure illustrates following steps of NW growth: I. The excess chemical potential $\delta\mu$ gives rise to a driving force for solidification of crystalline nuclei at the interface between the liquid catalyst and the substrate; II. The nucleus provides a step site for 2-D growth at the interface. Once a monolayer is finished, there are no sites which would promote further 2-D growth. In addition, the precursor concentration in the liquid was lowered by incorporation of atoms into the solid; III. If the precursor flux is maintained, the supersaturation level required for nucleation is reached again and a new nucleation event occurs, followed by 2-D growth of a full layer. Repetition of these events corresponds to a layer by layer growth in a steady state⁹³. This is localized to the interface between the liquid catalyst and solid phase and can progress faster than competing 2-D growth on the surrounding substrate.

Here the term 'catalyst' refers to the liquid phase, but in literature other terms such as seed particle, droplet etc. can be found. The discrepancy comes from the uncertainty surrounding its catalytic role⁹⁴. The role as a collection center for precursor atoms is clear. On the other hand, the catalytic role (i.e. lowering of the nucleation barrier) can depend on growth parameters and selected material combinations. During growth, the area of contact between the catalyst and the solid phase, which is given by its volume and contact angle, is of great importance. The catalyst wetting dynamics is strongly correlated to the NW diameter⁹⁵, affects the NW crystal structure^{89,96} and can be used for changing the

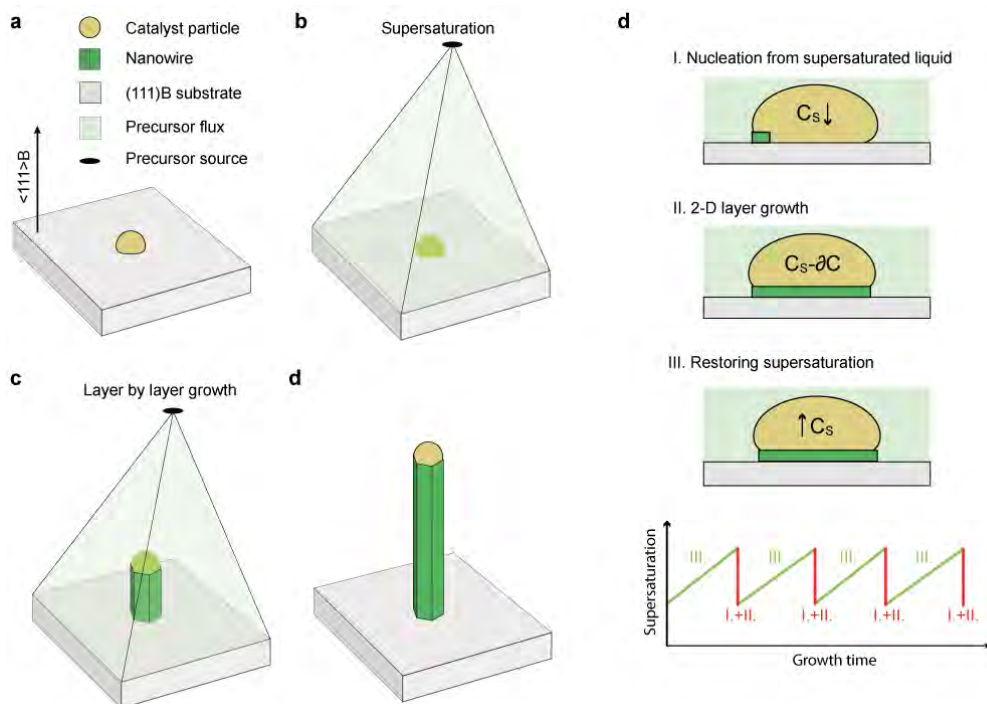


Figure 1.8: Schematics of VLS NW growth. (a) A catalyst nanoparticle is placed on typically (111)B oriented crystalline substrate. (b) Precursors are introduced in order to reach supersaturation of the catalyst. (c) Reaching the critical supersaturation results in nucleation and subsequent series of nucleation events and layer by layer crystal growth. (d) A free-standing faceted NW is grown, while the catalyst remains on the top-facet. (e) Scheme of the cycle of steady state layer by layer growth, where concentrations of precursors C_S correspond to supersaturated state and $C_S - \delta C$ to state after a monolayer is grown. The bottom panel shows the cycle in form of dependency of supersaturation on growth time.

NW growth direction in-situ⁹⁷. An additional secondary role of the catalyst droplets in NW growth was shown in Pub. 2 and will be presented in chapter 2.

Two main mechanisms contribute to the precursor collection and therefore to reaching the supersaturation within the catalyst. The atoms can either directly incorporate from the vapor phase or diffuse into the catalyst from the adatom phase. From the kinetic perspective, multiple transitions between phases take place during growth as depicted in Fig. 1.9: I) vapor-liquid; II) vapor-solid; and III) liquid-solid, where the overall fluxes are given by the difference in adsorption and desorption between the phases. Note that here the solid phase is considered solely as the NW crystal. Additional transitions can be

considered within the adatom phase⁷², which include the surface diffusion contributions of mobile impinged atoms: IV) adatom-liquid which includes contribution of species diffusing from the NW sidefacets to the liquid phase and vice versa; V) adatom-vapor, accounting for the adsorption and desorption of diffusing species on the NW side facets from and to the vapor phase; VI) adatom-solid includes the direct incorporation of diffusing species from the NW sidefacets to the NW, i.e. radial growth; and VI) adatom-substrate, which accounts for the diffusion between the substrate and the already grown NW crystal. Here again, the phenomena is tightly related to the kinetic formalism and the phase transition rates. These transitions then govern the NW growth and can be tuned by growth parameters in order to modify the growth rate, growth directions, crystal structure and material stoichiometry.

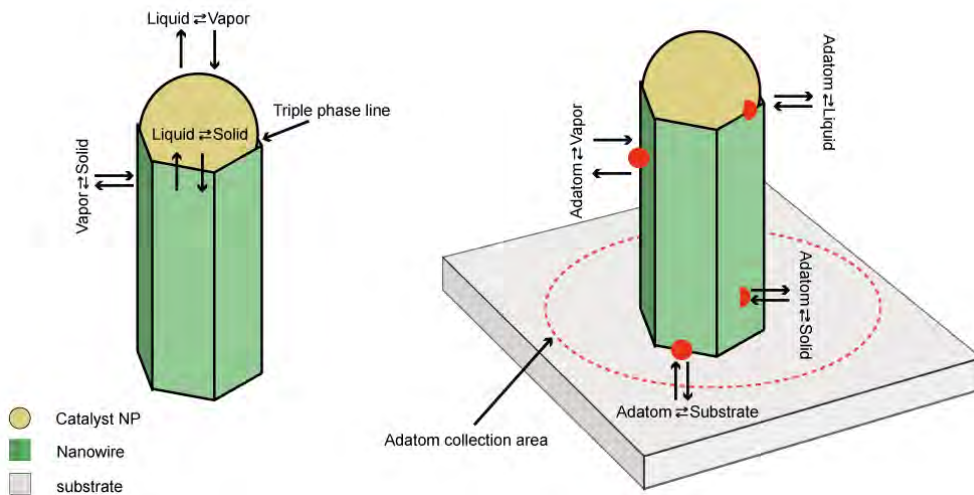


Figure 1.9: Schematics of phase transition contributions to NW growth, where the three main phases are described in the left panel and the transitions of the adatom phase in the right panel. The red circle on the right illustrates the adatom collection area, i.e. the area from which adatoms can diffuse to the liquid phase over the NW facets.

Due to the contribution of the adatom phase, VLS NW growth depends not only on the specific growth conditions, but also on substrate crystal orientation and morphology. The properties of the substrate in the close proximity of the NW set the size and properties of the 'adatom collection area', as shown in Fig. 1.9. The overall size of the collection area, which is defined by the diffusion length of adatoms on the substrate, affects the length of the NWs and symmetry of tapering⁹⁰. For example the diffusion length asymmetry along the $[1\bar{1}0]$ and $[110]$ directions can lead to asymmetrical NW tapering and formation of nanoflakes⁹⁸. As the NWs grow longer and exceed the diffusion length on the NW side facets, the material is more likely to incorporate near the stem of the

nanowire, which results in diameter gradient (NW tapering). The nanowires can also be radially overgrown intentionally, in a controlled manner. Reducing the growth temperature suppresses nucleation from the liquid phase and material can be directly deposited on the sidewalls in order to homogeneously increase the diameter or form various radial heterostructures⁹⁹.

As for the catalyst nanoparticle, various materials have been previously investigated and shown to have distinct effects on the NW properties^{100–103}. The choice of catalyst material affects the liquid eutectics and therefore have strong impact on the required growth conditions. Despite many interesting reports of alternative seed materials, Au remains the most typical catalyst.

1.4.1 Polytypism in InAs crystals

One of the important aspects of InAs NW growth is the crystal polytypism. The bulk InAs typically grows in the Zinc Blende F-43m, but the typical NWs grown in the $\langle 111 \rangle$ B direction adapt the Wurtzite P63mc structure^{104,105}. Figure 1.10 shows the WZ and ZB crystal structures projected from the typical [0001]/[111] NW growth directions and from the $[1\bar{1}00]/[11\bar{2}]$ directions which correspond to the related NW faceting. As described in Refs. [89, 96], such distinct crystal formation is caused by the surface energy relations at the triple phase line and the level of supersaturation, therefore depending on the overall growth conditions. These surface energy ratios between the phases can be correlated to the liquid catalyst droplet shape, i.e. the wetting angle dynamics. The favored condition for WZ nucleation is typically satisfied for large liquid volumes with small wetting angles and can be controlled by the V-III flux ratios during growth⁹⁶.

Due to the possibility of switching between different polytypes during growth, the NWs do not always maintain the same crystal structure, but form stacking faults along the [0001] or [111] directions. If the WZ stacking is intermixed with ZB, e.g. A-B-A-B-A-B turns into A-B-C-B-A-B, the natural stacking is interrupted and a stacking fault is formed. An example of a stacking fault in a WZ InAs NW is shown on TEM micrograph in Fig. 1.11. The formation of such defects is again related to free energy difference in formation of ZB and WZ crystals and optimized and stable growth conditions are a requirement for growth of stacking fault free NWs. Interestingly, it has been shown that the WZ is more likely to form in thin NWs (which are mostly targeted in this work), and therefore the stacking fault density can be reduced with the diameter of the NW^{106,107}.

The density of stacking defects has a significant effect on electron transport since there is a conduction band offset between the two phases, which acts as a barrier for electrons^{108–110}. Also other properties can be affected by defects, as for example mechani-

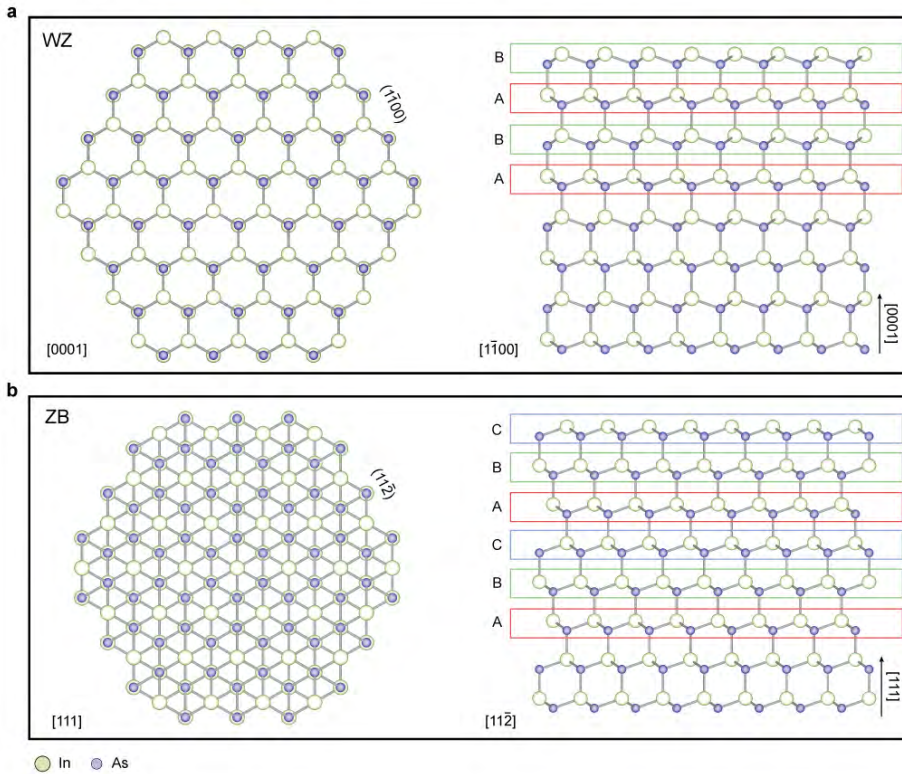


Figure 1.10: Schematics of the polytypes in InAs NWs. **(a)** WZ viewed from the $[0001]$ direction with $[1\bar{1}00]$ faceting (left panel) and from the $(1\bar{1}00)$ with highlighted A-B stacking. **(b)** ZB viewed from the $[111]$ direction with $(11\bar{2})$ faceting (left panel) and from the $[11\bar{2}]$ with highlighted A-B-C stacking sequence (In - green, As - blue).

cal properties¹¹¹. Therefore, significant effort is put into the synthesis of stacking fault free NWs^{112,113}. Alternatively, polytypism can be also intentionally controlled and used to form quantum dots in WZ/ZB intermixed structures¹¹⁴.

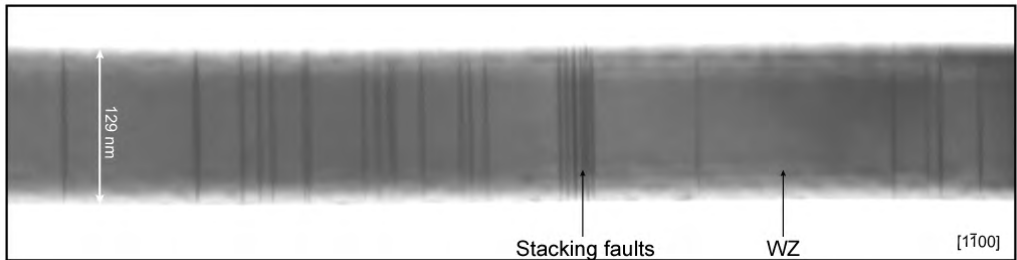


Figure 1.11: TEM micrograph of a single WZ InAs NW with clearly visible and highlighted stacking faults.

Many other defects, such as misfit dislocations in NW based heterostructures¹¹⁵, twinning¹¹⁶ or impurities¹¹⁷ can affect the growth results. Intense efforts are put into attempts to attain control over defect formation, but many transport and optical experiments still suffer from their impact on the NW properties.

1.4.2 Self-assembled, patterned and self catalyzed growth

NW growth can differ not only depending on the type of used catalyst material, but also on the way the catalyst droplets are synthesized. The simplest approach is to form the catalyst particles all over the substrate by thermal annealing of a thin film^{118,119}, which can be evaporated from an effusion cell, in-situ. This results in growth of NWs that are randomly dispersed over the substrate. In this case, the NW diameter and spacing can be controlled by evaporation and annealing conditions¹¹⁸. Alternatively, the substrates can be processed by electron beam lithography (EBL) in order to deposit catalyst material islands in specific patterns or arrays. It is possible to grow the NWs in predefined locations, as shown in Fig. 1.12. Compared to self-assembled growth, the electron beam lithography patterning allows for precise control of the catalyst island diameter on the same substrate*.

The control over catalyst volume is correlated to the NW diameter, which together affect its growth rate^{119,120}, as shown in Fig. 1.13 (a). The axial growth rate rapidly increases with catalyst volume, for small NW diameters (small catalyst volumes). This is related to the catalyst droplet surface curvature dependent increase in chemical potential,

*Here we refer to catalyst island diameter, since it is different from the catalyst droplet size into which the island dewets while annealing in the MBE system. The droplet size then also depends on the specific growth conditions when alloyed with the precursor materials.

known as the Gibbs Thomson effect¹²¹. As the liquid phase volume is decreased so is the precursor concentration, due to increase in desorption/adsorption ratio. This sets a limit for minimum catalyst volume that supports VLS NW growth. Above this limit the growth rate rapidly increases, until a stable wetting angle and the Gibbs Thomson effect contribution to the chemical potential diminishes¹²², as shown in Fig. 1.13 (b). As the volume is increased even further, the growth rate starts to drop again. That is because the material supply does not suffice for supersaturation of the catalyst, i.e. the group III concentration decreases.

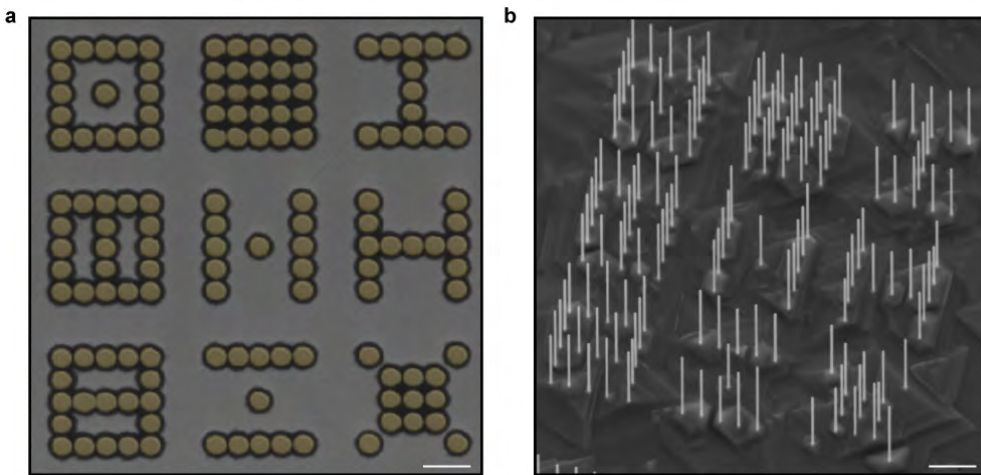


Figure 1.12: SEM micrograph of (a) gold islands deposited on InAs substrate in a pre-defined pattern and (b) an array of InAs NWs grown in the same arrangement, but from catalyst nanoparticles with 100 nm in diameter (30° tilt). The scale bars correspond to 1 μm .

Another factor that strongly affects the growth in MBE is the NW pitch (NW to NW distance)⁸⁸. When the NWs are brought close one to another, they approach the limit, where they start to share the adatom collection area. This can affect the adatom phase contribution to saturation and growth rate within the same growth, especially if regions with different patterning pitch are used. Another effect where the influx of precursors increases as NW spacing is lowered due to readsorption of precursors desorbed from neighboring NWs was proposed for various NW systems¹²³. This can have unwanted consequences on growth of from complex patterns, since the NW pitch can affect NW length distribution and morphology, based on relative position of the neighboring NWs.

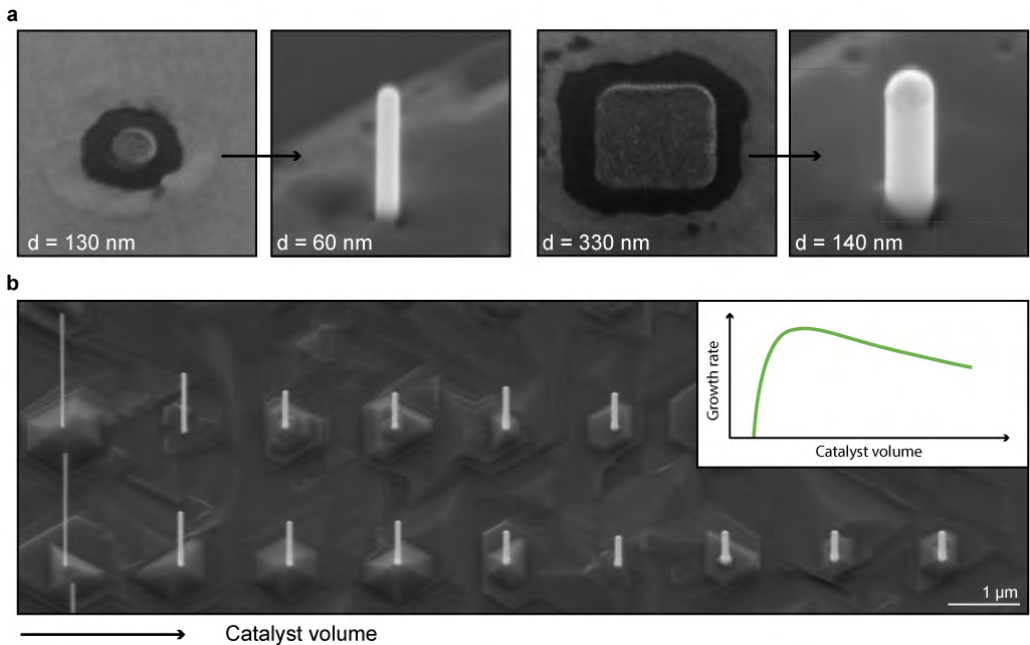


Figure 1.13: SEM micrograph of (a) gold islands of different diameter d , deposited within SiO_x mask on InAs substrate, together with SEM micrographs of NWs grown from catalyst of the same size. (b) Tilted SEM micrograph (30°) of an array of InAs NWs grown from different sizes of catalyst islands, which reflects the change in NW diameter and growth rate as a function of the catalyst volume. The inset shows expected dependence of axial growth rate on the catalyst volume.

An advantageous technique, allowing for even more precise control over the NW morphology is growth on patterned oxide masked substrates¹²⁴. The implementation of this technique can be more difficult in MBE compared to other methods like CBE, due to the low selectivity between growth on the mask and the substrate. At the relatively low temperatures typical for VLS growth of InAs NWs (around 420°C) the growth material tends to stick to the mask, which results in a roughened crystalline surface growth. Nevertheless, such a rough surface can be used in order to reduce the adatom collection area and allow for more homogeneous growth rate within complicated patterns, as will be shown in Chapter 2. An example of growth on InAs with wet etched SiO_x mask is shown in Fig. 1.12 and the details of fabrication will be discussed later in chapters 2 and 4 with detailed recipe given in appendix A2.

The last common approach is self-catalyzed growth. Here, no catalyst pre-deposition is used, but either pinholes or etched openings in an oxide mask serve as accumulation centers for group III adatoms, which take role of the liquid phase in the standard VLS

growth^{125–127}. This method is advantageous due to the possibility to remove foreign catalytic material from the growth process and therefore reduce the catalyst induced impurity levels¹¹⁷.

In this work, the majority of samples was grown from EBL patterned substrates. This method offers great control over the NW positioning and therefore opens the possibilities for engineering more complex structures in-situ, e.g. merging of multiple NWs together (shown in Chapter 2). Another important aspect of tuning the NW properties is the NW growth direction and associated morphology, which will be briefly reviewed in next section.

1.4.3 Changing NW structure and growth direction

The VLS NWs are known to typically grow in the $\langle 111 \rangle_B$ direction¹²⁸, but growth along many other orientations have been previously reported¹²⁹. There are many properties of the NWs that can be tuned by the crystal structure engineering, e.g. defect formation^{123,130}, spin-orbit coupling^{131,132}, morphology¹³³ and SU/SE heterostructure matching¹³⁴. The change of these properties is in often related to nucleation into different direction which modifies the longitudinal crystal structure. Furthermore, the NW crystal structure can also be modified by changing the substrate orientation¹³⁵. However, under most typical conditions the NWs maintain growth along the preferential $[111]_B$ direction (depending on growth conditions and substrate preparation¹³⁶). For example growth on (001) substrates can simultaneously yield NWs growing along either the $\langle 001 \rangle$ and $[111]_B$ directions. The $[111]_B$ NWs typically adapt WZ structure and grow under an angle inclined by $\sim 35^\circ$, whereas the NWs grown along the $\langle 100 \rangle$ direction are ZB and grow straight out of the plane of the substrate, as can be seen in Fig.1.14. Here, the same growth on pre-patterned substrate results in formation of two different types of NWs with different orientations and crystal structure.

Apart from influencing the growth direction by the choice of the substrate orientation, it can be also controlled in-situ, as previously reported in Refs. [97, 137–142]. Most of the approaches rely on an abrupt change of growth conditions, while being related to the catalyst and wetting conditions during growth. This provides an interesting mechanism for modification of the crystal properties, but also for in-situ engineering of complex structures, as will be shown in chapter 2.

The VLS approach offers a significant variability and has a lot of potential for in-situ structural engineering. In addition, the free-standing geometry is beneficial for growth of complex heterostructures and provides an interesting platform for studying the fundamentals of electron transport in semiconductor based devices, due to the possibility

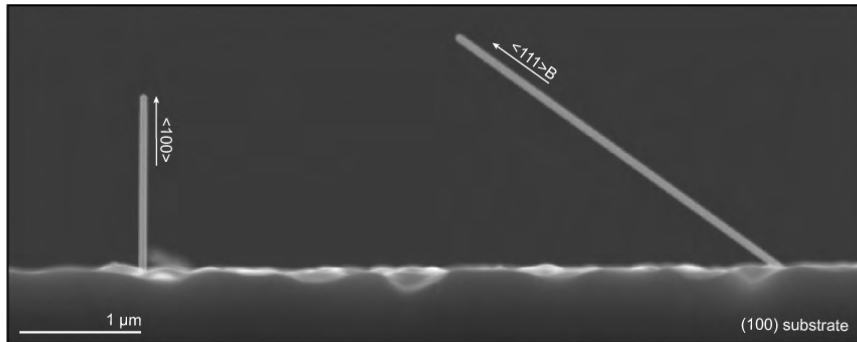


Figure 1.14: Cross-sectional SEM micrograph of NWs grown along $\langle 100 \rangle$ and $\langle 111 \rangle_B$ directions within the same growth on (100) substrate.

to achieve quasi 1-D spatial confinement of electrons in high quality crystal. The major issue is the scalability of fabrication. To address this, an increasing number of groups are turning their attention towards selective area growth.

1.5 Selective Area Growth of nanowires

The selective area growth is a relatively old method^{19,143–147} compatible with a variety of epitaxy based growth techniques and materials. It relies on growth selectivity between the surfaces of an oxide mask and crystalline substrate, as shown on an example in Fig. 1.15. In a typical scheme, a crystalline substrate is covered by dielectric layer, which is patterned by lithographically defined openings. The openings in the mask then serve as pre-designed areas for epitaxial growth.

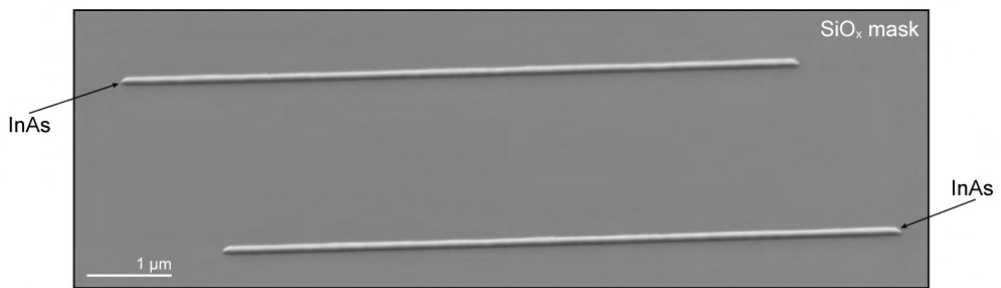


Figure 1.15: Tilted SEM micrograph (30°) of two SAG NWs selectively grown in lithographically defined openings in SiO_x mask on InP Fe doped (001) substrates.

Full selectivity of SAG growth is achieved when no material sticks on the mask and controlled crystal growth is maintained within the mask openings¹⁴⁷. This type of growth occurs within a specific growth parameter space, the selectivity window. The lower bound corresponds to a situation where desorption from the mask is equal or higher than the incoming material flux. The upper bound corresponds to the transition where desorption within the mask openings becomes equal or larger than the incorporation into the crystal. The main growth parameters that affect the selectivity are fluxes and growth temperature^{148–151}. In addition, the selectivity window is not affected only by the growth parameters, but also by material properties of used dielectric, since it can be related to the sticking coefficient and adatom diffusion length on the mask surface¹⁵¹.

The InAs and GaAs SAG NWs naturally adapt ZB structure, as they stem from ZB substrates. On the other hand, their crystal structure and morphology is strongly related to the substrate crystal orientation and spatial confinement of the mask^{152,153}.

The obvious advantage of SAG NWs is that the structures can be defined by standard top-down techniques, which gives the option to design arbitrary patterns. Therefore, the method also allows for large scale bottom-up growth of complex NW-like structures and networks^{154,155}. At the same time, the top-down processing is done prior to the growth step and does not directly influence grown surfaces.

Important progress was recently reported by Desplanque and Fahed in Refs. [153, 156], who have shown that the SAG method is feasible for growth of planar NW heterostructures by hydrogen assisted MBE. In their work, they used a buffer layer in order to selectively etch the InAs SAG NW part away and use in other experiments. In 2018, Friedl et al. reported electronic characterization of single SAG NWs grown on GaAs buffer layers and growth of well defined buffered SAG networks¹⁵⁴. In parallel, our results have demonstrated compatibility of InAs SAG NWs and networks with SU/SE epitaxy [Pub. 5] and that growth of InAs on GaAs(Sb) buffer layers improves electrostatic gating response of the devices and supports long electron coherence length in loop structures [Pub. 4]. Soon after, the Desplanque extended previous work in Ref. [157] and presented thorough measurements of InSb SAG NW metal-oxide-semiconductor field-effect transistors.

The SAG approach of InAs NWs will be discussed in detail in Chapter 3. The next section is dedicated to an overview of the major works on approaches that have been published about in-situ growth of NW networks up to date.

1.6 In-situ III-V Nanowire networks - an overview

As for the synthesis of NW networks, top-down approaches may seem to be a choice that offers great design variability and scalability. On the other hand, the fabrication often affects the crystal quality and makes the structures difficult to utilize in quantum transport experiments. To prevent external damage to the grown crystals, significant efforts are being put into research of in-situ methods, that would not only allow for formation of high-quality junctions, but also for growth of networks consisting of various in-situ grown heterostructures. Here, the VLS and SAG methods are excellent candidates, that provide enough control over the growth.

Even though VLS NW growth was successfully used to provide single NWs with promising transport properties^{33,37,57}, growth of NW networks seems to be very complex and often requires advanced growth techniques^{158,159}, complex substrate fabrication¹⁶⁰ and innovative NW transfer methods^{161–163}. The SAG approach offers a more scalable solution^{154,155}, yet without reports on growth of III-V multi-terminal electronic devices. The feasibility of SAG approach for growth of NW networks was greatly extended in Ref. [154], by demonstrating growth of well faceted and continuous NWs on top of a selectively grown buffer layer. In parallel, we have reported first low temperature transport measurements on SAG grown networks [Pub. 4, Pub. 5] together with SU/SE heterostructure growth compatibility. Apart from VLS and SAG the template assisted growth was recently shown to be suitable for growth of ballistic NW networks¹⁶⁴. Despite the high crystal quality, the encapsulation of the NWs in a Si template, so far seems to make this method less compatible with in-situ growth of radial heterostructures, but offer great potential for further developments.

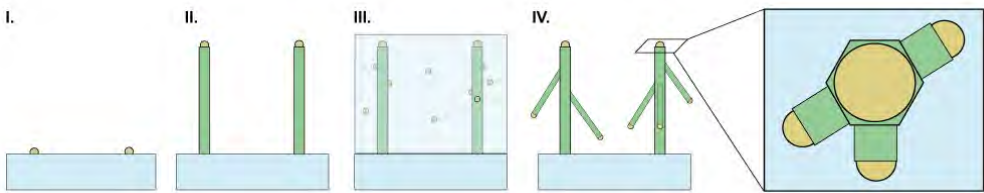


Figure 1.16: Schematics of the branched NW growth mechanism developed in Ref. [158]. I. Catalysts are deposited on crystalline substrate. II. NW stems are grown via VLS mechanism. III. Aerosol catalyst nanoparticles are deposited on the grown NW stems. IV. Growth of the branches continues from the particles deposited on NW facets. The zoom-in shows a top-view of the final structure, illustrating the 6-fold (faceting related) directionality of the branch growth.

The first report of branched semiconductor NW structures was presented by Dick, et al. in 2004 in Ref. [158], where a two-step growth process was used in order to grow 6-fold symmetrical tree-like structures, as illustrated in Fig.1.16. In the first step, GaP NWs were grown from Au catalysts by MOCVD. After, additional aerosol Au nanoparticles were randomly deposited on the grown NW stem. The second growth step resulted in growth of NWs perpendicular to the stem. Despite the secondary catalyst position after deposition, the NW branches grow along 6-fold symmetrical directions of the hexagonal NW stem, i.e. follow the directions along the NW side-facets. The same group pushed this mechanism further by growing on pre-patterned substrates, where rational positioning of the catalysts by EBL allows for growth of the stems at predetermined positions and for merging of multiple branched NWs together¹⁵⁸. In addition, polymer masks were used before the secondary catalyst deposition in order to attain control over the height of the branch formation¹⁶⁵. The potential of the method was further extended by application for other materials¹⁶⁶. The same approach was used by Wang et al., where the process was repeated multiple times to synthesize hyperbranched structures¹⁵⁹. The transport through such structures was characterized by Suyatin et al. in Ref. [167] and it was shown that the junctions are electrically transparent, but exhibit complicated non-linear behavior.

Another benchmark method for VLS synthesis of branched NWs was set in 2013 by Dalacu et al. in Ref. [160]. In this work, CBE was used to grow SAG nano-pyramids, that were patterned with catalyst droplets and their (111)B facets were used as standard surface for NW growth. Growth from two opposite facets was then used to merge two NWs together, as sketched in Fig.1.17. Even though this particular work was used to investigate catalyst/catalyst interaction during the NW merging process, it served as a guideline for other recent reports. First, Rieger et al. have shown similar growth of InAs crosses on wet-etched Si pyramids in Ref. [168]. Soon after, InSb hash-tag like structures grown in a similar manner on etched substrates were shown to support ballistic¹⁶⁹ and coherent quantum transport properties¹⁷⁰.

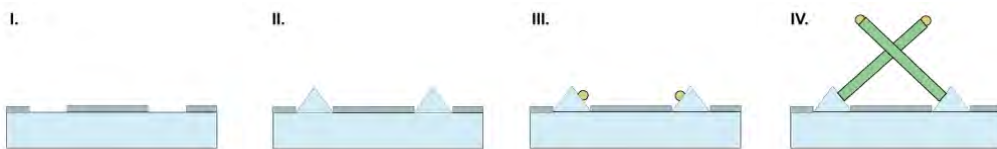


Figure 1.17: Schematics of the branched NW growth mechanism developed in Ref. [160]. I. Crystalline substrate is patterned with an amorphous mask. II. Pyramidal structures are selectively grown along a specific crystal direction, in order to form opposing (111)B facets. III. The pyramids are patterned with catalyst particles. IV. NWs are grown from opposing facets by VLS mechanism which allows them to merge into nanocrosses and other branched structures.

T-shaped and cross structure formation was demonstrated by Kang et al. in Ref. [171], by growing directly on (100) substrates. Here, the NWs nucleate into two degenerate $\langle 111 \rangle_B$ directions and merge into crosses in the same manner as in the case of Dalacu, while growing inclined with respect to the substrate plane. The work was targeted on InAs crosses, and shown that a Zinc-Blende (ZB) segment tends to form within the junction in between the two merged WZ NWs. That is different for InSb, where growth in ZB basis allows for single crystalline junction formation. In this work, it will be shown, that this type of growth can be used to form uniformly faceted structures with a symmetrical ZB inclusion within the junction [Pub. 1], that can be used as a crystal phase quantum dot [Pub. 3].

Promising results were reported by the group from TU Delft, where growth of InSb NWs from InAs stems resulted in formation of nanocrosses¹³⁸, which have shown promising transport properties. The directionality was later reduced from 6-fold to 2-fold by the same group using (100) substrates, which dramatically increased the nanocross yield.

This to my best knowledge summarizes the reported in-situ attempts for synthesis of high-quality III-V NW junctions. It seems that from the perspective of scalability and variability the SAG offers better solution than VLS growth. On the other hand, the free-standing nature of VLS NWs may have various advantages in terms of growth of both axial and radial heterostructures. Even though it may be difficult to push the VLS based structures towards industrial application, they may still play an important role in fundamental physics studies. Lets now turn to the last part of this chapter, which is SU/SE hybrid epitaxy.

1.7 Semiconductor/Superconductor hybrid NWs

The breakthrough experiment which showed the signatures of Majorana fermions in condensed matter systems³⁷ was performed on a semiconductor NW with ex-situ evaporated superconductor. Later, it has been shown, that the superconductivity proximity effect can be significantly enhanced by in-situ epitaxial growth of superconductor on selected facets of the NWs⁵³, as sketched in Fig. 1.18.

The in-situ deposition and crystal matching engineering, which are allowed by facet selective deposition, improve the interface transparency between the semiconductor and the superconductor. This is mainly due to avoiding ex-situ oxide removal and the possibility to precisely control the superconductor layer growth within MBE. As previously reported in Ref. [54], this type of structures can be used to induce so called 'hard superconducting gap' into the semiconductor. This means that the proximitized system in the can be tuned

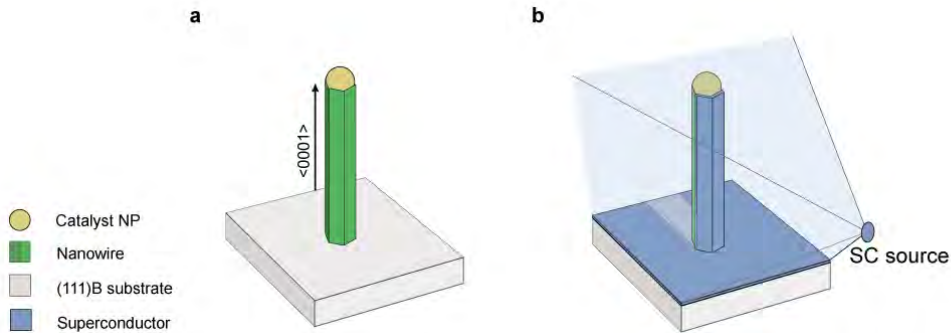
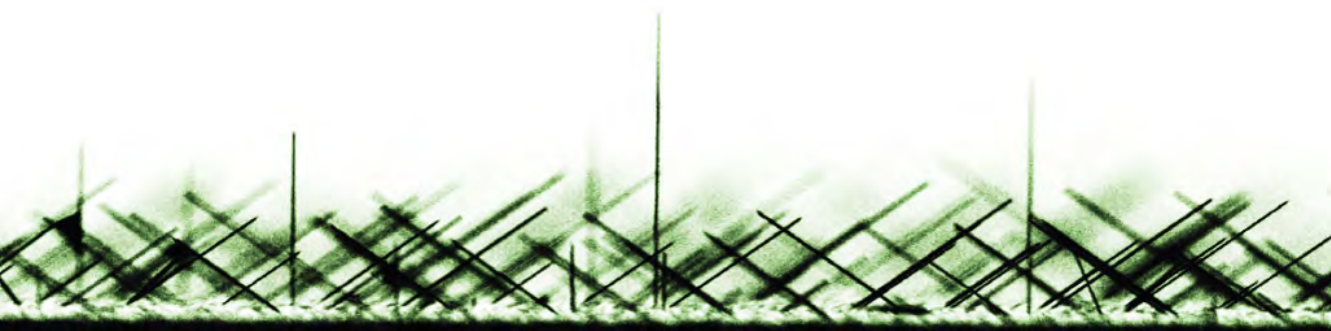


Figure 1.18: (a) A standard NW grown along the $\langle 0001 \rangle$ direction. (b) In-situ directional deposition of a superconductor on specific NW facets.

so that there are essentially no sup-gap electronic states. This gap is the key attribute that generates the protection in topologically protected system. The possibility of combining the superconductor epitaxy with growth of NW networks was previously reported by Gazibegovic et al.¹⁷⁰ and new results will be further discussed in Chapters 2 and 3.

This concludes the introduction of the basic phenomenon related to growth of NW networks that will be presented in this work. The following chapter will be focused on the VLS growth and description of novel methods for InAs nanocross synthesis.



2. VLS Nanowire Crosses

The data overlapping with Pub 1. and Pub. 2 are reprinted with permission from Copyright 2017, American Chemical Society.

In-situ growth of III-V VLS NW crosses often requires complex substrate fabrication.^{160,168,170} In addition, many approaches relying on catalyst positioning with respect to the crystal symmetries have previously resulted in formation of various branched structures.^{138,165,172} Even though, the VLS based structures provide an excellent basis for understanding fundamental physics in various quantum transport experiments,^{13,37,43,57} their application faces scalability and reproducibility challenges. In this chapter, we will focus on growth of three different types of WZ InAs NW crosses: 'inclined', 'kinked planar' and 'kinked vertical', which are shown in Fig. 2.1.

At first a more fundamental phenomenon will be addressed, which is the NW nucleation on (001) substrates. That provides important insight into growth of inclined WZ nanocrosses and the structure within their junctions, which incorporates a well-defined ZB segment. Such change in the crystal phase is related to growth originated from ZB basis of the substrate. Since the NWs grow as WZ, no coherent match exists for merging them along two opposite $\langle 0001 \rangle_B$ growth directions within the ZB basis. The situation is illustrated in Fig. 2.1 (a). The formation of the other two nanocross types relies on in-situ changing of the NW growth direction^{97,137–142}. The kinked planar nanocrosses, are coherently merged from two kinked NWs, where the WZ basis is provided by the standard $[0001]_B$ NW stems, as shown in (b). The kinked vertical structures are then similarly

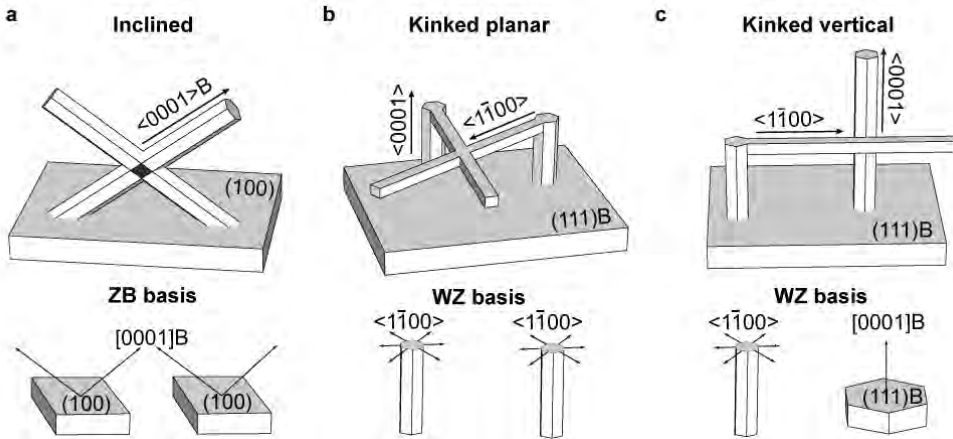


Figure 2.1: Schematics of the presented types of nanocrosses. **(a)** An inclined nanocross, formed by two WZ inclined NWs growing along $[111]_B$ directions related to (001) substrate, i.e. grow as WZ in ZB basis. **(b)** Kinked planar nanocross, which is formed by two kinked WZ NWs growing along $\langle 1\bar{1}00 \rangle$ directions from two $[0001]_B$ NW stems which serve as a WZ basis. **(c)** Kinked vertical nanocross, which is formed by a kinked WZ NWs growing along $\langle 1\bar{1}00 \rangle$ directions from $[0001]_B$ NW stem and a standard $[0001]_B$ NW, which both serve as a WZ basis. Adapted from Pub. 1.

formed from a kinked NW and standard $[0001]_B$ NW, as shown in **(c)**. In contrast to the inclined nanocrosses, both types have potential to form single crystalline WZ junctions. The later part of the chapter is dedicated to characterization of the nanocross crystal structure, basic transport properties and other interesting aspects of the growth methods. Presented results are based on data published in Pub. 1, 2 and 3.

2.1 Methods

The general steps of positioned VLS NW growth and substrate preparation are illustrated in Fig. 2.2. The process can be divided into substrate preparation, growth, device fabrication and measurements. This section summarizes the methods used in these processes. More specific details are then given in Chapter 4 and appendixes A for substrate fabrication, B for growth and C for device fabrication. The stated growth conditions are related to the successful results presented in this chapter.

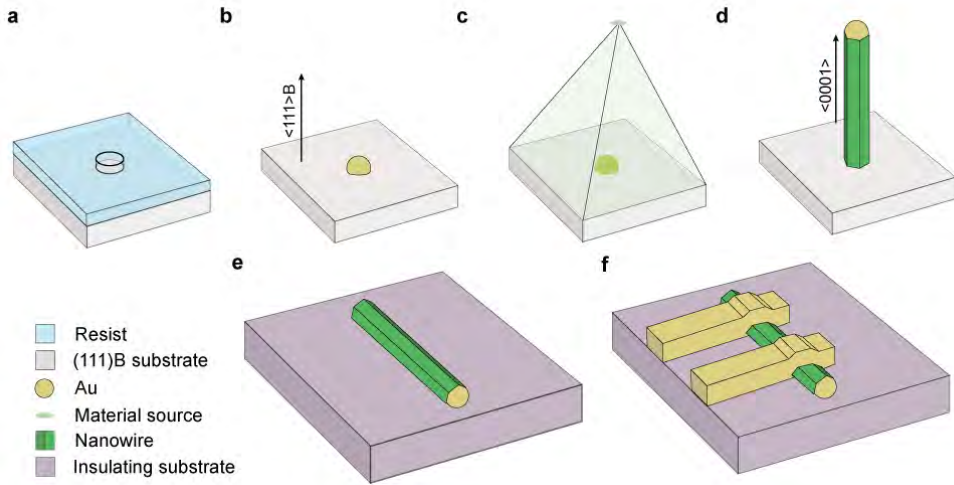


Figure 2.2: Schematics of standard the VLS synthesis process: (a) Epi-ready (111)B substrate of chosen orientation is pre-patterned in standard EBL process. (b) Arrays of Au catalyst nanoparticles are prepared by evaporation and resist lift-off. (c) The substrate is thoroughly cleaned, ran through routine MBE preparation process and subsequently the growth is initialized. (d) The NWs of desired length are grown and deposited on insulating substrate. (e) The transferred NWs are contacted using EBL and metal evaporation and are ready for measurements.

2.1.1 Patterned substrate preparation

For standard substrate preparation a double layer MMA/PMMA EBL resist was deposited on epi-ready (001), (111)B InAs and InP substrates and baked at 180°C for 2 minutes. After, the substrates were patterned in standard EBL process, see appendix A1 and A2 for details. In the next step, the native oxide was either etched by buffered HF ex-situ or by 15 W of RF argon plasma milling in-situ. Finally, 5-15 nm thick Au layers were deposited in a high-vacuum AJA e-beam evaporator.

Alternatively, an ALD AlO_x (10 nm) or e-gun evaporated SiO_x (70 nm) masks were deposited on the EPI ready substrates before patterning. Mask within the openings in the resist was etched in buffered HF etchant (ammonium fluoride - hydrofluoric acid mixture supplied by Sigma Aldrich) or Transene D Al etchant after development in 1:3 MIBK:IPA, before native oxide removal and metalization. The procedure is summarized in Fig. 2.3.

After 1 hour lift-off in 50°C acetone the samples were cleaned (cleaning sequence is discussed in Chapter 4). This procedure yields substrates patterned with gold islands with diameter ranging from 40 to 350 nm and varying thicknesses. The typical overetch of the

mask with respect to the size of the gold island was about 50 nm. Prior to loading into the MBE holder, the substrates were ashed in oxygen plasma and cleaned by 1:20 HF:H₂O solution and high purity H₂O.

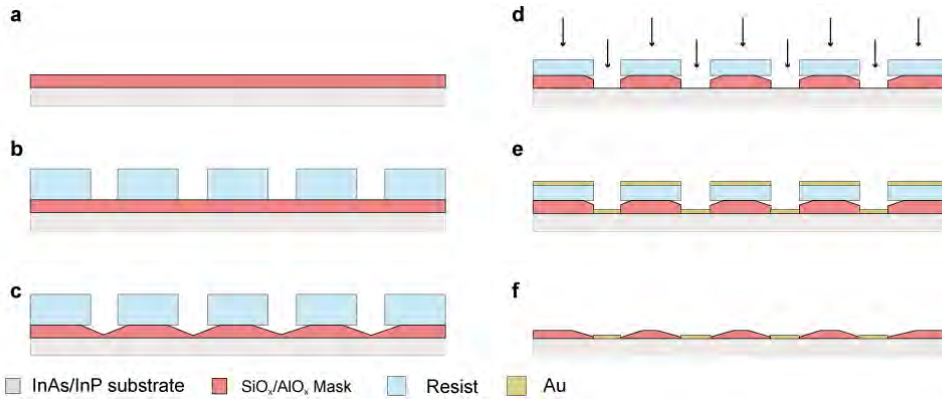


Figure 2.3: Schematics of masked substrate preparation: (a) AlO_x (10 nm) or e-gun evaporated SiO_x (70 nm) mask is deposited on epi-ready InAs or InP substrate. (b) The substrate is patterned with standard EBL. (c) The mask is partially removed within the patterns by wet etching. (d) The rest of the mask thickness and the substrate native oxide is removed by either RF plasma milling or additional wet etch step. (e) The mask is further thinned during MBE pre-loading HF acid cleaning step.

2.1.2 NW growth on (001) substrates

After sample loading, the MBE trolley was degassed in the system's loadlock for 1 hour at 200°C, until the pressure reached $5e^{-8}$ Torr. After moving into the buffer chamber, the sample holder was annealed at 250°C on heated station, in order to remove impurities until the pressure reached $5e^{-10}$ Torr. After cooldown the sample was moved to the growth chamber and heated in order to blow of the native oxide under As₂ or As₄ overpressure. The [0001]B NWs on (001) InP and InAs substrates were typically grown at ~410°C under In flux corresponding to 0.7 μm/h and As₂/In ratio of ~20*. For more details see appendix B1.

2.1.3 NW growth on (111)B substrates

The same procedure was used for the growth on (111)B substrates, where the NWs were grown at 420°C under the same In flux and As₄/In ratio of 10. In order to change the NW

*The given temperatures correspond to values measured by pyrometer, with emissivity set to 0.68

growth direction a short growth period of GaAs was introduced. The In shutter was closed and growth was paused for 2 minutes, while maintaining both growth temperature and As₄ overpressure. After the pause Ga flux corresponding to planar growth rate of 0.16 nm/s was introduced for up to 15 seconds. After the Ga shutter was closed, the growth was paused for 1 minute again, while maintaining the As₄ overpressure. Subsequently, the In shutter was reopened and the growth continued, while the growth rate was linearly reduced from 0.7 to 0.6 $\mu\text{m/h}$ in order to reduce NW tapering. For more details see appendix B2.

2.1.4 Structural characterization

The morphology and structure of the grown structures were characterized by scanning electron microscopy (SEM), atomic force microscopy (AFM), transmission electron microscopy (TEM)* and the crystal models were done in free-ware Vesta¹⁷³.

Scanning electron microscopy

The grown samples were characterized by scanning electron microscope FE-SEM JEOL 7800F. The typical overview, cross-sectional and tilted SEM images were taken at 20 kV, working distance of 15 mm and the secondary electron detector. The detailed images then at 5 kV, working distance of 6 mm and the back scattered electron detector or at 2 kV, working distance of 4 mm and the in-beam detector in gentle beam mode. The devices were then typically imaged with Raith Eline SEM at 20 kV acceleration voltage.

Atomic force microscopy

The AFM characterization was performed in tapping mode with Veeco Digital Instrument Dimension D3100 microscope, where 300 kHz frequency with force constant of 40 N/m silicon AFM probes were used.

Transmission electron microscopy

Selected structures were transferred onto Formvar/Carbon 200 copper TEM grids by micromechanical optical manipulator (see Chapter 4 for details). The high-resolution images were taken on JEOL 3000F (300 kV) after oxygen plasma ashing on grid. The dark-field and most of the lower resolution images were taken on CM20 Phillips LaB6 (200kV). The images were post processed in Fiji, a distribution of the ImageJ software¹⁷⁴.

*The TEM data in this chapter were taken together with Erik Johnson, Thomas Kanne and Martin Espineira from Center for Quantum Devices.

Crystal structure modeling

The models of the nanocross crystal structure were done in free-ware Vesta from JP-minerals¹⁷⁵. The P63mc space group with lattice constant of $a = 4.29 \text{ \AA}$ and $c = 7 \text{ \AA}$ were used for WZ and F-43m, $a = 6.06 \text{ \AA}$ for ZB.

2.1.5 Device fabrication

At first, specific structures were selected by SEM and later transferred on pre-patterned blank chips ($\text{Si} + 200 \text{ nm SiO}_x$) by micromechanical optical manipulator (details are given in Chapter 4). After transfer, Au alignment marks pre-existing on the blank chip were used to align and take positioned images in Raith Eline SEM. That allows for overlaying the SEM images of deposited NWs with the blank chip CAD file and for precise device designing.

For contact fabrication, $\sim 420 \text{ nm}$ thick PMMA resist was spun at 4000 RPM and baked at 180°C for 2 minutes. After standard EBL procedure, the native oxide was removed in-situ in high vacuum AJA e-beam evaporator by Ar radio frequency plasma milling at 15 W for 5 minutes with 18 mTorr Ar flow. After the oxide removal 5 nm of Ti sticking layer and $\sim 300 \text{ nm}$ of Au were deposited. The lift-off was done in 30 minutes in 50°C acetone. The specific tricks used in order to avoid damaging the structures (and nanocross branch breaking) during fabrication are given in Chapter 4 and detailed recipes are given in appendix C.

2.1.6 Resistivity measurements

The nanocrosses were characterized at room temperature after bonding (see chapter 4 for details). The four-probe DC measurements were carried using Keithley 2600 source meter to supply source-drain bias voltage and measure current. The voltage drop on the inner contacts was measured by an Agilent digital multimeter after amplification by Stanford SR560 noise pre-amplifier. A typical device design (multiple branches were contacted in real experiment) is shown in Fig. 2.4.

The measured resistance was converted into resistivity based on the dimensions extracted from SEM images. The extraction of the inclined NW doublecross resistivity will be discussed below in related section.

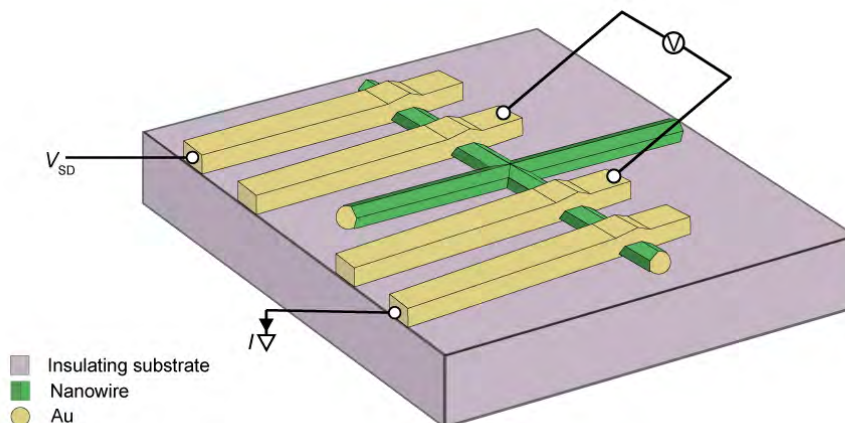


Figure 2.4: Schematics of typical 4-probe nanocross based device used for resistivity measurements. V_{SD} is the source-drain voltage, I is the measured current and V is the voltage drop over the inner probes.

2.2 Results and discussion

This section will provide a summary of results attained by methods described above. The growth methods not only allowed us to uncover an important role of the catalyst nanoparticles on (001) and other substrates, but also to synthesize three novel types of nanocrosses.

2.2.1 Catalyst role in inclined NW growth

As discussed in the introduction, the catalyst nanoparticle plays a crucial role in the VLS NW growth. The catalyst not only serves as a collection center for the precursor materials¹⁸, influences the crystal structure of the NW⁸⁹ and provides a mechanism for in-situ dynamic control¹⁷⁶ during growth, but as will be shown here, is of great importance for the successful nucleation during the early growth stages. In addition, the understanding of catalyst/substrate interaction allows for growth of the 'inclined' nanocrosses. The results in this section are mostly related to findings presented in Pub. 2.

The interaction of the catalyst nanoparticle with the growth substrate, e.g. during the oxide desorption growth step and warm up to the growth temperature, is of great importance to the NW community. Especially since it may be complicated to maintain consistency during such fundamental experiments. Nevertheless, such interactions were in-

investigated by several groups^{130,177–179}. Krishnamachari et al. first suggested in Ref. [130], that the initial interaction between the catalyst and the growth substrate predetermines the NW growth direction on (001) substrates. Later Ghosh et al. studied the interaction between the substrate before growth and in early growth stages by TEM in Ref. [177]. The impact of the annealing on the surface structure of GaAs substrates with different orientations was investigated by Whiticar et al. in Ref. [178].

In the most recent study Curiotto et al. have investigated the mechanism of motion (diffusion) of metallic particles on the surface in Ref. [179]. The studies are most often related to growth on the more exotic orientations than (111)B, where the growth seems to be more complex and difficult even for NWs which are still growing along the [111]B direction. The results show the importance of such studies, which may be crucial for future growth of novel NW based structures. Here we focus on growth on Au pre-patterned (001) InAs substrates, where another interesting role of the catalyst is observed, mediating the NW nucleation. The results were presented in Pub. 2 with focus on non-patterned substrates and the observed phenomena was shown to be related also to other surface orientations and materials.

Various substrates with different Au catalyst pitch were prepared in order to investigate the early growth stages of the NW growth on (001) InAs surfaces. The observed phenomena is summarized in Fig. 2.5. As will be shown in more detail later, the presence of the Au catalyst mediates growth of (111)B faceted craters elongated along the [110] direction, as shown in (a). The Au nanoparticle is still visible at the bottom of the crater. A similar structure is shown also in (b), where higher growth temperature (500°) promotes enlargement of the surface area of the substrate at the bottom of the crater. This is in agreement with Monte Carlo simulation presented in Pub. 2.

At given growth conditions the Au nanoparticles are usually not impinged at the substrate surface, but tend to diffuse over the surrounding surfaces. The overall trends observed for both non-positioned and pre-patterned growth indicate that the nanoparticles mostly migrate around their initial position. A significant fraction manages to end up on the (111)B facets of the craters. Once the nanoparticles reside on the (111)B surfaces the NW growth is initiated along the 2-fold degenerate [111]B direction, as shown in Fig. 2.5 (c) and (d). That is most likely caused by the increased collection area of the (111)B facet, that enables supersaturation by contribution of the adatom phase. The subsequent growth usually continues uninterrupted, as shown in (e) and (f). A general observation is that the growth on (001) substrates is characteristic by wide spread in NW length. That supports the suggestion about droplets migrating over the substrate surface, before they find an ideal NW nucleation site, in form of a large enough (111)B surface. The next few paragraphs will be dedicated to various aspects of this kind of NW growth and hopefully support the claims stated above. It is also important to mention, that the presented results apply

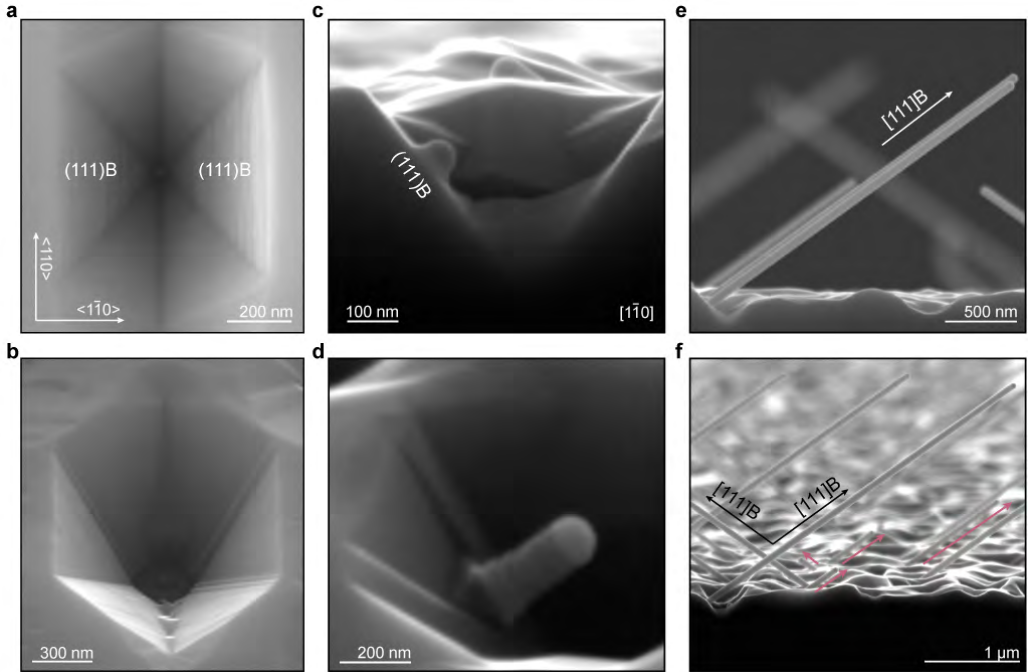


Figure 2.5: (a) A top-view SEM micrograph of a crater with (111)B side-facets grown on (001) InAs substrate, with a Au nanoparticle visible at the bottom. (b) Tilted-view SEM micrograph (30°) of a similar crater grown at higher growth temperature, where the Au droplet at the bottom is surrounded with a bare area of the initial substrate surface. (c) A cross-sectional SEM showing an initial stage of NW growth from a (111)B facet of a crater. The Au catalyst diffused from the initial position on the bottom of the crater, while mediating the NW growth. (d) A tilted-view (50°) SEM micrograph depicting similar situation at later stage. (e) and (f) Cross-sectional SEM micrographs showing further NW growth starting from the crater sidefacet and continuing along the 2-fold degenerate $\langle 111 \rangle_B$ directions. The red arrows highlight unusually wide spread in the NW length.

for specific growth conditions and only for NWs growing along the $[111]_B$ directions. Many different structures were previously reported for (001) substrates, such as $[001]$ ZB NWs¹³⁶ or nanoflakes⁹⁸, where the growth mechanism may be very different.

At first, it is important to investigate the mechanisms behind actual formation of the craters. The Au nanoparticles could either assist dissolution of the substrate and etch down the faceted craters, or mediate their growth. A formation of similar structures was previously observed and related to the InAs surface and surface impurities by Ye et al. in Ref. [180]. This strongly indicates that these defects are associated with growth itself and that they do not extend below the substrate surface.

A series of experiments were performed to investigate the morphology of Au patterned InAs (001) surfaces during growth. A surface of a such sample after oxide desorption and subsequent cooldown under As overpressure is shown in Fig. 2.6. The presence of the gold nanoparticles resulted in formation of ~ 60 nm tall molds elongated along the $\langle 110 \rangle$ direction. The shape is most likely related to the diffusion anisotropy of (001) surfaces¹⁸¹. The area inbetween the nanoparticles is flat with RMS ~ 1 nm. Since there are no indications of significant surface etching or dissolution, the formation of the craters does not seem to be related to the annealing procedure.

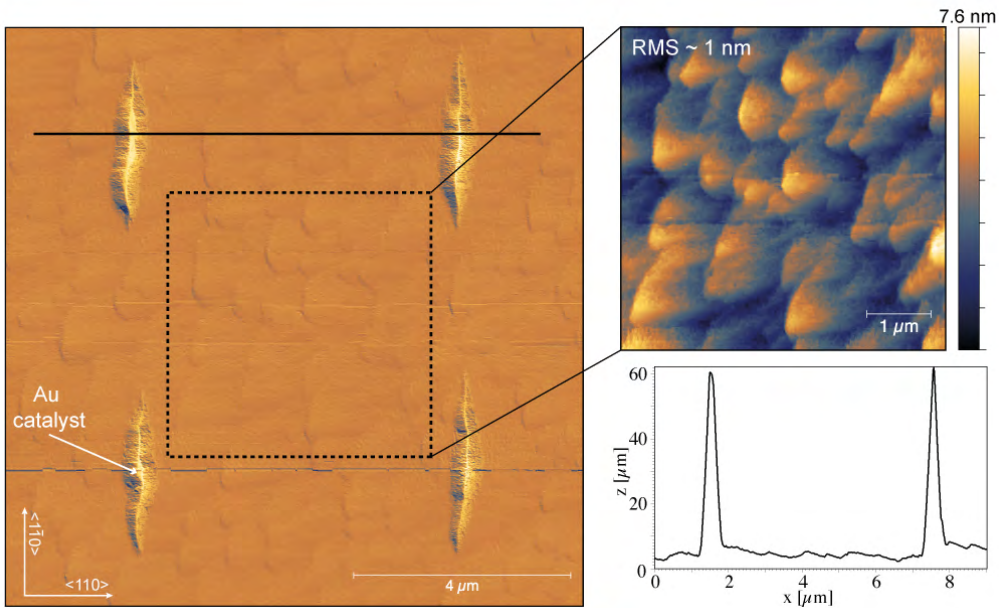


Figure 2.6: AFM surface micrograph of a patterned (001) InAs substrate after oxide annealing step during MBE growth. Four Au nanoparticles reside atop of material accumulated into ~ 60 nm tall molds elongated along the $\langle 110 \rangle$ direction, as indicated in the line-cut. A detail of the surface inbetween the nanoparticles is shown in the zoom-in.

A further evolution of the surface during growth is shown in Fig. 2.7. The surface remains smooth with material build up at the Au nanoparticle locations after annealing, shown in (a). After 45 s growth of InAs the surface of the whole sample is roughened by crater-like defects, as shown in (b). For much longer 30 min growth, the surface smoothens, while faceted craters evolve further at the initial locations of the Au nanoparticles shown in (c). Hollow volumes are observable at the original Au particle locations on substrate in (d), which is consistent with results in Ref. [180], where crater-like defects were associated with impurity on the substrate. These 'capsules' seem to be related to overgrowth of the

craters during longer growth times. The similarity of the results indicate that the craters can indeed be connected to the presence of the gold nanoparticles on the substrate.

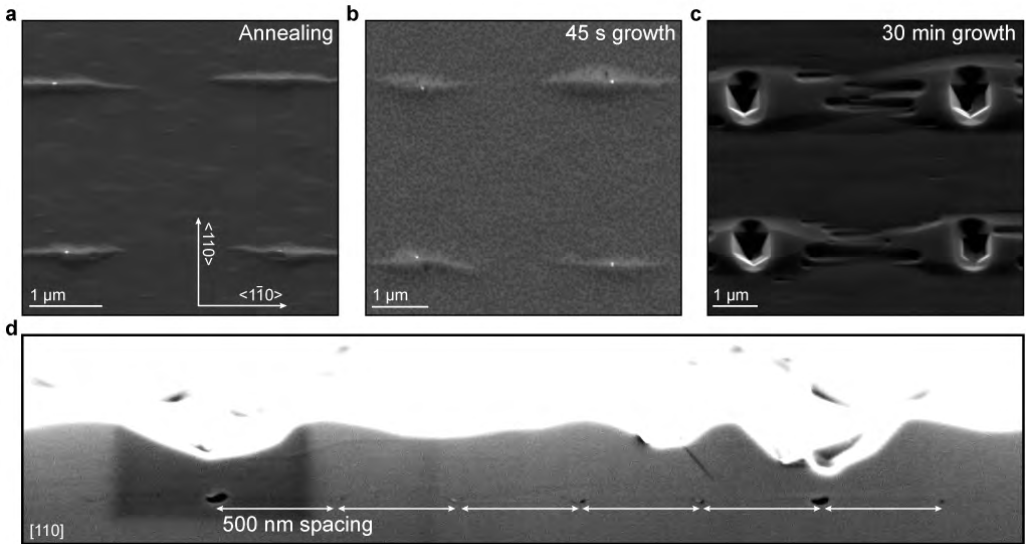


Figure 2.7: Tilted-view SEM micrographs (20°) of Au patterned InAs (001) surfaces after (a) annealing procedure, (b) 45 s growth and (c) 30 minute growth of InAs. (d) Cross-sectional SEM Micrograph of a similar substrate after growth, with 500 nm pitch between Au nanoparticles. The initial Au locations are observable in form of hollow defects, with the indicated spacing.

The next important phenomenon is the mentioned nanoparticle migration over the cratered surface during growth. Again, the nanoparticles seem to stay in their initial positions during annealing and their motion is most likely growth related. The first indication of the nanoparticle motion is already apparent in the fact that the inclined NWs seem to originate from the crater facets and not from their bottoms. In addition the very wide length distribution for NWs with the same diameter and within the same growth, shown in 2.5 (e), indicates that there are various time intervals between the nucleation of individual NWs. Interestingly, as was shown in Pub. 2, there is an incubation period before the NW growth starts, which is observable by RHEED pattern evolution. This period is related to the nanoparticle motion and the necessity to migrate to a specific location, in order to initiate the NW growth.

The motion of the particles is easy to observe, since the crater locations follow the initial patterning of the surface, as apparent from Fig. 2.8. In (a), a long growth time results in formation of surface with regular pattern of craters, but the particles are randomly dispersed. It is also apparent that some of the craters start to be filled with material and the

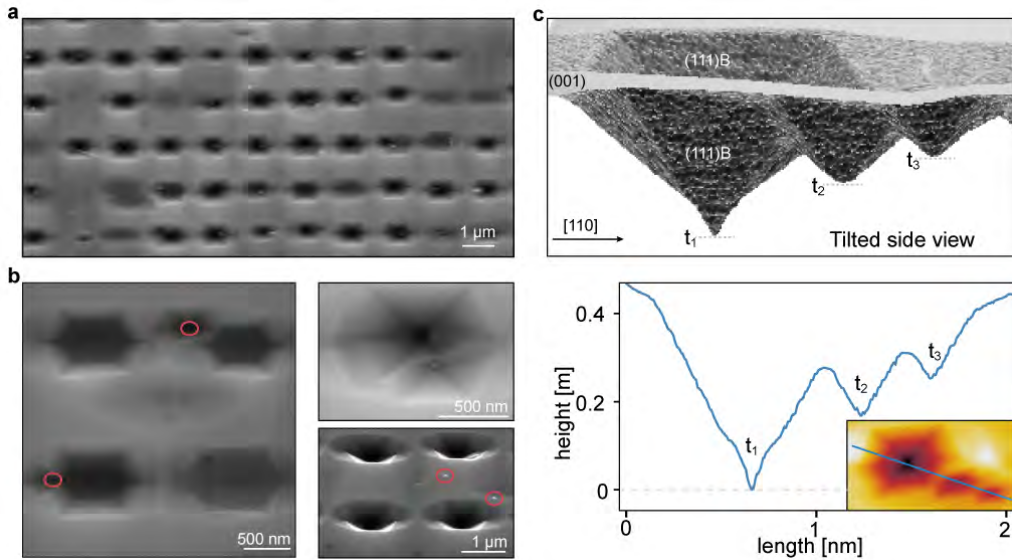


Figure 2.8: (a) SEM micrograph of Au patterned InAs (001) surfaces after growth, showing array of nucleated craters, Au nanoparticle migration and crater overgrowth. (b) SEM micrographs of the same growth, showing partially overgrown craters together with nanoparticles that migrated from the initial positions and nucleated new craters during further growth. The two smaller panels show the phenomena in more detail. The red circles highlight the position of the nanoparticles. (c) 3-D interpretation of AFM micrograph of three craters which were formed in different times during the growth (t_1 , t_2 and t_3), together with a line line cut profile through the bottoms of the craters. The surface scan is viewed from the bottom, to provide better view of the different depth of the craters. Partially adapted from Pub. 2.

surface locally smoothens. That is shown in (b), where the craters become flat bottomed. In addition, the nanoparticles either caused emergence of additional shallower craters at different locations (right top panel) or diffused to the (001) surface, as shown in (c) (right bottom panel). An AFM micrograph depicting three neighboring craters, with different depth indicates that they were indeed formed at different growth times. The appearance of the shallower craters with the nanoparticle residing in their center again suggests, that the Au nanoparticles play crucial role during the crater formation. Interestingly, the depth of the largest crater corresponds to expected thickness of 40 minute growth with planar growth rate of $0.7 \mu/h$ (447 nm).

Since the craters tend to maintain their shape during further growth, it seems that the diffusion length on the formed (111)B facets is much longer than on the neighboring roughened (001) surface, which collect most of the material and continue growing. That

also indicates, that the (111)B facets may not be the preferential sites for NW nucleation only because lower surface energy, but also because the adatom collection contribution is enhanced and significantly contributes to the supersaturation of the nanoparticles. The accumulation of material at the bottom of the craters for longer growth times can then be related to the diffusion length on the crater facets. As they grow larger, the material seems not to be able to reach the (001) surface anymore and starts to grow at the closest preferential incorporation site, the center of the crater.

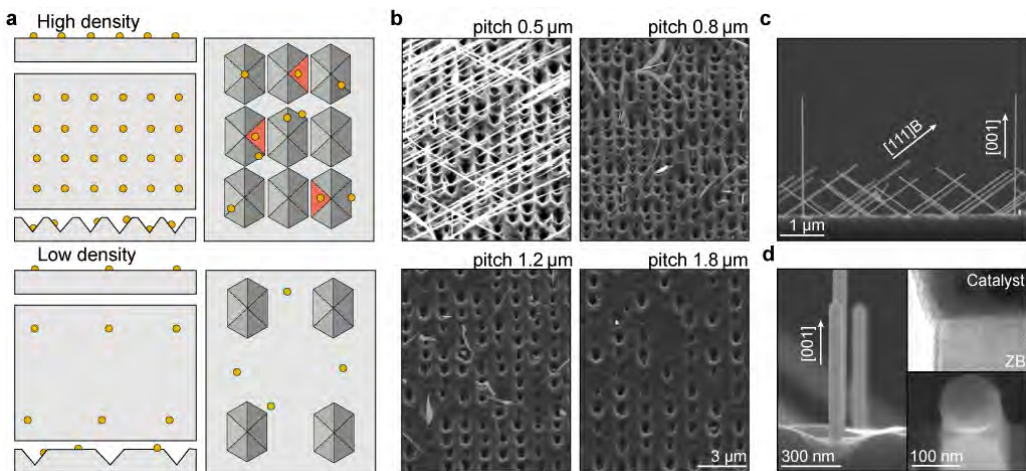


Figure 2.9: (a) Sketch of catalyst pitch effect on crater formation and NW growth. As the droplet density increases, so does the total area of (111)B facets. That increases the probability for the migrating catalysts to end up at (111)B surface and initiate NW growth (ideal configuration is indicated by red coloring). (b) Tilted-view (30°) SEM micrographs of positioned NW growth on (001) InAs substrate, where the density of nucleated NWs/nanoflakes dramatically reduces as the catalyst pitch is increased. (c) SEM micrograph showing NWs grown on patterned (001) InAs, where both [0001] and [001] NWs grow simultaneously. (d) Cross-sectional SEM micrograph of [001] NWs grown on (001) InAs substrate. The upper inset shows high resolution TEM showing the ZB structure of the NW and the bottom inset the square cross-section of [001] NW, corresponding to [110] faceting.

Another observation that supports the idea of Au nanoparticle migration is the dependence of NW nucleation probability on the nanoparticle pattern pitch. The situation is sketched in Fig. 2.9 (a). Lowering of the nanoparticle pitch increases the crater density, since it is defined by the initial density of the catalyst particles. That results in reduction of (001) surface and increases the area of (111)B facets. Therefore, the probability of the nanoparticles to migrate to (111)B facets, which seem to be the preferable [111]B NW nucleation sites, is increased. The trend was observed over variety of experiments and

wide range of growth conditions. An example for growth on pre-patterned InAs substrate is shown in Fig. 2.9 (b). This mechanism can be used to design specific patterns and increase the probability for formation of 'inclined' nanocrosses, as will be discussed in next section.

Interestingly, [001] InAs NWs are occasionally present within the growth, as shown in Fig. 2.9 (c). Their density within specifically designed patterns varies from growth to growth. For specific designs they represented just fraction of grown NWs, whereas in different areas, they were present significantly more than the [111]B NWs. Unfortunately, we were not able to see consistent trends, that would help to determine the specific growth conditions for such NWs. In contrast to the [111]B NWs which emerge from the crater side facets, the [001] NWs typically originate from the center of the craters, as shown in Fig. 2.9 (d). The [001] NWs are also interesting from the structural perspective, since the SEM and TEM analysis shown that they adopt ZB structure with rectangular cross-section. Further understanding of nucleation and growth of these structures could provide more insight and control over NW growth on (001) substrates. Apart from [111]B WZ and (001) ZB NWs, variety of other structures can be observed over the samples for different growth conditions, e.g. nanoflakes⁹⁸ and NWs grown along other orientations¹⁸².

The presented results together with Pub. 2 provide enough insight into the growth process to allow for growth of the 'inclined' nanocrosses, which will be discussed in the next section.

2.2.2 Growth of inclined nanocrosses

The (001) substrates promote growth of [111]B oriented NWs, which grow inclined to the substrate surface under the angle of 35.3° . In addition the [111]B direction degeneracy allows for the WZ [0001] NWs to grow in opposing directions along the $\langle 1\bar{1}0 \rangle$ axis and to merge into nanocrosses.

As discussed in previous section, growth of these NWs at specific positions seems to be very complicated, due to the necessity of the nanoparticles to spontaneously migrate onto the (111)B facets of nucleated craters. Here a specific patterning was used not only to increase the NW yield, but also the probability for the NWs growing in opposing [111]B directions to merge. As was shown in shown in Fig. 2.9, the NW yield increases with decrease in the NW pitch and growth from dense patterns indeed increases the nanocross formation probability. On the other hand, the high NW density makes it difficult to further process the structures in a controlled way. Therefore the nanoparticle pitch was varied between the $\langle 110 \rangle$ and $\langle 1\bar{1}0 \rangle$ axes. Spacing along one of the axes was kept in a range from 200 to 500 nm, while along the other axis between 2-6 μm , as illustrated in Fig.

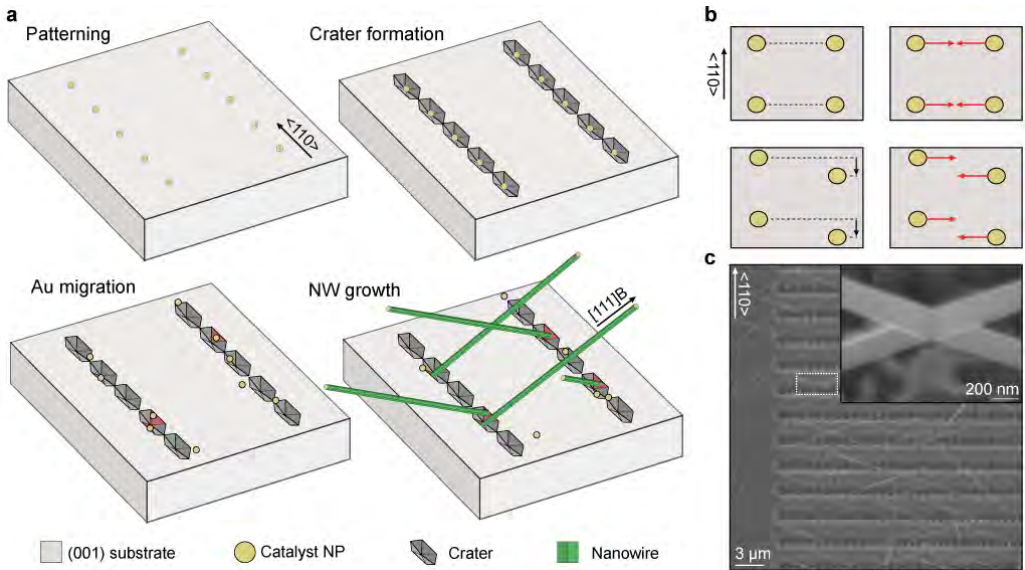


Figure 2.10: (a) Sketch of the patterning and related formation of inclined nanocrosses. At first the craters form at Au nanoparticle locations, which are positioned in lines with pitch from 200-500 nm along $\langle 110 \rangle$ axis and the lines are spaced between 2 - 6 μm along the $\langle 1\bar{1}0 \rangle$ axis (The axes can be switched yielding similar results but different [111]B NW nucleation probabilities.). Further during the growth the nanoparticles start to migrate from the crater centers, with a finite probability to end up on the (111)B crater facets (highlighted in red) and promote NW nucleation. (b) Sketch of intentional nanoparticle misplacement along the $\langle 110 \rangle$ axis (black arrow). The red arrows indicate the misplacement of growing NWs which can either hit one another or pass close one to another. (c) Tilted-view (30°) SEM micrograph of [111]B NWs grown on SiO_x masked InP (001) substrate from a pattern similar to (a). This allows for formation nanocrosses. The SEM micrograph in the inset shows detail of one of the nanocross junctions.

2.10 (a). Such patterning keeps the area of (111)B crater side facets around the catalyst nanoparticles relatively large and increases the probability of [0001]B NW nucleation. Maintaining larger spacing along the other axis provides enough space for picking up the structures by micromechanical manipulator and further processing (see Chapter 4 for details). The yield of the NWs is increased, when the $\langle 110 \rangle$ axis is selected for the low nanoparticle pitch. On the other hand, when $\langle 1\bar{1}0 \rangle$ is selected for the low pitch, the probability of nanocross formation is increased. The nanocross formation can be further controlled by slight misplacement of the nanoparticles along the $\langle 110 \rangle$ axis, as shown in Fig. 2.10 (b). The intentional misplacement allows for the merging NWs to pass close one to another instead of hitting directly. After passing in close proximity, the NWs are most likely snapped together due to electrostatic and Van der Waals interaction and overgrow

into well faceted structures. A recrystallization process is an essential part of the junction formation, as will be shown in Section 2.2.5.

Here, the catalyst does not play a role in formation of the junction due to the indirect merging process, which makes it unlikely for the catalyst material to contaminate the junction and negatively affect its transport properties¹⁸³. While hitting directly, the NW junctions are often either not well defined, or form 'T' and shaped structures instead of nanocrosses¹⁷¹.

Another important aspect of successful NW merging is growth on oxide masked substrates. An example is shown in Fig. 2.10 (c). The mask helps to maintain the integrity of the initial patterning and prevents particles from diffusing far from the initial crater. From the SEM image it is apparent that some of the nucleated NWs grow in random directions outside of the craters. That is most likely related to the presence of the mask which under given growth conditions does not support selective growth and affects the structure of surface surrounding the craters. Even though the crater positions are well defined, the yield is very low since it relies on the nanoparticle migration. Despite the low yield, a single growth on quarter of a two inch substrates provides large number of well defined nanocrosses, which are fairly simple to be located and processed for device fabrication. More details are given in Chapter 4.

The inclined nanocrosses were grown on oxide masked (001) InP substrates. Compared to growth on InAs under the same conditions, the InP substrates seems to affect initial wetting conditions of the catalyst and the NWs grow with thin segments located close to the end, as shown in Fig. 2.11 (a) and (b). Even single NWs do in general grow with very thin tip at the end, under given growth conditions. The SEM in (a) suggests that the thin segments allow for the NWs to pass one next to another and later overgrow into well defined nanocrosses as shown in (b). Such thin NW segment is often seen within variety of NW growths and is typically related to the cooldown step¹⁸⁴. In such case, the growth continues from material remaining in the adatom phase, liquid phase and background pressure present after closing of the In shutter and that affects the NW diameter. Under presented growth conditions, the morphology of the NWs is very different for growth on oxide masked (001) InAs substrates, even though the cooldown process is the same and the only difference is the material of the substrate. The cause of this growth regime remains to be investigated and may be related to many aspects of growth, e.g. difference in substrate surface temperature, different initial catalyst wetting conditions and/or presence of P atoms in the liquid phase during growth.

Interestingly, the NWs are homogeneous in diameter up to the gold nanoparticle, as apparent in Fig. 2.11 (c), if the same growth is carried on InAs substrate with same orientation and mask. This seems to also affect the nanocross formation. Two typical

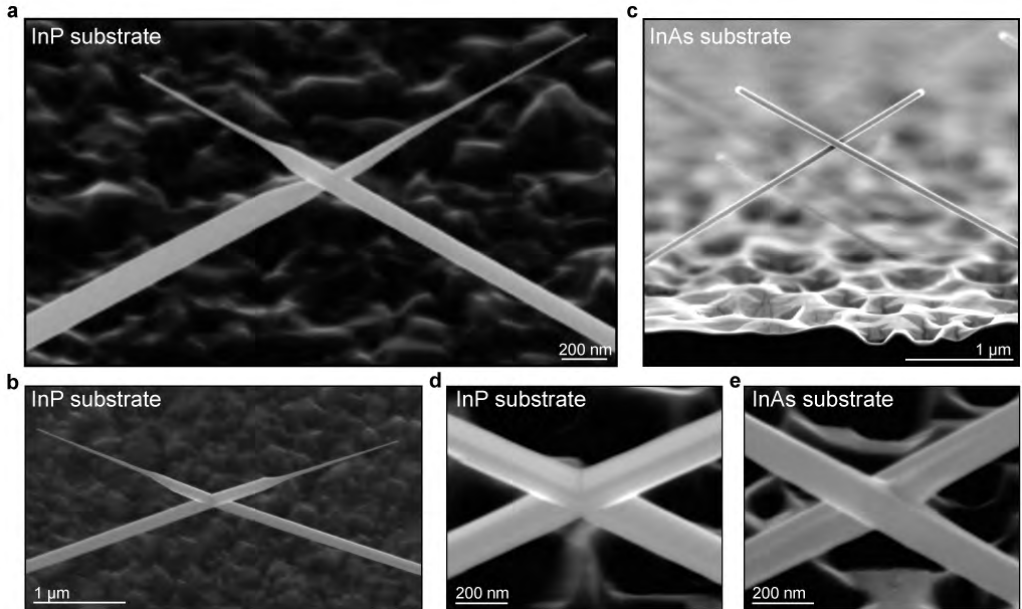


Figure 2.11: Tilted-view SEM micrographs in (a) (20°) and (b) (30°) show two different stages of inclined nanocross formation within the same growth but in regions with different catalyst spacing on masked (001) InP substrates. A tilted SEM micrograph of analogical growth on masked (001) InAs substrate is displayed in (c), showing different morphology at the end of the NWs. The typical nanocross junction morphologies associated with growth on InP and InAs are shown in (d) and (e), respectively.

cases are shown in (d) for growth on InP and (e) for InAs. On InP, it was possible to grow well defined nanocrosses, but on InAs the NWs typically hit one another form T-shaped structures¹⁷¹. If a respective catalyst misalignment of ~ 100 nm was used for InAs, as was illustrated in Fig. 2.10 (b), the yield of nanocrosses was increased, but the NWs seemed to be overgrown together (shown in (e)) instead of forming well faceted junction. The possible effects on the crystal structure of the junction will be discussed later in section 2.2.5. It is important to note, that structures similar to the one Fig. 2.11 (e) are also present within growth on InP substrates, but we have not found crosses with well defined junctions similar to the one in (d) within growths on InAs.

2.2.3 Changing NW direction by catalyst manipulation

Another interesting approach which allows for formation of advanced NW structures is change in growth direction induced by in-situ catalyst wetting angle manipulation^{137,176}. The resulting growth directions are often well defined and related to the crystal structure of the initial NW stems, that serve as platforms for the growth direction kinking process. Here we focus on kinking the NWs into one of the 6-fold degenerate $\langle 1\bar{1}00 \rangle$ directions which corresponds to the faceting of typical $[0001]_{\text{B}}$ WZ NWs grown on $(111)_{\text{B}}$ substrate.

A schematics of the process is shown in Fig. 2.12 (a). At first standard InAs NW is grown on oxide masked pre-patterned $(111)_{\text{B}}$ substrate and serves as a stem for the kinked NW growth. The change of the growth direction is achieved by terminating the In flux and therefore pausing the InAs growth. After the pause, Ga flux is introduced in order to change the wetting of the catalyst. After turning off the Ga flux and another pause, the In flux is reintroduced and the kinked NW growth starts. The growth can continue either along one of the six $\langle 1\bar{1}00 \rangle$ (with equal probability) or without a change along the $[0001]_{\text{B}}$ directions*. This is most likely related to the change of catalyst wetting, which pushes the triple phase line on one of the side facets, as the droplet volume increases by mixing with Ga atoms. That facet then becomes the preferable nucleation site and promotes kinked NW growth. The probability of growing a kinked NW then depends on the amount of Ga introduced. The probability to grow close to 100% of kinked NWs was achieved by introducing Ga flux for 15s, which corresponds to GaAs planar growth thickness of 2.5 nm of GaAs. An example of a close to 100% kinked NW yield growth is shown in Fig. 2.12 (b). The ratio between the $[0001]_{\text{B}}$ and kinked NWs can therefore be controlled by reduction of the Ga flux.

A successful kinking of the NW growth direction seems to be strongly affected by the cleanliness of the fabricated substrate. The probability to kink seemed to reduce, for growths where the substrates were visibly contaminated (after growth) from the pre-processing. Another problematic aspect of this growth that was observed, is that the NW stems occasionally adapt $\langle 11\bar{2}0 \rangle$ faceting. That effectively makes the kink direction degeneracy to 12-fold and reduces the fraction of kinked NWs. The switching of the facet families is most likely caused by impurities and their effect on the chemical potentials that define the nature of NW nucleation. Our system is often exposed to Sb species. Their presence could affect the surface energetics due to the surfactant properties of Sb^{185,186}. Also any contamination of the catalyst related to the fabrication procedures can have similar effects.

*The same method can be also used for growth along the $\langle 11\bar{2}0 \rangle$ family of directions, depending on the faceting of the stem $[0001]_{\text{B}}$ NW. Under given growth conditions the stem faceting is preferentially $(1\bar{1}00)$.

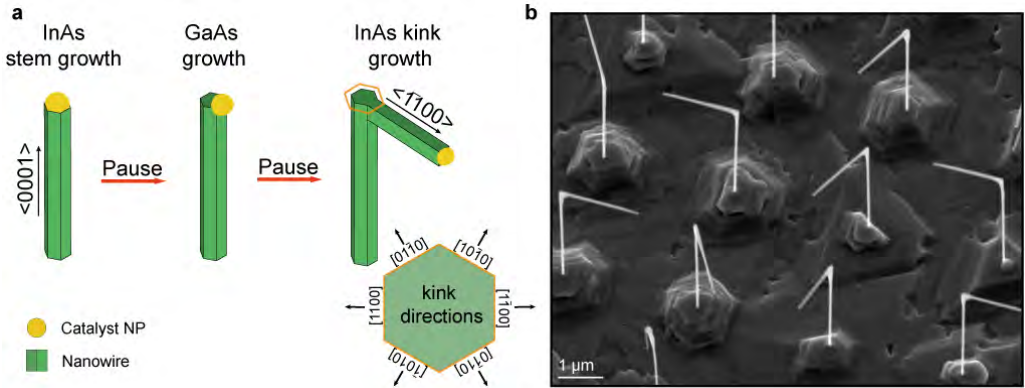


Figure 2.12: (a) Schematics of in-situ changing of $[0001]_{\text{B}}$ NW growth direction by three step kinking process: InAs Stem growth, GaAs growth and kinked InAs NW growth. The bottom right inset shows the 6-fold degeneracy of the possible kinked NW growth directions. (b) Tilted-view (30°) SEM micrograph of kinked InAs NW array grown on a pre-patterned $(111)_{\text{B}}$ substrate.

Another important aspect of this growth is control over the catalyst volume. The designed volume of the deposited Au islands can be used to control the height at which the NWs kink, since it affects the stem growth rate, as shown in Fig. 2.13 (a). The catalyst nanoparticle position can also affect the growth as the transition from adatom to liquid phase can be locally reduced, if multiple NWs share the adatom collection area⁸⁸. That can become an issue when more complex patterns with varying NW spacings are used, as it can introduce spread in growth rates. This effect can be partially suppressed by use of the oxide mask. Roughened growth on the mask around the NWs reduces the adatom collection area, even though full selectivity of the growth was not achieved at the VLS NW growth temperatures. That allows for maintaining stable growth rates even for patterns with wide NW pitch distributions. Dependence of the NW kink height on the NW pitch for different diameters of the Au islands is shown in Fig. 2.13 (b). The kink height was measured for 50 NWs for each of three different island sizes and 6 different NW pitches. The total average standard deviation in the NW kink height is 120 ± 23 nm, which is comparable to the kinked NW diameter. The growth rate of the NW stems under given conditions is ~ 200 nm/min, ~ 240 nm/min and ~ 250 nm/min for Au island diameter of 100 nm, 135 nm and 170 nm respectively. Interestingly, the deviation of growth rate for the kinked NW part is much larger and the kinked NW length varies within the pattern. A rough growth rate of the kinked NW part is ~ 330 nm/min.

As the catalyst volume is further increased, the growth direction of the kinked NW changes, as shown in Fig. 2.13 (e). That is most likely due to second order twinning

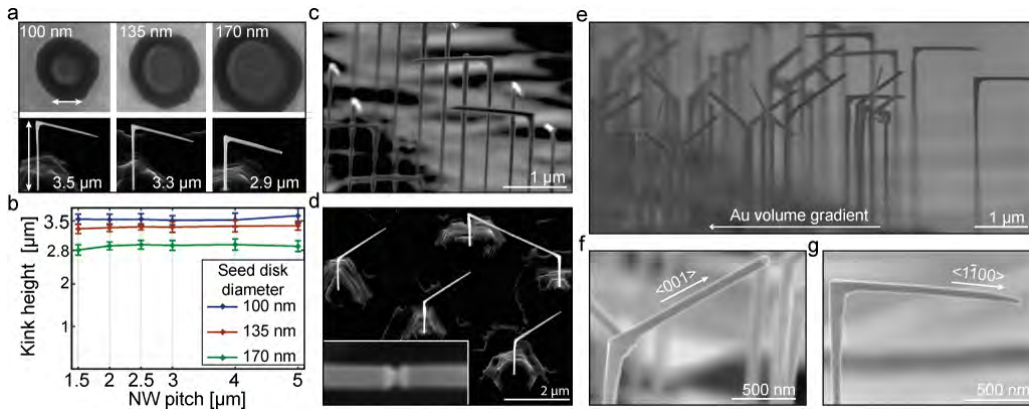


Figure 2.13: (a) SEM micrographs of kinked NWs grown on oxide masked InAs (111)B substrates, showing a relation between the diameter of deposited Au island and the height at which the NWs kink. (b) Dependence of NW kink height on the NW pitch for three different Au island diameters, showing a distribution comparable to the NW diameter. (c) and (d) Tilted-view SEM micrographs of NWs kinked at the same height. The inset shows a detail of the catalysts at the end of the kinked NW part, which kinked into opposite directions at the same height. (e) Tilted SEM micrograph showing that the NW kink direction can be modified within the same growth by increasing the Au nanoparticle volume. Details of the kinked NWs for large (f) and small (g) catalyst volumes.

into differently oriented $\langle 0001 \rangle$ structure, as described by Uccelli et. al in Ref. [116]. This direction is inclined by $\sim 35^\circ$ with respect to the plane of the substrate and aligned along the $\langle 1\bar{1}00 \rangle$ in plane directions, as shown in (f). A saturation point was observed for large Au volumes for given growth conditions. The NWs grown from Au islands with above ~ 300 nm diameter did not change the direction at all and the growth continued uninterrupted at all sites.

The kinked NWs maintain WZ structure as shown in Fig. 2.14. A standard kinked NW with 90° angle between the stem and the kinked part is shown in (a). Here the NW is WZ and grows along one of the $\langle 1\bar{1}00 \rangle$ directions. The WZ structure is disturbed by stacking faults inherited from the NW stem, that progress through the whole kinked NW part in parallel to the substrate surface. Therefore, controlled growth of stacking fault free NW stems¹⁸⁷ is important for achieving pristine crystal structure within the kinked parts of the NWs. That is hard to achieve all over the substrate due to the used variation of Au volume, NW pitch etc. and should be optimized for a specific growth. The (0001)B top-facet of the kinked part is typically overgrown by ZB originating from direct deposition. The tapering onsets directly at the kink site and gradually progresses towards the end of the NW. This overgrowth can be significantly reduced by linear lowering of both



Figure 2.14: (a) TEM micrograph of a standard kinked NW, where the angle between the stem and the kinked part is 90° . The NWs are WZ, but usually consist of a thick layer of ZB overgrowth on the top part, as seen in the inset. The kinked part also often inherits stacking faults from the NW stem. (b) TEM micrograph of the other kinked NW family with $\sim 124^\circ$ angle and twinned ZB between the stem and kinked NW part, where the $[0001]B$ direction switches by second order twinning.

the In and As fluxes during the kink growth step, i.e. linearly reducing the growth rate. The reduced growth rate lowers the adatom density on the $(111)B$ topfacet as the kinked NW part grows longer than the characteristic diffusion length on the topfacet. Once the adatoms deposited close to the kink site can not diffuse to the catalyst, i.e. contribute to the longitudinal growth rate, the flux reduction maintains the adatom density on the top-facet below critical, i.e. suppresses nucleation and overgrowth⁷². The other kink family with $\sim 124^\circ$ angle between the kinked part and the stem is shown in TEM micrograph in Fig. 2.14 (b). A ZB segment is visible right at the kink site, which is consistent with the hypothesis that the growth direction changes by second order twinning and continues to grow in WZ structure along the $[0001]B$ direction. The growth direction seems to correspond to the $\langle 100 \rangle$ family of directions related to the ZB substrate.

The standard kinked NWs can be used for formation of two different novel types of nanocrosses, as will be shown in next section.

2.2.4 Growth of kinked-vertical and kinked-planar nanocrosses

Kinking the growth direction in-situ in combination with relative positioning of the Au nanoparticles along the $\langle 11\bar{2} \rangle$ directions on the substrate allow for synthesis of two distinct types of nanocrosses. Either the kinked planar or kinked vertical nanocrosses can be grown, depending on patterning and adjustment of the Ga growth time during the kinking step.

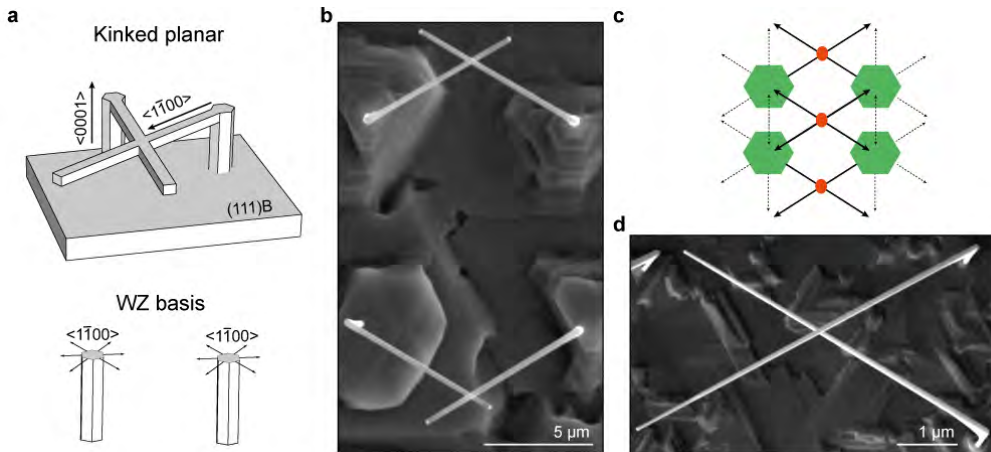


Figure 2.15: (a) Illustrations of a kinked planar nanocross, together with the respective basis (More details were given in Fig. 2.1). (b) Top-view SEM micrograph of two kinked planar nanocrosses merged from kinked NWs in plane parallel to the substrate. (c) Schematics of how rectangular substrate patterning results in formation of kinked planar nanocrosses. Possible growth directions (arrows), junctions (red) and NW stems (green). (d) Top-view SEM micrograph of a kinked planar nanocross. Adapted from Pub. 1.

While the probability to kink the growth direction is maintained close to 100%, two kinked parts of the NWs can merge in order to form a kinked planar nanocross in a plane parallel to the substrate, as shown in Fig. 2.15 (a). In contrast to the inclined NWs, the faceting of the stems locks the structure of the merging kinked NW parts into the WZ basis. That is almost like if the whole structure is carved from a single piece of crystal and the junction is potentially single crystalline. Therefore the kinked NW parts are WZ and have a square cross-section with $(11\bar{2}0)$ side, $(111)B$ top and $(111)A$ bottom facets. An example of two kinked planar nanocrosses is shown in (b). Here, a simple rectangular substrate patterning allows for formation of the nanocrosses as sketched in (c). The nanocross yield is low due to the 6-fold randomness in the growth directions. On the other hand it is high enough to allow for controlled nanocross transfer and devices processing, as will be shown in chapter 4.

Formation of the nanocrosses relies on the kinked NW parts to grow in very close proximity to the mutual kinking plane. Once they pass by without hitting one another during the kinked part growth, they are attracted by Van der Waals and electrostatic forces. After merging by facets the NWs start to overgrow together. While the kinked NWs are grown with diameter below 100 nm, the 120 nm spread in the kinked height (that was shown in Fig. 2.13) promotes such junction formation. For larger NW diameters, a variation in Au volume needs to be part of the patterns, in order to kink the NWs in

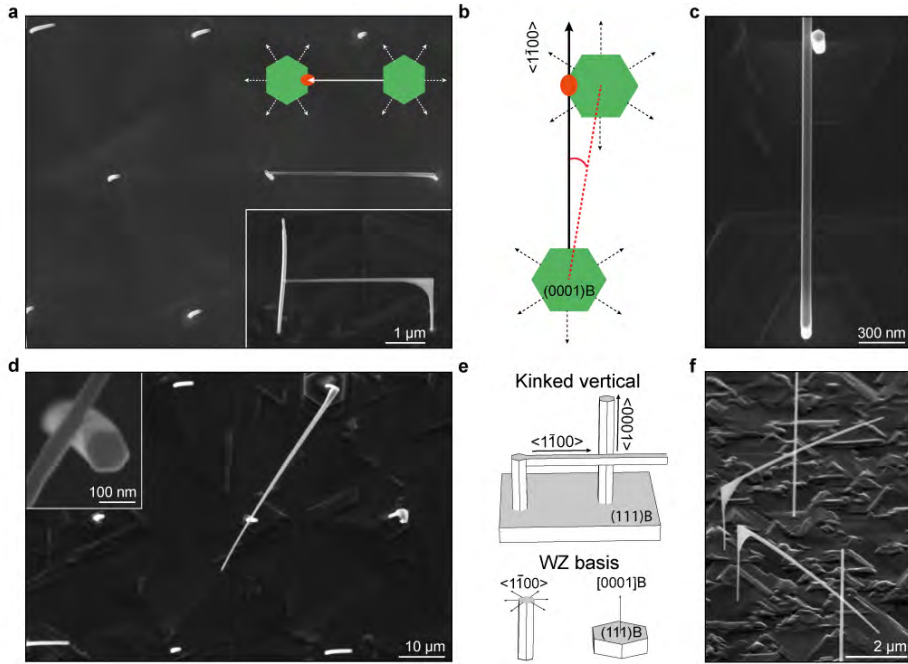


Figure 2.16: (a) Top-view SEM micrograph, showing a NW array grown from a hexagonal pattern, where reduced probability to kink promotes formation of a vertical 'h' structure (side-view in the inset) by merging a kinked and free-standing $[0001]_B$ NW. (b) Schematics of how a slight pattern rotation with respect to the $\langle 1\bar{1}00 \rangle$ directions allows for the kinked NW to pass by a free standing $[0001]_B$ NW and form a kinked vertical nanocross. A real example of the same situation is shown on SEM micrograph in (c). (d) Top-view SEM micrograph, showing a NW array grown from a hexagonal pattern, where reduced probability to kink and rotation of the pattern (as in (c)) promotes formation of a kinked vertical nanocross, with detail of the junction shown in the inset. (e) Illustrations of a kinked vertical nanocross, together with the respective basis (More details were given in Fig. 2.1). (f) Tilted-view (30°) SEM micrograph of two kinked vertical nanocrosses. Adapted from Pub. 1.

different heights. That prevents the NWs from hitting one another and form 'y' shaped structures rather than nanocrosses.

As the Ga flux is reduced during the NW kinking, the probability for the NWs to not kink and maintain the $[0001]_B$ growth direction increases, i.e adjusting the GaAs growth time provides control over the kinked and free-standing NW ratio. A low ratio of kinked NWs combined with hexagonal substrate patterning aligned with the $\langle 11\bar{2} \rangle$ directions on the substrate, then allow for formation of 'h' shaped structures, as shown in Fig. 2.16 (a). Here, each NW is surrounded by 6 other NWs placed exactly at the direction of the kinked

NW growth. Therefore, the kinked NW has high probability to directly hit one of the surrounding [0001]B NW. Obviously, the desired structure is not formed if the targeted NW also kinks. The junction is most likely contaminated by the catalyst nanoparticle, due to the direct catalyst-NW interaction during the merging process.

In order to synthesize a kinked vertical nanocross, the hexagonal substrate patterning was rotated by angle corresponding to 50-300 nm misplacement with respect to the $[11\bar{2}]$ direction of the substrate, as shown in Fig. 2.16 (b). Result of the growth is shown in (c) where the kinked NW grows past the [0001]B NW, but both of them seem to be attracted one to another and slightly overgrown together, similarly to the previous case. The same structure is shown within the rotated hexagonal patterning in (d). If the standard/kinked NW ratio is kept high, each kinked NW has high probability to pass close by one of the six neighboring NWs and form the desired structure. The resulting junction is again potentially single crystalline, since both NWs are WZ and merge within the same basis of the NW stem side facets as shown in (d). Yield of the structures is again limited mainly by the randomness in the directionality of the growth.

The nature of the junction formation does not seem likely to form high-quality crystals within the junctions. Surprisingly, the TEM analysis in the next section will show that the junctions can indeed form as single crystals.

2.2.5 Crystal structure within the nanocross junctions

The inclined nanocrosses stem from the ZB basis of the substrate, which then sets the angle of inclination between the substrate plane and the $\langle 0001 \rangle$ B growth direction. Analysis of the crystal formed while two NWs merge growing in the two opposite $\langle 0001 \rangle$ B directions (two respectively rotated WZ bases) shows that there is no coherent match within the junction, since the relevant symmetry does not exist in the WZ structure that the NWs grow in. In order for the NWs to coherently match together, a ZB segment can be inserted within the junction^{168,171,188} as shown in crystal model in Fig. 2.17 (a). Depending on the size of the ZB segment, WZ/WZ incoherent boundaries can form at the junction, as highlighted by red arrows.

The NWs merge under the angle of 109.4° , as indicated in Fig. 2.17 (b) for an inclined nanocross transferred to a TEM grid. The TEM micrograph in (c) then shows the real structure of the junctions, which consists of four WZ branches and a diamond shaped ZB segment embedded at the center. The branches continue to grow past the junction uninterrupted with a negligible amount of stacking faults.

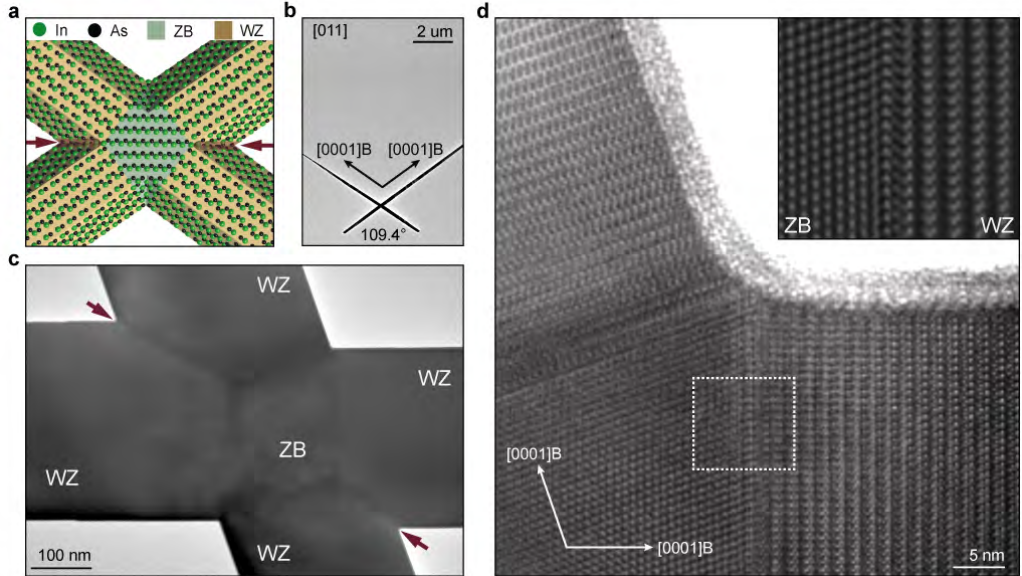


Figure 2.17: (a) Crystal structure model suggesting appearance of ZB segment within WZ inclined nanocross junction. (b) Overview TEM micrograph of an inclined nanocross placed on a TEM grid. (c) Zoom-in on the nanocross junction, indicating crystal phase change from ZB to WZ within the junction. Two WZ/WZ incoherent boundaries are highlighted by red arrows. (d) High-resolution TEM micrograph of the upper corner of the junction showing a WZ/ZB/WZ transition between the branches of the nanocross. A processed zoom-in of a single plane WZ/ZB transition is shown in the inset. Adapted from Pub. 1.

The shape of the ZB segment is highly reproducible under given growth conditions. Its origin is most likely related to energy minimization of the crystal within the junction by recrystallization of the high energy incoherent grain boundaries formed between the two merging WZ crystals. The change from the WZ to ZB is abrupt and occurs within one atomic layer as shown in 2.17 (d).

Interestingly, the crystal structure within the junction can be significantly affected by change of the growth temperature, in this case from $\sim 410^\circ\text{C}$ to $\sim 500^\circ\text{C}$. If the inclined NWs are not merged together, they maintain WZ structure and no obvious changes happen, apart from growth rate. The situation is very different when they merge into a junction. An example is shown in Fig. 2.18 (a). The ZB inclusion disappears and an intermixing of WZ and multi-twinned ZB progresses into the NW branches. That is interesting since all observed single NWs seem to be WZ with only low density of stacking faults. This indicates that the whole nanocross recrystallizes in order to reduce incoherent boundaries

at the edges of the junctions. As a result, complex crystal forms within the junction as shown in Fig. 2.18 (b).

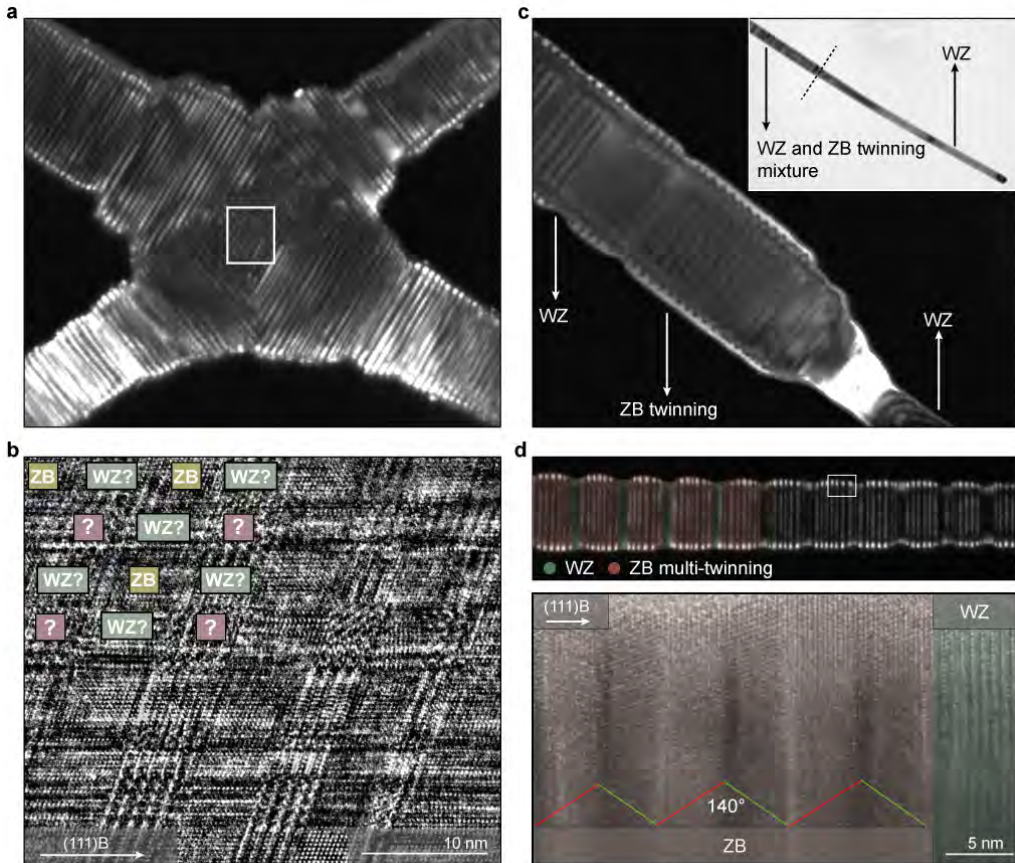


Figure 2.18: (a) Dark field TEM micrograph showing crystal structure within the junction of an InAs inclined nanocross, grown at a temperature of $\sim 500^\circ\text{C}$. (b) Fourier filtered high-resolution TEM micrograph of the crystal in the center of the junction (area highlighted in (a)), showing a periodic structure comprised of three different segments: yellow - ZB, green - structure similar to WZ and red - unidentified. (c) Dark field TEM micrograph showing a transition from periodic WZ/ZB multi-twinning structure into a pure WZ NW segment. The inset shows an overview image of the segment. (d) Darkfield TEM micrograph of a segment of one of the NW branches between the junction and the catalyst showing periodic crystal arrangement of WZ and multi-twinning ZB (top-panel), similarly to (c). WZ is highlighted in green and multi-twinning ZB in red. The bottom panel shows detail of one of the transitions between WZ and ZB.

It is possible to identify rectangular ZB segments. Those are surrounded by narrower segments, which seem to be WZ. Unfortunately, it can not be conclusively confirmed without further measurements. The nature of the secondary rectangular segments, which share corners with the ZB and are bound by WZ is not clear. They appear in the areas where the suspected WZ segments can not coherently match, since they correspond to opposing (111) directions stemming from the ZB basis of the substrate. Even after analysis of Fourier spectra of the image, it is not clear if the main features represent the real atomic structure. We suspect that the visible periodicity could also correspond to a Moiré pattern. That could be a result of different overlapping ZB twins, other types of complex 3-D stacking or overlapping of incoherently matched or opposing (0001) WZ planes. The structure needs to be further investigated by dark field TEM in order to determine its true nature.

All the four NW branches turn into pure WZ, after few micrometer long segments consisting of periodic mixing of WZ and multi-twinned ZB¹⁸⁹, as shown in Fig. 2.18 (c) and (d). These segments extend from the junction towards the ends of the branches, where they again adapt pure WZ structure. That confirms that the merging process does not only affect the very junction, but that the recrystallization progresses throughout the whole nanocross structure. That is most likely enabled by the additional energy related to the 90°C higher growth temperature.

This is an interesting mechanism for crystal phase engineering, which is not a direct consequence of changing the growth conditions, but requires specific geometry of the merging crystals. The presented results are preliminary, but details of the recrystallization process will be further studied*. It would be especially interesting to investigate effect of different growth temperatures on the crystal structure, periodicity of WZ and ZB multi-twinning dependence on NW diameter and other related effects.

The kinked planar nanocrosses merge within the same WZ basis which is set by the stem NW faceting. That is supported by crystal model in Fig. 2.19 (a), where two kinked NWs merge under the angle of 120°. A TEM micrograph of a kinked planar nanocross junction is shown in (c) for a nanocross deposited on a TEM grid shown in (b). The darker contrast within the junction is related to the increased thickness, which confirms that the NWs do not grow together via bulk but via facets, as was described above. High resolution micrograph and diffraction pattern of the junction are shown in (d). The junction is clearly single crystalline. A-B-C stacking is apparent from both the micrograph and the diffraction pattern. That is most likely due projection of planar ZB stacking faults and overgrowth of the (0001)B top-facet, which were discussed in section

*The TEM and related analysis was done together with Martin Espineira, Thomas Kanne and Erik Johnson from the Center for Quantum Devices.

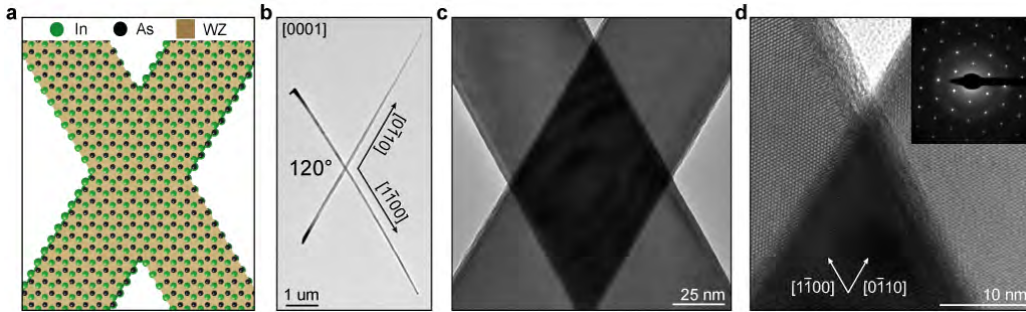


Figure 2.19: (a) Crystal structure model of a kinked planar nanocross junction showing a coherent match between two merged kinked NWs growing along $\langle 1\bar{1}00 \rangle$ directions. (b) Overview TEM micrograph of a kinked planar nanocross placed on a TEM grid. (c) Zoom-in on the junction region and (d) further zoom in on the upper corner of the junction indicating a single crystalline match between the NWs. The diffraction pattern taken within the junction is shown in the inset. Adapted from Pub. 1.

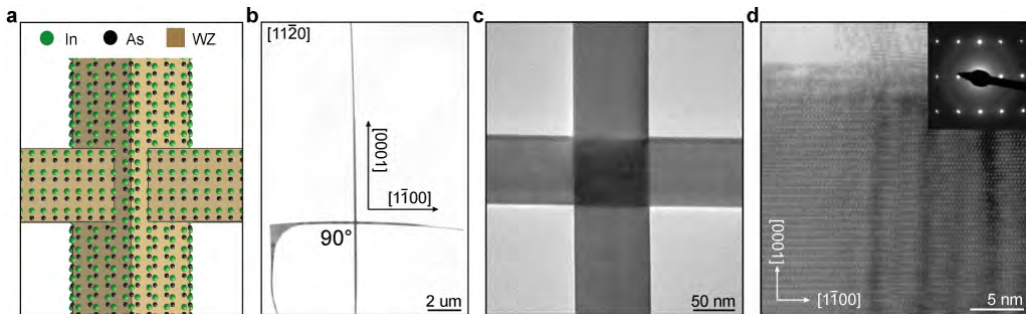


Figure 2.20: (a) Crystal structure model of a kinked vertical nanocross junction showing a coherent match between a kinked and [0001]_B NW. (b) Overview TEM micrograph of a kinked vertical nanocross placed on a TEM grid. (c) Zoom-in on the junction region showing Moiré pattern which indicates slight mismatch between the two NWs. (d) High-resolution TEM micrograph showing two slightly rotated WZ NWs. The diffraction pattern taken within the junction is shown in the inset. Adapted from Pub. 1

2.2.3.

Similarly, the kinked vertical nanocrosses also merge within the WZ basis set by the stem faceting. Crystal model of the 90° junction shown in Fig. 2.20 (a) suggests that a single crystalline match should be possible. A TEM micrograph of a kinked planar nanocross junction is shown in (b) for a structure deposited on a TEM grid shown in (c). Again, the darker contrast within the junction confirms that the NWs merge together via facets. NWs forming the examined junction seem to be respectively rotated as apparent

from visible Moiré pattern (corresponding to $\sim 2^\circ$ rotation) and diffraction patterns with distorted Bragg peaks in Fig. 2.20 (d). Despite of the rotation, the crystal coherency could be retained by strain since there dislocations were observed within the junction. Therefore the structure seems to be single crystalline, similarly as for the kinked planar nanocross.

The observed structure within the junctions should support its transparency to electron transport, which will be discussed in next section.

2.2.6 Electron transport transparency of the junctions

Simple four probe measurements were used in order to address the electron transparency of all three presented types of nanocross junctions. Series of measurements on the inclined nanocrosses, did not show resistance dependence on measured branch combinations. That is interesting, since the shortest physical electron path through the junction can either go through the ZB segment or through the in-coherent WZ/WZ boundaries, depending on source-drain branch combination. In addition, a very weak length dependence of measured resistance was observed for devices with varying probe to junction distances. That suggests that the resistance is associated with the very junction.

A double cross device based on inclined NWs, shown in Fig. 2.21 (a), was characterized in order to extract the junction contribution to the total resistance. The extracted resistivities were homogeneous through different measured combinations of the nanocross branches (illustrated in bottom panel of (a)), yielding total average resistivity of $\bar{\rho}_{NW+R_1+R_2} = 700 \pm 75 \times 10^{-4} \Omega \cdot \text{cm}$. That is approximately one order of magnitude higher than the resistivity for a single NW of the same diameter. The measurement results acquired through different sets of doublecross branch combinations allow for calculation of the bare NW resistivity $\rho_{NWcalc} = 54 \pm 2 \times 10^{-4} \Omega \cdot \text{cm}$ and resistance contributions of both junctions $R_1 = 5.9 \pm 0.8 \text{ k}\Omega$ and $R_2 = 6.3 \pm 0.9 \text{ k}\Omega$. The typical resistance value for approximately $2 \mu\text{m}$ doublecross segment which included the junction was $\sim 10 \text{ k}\Omega$. Therefore, the $\sim 100 \text{ nm}$ long ZB segment dramatically increases resistance for transport through the junction.

The ρ_{NWcalc} was calculated from measurements through 8 different branch combinations which allowed for solving 4 sets of following equations

$$R_{measured1} = R_1 + \rho_{NWcalc} \cdot C_{i,j} \quad (2.1)$$

$$R_{measured2} = R_2 + \rho_{NWcalc} \cdot C_{i,j} \quad (2.2)$$

$$R_{measured3} = R_1 + R_2 + \rho_{NWcalc} \cdot C_{i,j} \quad (2.3)$$

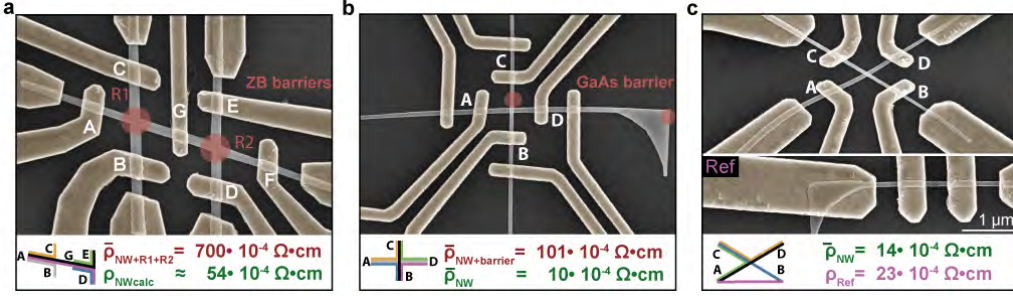


Figure 2.21: Colored SEM images of four-probe devices based on (a) inclined double cross, (b) kinked vertical nanocross and (c) kinked planar nanocross with a reference kinked NW. The expected transport barriers are highlighted in red for ZB inclusion R_1 and R_2 and for the growth induced GaAs barrier. The measured branch combinations are sketched below the panels together with measured mean resistivities including and excluding the barriers. Adapted from Pub. 1.

Resistivity scaling factors $C_{i,j}$ extracted from the SEM micrographs correspond to the length and diameter of the measured NW segments. The length corresponds to the expected electron path from terminal i to terminal j or junctions R_1 or R_2 . As an example of the electron path for measurement from terminal A to terminal E, the scaling factor takes following form

$$C_{A,E} = \frac{l_{A,R_1}}{\pi \cdot r_{A,R_1}^2} + \frac{l_{R_1,R_2}}{\pi \cdot r_{R_1,R_2}^2} + \frac{l_{R_2,E}}{\pi \cdot r_{R_2,E}^2} \quad (2.4)$$

where $r_{i,j}$ and $l_{i,j}$ are the diameter and length of the selected nanocross segment.

The result suggests that a transport barrier is associated with the very junction. That is supported by the TEM results, which show that the WZ/ZB interfaces are single plane and no strain was observed around the interfaces. Therefore the barrier is most likely connected to the band offset between the ZB and WZ crystal phases, which is consistent Refs. [114, 190, 191], where similar transitions were used to form barriers in crystal phase quantum dot related experiments. The symmetry of the resistance while measuring through different branch combinations indicates that the electron wavefunction localizes within the ZB segment. More data related to the quantum dot formation will be discussed in next section and confirm the nature of the ZB barrier.

The same measurements on the kinked vertical nanocross also suggested presence of a transport barrier, as shown in Fig. 2.21 (b). Measurements through branch combinations where branch C was excluded have shown expected resistivity value for a bare NW,

$\bar{\rho}_{NW} = 10 \pm 9 \times 10^{-4} \Omega \cdot \text{cm}$. When branch C was included in the measurement the resistivity increased to $\bar{\rho}_{NW+barrier} = 101 \pm 8 \times 10^{-4} \Omega \cdot \text{cm}$. The most likely explanation is that a GaAs barrier forms in the vertical NW during the growth direction kinking step, was confirmed by EDX analysis of the junction, as was shown in Pub 1*. The same barrier forms at the corner of the kinked NW, but does not contribute to the transport, since it is excluded from measurement by device geometry. Formation of the barrier can be avoided by altering the growth direction change step, for example by implementation of temperature change induced kinking^{140,176}. While the GaAs barrier is excluded, the junction seems fully transparent through all other branch combinations. That makes the structure a good potential candidate for three terminal quantum transport experiments⁴².

As expected based on the TEM characterization, the kinked planar nanocross junction is also fully transparent and its average resistivity $\bar{\rho}_{NW} = 14 \pm 10 \times 10^{-4} \Omega \cdot \text{cm}$ is comparable to a single kinked NW. In addition the presented data confirm that all three structures are feasible for electronic device fabrication and can be utilized in more complex low temperature experiments. Even though, the inclined nanocrosses are not feasible for barrier free experiments, as are their kinked counterparts, they offer other interesting possibilities which will be discussed in next section.

2.2.7 Crystal phase quantum dots in inclined nanocrosses

The transport barrier within the inclined nanocross junctions seems to be related to the crystal phase change from ZB to WZ. Since the WZ structure does not form in bulk InAs, the NWs offer an interesting platform for crystal phase engineering^{89,190}. The band conduction band off-set of ~ 100 meV between the two phases^{191,192} was shown to allow for in-situ formation of transport barriers during MBE growth without changing the material composition^{114,193}.

Based on the results described in previous section, multiple inclined nanocrosses and double-crosses were measured in dilution refrigerators with base temperature $T \sim 15$ mK, in order to investigate the properties of the ZB segment within the junctions. The results were reported in Pub. 3. A combination of global and local electrostatic gates were used in order to tune the intersection between weakly/strongly coupled quantum dot regimes and an open regime, where the ZB contribution becomes negligible. An example of a measured device is shown in Fig. 2.22 (a). The schematics in Fig. 2.22 (b) then illustrates the expected effects of standard quantum dot characterization⁶⁵ for different gate configurations.

*The EDX measurement and analysis was performed by Thomas Kanne. See Pub. 1 for affiliation.

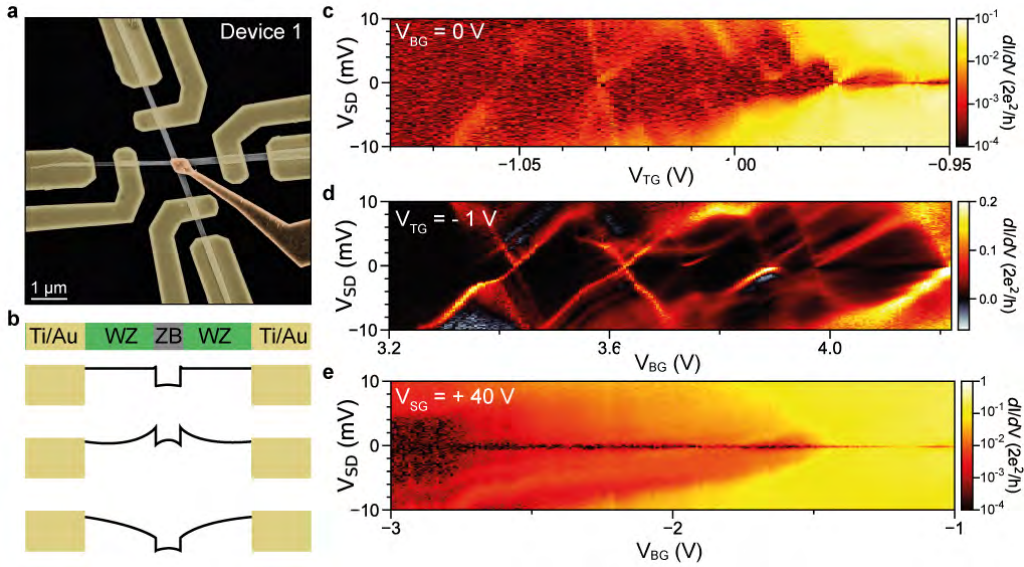


Figure 2.22: (a) SEM micrograph of a inclined nanocross device with eight ohmic contacts (gold) and a top-gate (brown) insulated from the nanocross by HfO_x . (b) Diagrams of expected gate dependent conduction band profiles of the WZ/ZB/WZ junction. The top diagram corresponds to zero gate voltages; middle to negative local top-gate and positive backgate; bottom to positive local top-gate. The measurement results for the three configurations are shown in: (c) negative top-gate voltage V_{TG} and zero backgate voltage V_{BG} are applied showing a faint coulomb diamond structure in differential conductance $\frac{dI}{dV}$ as a function of V_{TG} and source drain voltage V_{SD} . (d), $V_{TG} = -1$ V and V_{BG} is swept positive in order to raise the tunnel barriers resulting in a well defined coulomb diamond structure. (e), a side gate voltage $V_{SG} = 40$ V is applied to on a similar device and V_{BG} is swept, with no visible coulomb diamond structure, indicating that the effect of the quantum dot has diminished. Adapted from Pub. 3.

The first situation in Fig. 2.22 (b) corresponds to zero gate voltages, where the ZB segment gives rise to transport barriers due to the difference in band gap sizes and electron affinities of both involved crystal phases. That corresponds to the source-drain bias V_{SD} spectroscopy data in (c), where top-gate voltage V_{TG} is used to locally probe the electronic states. Without use of the backgate, the barrier height comes only from the band alignment and its effect is weak. The differences in conductance at $0 V_g$ and finite bias can be related to the barrier resistance presented in previous section. The second situation, corresponding to data in (d), shows bias spectroscopy of a quantum dot. Here, the local topgate V_{TG} is set to -1 V to keep the quantum dot near depletion, while global backgate is swept positive in order to fully open the remaining parts of the structure. This configuration results in clear Coulomb diamond structure. During the last investigated

regime that corresponds to measurements in n Fig. 2.22 (e) (a different device with similar trends but side gate geometry), the effects of the barrier were reduced by setting a side gate voltage V_{SG} to + 40 V and the energy states within the structure were probed by sweeping V_{BG} . Here, no coulomb diamonds appear and the quantum dot does not affect the transport anymore.

For results of characterization of more similar structures, including an inclined doublecross, I refer the reader to Pub. 3. As an example, the double-cross characterization has shown that energetics of separate junctions can be independently tuned within the same structure, in the same manner as was described above for single junction geometry. The consistency in the measurement results shows that the impact of the crystal phase on electron transport can be tuned within standard gating schemes.

Such multi-terminal semiconducting structures that intrinsically exhibit energetics that can be tuned between fully open and quantum dot like regimes, may have potential in Majorana bound state related quantum transport experiments⁶². Especially if more controlled methods for growth of inclined nanocrosses are developed in order to increase the scalability and provide better control over the overall nanocross morphology, e.g. junction spacing, branch length etc. An outlook on such a method will be given at the end of this chapter.

2.2.8 Scaling of kinked nanocrosses into larger networks

It was previously shown that the inclined NW growth allows for scaling up into larger NW networks¹⁷⁰. The presented kinked NW growth method can also be used for in-plane merging of multiple NWs together, despite the 6-fold directionality. The main factors allowing for scaling the growth up are specific patterning of the substrate with respect to its crystal structure together with the ability to precisely control the height of the kink of the NWs, as was shown in Fig. 2.13.

An example of such growth is shown in Fig. 2.23 (a), where hexagonal substrate patterning resulted in merging of multiple NWs. Here the structures form in-plane networks, which are ready for on chip-fabrication. Ref. [194] suggests a method allowing for fabrication of such devices. In short, it was proposed that a resist could be spun up to the kinks and hard baked. After, the excess resist that could be also covering the kinked parts of the NWs can be ashed away and common device fabrication is carried on top of the hard baked resist layer.

Results of a similar approach are shown in Fig. 2.23 (b). Here, multiple NWs merge similarly to kinked planar nanocrosses. The SEM micrographs depict kinked planar NW

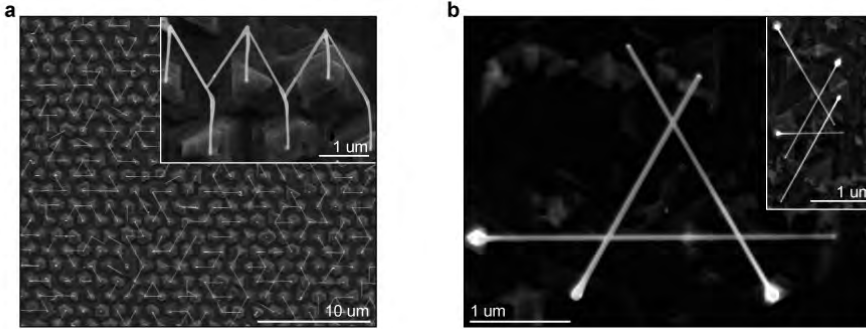


Figure 2.23: (a) Top-view SEM micrograph of a kinked NW growth on a hexagonally patterned substrate. The NWs kinked at the same height form larger networks while following the 6-fold directionality of the kinked NW growth. Inset shows a tilted SEM micrograph (30°) of a network connected from 6 NWs. (b) Top-view SEM micrograph of two kinked nanowire loops, that were grown based on the kinked planar nanocross synthesis.

loop structures, which maintain the single crystalline nature discovered within the kinked planar nanocross junctions. These structures are in principle feasible for both on-chip device fabrication or micromechanical transfer, but the actual fabrication procedure still remains to be developed. Here again the yield of the structures is limited mainly by the lack of precise control over the NW growth direction.

2.2.9 Shadowing VLS superconductor/semiconductor hybrid NWs

All the presented NWs are compatible with the SU/SE hybrid epitaxy⁵³ and may even offer interesting possibilities to tune the crystal interface matching^{134,195}. In addition, the change of the growth direction also allows for in-situ patterning of the radial SU/SE NW heterostructures, similar to the one introduced for growth on (001) substrate by Gazibegovic et al. in Ref. [170]. The idea is to utilize such shadow patterning in devices relying on normal (non-proximitized) and superconducting (proximitized NW segments) present on the same NW. The Al shell patterning was previously successfully used in experiments with tunnel probe devices⁵⁷, Josephson junctions¹³ and superconducting islands⁵⁸.

Fabrication of the bare semiconductor segments after growth is often limited by availability of etching methods that must be selective to the NW material. In addition, wet etching can result in formation of unintentional quantum dots within the etched segments that affect the experiments by introducing undesired energy states¹⁹⁶. Therefore, such

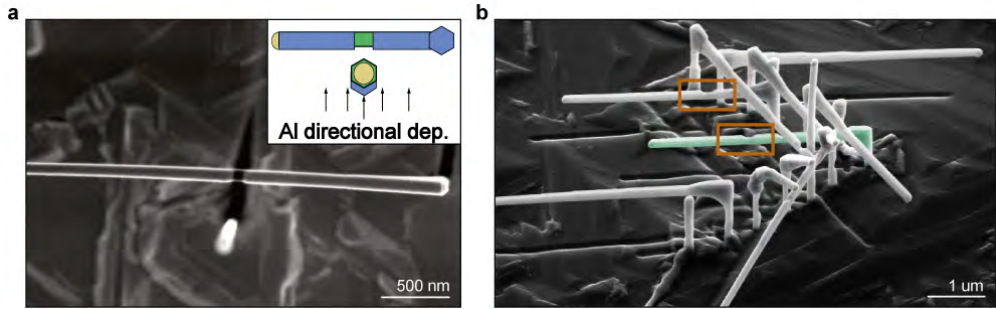


Figure 2.24: (a) Top-view SEM micrograph of a shadowed kinked InAs/Al NW heterostructure. The directional Al deposition is selectively shadowed by a nearby [0001]B NW, as illustrated in the inset (NW is green, Al is blue, Au nanoparticle is yellow). (b) Tilted-view (30°) SEM micrograph of a shadowed kinked InAs/Al heterostructures, where the NWs are kinked in different height by growth from patterns with different catalyst size. Adapted from Pub. 1.

shadow based patterning can widen the choice of available superconducting materials and ensure suppression of any etching related damage to the NW surface. InAs NW with patterned Al shell is shown in Fig. 2.24. In (a) the reduced probability to kink is used together with specific patterning, to shadow a segment of 2-facet kinked SU/SE NW heterostructure by a neighboring [0001]B NW. Another option is shown in Fig. 2.24 (b) where control over the NW kink height is used in order to shadow the kinked part of another NW*. In this case, the geometry allows for deposition of the superconductor from the top just on a single facet of the kinked NW with square cross-section. Characterization of the materials will be subject of future work.

2.3 Conclusion

The results presented in this chapter demonstrate the versatility of the VLS growth method, and how it can be extended when combined with growth on pre-patterned substrates. Three novel types of NW crosses were grown and characterized [Pub 1]. Two form a single crystalline junction and the third embeds a well defined crystal phase quantum dot within the center of the geometry.

Specifically, the progress in understanding NW nucleation on non-standard substrate orientation allows for growth of inclined NWs and nanocrosses on (001) substrates [Pub 2]. Apart from the various advantages connected to the specific geometry, it offers an

*The results were produced by Thomas Kanne and Peter Krogstrup. See Pub. 1 for affiliations.

unusual tool for engineering of NW crystal structure. When two inclined NWs are merged, the natural incoherency results in recrystallization and crystal phase change within the very junction. The formed well defined ZB segment can then serve as a crystal phase quantum dot [Pub 3].

The presented kinking mechanism can be used to change NW growth direction and form kinked planar and kinked vertical WZ nanocrosses. Their formation is mainly facilitated by consistent substrate fabrication, which is tightly related to the crystal structure of the growth substrate. The novel types of NW junctions can be single crystalline and are fully transparent to electron transport at room temperature. The kinking method has further potential in growth of more complex NW structures consisting of multiple junctions as well as for in-situ shadowing of SU/SE hybrid NWs. As a very important result, all three types of nanocrosses are suitable for fabrication of complex electronic devices.

The level of control offered by the VLS growth mechanism offers many possibilities¹⁹⁷, including synthesis of advanced 3D structures and networks. The next challenge is to reliably fabricate and characterize these new materials. As will be shown in the next chapter, the SAG is clearly few steps ahead, since the yield of presented VLS based structures is limited by the degeneracy of growth directions, associated with the growth method. Nevertheless, the presented structures provide an interesting platform for variety of transport experiments and studies of fundamental physics, but may be of interest also in other applications.

2.4 Outlook

The presented growth methods offer many other possibilities that are not yet fully developed. Especially the merging of inclined NWs seem to offer further options for not only growing complex InAs structures by MBE and in-situ shadow masking of NW based heterostructures, but also controlled recrystallization of polytypic NWs.

Preliminary results in attaining complete control over the growth of inclined NWs in MBE are shown in Fig. 2.25. The idea of the growth method, which is similar to results achieved by MOCVD by Gazibegovic et al. in Ref. [170] is illustrated in Fig. 2.25 (a). At first V-shaped trenches are etched into InAs (001) substrates. After, Au catalysts are deposited on the exposed (111)B sidefacets. That allows for controlled growth of [0001] inclined NWs with high yield and also reduces the 2-fold growth direction degeneracy to 1-fold, as shown in Fig. 2.25 (b). The fabrication of the substrates is described in more detail in Chapter 4. The growth was done and the project will be continued by Sabbir A. Khan from the Center for Quantum Devices, under supervision of Peter Krogstrup.

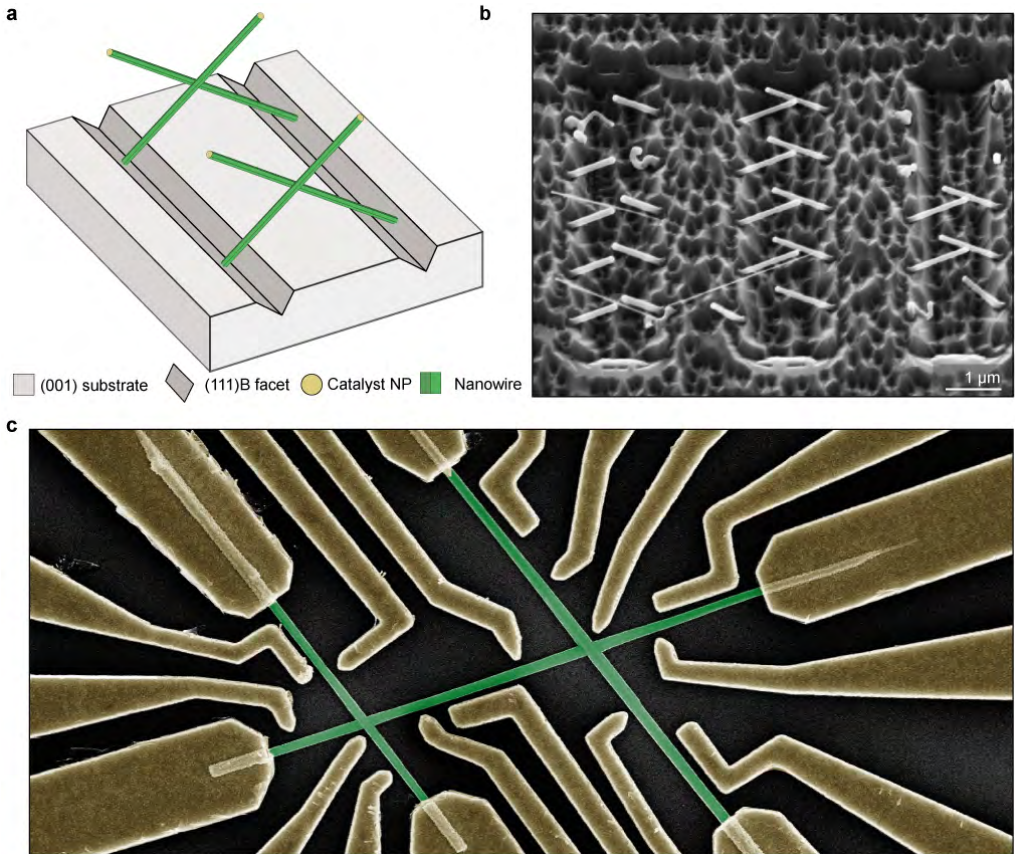
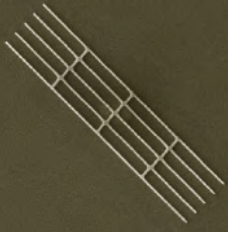


Figure 2.25: (a) Schematics of a proposal for fully controlled growth of inclined NWs on InAs substrates pre-patterned by wet-etching and Au catalysts. (b) Tilted-view (30°) SEM micrograph of an early stage of development growth on such substrates (grown by Sabbir A. Khan from the Center for Quantum Devices). (c) SEM micrograph of double nanocross devices, showing the consistency of fabrication on these types of structures.

This growth geometry has potential for both in-situ shadowing of SU/SE heterostructures and connecting inclined NWs into multi-terminal networks. The scaling up could be especially interesting for making in-situ arrays of quantum dots embedded in multiterminal NW based structures. An example of a device which could help to investigate the potential of these structures is shown in Fig. 2.25 (c). If the inclined multi-cross formation can be precisely controlled, so can be the distance between the ZB inclusions within the junctions. This may enable specific positioning and potential coupling of the embedded crystal phase quantum dots.



3. SAG Nanowire Networks

The data overlapping with Pub 4. are reprinted with permission from Copyright 2017, American Physical Society.

Despite the variability and crystal quality of VLS nanowires, they face many challenges related to scalability into larger quasi 1-D systems, as was apparent in previous chapter. This at the moment presents a limitation for industrial applications, but can be solved by using the SAG of in-plane NWs, which combines the variability of top-down fabrication methods and the purity of in-situ growth in MBE system. This chapter is focused on the structure optimization in relation to electronic transport properties of SAG NW networks and will be mostly based on results published in Pub. 4 and Pub. 5. Even though the approach of growing III-V semiconductor with SAG is over 50 years old¹⁹, our results report the first field effect gating, quantum coherence and superconducting transport data taken on these systems, which is a crucial step towards application of SAG structures in state of the art quantum experiments.

Selective growth of a buffer layer is introduced in order to reduce disorder between the SAG transport channel and the substrate, as shown in Fig. 3.1 (a). The buffered growth strongly enhances the interfacial quality between the NW and the substrate in form of partial elastic strain relaxation. The improved interface then enhances the transport properties of the structures. Apart of the NW/substrate interface, the substrate symmetry plays an important role in SAG and affects the structure and faceting of the NWs, as illustrated in Fig. (b). The NW alignment with respect to the substrate axes also affects

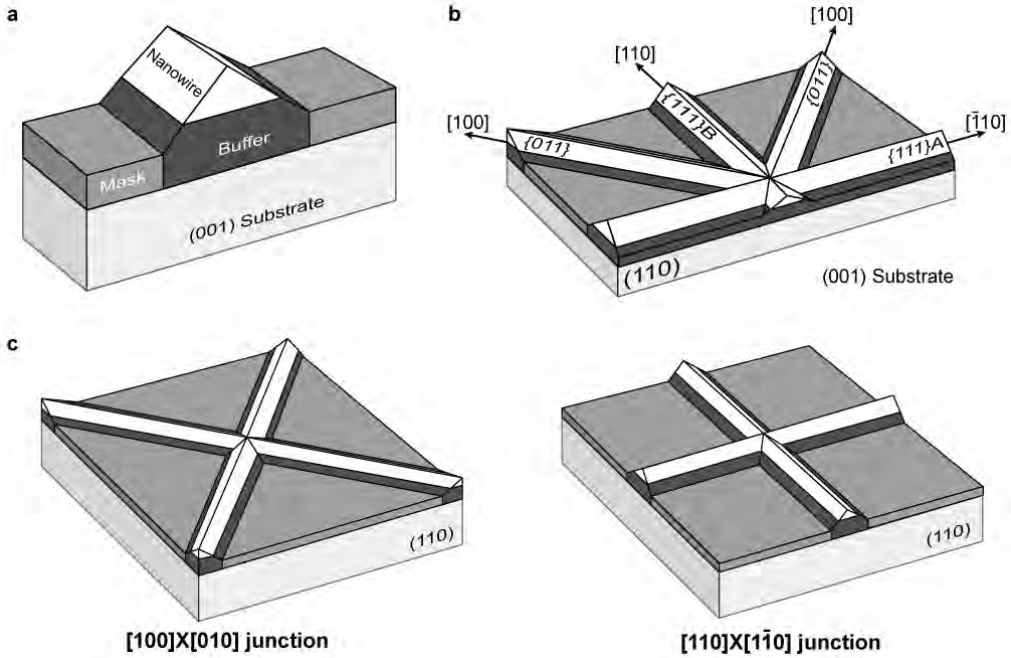


Figure 3.1: (a) Illustration of the buffered SAG NW structure. (b) Schematics of the stereographic projection showing the high symmetry orientations of (001) substrates put into relation with the expected SAG NW faceting for NWs grown along the high-symmetry orientations. (c) Illustration of the $[100] \times [010]$ and $[110] \times [1\bar{1}0]$ SAG NW networks.

the growth and different NW families often require specific growth conditions in order to synthesize desired structures. These effects are strongly related to the choice of substrate orientation, which here is the (001). This work focuses on two types of 90° junctions, the $[100] \times [010]$ and $[110] \times [1\bar{1}0]$, which are sketched in (c).

Specifically, the first part of this chapter is dedicated to growth of the SAG NWs directly on the substrate and its general aspects, e.g. faceting, symmetries, growth details etc. The second part then focuses on the growth of the NWs on top of a buffer layer. Later the electron transport measurement results are presented and discussed in relation to the implementation of the buffer layer and the NW scalability into quantum networks. At last results from measurements of semiconductor/superconductor SAG hybrids are shown, in order to demonstrate the potential of this material in superconducting quantum experiments.

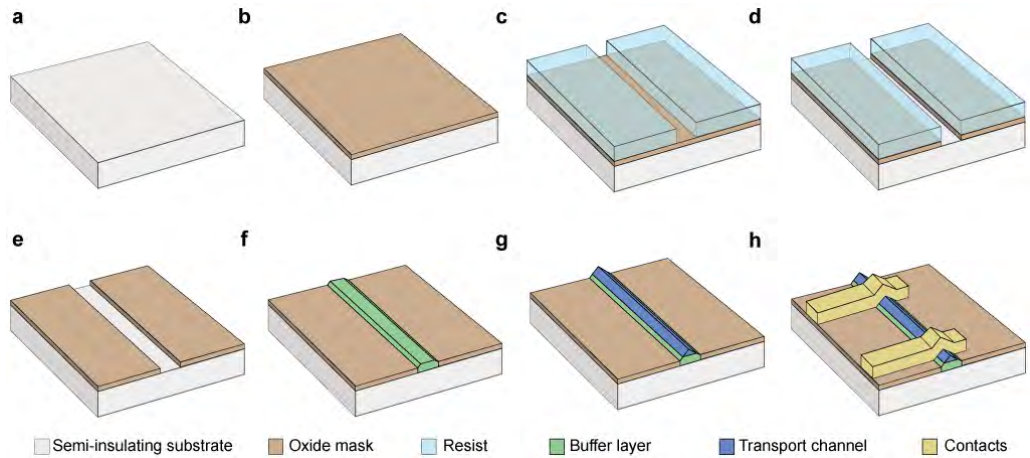


Figure 3.2: Schematics of the SAG synthesis process: **(a)** Semi-insulating substrate of chosen orientation is prepared. **(b)** An oxide layer is deposited. **(c)** A mask is fabricated in standard EBL process. **(d)** The prepared masked is etched into the oxide layer. **(e)** The substrate is thoroughly cleaned of any impurities induced in the fabrication process. **(f)** A buffer layer is selectively grown, e.g. GaAs. **(g)** The buffer layer is capped with the transport channel material, e.g. InAs. **(h)** Devices are fabricated directly on the grown substrate.

3.1 Methods

Synthesis of a SAG NW sample can be divided into several main steps as shown in Fig. 3.2. Here, Fe-doped InP and GaAs un-doped semi-insulating substrates were used. While cooled down to low temperatures, they become fully insulating and limit substrate leakage currents during transport experiments and therefore allow for device fabrication directly on the growth substrate, as-grown. In addition the lattice mismatch is close enough to InAs to make standard heteroepitaxy possible. More details are given in chapter 4 and full recipes are given in appendixes A, B and C.

3.1.1 Oxide mask

The substrates were covered by PECVD grown SiO_x , which serves as a mask for selective growth. The mask was patterned by standard EBL and wet etching. Resulting openings then serve as selected areas for epitaxial crystal growth. The typical mask opening (NW) width used in this work is between 100 and 350 nm. Single NWs were grown with roughly 10 μm spacing, whereas the NW to NW distance in networks depends on their design.

3.1.2 Growth of non-buffered NWs

The substrates were first thoroughly cleaned after processing (detailed steps are given in chapter 4), since the standard pre-growth acid cleaning was avoided in order to prevent damaging of the mask surface. After fabrication, a quarter of 2-inch substrate was inserted in the sample holder which was loaded on to the MBE transfer trolley and degassed at 200°C until the pressure in the load-lock reached $\sim 5e^{-8}$ Torr. After moving into the buffer chamber, the sample holder was annealed at 250°C on heated station, in order to remove impurities until the pressure reached $\sim 5e^{-10}$ Torr. After cooldown the sample was moved to the growth chamber and heated to $\sim 530^\circ\text{C}$ in order to blow of the native oxide under As_2 or As_4 overpressure.

Following cooldown to growth temperature $\sim 510^\circ\text{C}$, InAs was grown with a corresponding planar growth rate of $\sim 0.1 \mu\text{m/h}$ on InP and $\sim 0.26 \mu\text{m/h}$ on GaAs substrates*. The As_2/In ratio was 10 for growth on InP. Finally, the samples were cleaved into individual 0.5×0.5 mm chips and stored in nitrogen atmosphere. Detailed recipe is given in appendix B3.

3.1.3 Growth of GaAs(Sb) buffered NWs

The pre-growth procedure for buffered NWs was the same as for non-buffered up to the loading to the growth chamber step. The sample was at first annealed at $\sim 630^\circ\text{C}$ for 1 minute prior to cooldown to the growth temperature $\sim 615^\circ\text{C}$. The GaAs(Sb) buffer was grown with corresponding planar growth rate of $\sim 0.1 \mu\text{m/h}$, V-III ratio of ~ 20 and an $\text{As}_2/\text{Sb}_{2+4}$ ratio of 7.

After the buffer growth, the sample was cooled down to $\sim 510^\circ\text{C}$ and the InAs transport channel was grown at the same temperature with corresponding planar growth rate of $\sim 0.1 \mu\text{m}$ and As_2/In ratio of ~ 10 . Detailed recipe is given in appendix B4.

3.1.4 Superconductor in-situ deposition

Selected samples were cooled down after growth for in-situ Al deposition. Before cooldown the beam-flux ion gauge and sample heater power were turned off once the pressure in the growth chamber reached $3e^{-10}$ Torr in order to help the sample passively cool-down. Once the temperature reached $\sim -30^\circ\text{C}$, 4 nm of nominal Al thickness were deposited on the sample with growth rate of 0.04 nm/s, from a specific direction. After the deposition

*Corresponding growth on InAs directly on GaAs substrates was performed by the group at Technical University of Delft as listed in the author list of Publication 4.

the samples were unloaded before warming up, in order to prevent Al dewetting. Once removed from the system, water from the ambient atmosphere that condensed on the surface was removed by blowing nitrogen on the sample. That allowed for the top layers of Al to oxidize in ambient atmosphere and prevent further dewetting.

3.1.5 Structural characterization

The morphology and structure of the samples were characterized by scanning electron microscopy, atomic force microscopy and transmission electron microscopy*.

Scanning electron microscopy

The grown samples were characterized by scanning electron microscope FE-SEM JEOL 7800F. The typical overview and tilted SEM images were taken at 5 kV, working distance of 15 mm by secondary electron detector. The detailed images then at 2 kV, working distance of 4 mm by in-beam secondary electron detector in gentle beam regime or with backscattered electron detector at 5 kV and working distance of 6 mm. The devices were then typically imaged with Raith Eline microscope at 20 kV acceleration voltage.

Atomic force microscopy

The AFM characterization was done on Veeco Digital Instrument Dimension D3100 in tapping mode, where 300 kHz frequency with force constant of 40 N/m silicon AFM probes were used[†].

Transmission electron microscopy

Selected devices were covered by 15 nm of ALD Al₂O_x, thin layer of Pt and SiO_x and thinned into cross-sectional lamellae. Several cross-sectional lamellae on selected NWs were cut by focused ion beam. Subsequently, HR-TEM, HAADF scanning TEM (STEM) and EELS spectrum imaging (SI) were performed using a TECNAI F20 field emission gun microscope operated at 200 kV with a point to point resolution of 0.14 nm coupled to a GATAN Quantum EELS spectrometer. The atomic resolution HAADF-STEM images were acquired on a probe corrected FEI Titan 60-300 equipped with a high brightness field emission gun (XFEG) and a CETCOR corrector from CEOS to produce a probe size below 1 Å. The microscope was operated at 300 kV, with a convergence angle of 25 mrad

*The experimental part of TEM sample preparation and characterization was performed by Sara Martí-Sánchez and Jordi Arbiol. See Publication 4 and 5 for affiliations.

[†]The AFM data on NW networks were taken by Sabbir A. Khan. See Publication 4 and 5 for affiliations.

and an inner collection angle of the detector of 58 mrad. Atomic resolution aberration corrected HAADF-STEM was used to determine with high accuracy the atomic column positions, allowing the detailed study of polarity¹⁹⁸ as well as the final strain analysis by means of GPA¹⁹⁹. The characterization, lammellae preparation and part of data processing were done by Sara Martí-Sánchez and Jordi Arbiol, see Pub. 4 and 5 for affiliations.

Strain simulations

The rotational deformation fields were modeled by finite element method within COMSOL Multiphysics[®]. The 2-D problem was set, where the GaAs buffer layer and InAs transport channel are separated by continuous boundary. Different values of compressive strain were applied to InAs layer, in order to simulate the lattice mismatch to the buffer. The anisotropic linear elasticity tensor values were taken from Ref. [200] for GaAs and Ref. [201] for InAs.

3.1.6 Device fabrication

The devices were fabricated in standard EBL process directly on the semi-insulating growth samples. The alignment marks used, were part of the growth mask design and therefore grown from the SAG material, which allows for alignment with sub 50 nm precision. First the contacts and bonding pads were exposed directly on the growth chip. Then 5 nm of Ti sticking layer and 180 nm of Au were deposited in high vacuum AJA e-beam evaporator, after in-situ removal of the native oxide by Ar radio frequency plasma milling at 15 W for 5 min with 18 mTorr of Ar flow.

For top-gated devices 7 nm of HfO_x was deposited by ALD on the whole contacted chip after pumping on the sample for 10 hours. The growth was done at ~95°C during 70 cycles, with 180s waiting time between pulses. After, the sample was again patterned in standard EBL process and 5 nm of Ti sticking layer and 180 nm of Au were deposited as top-gates. The details of designing and preparation for loading are given in Chapter 4. The detailed fabrication recipe is given in appendix C.

3.1.7 Electronic Characterization

The fabricated devices were characterized at low temperatures in order to assess their electron transport properties. In each case the samples were cooled and out-gassed overnight before measurements. The field effect mobility was measured in a Lakeshore 4K cryo-free probe station at a base temperature of $T \sim 5$ K. Here, four-probe DC measurements were carried using Keithley 2600 source meter to control the gate voltage,

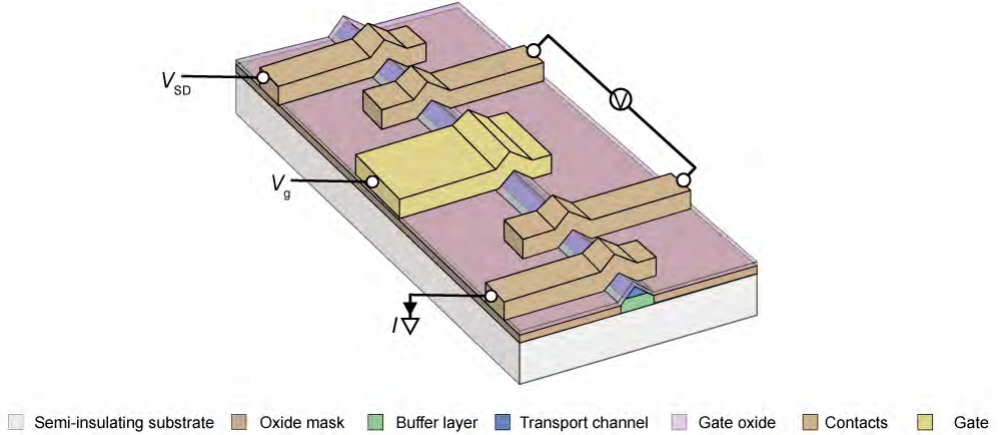


Figure 3.3: Schematics of a typical SAG 4-probe device geometry used in this work. V_{SD} is the source-drain and V_g the gate voltage. I is the measured current and V is the voltage drop over inner probes.

the source-drain bias and measure the current. An Agilent digital multimeter was used to probe the voltage drop on the inner contacts, after amplification by Stanford SR560 noise pre-amplifier with 100 M Ω impedance. A simple scheme of the measurement is shown in Fig. 3.3

Capacitance modeling

The gate-NW capacitances were simulated by finite element method in the electrostatic module of COMSOL Multiphysics[®]. The geometry and input parameters are summarized in Fig. 3.4. The dimensions of the problem were extracted by measuring the devices from cross-sectional TEM and top-view SEM micrographs. When the TEM data were not available, the dimensions were scaled correspondingly to the differences in the SEM micrograph. For the model input, NW geometry was approximated by a rectangular cross-section with the top-facet area corresponding to $S_{surf} \cdot L_{SAG}$, which is the real gate-NW area extracted from the TEM micrographs.

For the simplicity of the problem, the height of the gold contacts $h_C = h_{SAG} + 1/2 \cdot h_{ALD}$. Here h_{SAG} is the height of the SAG NW which was determined so that the cross-sectional area of the NW after flattening is conserved with respect to the real case. h_{ALD} is the real thickness of the ALD oxide layer. That corresponds to reality between the NW and the gate, but around it is given as $h = h_{SAG} + h_{ALD}$. The last parameter is the effective dielectric constant, which reflects both the HfO_x and InAs native oxide. The

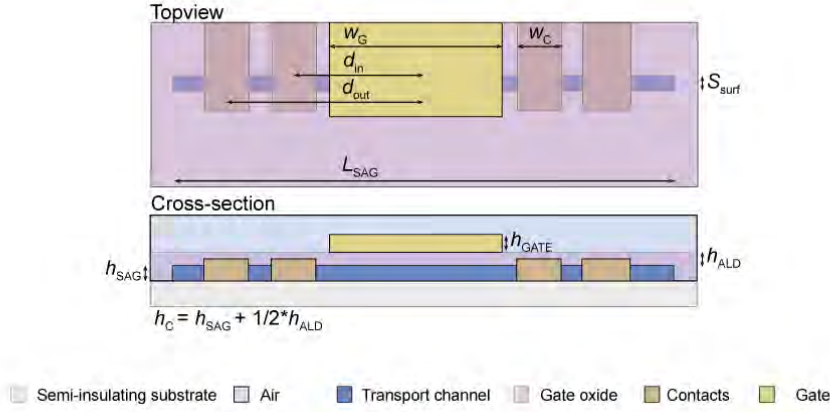


Figure 3.4: The geometry of the capacitance model. In the top-view: gate width V_G , contact width V_C , distance from center to the inner probe d_{in} and outer probe d_{out} , width of the SAG NW S_{surf} and length of the NW L_{SAG} . In the side-view the height of the NW h_{SAG} , height of the gate h_{SAG} and ALD thickness h_{ALD} .

dielectric constant was extracted from thickness series of saturation capacitance in capacitance/voltage curves. Unfortunately, only the bulk value was reliably extracted from the measurements. Therefore, the contribution of native 2 nm thick oxide InAs was estimated and the total dielectric constant of the two materials in series yielded $k = 6.5^*$. The calculated capacitance was multiplied by factor of 0.8, consistently with approach described in Ref. [33].

Field effect mobility fitting

The field effect mobility values were obtained from fitting the data with formula adapted from Ref. [33],

$$G(V_g) = \left(R_s + \frac{W^2}{\mu C (V_g - V_{th})} \right)^{-1},$$

to the pinch-off curves measured at ~ 5 K. Here $G(V_g)$ is measured conductance, W is the length of the transport channel between inner probes and mobility μ , threshold voltage V_{th} and probe resistance R_s are the fit parameters. The capacitance C was determined as

*The dielectric constant measurements were done on similar samples by Karthik Jambunathan and Shivendra Upadhyay.

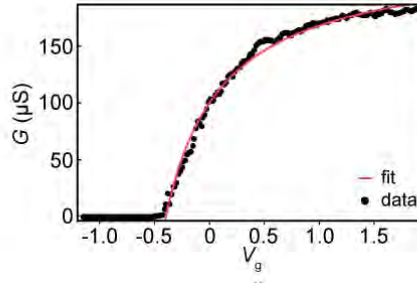


Figure 3.5: An example of measured gating data and corresponding fit of the field effect mobility, where G is measured conductance and V_g is applied gate voltage.

described in previous section. An example of a fit is shown in Fig. 3.5.

Magneto-conductance measurements

The weak anti-localization (WAL) was measured in a Bluefors XLD-400 dilution refrigerator operating at a base temperature of $T \sim 20$ mK. The devices were prepared in the manner as in the case of field effect mobility measurement (above) and conductance data were measured by standard current-biased AC lock-in techniques*.

The Aharonov-Bohm (AB) oscillations were measured in an Oxford Triton 100 dilution refrigerator with a base temperature of $T \sim 20$ mK. The devices were prepared in the same manner as in the case of field effect mobility measurement, but on SAG loop structures without top-gates and measured by standard current-biased AC lock-in techniques. Magnetic fields on the order of 900 mT were aligned to the $[110]$ and $[1\bar{1}0]$ directions in order to suppress the WAL effect while sweeping the perpendicular magnetic field[†].

Weak anti-localization analysis

The spin-orbit length l_{SO} and phase coherence length l_ϕ were extracted for both diffusive and ballistic regime, by fitting the measured differential conductance Δg to the following models. For the diffusive case to^{195,202}

*The measurements were performed by Lucas Casparis, see Pub. 4 for affiliation.

†The measurement was done with Saulius Vaitiekėnas, see Pub. 4 for affiliation.

$$\Delta g(B) = -\frac{3e^2}{hL} \left[\left(\frac{1}{l_\phi^2} + \frac{4}{3l_{SO}^2} + \frac{1}{D\tau_B} \right)^{-1/2} - \left(\frac{1}{l_\phi^2} + \frac{1}{D\tau_B} \right)^{-1/2} \right], \quad (3.1)$$

where h is planck constant, L is the device length, D is the diffusion length and τ_B is the dephasing time defined as

$$\tau_B = \frac{3l_m^4}{W_{eff}^2 D}, \quad (3.2)$$

where $l_m = \sqrt{\hbar/eB}$ is the magnetic length and W_{eff} is effective width of the transport channel. For the ballistic case²⁰², the same data were fitted by

$$\Delta g(B) = -\frac{2e^2}{hL} \left[\frac{3}{2} \left(\frac{1}{l_\phi^2} + \frac{4}{3l_{SO}^2} + \frac{1}{D\tau_B} \right)^{-1/2} - \frac{1}{2} \left(\frac{1}{l_\phi^2} + \frac{1}{D\tau_B} \right)^{-1/2} - \frac{3}{2} \left(\frac{1}{l_\phi^2} + \frac{1}{l_e^2} + \frac{4}{3l_{SO}^2} + \frac{1}{D\tau_B} \right)^{-1/2} + \frac{1}{2} \left(\frac{1}{l_\phi^2} + \frac{1}{l_e^2} + \frac{1}{D\tau_B} \right)^{-1/2} \right], \quad (3.3)$$

where l_e is the elastic scattering length and τ_B becomes

$$\tau_B = \frac{C_1 l_m^4 l_e}{W_{eff}^3 D} + \frac{C_2 l_m^2 l_e^2}{W_{eff}^2 D}. \quad (3.4)$$

where constants $C_1 = 19/2$ and $C_2 = 24/5$ are set by the boundary scattering in the NW²⁰². Both models are applicable for $l_m \gg W_{eff}$ and in addition $l_e \gg W_{eff}$ in the ballistic regime. The data were averaged from gate dependent measurements over an interval of 80 mV.

Aharonov-Bohm oscillations spectral analysis

After acquiring the measurement data, the aperiodic oscillating background was removed by Savitzky-Golay filtering^{*203}. The phase coherence length $l_\phi(T)$ was extracted by fitting the temperature dependence of the AB oscillation amplitude A , obtained from the Fourier spectra. Here the exponent m in $l_\phi(T) \propto T^{-m}$, which determines the coherence length is extracted by assuming that the amplitude scales as $A(T) \propto \exp(-\frac{O}{l_\phi(T)})$, where O is the loop circumference²⁰⁴.

3.2 Results and discussion

The methods described above allow for growth of homogeneous and high crystal quality single NWs and also NW networks. That is confirmed by TEM characterization and by low temperature electron transport characterization as demonstrated by following results.

3.2.1 Growth of single nanowires

The growth of single non-buffered SAG NWs can still be challenging. Here we will focus on post substrate fabrication aspects, since the details of fabrication are discussed in chapter 4. As the pre-growth procedures, such as oxide desorption, can be adapted from the VLS growth, the first challenge is to achieve selectivity of the growth between the crystal and the oxide mask. An example is shown in Fig. 3.6, where samples with different masks ((a) ALD HfO_x, (b) e-gun evaporated SiO_x and (c) ALD deposited Al₂O_x) were glued on a holder wafer by liquid gallium and grown together in the same step. There are significant differences in the results ranging from full mask overgrowth to partial overgrowth and to significant diffusion over the oxide mask.

In addition the change in the selectivity and the type of the mask have impact on the morphology of the NWs. We have observed that the selectivity is affected by various growth parameters, e.g. choice of material, growth rate, V-III ratio. Although, the growth temperature seems to have most significant effect. An example is shown in Fig. 3.6 (d) where reducing the growth temperature on the same substrate resulted in inversion of the selectivity compared to (c), i.e. the mask was homogeneously overgrown and no material is deposited within the mask openings. In general, the lower bound of the selectivity window corresponds to growth where desorption of adatoms from the mask surface is higher than adsorption. In essence, no material sticks on the mask. The upper bound is then set by the point in parameter space, where the desorption within the mask opening

*The spectral analysis was done by Alexander M. Whitticar, see Pub. 4 for affiliation.

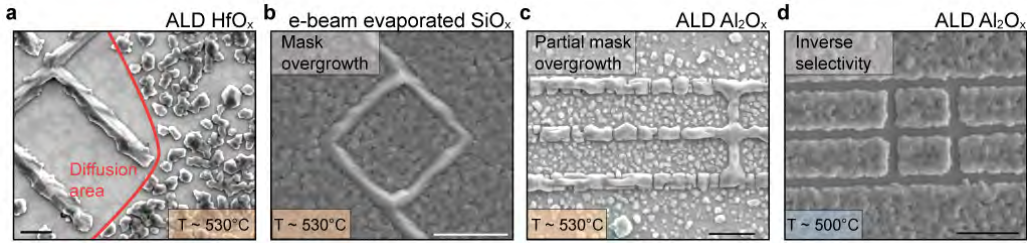


Figure 3.6: SEM micrographs of growth on different substrate masks (same growth for (a), (b), (c) and at lower temperature for (d)). In (a) growth on HfO_x indicates that material diffuses on the mask, since the area around the SAG network is partially cleared. On e-gun evaporated SiO_x in (b) the mask is fully and homogeneously overgrown by the grown material. For the ALD deposited Al_2O_x in (c) the mask is only partially overgrown, without any indication of significant diffusion area near the SAG network. The lower temperature growth in (d) (grown on the same substrate as c) then shows that change of one growth parameter can result even in inversion of the growth selectivity. The scale bars correspond to 1 μm .

becomes too high and the growth rate becomes negative.

In this work, the best results were achieved on PECVD grown SiO_x masks. For given growth conditions the selectivity temperature window starts around 510°C for InAs growth and about 100°C higher for GaAs(Sb) under given fluxes and growth rates. The bounds were determined by RHEED for growth on 2" substrate covered with the dielectric mask without patterning. The growth was initiated at high temperature, which was lowered in steps until deposition on the mask started to be apparent from emergence of a diffraction pattern. That sets the lower bound of the selectivity window. The PECVD process seems to provide enough consistency in both surface quality and reproducibility of wet etching to ensure stable growth results. In some cases a variation was observable even while maintaining the same growth conditions and formation of crystallites on the mask surface could be observed after growth. That is most likely related to the uncertainty in growth temperature, which is mainly related to variations between the used MBE holders.

The NWs are homogeneous and not interrupted over a variety of dimensions and the growth is fully selective, as shown in Fig. 3.7. On the other hand, the NW shape, conformity and morphology are related to its alignment with respect to the substrate crystal orientation. Therefore the many different properties can be achieved within the same growth by specific choice of substrate orientation and alignment of the mask to its crystal structure.

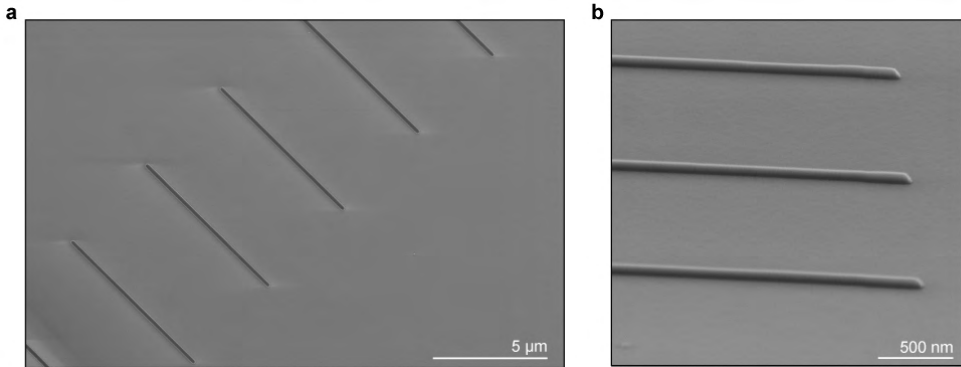


Figure 3.7: SEM micrographs of InAs SAG NWs grown on InP substrate, from (a) top-view and (b) tilted view (50°).

3.2.2 Crystal symmetry and nanowire morphology

The majority of growth in this work was done on (001) substrates. The substrate orientation significantly impacts the results and needs to be considered while designing the mask patterns. Figure 3.8 clearly illustrates how the NW orientation can affect their morphology. The pattern consists of single NWs incrementally rotated by 3° with respect to the $\langle 110 \rangle$ direction. The difference in morphology of individual NWs is clear in (a) where As_4 was used for growth. The discrepancy between morphologies that are associated with specific NW alignment can be reduced by changing the growth species to As_2 , as shown in (b). That clearly demonstrates the importance of tuning the growth conditions in order to grow uniformly faceted NWs^{153,156}, but also of taking the crystallography into account while designing and aligning the mask during EBL step.

Even though it seems that tuning of the growth conditions diminishes the effect of the NW alignment, more thorough analysis will show its importance. A stereographic projection related to the (001) substrate is shown in Fig. 3.9 (a). If the NW is grown along one of the highlighted high symmetry directions, it not only exhibits the related high-symmetry faceting, but tends to have smoother surface and better defined geometry in comparison to the miss-aligned NWs. The effect of miss-alignment is clear in (b), where miss-alignment from [100] directions by only 3° increases the roughness of the NW side-facets. The roughening is a result of tendency of the NWs to minimize energy by aligning to the high-symmetry orientations and maintain the relevant faceting. Therefore the angular miss-alignment with respect to these orientations often results in 'zig-zag' like longitudinal profiles of the NWs, as they tend to align to the closest high-symmetry axis, while being confined within the mask opening.

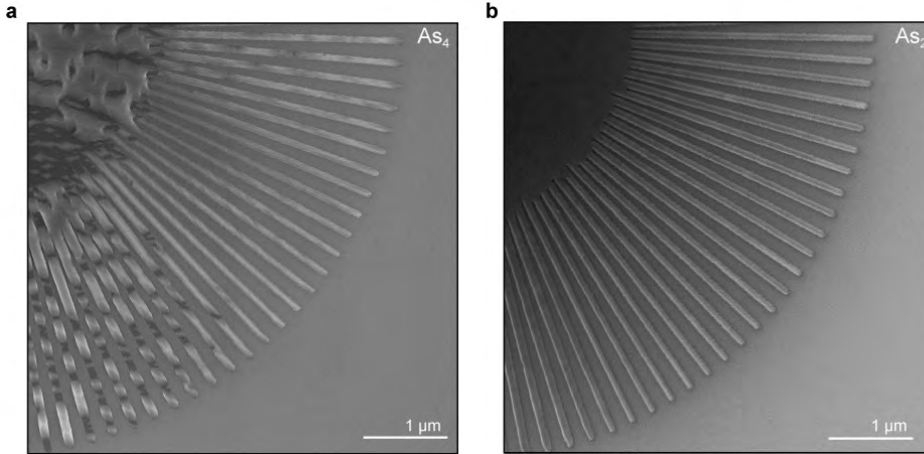


Figure 3.8: SEM micrographs of InAs SAG NWs grown with gradual 3° miss-alignment to the $\langle 110 \rangle$ direction of (001) substrate, forming a 'sun like' pattern. Here the samples were grown on similar substrates and under similar conditions, where As_4 was used for sample (a) and As_2 for sample (b).

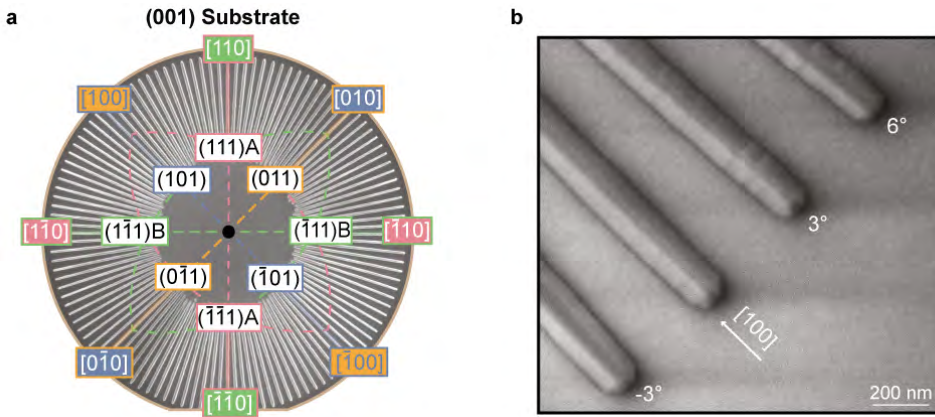


Figure 3.9: (a) SEM micrograph of NW array grown with increment of 3° , overlaid by stereographic projection that summarizes the high-symmetry orientations of a (001) substrate and expected NW faceting. The directions along the outer rim correspond to high-symmetry in-plane NW directions (box fill color). The expected low energy faceting for each of the directions is highlighted in the inner boxes and related to the directions by the outline coloring. (b) SEM micrograph of a well-faceted InAs NW aligned along the [100] direction, where neighboring NWs are miss-aligned from the [100] direction by -3° , 3° and 6° . Adapted from Pub. 4.

Here the focus is going to be on growth along the $[100]$, $[1\bar{1}0]$ and $[100]$ directions*, which exhibit uniform high-symmetry faceting. An example of $[100]$ NW cross-section is shown in Fig. 3.10 (a). The layering of the materials corresponds to the full processing: substrate preparation, growth, device fabrication and lamellae preparation. The composition in (b) then shows the distribution of In, As and Si and does not uncover any measurable traces of Si in the transport channel. The NW exhibits a 'fully developed' triangular shape, with the low-energy (110) faceting expected from the stereographical projection. The term 'fully developed shape' means, that the growth was long enough for the (001) surface on the top of the NW to disappear. In addition, the growth time was precise enough for the NW not to outgrow from the mask opening, which would most likely result in formation of additional faceting close to the mask.

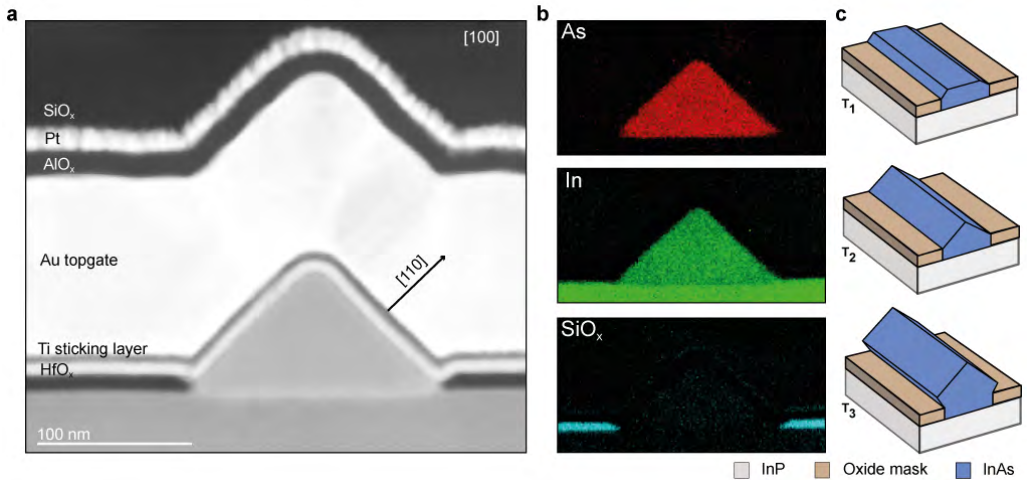


Figure 3.10: (a) ADF STEM micrograph of cross-section of a $[100]$ InAs NW grown on InP substrate taken after device fabrication and measurement. The faceting corresponds to the stereographic projection of (001) substrate. (b) EELS map showing the distribution of In, As and Si. (c) Schematics of expected SAG NW shape evolution with growth time. The data were taken by Sara Martí-Sánchez and Jordi Arbiol (see Pub. 4 and 5 for affiliations).

An illustration of three different situations is sketched in Fig. 3.10 (c), where short growth time T_1 results in a structure with (001) facet on the top. For ideal growth time, which is also related to the width of the NW mask opening, a fully developed shape forms following the volume dependent Wulff construction of a crystal constricted within the mask. Further increase in growth time, T_3 , then most often results in appearance of additional faceting close to the mask edges and also facet roughening by overgrowth.

*As an example, NW grown along the $[100]$ direction will be called $[100]$ NW throughout the rest of the work.

Therefore, for a specific mask opening size and NW orientation, there is a specific material volume associated with formation of the fully developed shape.

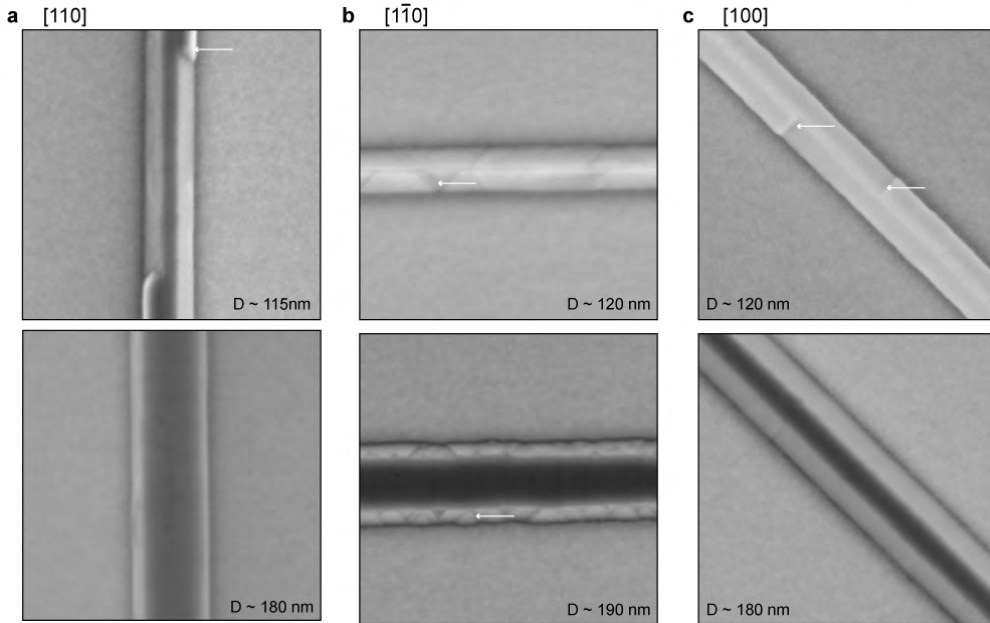


Figure 3.11: SEM micrographs of (a) [110], (b) $[1\bar{1}0]$ and (c) [100] NWs, where top panels show thin (overgrown) and bottom panels wide (undergrown) NWs from the same growth. The white arrows highlight the microfaceting on the roughened NW facets.

An non-ideal growth time therefore affects the NW morphology, but also detailed structure of the facet surface. The surface quality is especially important in InAs based devices, where surface roughness can strongly impact electron scattering. That is because the electron wave function localizes close to the surface, even while coupled to a superconductor²⁰⁵. An example of NWs which are overgrown (top panels) and undergrown (bottom panels) with respect to the fully developed shape is shown in Fig. 3.11. The different NW orientations exhibit different microfaceting as shown in (a) for [110], (b) for $[1\bar{1}0]$ and (c) for [100] NW. The specific kinds of parasitic faceting are then highlighted by white arrows. The presented trends were observable over various samples and show how important is it to tune the ratio of mask width and growth time in order to grow NWs with well defined and smooth faceting. More details will be shown in the next section in relation to buffered NWs.

3.2.3 Growth of SAG networks

Even though single NWs provide an important element of many experiments, the possibility of large scale NW network growth is the main advantage of the SAG approach. As discussed above, changing the angle of alignment of the NW with respect to the crystallographic directions of the substrate affects the NW morphology. That is of great importance in design of SAG NW networks, especially for synthesis of high quality junctions, which are also affected.

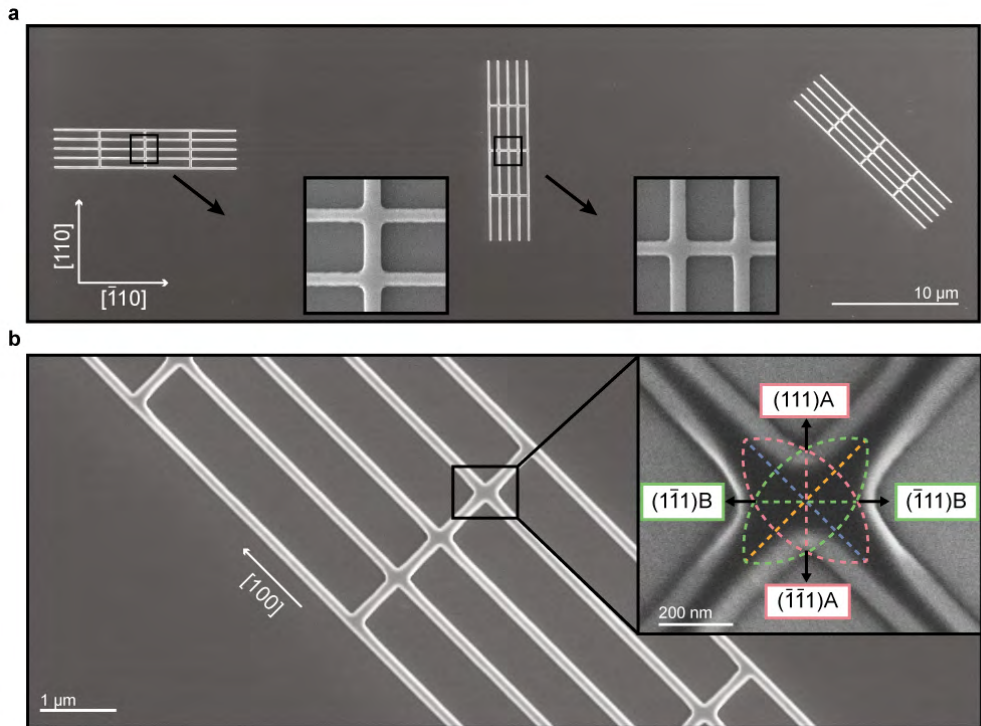


Figure 3.12: (a) SEM micrographs of $[110] \times [1\bar{1}0]$ and $[100] \times [010]$ InAs SAG NW networks, where the zoom-ins show details of the $[110] \times [1\bar{1}0]$ junctions. (b) A zoomed-in SEM micrograph of the $[100] \times [010]$ InAs network, where the inset shows details of one of the junctions. The asymmetry comes from the formation of polar (111)A and (111)B facets. Adapted from Pub. 4.

While focusing on the high-symmetry NWs, the (001) substrates offer the possibility of connecting them either under 90° or 45° . Here we will focus on two types of networks consisting of $[110] \times [1\bar{1}0]$ NWs or $[100] \times [010]$ NWs, which are shown in Fig. 3.12. Growth under given parameters promotes formation of homogeneous symmetrical junctions of both types, where the detailed structure is related to the relevant crystal symmetry.

An example in Fig. 3.12 (b) shows that the $[100]_x[010]$ junctions have asymmetrical shape due to formation of the low energy $(111)_B$ and $(111)_A$ facets. The additional faceting can result in larger growth rate within the junction and potentially lead to significant overgrowth with respect to the branches of the network. The $[110]_x[1\bar{1}0]$ junctions are merged from NWs that have different faceting and therefore also different surface energies. In addition, if the NWs did not yet reach the fully developed shape, the growth is affected by the significant diffusion asymmetry of the (001) top-facets along $[110]$ and $[1\bar{1}0]$ directions. That dictates the local growth kinetics and results in overgrowth of the junctions which was observed during long growth times. This effect will be shown in more detail on buffered NW networks in next section (Fig. 3.17). The experiments have shown that specific NW orientation, width and network morphology require different volume in order to achieve fully developed shape. Therefore, the growth conditions (especially the growth time) should be individually tuned for specific structures. Further on, we will focus mainly on characterization of the $[100]$ NWs and $[100]_x[010]$ networks, which offered the most flexibility of design while maintaining fixed growth conditions.

It is clear that SAG offers a fully scalable solution for growth of NW networks. On the other hand, the SEM characterization provides just an overall feedback for tuning of the growth parameters. The electronic transport characterization which will be presented in section 3.2.7, shows that the InAs SAG NWs on InP and GaAs substrates (non-buffered) are not fully gateable. The data suggested that this issue is most likely related to poor crystal quality of the NW/substrate interface. Therefore, the next section will be focused on engineering of the interface by growth of buffered SAG NWs.

3.2.4 GaAs(Sb) buffered NWs

In order to improve the interface quality of the heteroepitaxial growth, GaAs and GaAs(Sb) buffer NWs were grown prior to deposition of the InAs transport channel. At first, the intention was to use Sb in order to tune the lattice matching from InP or GaAs to InAs, by changing the composition x of $\text{GaAs}_{1-x}\text{Sb}_x$.

First growth attempts on InP substrates were not successful, since the lower boundary of selectivity window for $\text{GaAs}_{1-x}\text{Sb}_x$ was found to be in temperature range, where the InP substrates starts to desorb and melt. Even if the growth conditions were tuned so that the surface was kept stable by As overpressure, the temperature was high enough to melt the backside of the substrate. Therefore, more temperature resistant GaAs was chosen for the substrate material, even though the lattice mismatch to InAs is $\sim 4\%$ larger than for InP substrates.

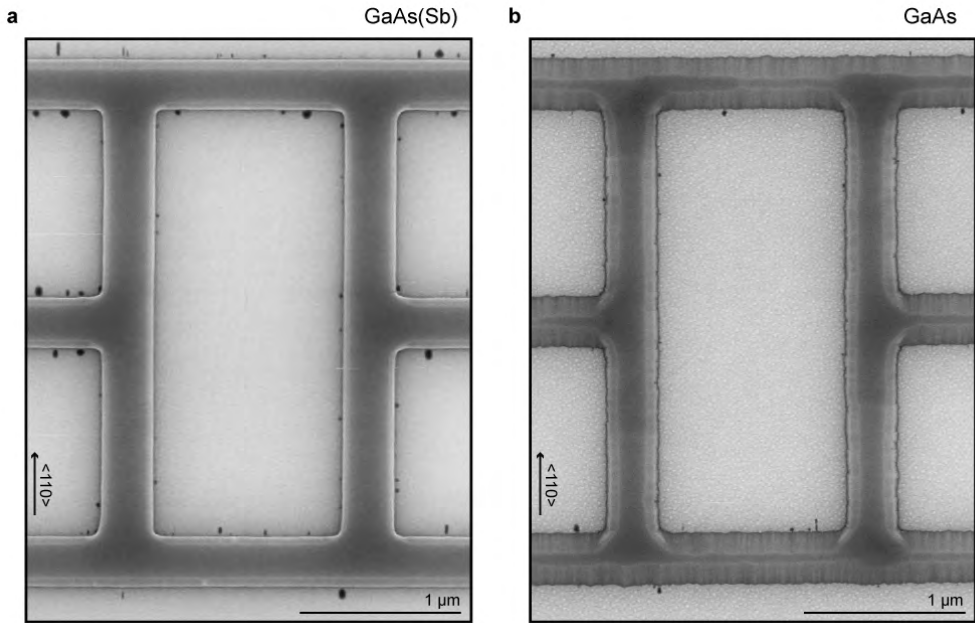


Figure 3.13: (a) SEM micrographs of $[110] \times [1\bar{1}0]$ GaAs(Sb) buffer networks, which were grown (a) with and (b) without Sb, where a surface smoothing is apparent as a result of surfactant properties of Sb. Adapted from Pub. 4.

EELS and EDX characterization* of the GaAs(Sb) buffer have shown that Sb concentration is below detection level or at the most $\sim 2\%$ at the top interface. That is low compared to $\sim 7\%$ which would be expected for the given flux ratios if incorporation of As and Sb would be equal. However, low incorporation rates of Sb at given growth temperatures were previously reported in literature^{206,207}. Despite the low Sb content, its presence plays an important role in the buffer growth, as shown in Fig. 3.13. It is apparent that Sb has a strong surfactant effect^{185,186} which changes the surface energetics and results in smoothing of the buffer facets. AFM measurements on the GaAs(Sb) buffer NWs have shown uniform surface roughness with RMS $\sim 3 \text{ \AA}$ in all regions of the grown sample. The smooth, well defined buffer provides an ideal platform for capping with the transport channel. Despite of the inability to bridge the lattice mismatch, the GaAs(Sb) buffer can promote elastic relaxation in the structures and improve transport properties, as will be shown in section 3.2.7.

*Performed by Sara Marti-Sanchez and Jordi Arbiol, see Pub 4 for affiliations.

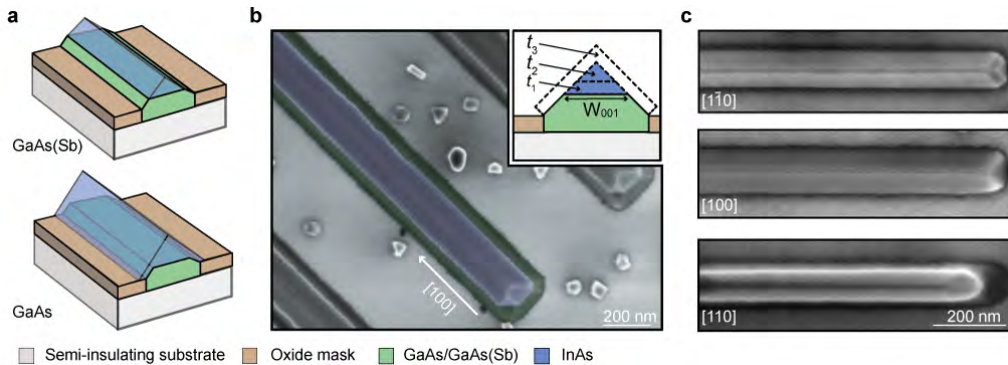


Figure 3.14: (a) Illustration of different growth results for InAs capping of SAG buffered NWs. In case of GaAs(Sb) buffer it was possible to achieve selective growth on the (001) buffer top-facet. On the other hand, GaAs buffer becomes fully overgrown even after short growth time. (b) SEM micrographs of [100] buffered NW, where InAs was selectively grown on the top-facet of the GaAs(Sb) buffer. The inset illustrates the shape evolution for a specific growth time in relation to a specific (001) top-facet width W_{001} (i.e. to the buffer growth time and mask opening width.). (c) SEM micrographs showing the distinct faceting of overgrown NWs, which are oriented along all the three high-symmetry orientations. Adapted from Pub. 4.

As was discussed above, the different SAG NW orientations have different faceting. The same symmetries apply for the buffered NWs. On the other hand, the surface energy distribution and therefore also the Wulff shape are affected by presence of the Sb surfactant. To our advantage it seems that Sb homogenizes the surface energies and promotes formation of crystals with large areas of the (001) top-facets.

Interestingly, growth of InAs on the GaAs buffer without Sb resulted in homogeneous coverage of all its facets. In contrast to that, while growing on top of the GaAs(Sb) buffer, it was possible to deposit InAs just on the (001) top-facet as shown in Fig. 3.14 (a) and (b). The different results could be related to the roughness of the GaAs buffer, which affects the local kinetics and prevents In adatoms from effectively diffusing to the (001) top-facet.

A successful selective growth on the top-facet requires careful tuning of the mask opening width and growth time of the buffer with respect to growth time of InAs. The resulting shape of the crystal is then related to two spatial constrictions, the mask width and the top-facet width. That makes the final shape of the crystal strongly dependent on both InAs and GaAs(Sb) volumes. The idea is illustrated in Fig. 3.14 (b). Deviation from the ideal ratio of these parameters results in either not fully developed shape or overgrowth. The selective growth on the top-facet has many potential advantages, e.g. placement of the transport channel further from the electrostatic disorder of the oxide mask, ensuring single interface between the buffer and the NW including just the (001) facet or allowing

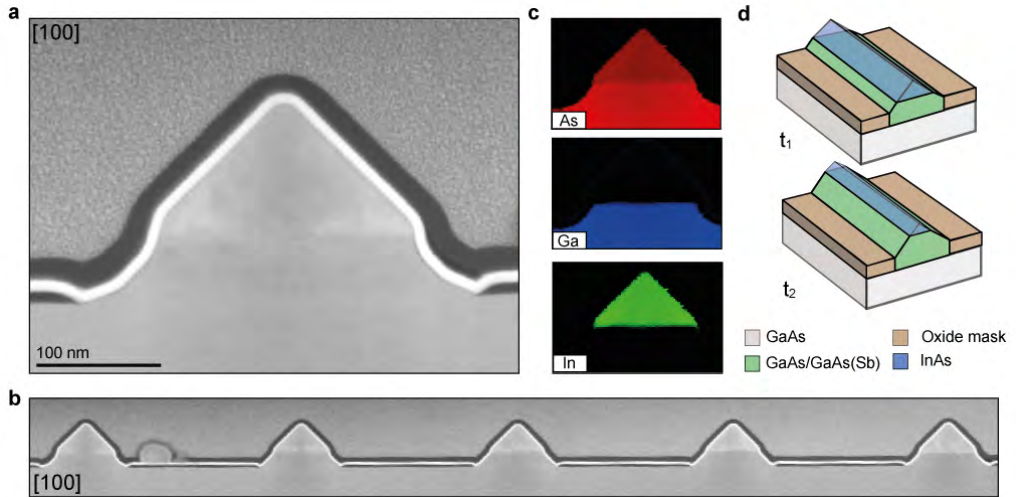


Figure 3.15: (a) Low magnification ADF-STEM micrograph of a buffered SAG NW grown along [100] direction, with an overview of multiple NWs at once in (b). (c) Corresponding areal elemental density maps obtained by STEM-EELS. (d) Illustration of how NWs can be defined by tuning the buffer growth time t_1 and t_2 . The TEM results were taken and processed by Jordi Arbiol and Sara Martí-Sánchez.

for elastic strain relaxation in the transport channel, as will be shown in section 3.2.6.

Buffered NWs grown along all the high-symmetry orientations are shown in Fig. 3.14 (c). Surprisingly, it is possible to achieve continuous morphology and well defined faceting for all the three orientations. Here, the $[1\bar{1}0]$ and $[100]$ NWs are fully overgrown, while the $[110]$ NW sits on the buffer top-facet. That is most likely related to different incorporation rates, as will be demonstrated in section 3.2.5. In order to also grow the $[1\bar{1}0]$ and $[100]$ just on the top-facet, either the growth time needs to be reduced or the mask opening width increased. This again shows, that the growth conditions needs to be tuned with respect to a specific NW type and width. The presented single NWs are similar to the ones used for field effect mobility measurements.

An example is shown in Fig. 3.15*. The InAs is clearly selectively grown on top of the buffer top-facet in (a) and such trend is observable over multiple NWs in (b). In addition, no detectable incorporation of Ga into the InAs transport channel has been detected as shown in STEM-EELS maps in (c). Similar TEM analysis of structures within the same growth has shown clear relation between the width of the buffer top-facets and

*TEM characterization and data processing was done by Sara Marti-Sanchez and Jordi Arbiol, see Pub. 4 for affiliations.

the amount of deposited InAs. So far, the best results of the selective top-facet growth were achieved for structures with mask-opening width above 200 nm for 190 MLs of the GaAs(Sb) buffer and 150 MLs of InAs. It is expected, that precise tuning of this type of selective growth will allow for formation of very thin SAG NWs, with high-quality interface between InAs and the buffer, which will result in improvement of transport properties.

Variety of quantum transport related experiments benefit from measurements on thin NWs. It is hard to fabricate very thin mask openings with the used wet-etching approach, since it results in significant over-etching and inconsistency for widths below ~ 90 nm. This issue can be overcome by improvement of the etching method, e.g. dry etching techniques. But also the buffer offers the possibility to form very thin NWs by tuning the ratio of buffer/transport channel growth time. The idea is illustrated in Fig. 3.15 (d). If a constant mask opening width is considered, an increase in the faceted buffer growth time reduces the (001) top-facet area. The top-facet width then determines InAs growth time necessary to reach the fully developed shape. Precise tuning of the relative growth times is complex because diffusion depends on ratio of nearby facet areas which evolve during growth. The typical growth of 190 MLs of GaAs(Sb) required ~ 150 MLs of InAs growth, in order to selectively cover top-facet of [100] NWs grown with mask opening of 320 nm as was shown in Fig. 3.15 (a). In order to form very thin transport channel, the buffer growth time needs to be increased, or the mask opening needs to be reduced together with the InAs growth time, as will be shown in Fig. 3.17.

Interestingly, the undergrown buffered NWs exhibit clear trends in the early growth stages, which can be related to the nucleation theory, adatom collection area and growth regimes introduced in chapter 1. In order to investigate the initial growth stage, 30 monolayers of InAs were grown at the top of the $\sim 20 - 50$ nm thick GaAs(Sb) buffer layer (depending on the width of the masking opening and orientation). An overview of the results is shown in Fig. 3.16. At first it is noticeable, that the volume of InAs is different among 4 NWs, which are spaced by $1 \mu\text{m}$ one from another. Less material is incorporated to the NWs located on the edges of the pattern. That could be related either to patterning dependent gradient of the growth temperature, or more likely to adatom collection area and diffusion length on the mask. This effect would cause redistribution of the material and change in growth rates if the diffusion length is larger than the NW spacing. The second explanation would imply, that there is a significant flux of adatoms from the NW to the neighboring surface of the mask and that their diffusion length over the mask is longer than $1 \mu\text{m}$. That would provide an explanation for the fact that NWs in the center of the pattern have two adatom sources at both sides and therefore higher material influx in comparison to the outer NWs. The effect of NW to NW pitch needs to be further investigated by growth on designated patterns with different mask opening

pitch and width in future experiments.

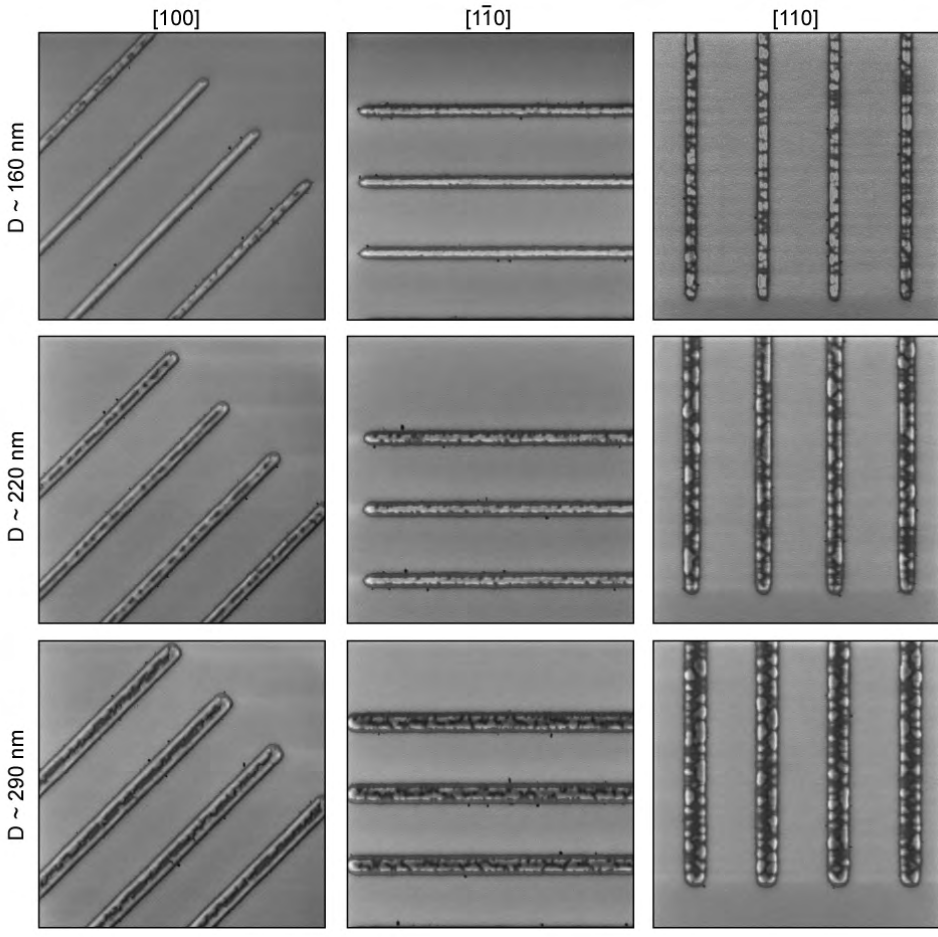


Figure 3.16: SEM micrographs of 30 MLs of InAs selectively grown on top of 190 MLs of GaAs(Sb) buffer layer for all the three high symmetry orientations and buffer width of 160, 220 and 290 nm.

The results in Fig. 3.16 also show a trend in initial nucleation. The NWs seem to be growing in the Volmer-Weber regime, where the preferential nucleation sites are at the edges of the buffer top-facet. That is clearly visible for growth on the 290 nm wide buffer, where an empty area is visible in the center of the top-facet. This trend is comparable to results reported for growth of InSb NWs on AlGaSb by hydrogen assisted MBE in Ref. [157]. For the thinner $[1\bar{1}0]$ NWs, it may seem that the nucleation occurs in the center, but that is most likely related to the structure of the buffer layer, which adapts more rounded

top-facet profile, with not so well defined edges as compared to the other two orientations. The shape of the buffer will be shown in more detail in next section.

Analyzing the nucleation on the wider top-facets, it seems that the distribution of initial nuclei depends on the orientation of the NW. For $[100]$ NWs, the edge of the buffer is homogeneously covered by InAs and the growth gradually progresses inwards. For $[1\bar{1}0]$ the material accumulates in isolated grains elongated along the $[110]$ edge of the NW. When the structures are thinner than ~ 250 nm, the material tends to form roughened strip in the middle of the top-facet. For $[110]$ orientation, isolated islands concentrated at the sides of the buffer top-facet are formed. Here the grains extend more towards the center of the buffer. The different grain configurations on for $[1\bar{1}0]$ and $[110]$ orientations are most likely related to the anisotropic diffusion on the (001) top-facet. Since the diffusion along the $[1\bar{1}0]$ is longer¹⁸¹, the nuclei tend to elongate along this direction.

The faceting of the grains mostly corresponds to the high-symmetry faceting, as indicated in Fig. 3.17 (a) for initial stages of InAs growth on buffer networks. The nucleation progresses in the same manner as described above, even when the NWs are connected together and large areas are exposed at the center of the buffer. The growth within the very junction seems to also progress from edge to the center for both $[110]X[010]$ and $[110]X[1\bar{1}0]$ types of networks. The growth on top of the $[110]X[1\bar{1}0]$ buffer is strongly affected by the diffusion asymmetry and material tends to diffuse and accumulate to the $[110]$ oriented parts of the networks. That is clearly visible in Fig. 3.17 (b) where the inset shows distribution of InAs for longer growth (~ 150 MLs). The $[110]$ oriented parts are overgrown, while almost no material grows on the $[1\bar{1}0]$ orientation. That makes growth of well defined $[110]X[1\bar{1}0]$ junctions on NWs with wide openings complicated. This material redistribution is much less prominent in growth with narrow mask openings. Longer growth of $[100]X[010]$ networks results in less junction overgrowth without significant accumulation of the material around the junctions. Details of the structures are shown in section 3.2.8.

There is a trend in distribution of the nuclei, which follows a 'zig-zag' like structure along the opposing edges of the buffer. That can be related to the adatom collection area on the buffer top-facet, as illustrated in Fig. 3.17 (c). Once a nuclei forms and starts to grow, it also collects adatoms within the surrounding collection area, which is defined by diffusion length on the top-facet. That reduces the probability of other nuclei to form close by or directly on the opposite edge. This effect will most likely diminish as the buffer top-facet gets wider and the collection areas of the nuclei on the opposing edges do not overlap anymore.

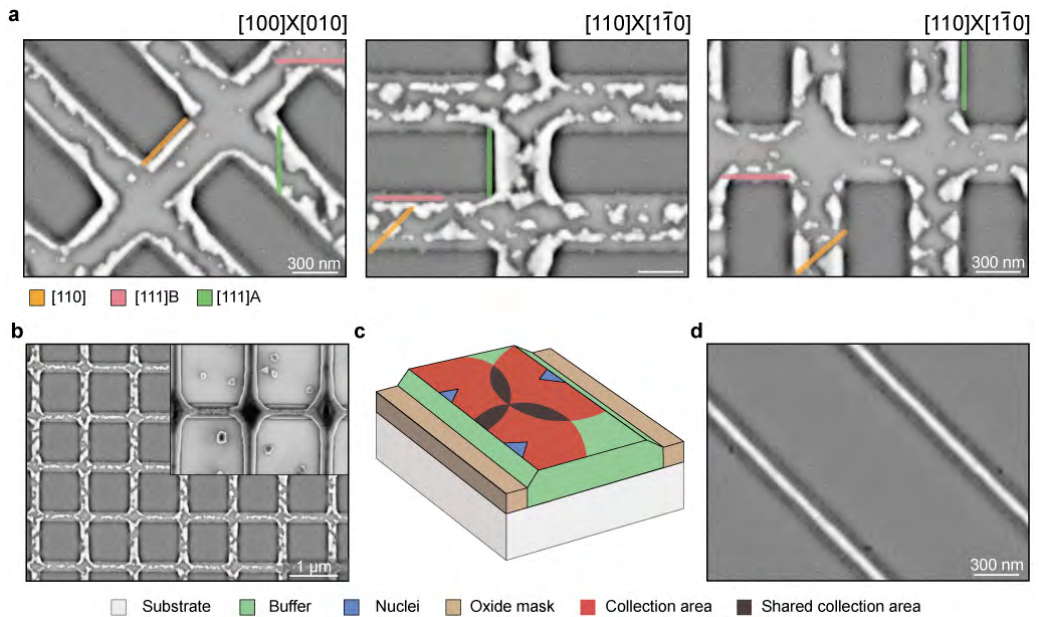


Figure 3.17: SEM micrographs of (a) 30 ML of InAs selectively grown on top of GaAs(Sb) buffer layer, in a geometry consisting of multiple junctions along $[100]$, $[1\bar{1}0]$ and $[110]$ orientations. (b) SEM micrograph of a larger network with an inset showing a detail of similar junction, but with 150 ML growth of InAs. (c) Schematics of the initial nucleation stage, where the nuclei arrange in a zig-zag structure on the opposing edges of the NWs. (d) SEM micrograph of a 70 nm diameter InAs NW grown at the same conditions.

This form of growth, where many isolated grains connect together in order to form a homogeneous continuous NWs is not ideal and can introduce defects into the structures. Further investigation of the growth parameter space is necessary in order to shift the growth towards Stranski-Krastanov or Frank–van der Merwe regimes, where development of lattice matched buffer layers could potentially result in more homogeneous growth. In addition, growth at lower temperatures could reduce the adatom diffusion length and result in homogeneous material deposition. That requires finding means to reduce the lower boundary of temperature window for selective growth, as was for example shown for hydrogen assisted MBE¹⁵³.

A simpler solution at hand is to grow on thin buffers, as shown Fig. 3.17 (d), where a homogeneous NW with diameter of 70 nm is formed during the growth of 30 MLs of InAs. It seems that the spatial constriction promotes homogeneous buffer coverage even for low InAs volumes. That can be achieved either by improvement of the etching method or by tuning the growth time of the buffer layer in order to reduce the width of the top-facet.

3.2.5 Crystal structure of buffered NWs

The cross-sectional TEM analysis[†] has confirmed that the shape and detailed structure of the buffered NWs is indeed strongly affected by the width of the mask openings, as shown in Fig. 3.18 (same scale bars). It also seems that the vertical growth rate has a strong dependency on this width, as it is clear from the comparison between the top and bottom rows. The increase of cross-sectional area of both the buffer and the InAs transport channel increases with the width of the mask opening. That is an important observation which after more investigation could give the possibility to tune the growth in order to yield continuous and high-quality NWs with wide range of diameters and within the same growth. In addition, this discrepancy in deposited volume highlights the importance of diffusion processes in SAG. That is also apparent from the fact that the NW volume can exceed the nominal planar growth corresponding thickness of 50 nm for the GaAs buffer and 35 nm for the InAs, as visible in Fig. 3.18, especially for [110] NWs. That indicates that the growth rate is affected by contribution of adatoms diffusing to the NWs from the mask. The reasons for the differences in growth rates between the different orientations can be of both thermodynamic and kinetic origin, i.e. due to differences in surface energies and activation barriers for diffusion and incorporation. Under the given mass transport conditions, the dynamics of the shape evolution is thermodynamically driven by the excess chemical potential of the crystal phase, which can be described by relevant shape parameters⁷². In the case of continuous and uniform SAG NWs, that are constrained to the selective area, the relevant shape parameters are only the sidefacet sizes (and their relative surface energies). However, the differences in adatom kinetics between the orientations could also play an important role and future studies will be needed to identify the main mechanisms for the differences in growth observed between the orientations [Pub 4].

The insets in Fig. 3.18 (a), (b) and (c), show the detailed atomic structure of the InAs SAG NWs. The highlighted high-symmetry faceting planes determine the facet polarity. The [100] and $[1\bar{1}0]$ NWs clearly form the fully developed shape, as introduced above, but the [110] NW adapts a different shape. Under the given conditions, the (111)B facets of InAs are visible, but larger area is taken by $(1\bar{1}0)$ facets. In contrast, the buffer layer mainly adapts the (111)B faceting. From similar growths which were done in collaboration with Lucia Sorba from CNR Nano and Chris Palmstrøm from UCSB and also previously reported by Dalacu et al. in Ref. [160], it is clear that it is possible to achieve pyramidal shape with full (111)B faceting also for the [110] NWs.

Interestingly, inverse faceting between the [110] and $[1\bar{1}0]$ NWs was reported by Fahed et al. in Ref. [153] for GaSb NWs grown by MBE. Therefore, it seems that the

[†]Measurements were done by Jordi Arbiol and Sara Martí-Sánchez, see Pub. 4 for affiliations.

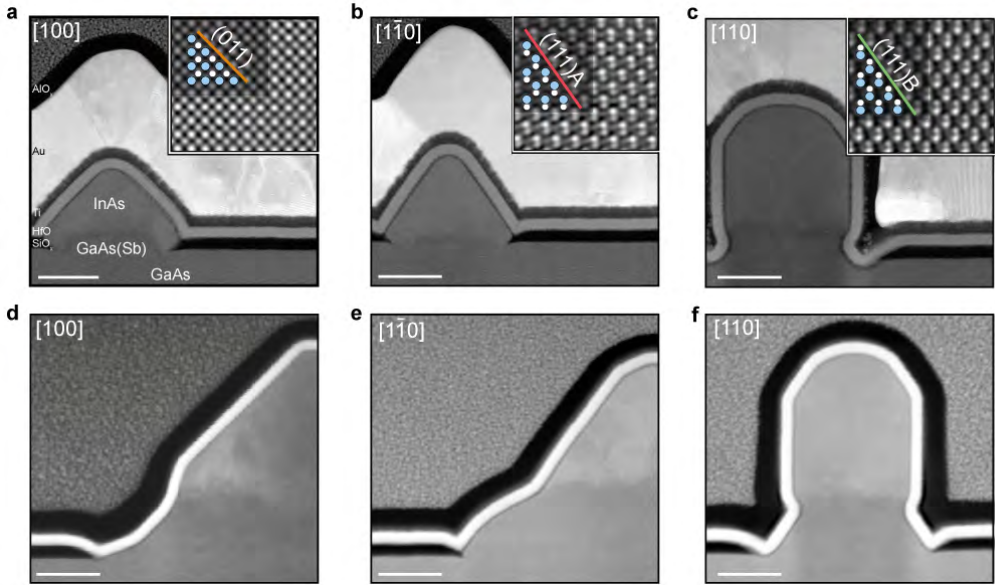


Figure 3.18: Cross-sectional TEM micrographs InAs NWs grown on top of GaAs(Sb) buffer layers along the $[100]$ ((a) thin, (d) thick), $[1\bar{1}0]$ ((b) thin, (e) thick) and $[110]$ ((c) thin, (f) thick) orientations, where the top row was cut by focused ion beam from top-gate regions of actual devices and bottom row from other NWs within the same growth. The insets show cross-sectional HAADF-STEM images of the InAs transport channel, where the planes indicate the dominant high-symmetry faceting and polarity of the NWs (As - white, In - blue). The scale bars correspond to 50 nm. Adapted from Pub. 4.

shape can be influenced by growth conditions and their careful tuning will hopefully allow for growth of pyramidal InAs NWs along the $[110]$ direction. It is important to mention that the three different types of facets of fully developed NWs (non-polar, A-polar and B-polar) could provide additional interface engineering possibilities for heterostructure synthesis due to different electron affinities, atomic plane spacings and surface energies.

The crystal structure of the transport channel is pristine, without any defects observed within the presented growth. We have not observed any threading dislocations, similarly to the Ref. [153]. For the wider NWs with width around 250 nm we have observed formation of stacking faults. Determination of their origin requires further research. What we will focus on here, is the quality of the interface between the transport channel and the buffer or substrate.

3.2.6 Interface to the transport channel

Geometrical analysis of InAs SAG NWs grown directly on InP (lattice mismatch $\sim 3\%$) has shown that the transport channel is fully relaxed via formation of periodic arrays of misfit dislocations, as shown in Fig. 3.19. This is expected, because the structure is confined within the mask opening, which most likely suppresses the possibility for elastic relaxation.

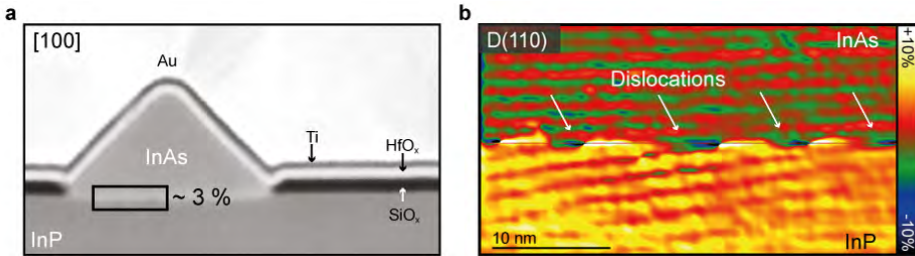


Figure 3.19: (a) ADF STEM micrograph of a cross-section of a [100] InAs NW grown on InP substrate taken after device fabrication and transport measurements, with indication of the $\sim 3\%$ mismatch between InAs and the substrate. (b) Geometrical phase analysis of dilatation along the [110] direction of the InAs/InP interface shows a fully strain relaxed interface with periodic misfit dislocations. The data were taken and processed by Sara Martí-Sánchez and Jordi Arbiol. Adapted from Pub. 4.

The situation is very different when growing on the GaAs buffer layer (lattice mismatch $\sim 7\%$). Since the buffer protrudes out of the substrate plane, the spatial constriction set by the mask is removed and the structure has the lateral freedom to elastically relax. This situation is illustrated in a qualitative simulation of the rotational displacement field for a fully and partially strained buffered NW in Fig. 3.20 (a). As the initial strain value is increased, the magnitude of rotation at the edges of the structure also increases.

The same effect was observed in a range of grown NWs, as shown in the rotational GPA maps for all three high-symmetry NW orientations. Here, all three NWs (TEM overview presented in Fig. 3.18) display a rotation on the edges close to the mask, as shown in Fig. 3.20 (b). The rotation magnitude varies among the structures in the range from $\sim 2^\circ$ to 4.5° . We also observe a gradual release of strain in form of lattice constant shift from GaAs to InAs, typically within ~ 20 nm, as shown in dilatation map in 3.20 (c). The fact that no major Sb concentration was detected and the GPA analysis shows significant amount of crystal plane rotation, is a signature of a gradual and partially elastic change in the lattice spacing. This is supported by data shown for $[1\bar{1}0]$ and $[110]$ NWs in Fig. 3.20 (d) and (e). In the first case the interface accommodates aperiodic

arrays of misfit dislocations, which are clearly visible after Fourier filtering of the TEM image. That combined with the rotation indicates partially plastic and partially elastic relaxation of the structure. For the $[110]$ NW, no misfit dislocations were observed, which together with the rotation peaking at 4.5° indicates that the structure is close to be fully elastically relaxed in the transverse direction. A similar strain relaxation mechanism was previously observed in VLS axial heterostructures²⁰⁸ and in other InGaN/GaN²⁰⁹ and InAs/InSb^{115,210} heterostructures.

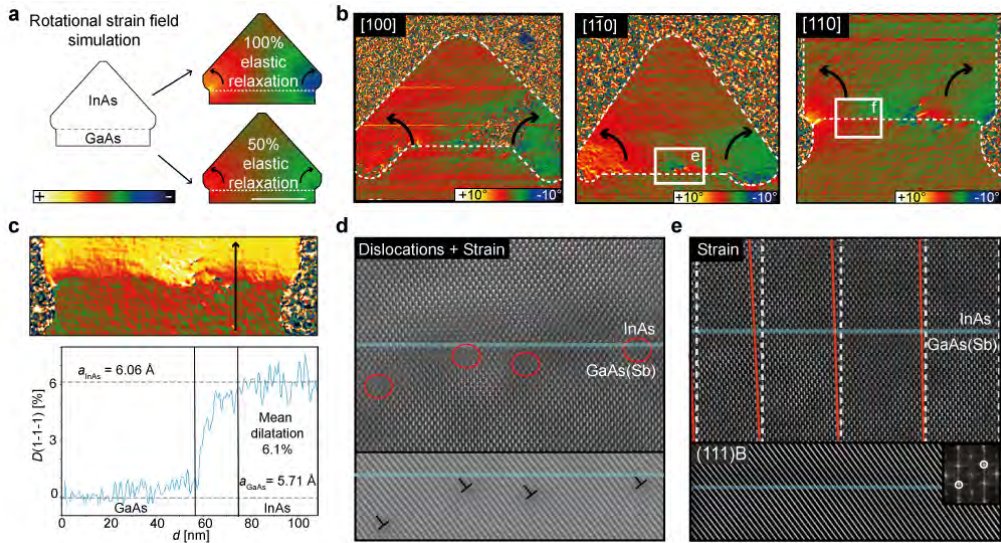


Figure 3.20: (a) Simulation of a rotational deformation for a $[100]$ buffered NW showing elastic strain relaxation profiles for fully and partially elastically strained structures. Scale bar is 50 nm. (b) Rotational GPA maps taken around the (111) planes, for $[100]$, $[1\bar{1}0]$ and $[110]$ NWs presented in Fig. 3.18. (c) GPA dilatation map along the $(1\bar{1}\bar{1})$ planes of the $[110]$ NW, where the plot shows a line cut profile. (d) Atomic resolution aberration corrected HAADF-STEM micrograph of the $[1\bar{1}0]$ interface, indicated in (b) showing misfit dislocations and strain. The bottom panel is the same image after FFT filtering, with a highlighted aperiodic misfit dislocation array. The blue line indicates the interface. (e) Atomic resolution aberration corrected HAADF-STEM micrograph of the $[110]$ NW interface indicated in (b) showing no misfit dislocations and pronounced strain as indicated by the white dashed lines (no strain) and red line (the actual plane displacement). The bottom panel is the same image after FFT filtering, with no visible misfit dislocations, where the inset indicates the Bragg peaks selected for the filtering. The TEM images were taken and GPA maps were produced by Sara Martí-Sánchez and Jordi Arbiol. Adapted from Pub. 4.

The buffered SAG NW growth provides a very important technique for engineering of the NW/substrate interface crystal quality. The lateral freedom to expand the lattice

constant can help to remove the inter-facial defects by elastically straining the structure, which as will be shown in next section seem to negatively influence transport properties of the InAs NW.

3.2.7 Field effect mobility

Since the ability to efficiently tune the chemical potential and achieve the limit of complete current pinch-off in the NWs is one of the important requirements of Majorana related experiments, the grown structures were compared from the perspective of electrostatic gateability²¹¹. Here, top-gate device schemes were used (an example of a general device design is shown in Fig. 3.21), because side-gating is not very effective due to pyramidal NW shape and back gating schemes are difficult to implement due to leakage through the semi-insulating substrates. The measurements were performed on single NWs with width varying between 100 and 160 nm and which were spaced at least 10 μm from other structures.

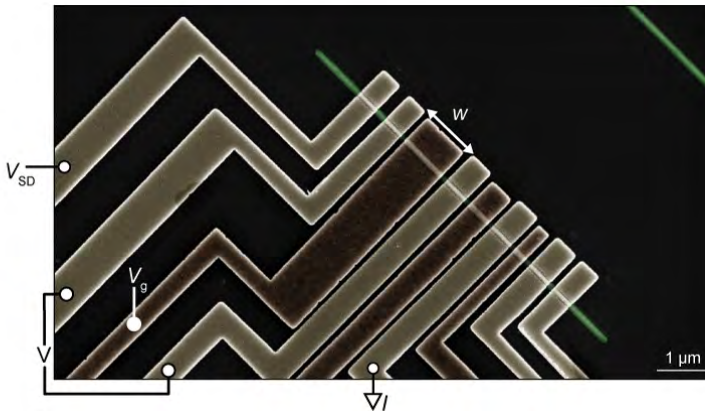


Figure 3.21: SEM micrograph of a multi-gate four-probe NW device, where the gate width varies as 250 nm, 500 nm and 1 μm . The gold corresponds to Ti/Au contacts, brown to Ti/Au top-gates and green to InAs SAG NW. V_{SD} is the source bias voltage, I is the measured current, V_g is the gate voltage and W is the varying gate width.

A general trend observed in gate dependent measurements of non-buffered NWs grown directly on InP and GaAs substrates is shown in Fig. 3.22 (a). As an explanation of the conductance G dependence on gate voltage V_g , two regimes are considered, which correspond to different regions in the gate space, as sketched in the insets. At lower negative V_g , the carriers are first pushed away from the upper interface, which is the most likely situation for the top-gated geometry. Here the slope is relatively steep and therefore the field effect mobility is higher. As V_g is tuned more negative, the slope becomes smaller

and significant current still runs through the device, i.e. it is not possible to fully pinch of the transport. In this regime, the carriers are pushed to the interface with the substrate. The leftover current is then most likely connected to the quality of this interface, which for non-buffered NWs hosts dislocation arrays and the substrate surface may be roughened during the wet etching fabrication step. The high transconductance regime corresponds to the superior crystal quality of the bulk part of the NW. The leftover current, related to the interface, could be also related to the semi-insulating nature of the substrates. That is not likely because other experiments on the same substrates and same temperatures did not show any significant leakage between two contacts deposited directly on the substrate surface.

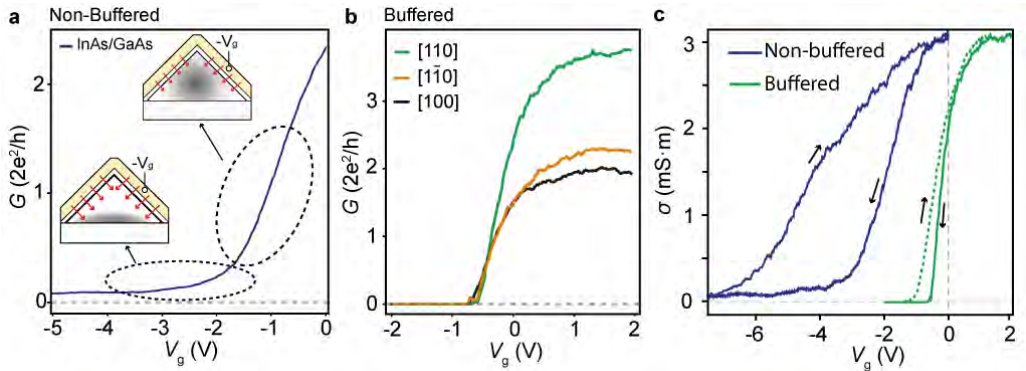


Figure 3.22: (a) Conductance, G , as a function of gate voltage V_g , for InAs grown on a GaAs substrate. Sketches illustrate the carrier density distribution as a function of V_g . The two regimes correspond to transport residing in the bulk of InAs transport channel (less negative V_g) and at the InAs/substrate interface (more negative V_g). (b), Conductance as a function of V_g for InAs NWs grown on the GaAs(Sb) buffer along the $[110]$, $[1\bar{1}0]$ and $[100]$ directions. (c) Conductivity σ as a function of V_g for buffered and non-buffered devices, showing up and down sweeps. Figure is adapted from Pub. 4.

The gating response can be clearly enhanced by introduction of a GaAs(Sb) buffer layer, as shown in Fig. 3.22 (b) for all three high symmetry NW orientations. The conductance is fully pinched off at the same threshold voltage, even though the cross-sectional areas of the NWs differ (the areas corresponds to the device cross-sections presented in Fig. 3.18). That is most likely enabled by the flatness and high-quality of the interface between the NW and the buffer. Band alignment between the materials does not seem to play a significant role, since the structure is analogical to the non-buffered NWs grown on GaAs. Compared to the non-buffered NWs, the buffer layer also significantly reduces the hysteresis for up and down V_g sweeps, as shown in Fig. 3.22 (c).

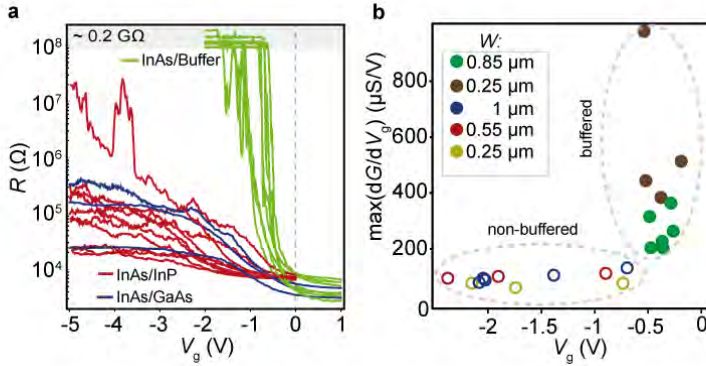


Figure 3.23: (a) Resistance, R , as a function of V_g for multiple NW samples grown directly on InP, GaAs and the GaAs(Sb) buffer layer for various gate widths W and NW orientations. (b) The peak transconductance as a function of V_g for the same devices as shown in (a), where the color coding corresponds to the different W . Figure is partially adapted from Pub. 4.

The trends are more clear in the resistance data shown in Fig. 3.23 (a). Here multiple devices grown on either GaAs or InP with a gate width variation between 250, 500 and 1000 nm show that the resistance stays around $5 \cdot 10^5 \Omega$ even at $V_g \sim -5$ V. The same measurements on the buffered NWs show reproducible conductance pinch-off even for the narrow (250 nm) gates. The importance of the buffer is also reflected in the peak transconductance shown in Fig. 3.23 (b) and extracted from the data in (a). The peak transconductance²¹¹ also reflects the value of the field effect mobility. The value is clearly higher for the buffered NWs and corresponds to similar values of V_g . In contrast to that, the peak transconductance is lower for the non-buffered NWs, and the values are scattered over a wide range of V_g , showing inconsistency in the electrostatic gating.

The extraction of field effect mobility values requires the capacitance between the gate and the device as an input parameter (details are given in Methods). The electrostatic capacitance simulations are complicated due to the atypical and varying cross-sectional shapes of the NWs, which most likely have strong effect on the charge carrier distribution. Since the used FEM simulation assumes a rectangular shape of the NWs, the given values should be used only for comparison between SAG device where capacitance is extracted in the same manner. For the InAs NWs grown on the GaAs(Sb), we extracted the average field effect mobility of $\bar{\mu} \sim 5600 \pm 1300 \frac{\text{cm}^2}{\text{V}\cdot\text{s}}$ with a maximum at $\sim 7600 \frac{\text{cm}^2}{\text{V}\cdot\text{s}}$ (extracted from 24 data sets - 6 buffered devices at 1, 2, 5 and 10 mV bias). Interestingly, for 17 similar devices based on InAs NWs grown on GaAs buffer without Sb*, we have extracted $\bar{\mu} \sim 3210 \pm 721 \frac{\text{cm}^2}{\text{V}\cdot\text{s}}$, using the same capacitance model. That again confirms, that the interface

*Grown in collaboration with the group at Delft Technical University and Microsoft station Q Delft.

between the NW and the buffer/substrate is of great importance, since the the decrease of mobility is most likely related to the GaAs buffer roughness (see Fig. 3.13). In addition standard Hall mobility measurements were performed on Hall-bar SAG NW structures based on the GaAs buffer yielded average mobility of $\bar{\mu} \sim 3752 \pm 1933 \frac{\text{cm}^2}{\text{V}\cdot\text{s}}$ [†]. The similar mobility values yielded by two independent experiments indicate certain reliability of the capacitance extraction. Although, it is necessary to stress that the capacitance simulations are very basic and further work should be focused on including the quantum coupling effects and relate them to the actual NW shape. For the non-buffered devices, the data are not viable for the fit referred to in Methods section. Therefore, only the corresponding mobility extracted by fitting the gate trace close to peak transconductance region can be obtained and is roughly one order of magnitude lower than for the GaAs(Sb) based buffered devices, with highest value at $\bar{\mu} \sim 665 \frac{\text{cm}^2}{\text{V}\cdot\text{s}}$. The mobility and gating properties seemed to be relatively stable up to 120 K. At that point the open regime conductance of the device, mobility and pinch off threshold voltage start to decrease, most likely due to leakage through the warmed substrate.

Detailed characterization of dependence of field effect mobility on the NW width, orientation and buffer/transport channel ratio are necessary to properly optimize presented material. That will be part of future experiments. Even though single buffered NWs already show promising properties in terms of the field effect gating response, they do not reflect the properties of networks and their junctions. Those can be investigated in magnetotransport measurements on loop structures.

3.2.8 Electron coherence and magnetotransport

A basic transport experiment that allows for probing the quality of the SAG network junctions is the Aharonov-Bohm experiment. Here simple loop structure is used for an electron interference experiments, where the electron path through a symmetrical structure is adjusted by magnetic field perpendicular to the structure and electron coherence length l_ϕ can be extracted from temperature dependence of the oscillations⁶⁵. The principal of the experiment is illustrated in Fig. 3.24 (a).

Symmetrical GaAs(Sb)/InAs buffered SAG NW loop structures were used for the experiment. The fabricated four-probe devices had different circumference of $5.1 \mu\text{m}$ (large loop) and $2.24 \mu\text{m}$ (small loop), which are shown in Fig. 3.24 (a) and (b). The measured resistance oscillations in perpendicular magnetic field, B_\perp , are shown in Fig. 3.24 (c) and (d). The oscillation frequency is $\sim 2.5 \text{ mT}$ (large loop) and $\sim 14 \text{ mT}$ (small

[†]The fabrication and measurements on GaAs buffer without Sb based devices were done by Marina Hesselberg, Lucas Casparis, Karthik Jambunathan, Andrew Higginbotham, Denise Puglia, Esteban Martinez and Gerbold Ménard from Center for Quantum devices and Station Q Copenhagen

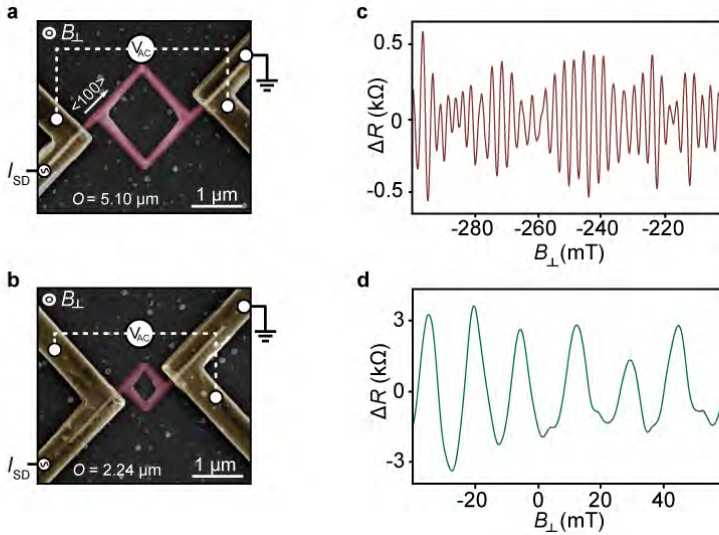


Figure 3.24: SEM micrographs of four-probe NW loop devices with $5.1 \mu\text{m}$ circumference (a) and $2.24 \mu\text{m}$ circumference (b), where contacts is gold and the SAG NW is red. Change in resistance ΔR , as a function of perpendicular magnetic field, B_{\perp} for the large (c) and small (d) loops. Data are shown over a 100 mT range displaying electron phase interference oscillations. Figure is adapted from Pub. 4.

loop) and corresponds to the areas defined by the the loop circumference as $\sim h/(e \cdot S)$, where h is the Planck constant and e is the electron charge.

The post-processed Fourier transform of the small loop oscillations is shown in Fig. 3.25 (a). Different peaks are visible within the frequency area defined by the outer A_{out} and inner A_{in} loop circumference. The amplitude with the highest magnitude likely correlates to the AB oscillations corresponding to the electron interference in the main transport channel. The higher frequency peaks, labeled to A_2 and A_3 , are most likely result of one of the following explanations. (1) The asymmetrical cross-section of the InAs NWs grown on the GaAs(Sb) buffer, which is shown in Fig. 3.25 b. The shape seems to be related to the surface to volume ratio minimization at the junction between the two high-symmetry orientations. Indeed, the SEM micrograph displays an asymmetrical tapering of the junction and subsequent overgrowth of the ring arms. The overgrowth can be partially suppressed with shorter growth time, as was mentioned in the section 3.2.4. The cross-sectional shape suggests that there may be multiple effective electron paths available within the structure. That is supported by the fact that the secondary peaks lie within the frequency range bounded by A_{out} and A_{in} areas. (2) The electrons travel through the loop multiple times and the additional amplitude peaks are results of higher order

harmonics in the interference. This explanation is less likely, since none of the frequencies exactly correspond to any integer multiple of the main frequency.

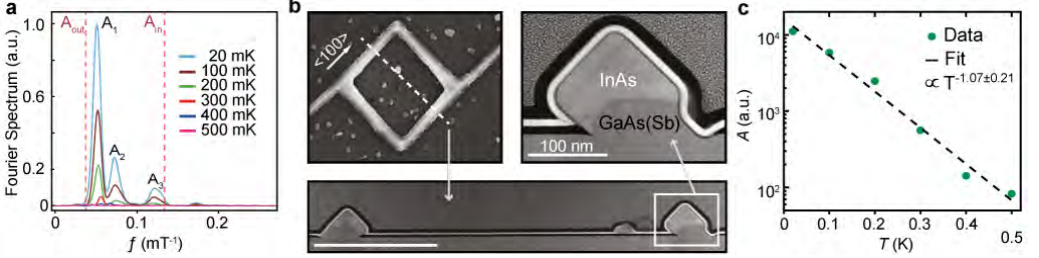


Figure 3.25: (a) Normalized Fourier spectrum amplitude of the Aharonov Bohm oscillations as a function of frequency at temperature range varying from 20 to 500 mK. The amplitude peaks A_1 , A_2 and A_3 correspond to different frequencies. The areas A_{out} and A_{in} then correspond to inner and outer circumference of the large loop shown in Fig. 3.24. (b) Overview cross-sectional HAADF-STEM micrographs of the Aharonov-Bohm loop structure, where the SEM micrograph in the upper left panel highlights where the FIB cut was taken. The TEM detail in the upper right panel shows the asymmetric cross-section of the NW. Scale-bar corresponds to 500 nm. (c) Integrated FFT of the oscillations plotted as a function of temperature. The line corresponds to the linear fit to the logarithmic amplitude of h/e oscillation extracted from (a), where $l_\phi \sim 13 \mu\text{m}$. Figure is adapted from Pub. 4.

The phase coherence was extracted from the small loop data, since the temperature dependence was blurred for higher temperature measurements. The temperature dependence exponent and the phase coherence length were extracted by fitting to the logarithm of the amplitude, yielding $m = 1.07 \pm 0.21$ for the exponent and $l_\phi(20\text{mK}) = 13 \pm 1 \mu\text{m}$ for phase coherence, see Fig. 3.25 (c) and methods. The exponent can be used to identify the transport regime in the structure. In the diffusive regime the temperature dependence of the coherence length follows $l_\phi \propto T^{-1/2}$, while in the ballistic regime $l_\phi \propto T^{-1}$ as reported in Ref. [212–214].

This is interesting for comparison with similar measurements on non-buffered InAs SAG loops grown on InP, that we have reported in Pub. 5. There, $m \sim 0.5$ for the exponent and $l_\phi(20\text{mK}) \sim 4 \mu\text{m}$. Since the coefficient is much closer to 1 for the buffered NWs, it indicates that the small loop resides in the ballistic regime below ~ 500 mK, while the non-buffered loop in the diffusive regime. Even though from the SEM characterization the structure and morphology of the non-buffered NWs, especially networks, looks better defined, the transport properties are significantly improved by implementation of the buffer.

The WAL experiment provides another mean to extract the phase coherence as well as spin-orbit length l_{SO} ⁶⁵. WAL measurements were performed on single buffered NW

devices (design is similar to the field-effect mobility related devices). There is a significant difference compared to the AB measurements, which is likely due to the difference in dephasing mechanisms²¹⁵. Here both the diffusive and ballistic models introduced in Ref. [202] are used to fit the data (see section 3.1.7). This particular model assumes a cylindrical cross-section of the NWs. The fit quality is quantified based on standard deviation of the difference between the data and the fitted function. The results are shown in Fig. 3.26, where the best fit is plotted for all combinations of effective NW width W_{eff} and elastic scattering length l_e , showing the relation between the parameters. The width W_{eff} is treated as an effective parameter, since the spatial confinement in transport does not necessarily correspond to the real dimensions of the NW. The fits of both diffusive and ballistic models are shown in Fig. 3.26 (a). The standard deviation magnitude as a function of W_{eff} is shown in (b). Here, $l_{SO} \sim 85$ nm and $l_\phi \sim 210$ nm for the best fit, which corresponds to $W_{eff} = 142$ nm. Similar dependence of standard deviation between the fit and the data for the ballistic model is shown in (c), where the best fit yields $l_{SO} \sim 298$ nm and $l_\phi \sim 459$ nm for $l_e = 138$ nm and $W_{eff} = 115$ nm.

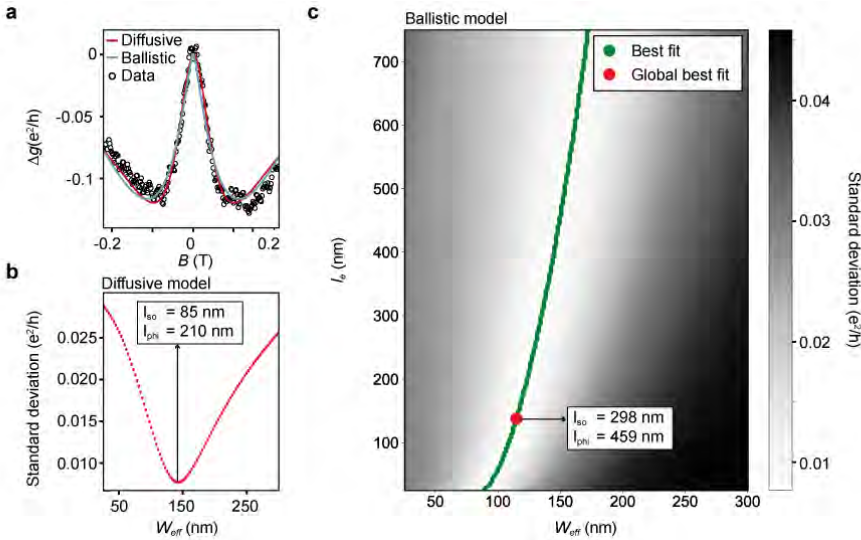


Figure 3.26: (a) Fit of diffusive and ballistic WAL models (described in section 3.1.7) to the measured and off-set magneto-conductance data. Standard deviation between the fit and the data for: (b) diffusive model as a function effective NW width W_{eff} , yielding $l_\phi \sim 210$ nm and $l_{SO} \sim 85$ nm for the best fit. (c) ballistic model as a function of W_{eff} and elastic scattering length l_e , yielding $l_\phi \sim 459$ nm and $l_{SO} \sim 298$ nm for the global best fit with respect to both W_{eff} and l_e . Figure is adapted from Pub. 4.

In both ballistic and diffusive cases, the extracted l_ϕ is significantly smaller than for the measured loop structure, which was previously observed for example for GaAs/AlGaAs

structures²¹⁶. The discrepancy between the WAL fitting in diffusive and ballistic regimes is most likely related to the assumptions of the models and the regime that the transport really resides in needs to be taken into account. Interestingly, the W_{eff} seems to be the dominant parameter, determining the quality of the fit in both regimes and therefore introducing the most uncertainty into the result. The elastic scattering length value can be varied for a fixed W_{eff} , without such a significant impact on the fit quality. On the other hands, both l_ϕ and l_{so} increase with increase in l_e . The extracted values provide mainly relative measures of the relevant length scales and should be used only for comparison between SAG NW structures. If the diffusive model is considered, the extracted values are comparable to similar measurements on VLS grown InAs, InSb and InAs_{1-x}Sb_x NWs^{35,132,195,202,217}.

3.2.9 Superconductor/semiconductor hybrid nanowires

As was stressed in the introduction, the implementation of presented structures relies on SU/SE hybrid epitaxy. Compared to VLS NWs, the SAG approach again offers multiple advantages. Most importantly it allows for selection of different facet families to match with the SU, which offers variability in interface engineering⁵³.

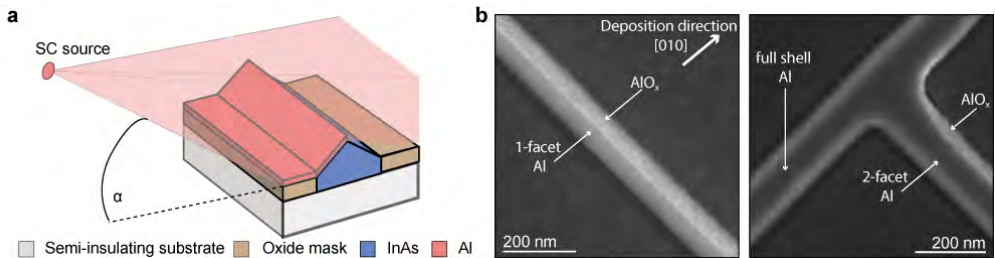


Figure 3.27: (a) Schematics of in-situ superconductor deposition on SAG NW, where α is the angle between the source and the plane of the substrate. (b) SEM micrographs of InAs non-buffered SAG NWs covered with 4 nm of corresponding planar growth of Al.

The Al deposition scheme is shown in Fig. 3.27 (a). The NW coverage can be controlled by the angle α between the source and the plane of the substrate. In our system, $\alpha = 66.7^\circ$. Therefore, if the material is deposited on [100] NW with 45° inclined [110] faceting, fraction of the nominal Al thickness is also deposited on the opposing other facet during deposition along [010] direction, as shown in Fig. 3.27 (b). The Al on the facet facing the source is very smooth, while on the facet with thinner layer it has dewetted into droplets, which most likely fully oxidize. The oxidation suppresses screening of the initially metallic layer, allowing for efficient tuning of the NW chemical potential by side gates. In Fig. 3.27 (b) three different types of heterostructures are formed within the same deposition. In the left panel, 1-faceted heterostructures is formed, since one of the facets

is shadowed by the structure itself, which corresponds to the one used for experiments in Pub. 5. In the right panel, two faceted structures are formed due to the non-fully developed shape of the NW. For the part aligned to the [010] direction a full shell heterostructure is formed, which have shown potential in various VLS NW based experiments^{38,218}.

The properties of the 1-facet SU/SE SAG non-buffered InAs/Al NW hybrids were characterized in Pub. 5. As shown above, the chemical potential tuning of the non-buffered NWs is very challenging, which makes it difficult to perform tunneling spectroscopy experiments⁵⁸, which often rely on the ability to fully pinch-off the conductance. Despite the imperfection of the material, an induced hard-superconducting gap⁵⁴ and $2e$ -periodic Coulomb oscillations⁵⁸ suggest strong suppression of quasi-particle poisoning²¹⁹ and even signatures of presence of Majorana zero modes⁵⁸.

3.3 Conclusion

Even though the SAG approach has been known for decades, the presented results widely expand its potential for applications in low temperature electronics. The scalability into complex structures and the freedom of network designing comparable to 2-D top-down methods while maintaining the advantages of in-situ growth, have not yet been matched by any of the other semiconductor NW growth methods. That is well captured by the growth results presented in this chapter, which demonstrate growth of well defined SAG NW networks and provide details of the early buffered SAG NW growth stages, which are crucial for further improvements and understanding of the structures.

The presented comparisons of non-buffered and buffered SAG NW properties demonstrate the variability and importance of the interface engineering within SAG structures. The implementation of the buffer layers at first allows for strain engineering, which not only improves the crystal quality of the interface between the NW and the substrate, but also enhances the transport properties [Pub. 4].

The measured buffered structures exhibit good response to field effect chemical potential tuning, strong spin orbit coupling and coherent electron transport in NW networks. That put together with compatibility with SU/SE hybrid NW growth and results of the first measurements on these structures [Pub. 5] indicates, that the SAG semiconductor materials provide the ultimate scalable platform for experiments necessary for success in the quest for taming the elusive Majorana Fermions. And hopefully in the end, could become the material basis for quantum computing.

3.4 Outlook

Despite the presented results and great advancements presented in Refs. [153, 154, 156, 157] the III-V semiconductor SAG NW based transport experiments are still in the very early stages. Therefore, a lot of questions remain unanswered and a lot of possibilities are opened for further research. Especially, investigation of SAG NWs grown on various substrate orientations and from wider variety of materials could significantly increase the potential of the material for various applications.

The first that comes in mind is the improvement of the buffered NW growth^{153,157}. In particular, since available heterostructures potentially offer the possibility to grow lattice matched or fully elastically relaxed structures. The buffer engineering also provides control over the overall NW morphology, as for example growth of very thin NWs. In addition, elastic strain relaxed structures could potentially affect distinct material properties, e.g. induce Dresselhaus spin-orbit coupling, which is related to the crystal inversion asymmetry²²⁰.

Another important aspect of the growth that needs to be studied in more detail is the mask selectivity, which is tightly related to the available growth parameter window. Once the growth parameter window is extended, one may be able to control the NW faceting, early growth stages, junction formation mechanism and even more.

The variety of structures and especially available facets could significantly enhance the properties and possibilities of material combinations of SU/SE hybrid structures. Since their properties seem to be related to the interface and crystal matching⁵³, the facet variability could open the road to grow new epitaxially matched heterostructures using various materials²²¹.

At last, as for the VLS NWs in Chapter 2, there are many advantages in in-situ shadowing of various heterostructures. So far, the shadowing schemes for VLS NWs seem to be quite complex and require complicated substrate engineering. For SAG NWs, the situation seems very simple, as shown in Fig. 3.28, where deposition of SiO_x pillars can serve as a shadowing template in directional depositions. The variability and simplicity of this approach remains to be tested.

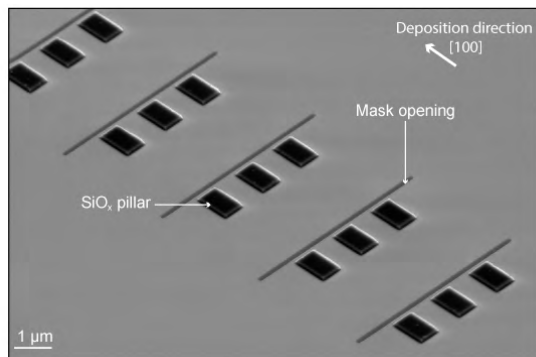
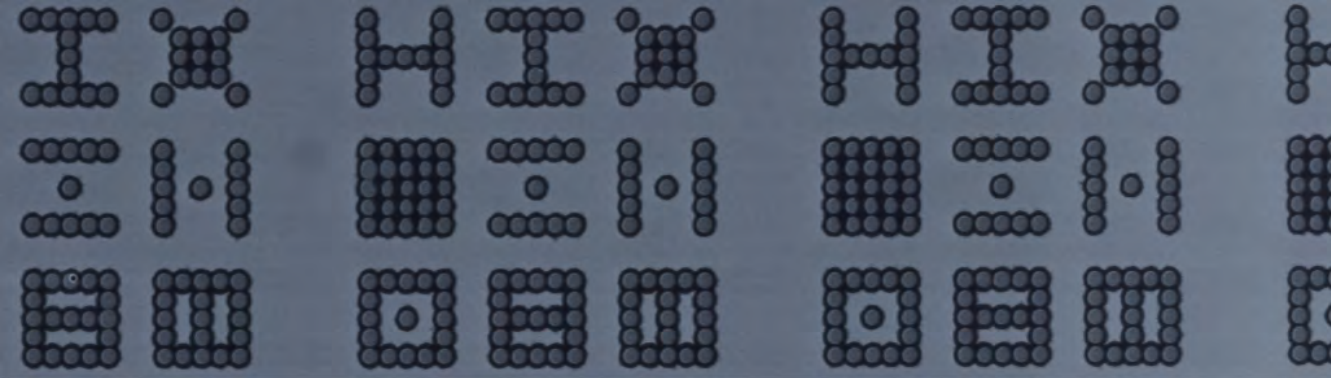


Figure 3.28: SEM micrograph of a masked substrate with etched mask opening and shadowing SiO_x pillars that is ready for growth and subsequent SC deposition.



4. Fabrication

In-situ merging of NWs often requires advanced approaches to substrate fabrication, which makes it an essential element of this work. Any successful VLS nanocross growth requires thorough analysis of crystal growth directions and precise positioning of individual NWs. The same applies for the SAG where alignment of the structures with respect to the crystal axes affects the NW morphology. Successful device fabrication is another key aspect of this work, since all structures are grown to be utilized in transport experiments. Especially for VLS nanocrosses and networks, it is crucial to prove that the structures are actually suitable for transfer from growth substrate and for subsequent device fabrication. This chapter summarizes all the different fabrication approaches which were used in this work and have potential in future crystal growth.

4.1 Electron beam lithography in growth substrate preparation

Substrate patterning by electron beam lithography is a well developed and established process which allows for preparation of very complex growth substrates. For this work we used Poly(methyl methacrylate) (PMMA) and methyl methacrylate (MMA) polymers. The choice depends mainly on the native/mask oxide removal process. MMA has shown good resistance to hydrofluoric acid (HF) based oxide etchant. On the other hand, if radio frequency (RF) plasma oxide removal is used, MMA suffers from strong redeposition and therefore using PMMA is advantageous. In this work, the resist is either spun directly on

the epi-ready substrates, after breaking the manufacturers sealed package or after oxide deposition in the case of oxide masked substrates. The spinning speed is 4000 RPM for 45 seconds for flat samples. For prefabricated samples with complicated morphology (i.e. samples patterned with etched v-grooves and depth on order of micrometers), gradual increase in spinning speed terminated with 4000 RPM for 45 seconds was used. That secures homogeneous dispersion of the resist over features with significant height differences. After baking the resist for 2 minutes at 185°C, the samples are ready for EBL patterning.

The lithography processes were carried on a 100 kV Elionix EBL system. Due to high exposure voltages and complexity of the patterns (where spacing on order of 100 nm is often needed) the process is prone to proximity effect. That means that nearby features are affected by dose distribution within the exposed areas, i.e. share the dose due to being close one to another. The proximity error correction package in BEAMER software²²² was used during all exposures, which ensured homogeneous dose distribution in all regions of complex patterns.

4.1.1 Catalyst size and beam defocusing

In order to maintain constant conditions during the VLS nanowire growth it is important to maintain consistent volume of the catalyst nanoparticles before annealing. That is not difficult to achieve when EBL processing is carried on flat substrates. The situation is more complicated for substrates with structured surfaces, where the thickness of the resist can vary after spinning and affect size of the exposed features. In this work, electron beam defocussing was used in order to change the diameter of the designed catalyst islands. The same size of a dot* was used in the whole CAD design, but the real size after exposure was determined by intended defocussing of the electron beam and intentional overexposure, as demonstrated in Fig. 4.1.

When the exposure dose is saturated, the size of the single shot profile scales with dose time very slowly. That means that the resulting feature size is also less prone to variations in resist thickness and surface roughness. That is very useful during exposures on pre-patterned and tilted surfaces, as will be shown bellow.

*5 nm dot size was used as it is the minimal recognizable feature size in the Elionix Wecas operation software. That ensures that all features are exposed by single beam shots with designated exposure time.

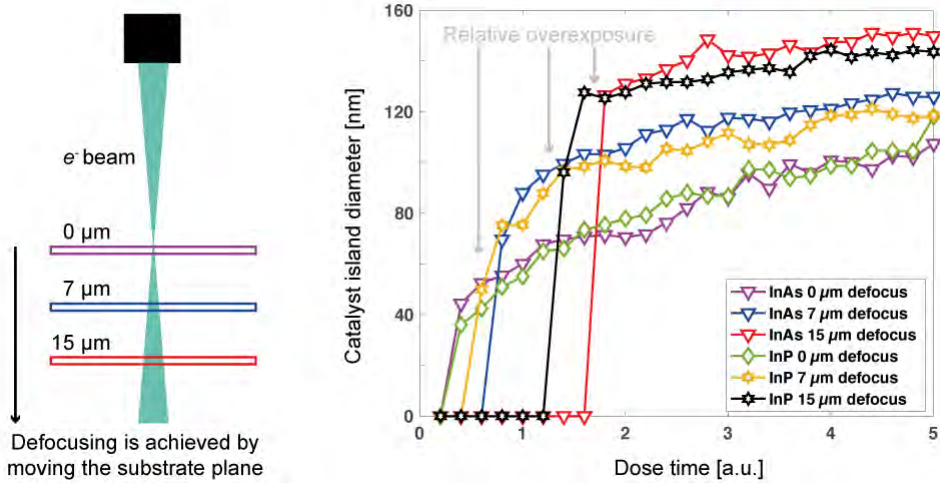


Figure 4.1: A scheme of how electron beam spot size is changed by moving the substrate surface plane out of focus, together with dependency of the catalyst island size after metalization and lift-off on the EBL dose time per dot, for InAs and InP substrates.

4.1.2 Pattern alignment to substrate crystal axis

For selective crystal wet-etching²²³, but also for VLS (Pub. 2) and SAG¹⁵³ network growth, the alignment of EBL design with respect to the crystal strongly affects the resulting morphology, as was shown in previous chapter. VLS networks rely on precise catalyst placement along specific crystal directions, SAG NW quality and faceting are strongly affected by misalignment with respect to the high-symmetry substrate axes. For selective crystal etching, the misalignment of the mask with respect to specific crystal directions affects sidewall roughness and overall etch profile.

Since even small angular deviations in the alignment affect the subsequent processing, aligning 'by eye' or to the sample holder is often not sufficient. Here, the major flat edge of the 2-inch wafer is used as a natural alignment mark in order to compensate for the rotation of the design. The position of the alignment marks in a 2-inch sized design is illustrated in Fig. 4.2 (a). The sample is often rotated with respect to the design after loading in the EBL system, as sketched for an extreme situation in Fig. 4.2 (b). Figure 4.2 (c) illustrates the aligned situation. For small rotations it is usually sufficient to perform the vertical alignment to the major flat edge, disregarding the horizontal component. It needs to be stressed, that the alignment does not stretch, but only determines the absolute position of the design for 2 point registration.

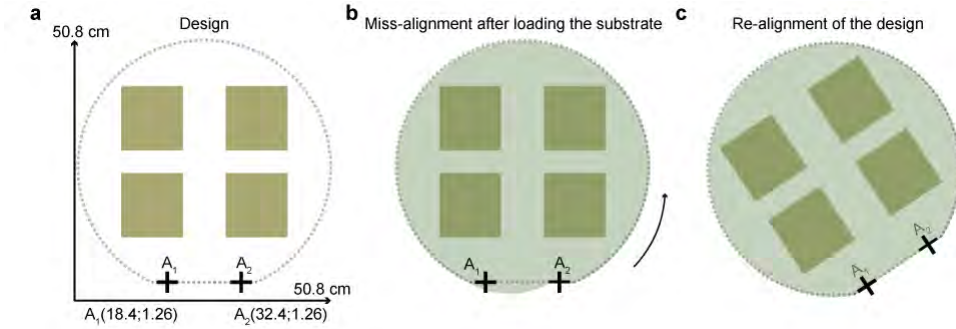


Figure 4.2: (a) Illustration of a 2-inch wafer design, where alignment marks A_1 and A_2 are placed at specific co-ordinates (in cm). (b) Extreme situation after loading where the design is misaligned to the real sample. (c) Corrected alignment of the design.

This method can be used for precise angular alignment on the order of ~ 0.01 mrad, which is essential for achieving growth of high-quality SAG structure and formation of VLS NW crosses, as was demonstrated in previous chapter. The alignment quality is then also determined by the smoothness of the major flat on supplied wafers. That was not an issue for 500 μm thick substrates from WaferTech, LLC.

4.2 Fabrication of substrates with trenches

Wet etching of crystals can be used to pattern substrates and expose surfaces with various orientations prior to MBE NW growth. In addition, it is a useful method which is often utilized to clean pre-processed substrates prior to growth. One of the interesting approaches, where (111)B facets were exposed on Si (100) substrates in order to merge non-positioned VLS NWs into nano-crosses was previously reported by Rieger et al. in Ref. [168]. It is an alternative approach to growth on (111)B sidewalls of CBE grown pyramid¹⁶⁰.

This section is dedicated to discussion of wet etching of InAs and InP substrates, in order to achieve (111)B faceted v-shaped grooves, which can be further patterned with catalyst nanoparticles and serve as (111)B platforms for inclined NW growth. This approach utilizes both techniques described in sections 4.1.1 and 4.1.2 and has great potential in growth of NW crosses. The idea and preliminary growth results were shown in more detail in the outlook of chapter 2.

As mentioned above, the selective etching of pre-patterned crystalline substrates strongly depends on the design alignment to the crystal. This effect has been previously

discussed in detail by Wang et al. in Ref. [223]. Figure 4.3 shows an example from the same work, where the lithography misalignment has strong impact on the resulting etch profile.

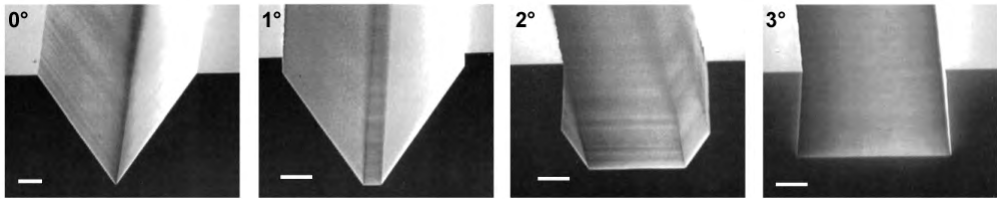


Figure 4.3: Tilted SEM images of grooves etched by HCl:H₃PO₄ (5:1) with photoresist masks aligned misaligned with respect to [110] orientation of (001) substrate by 0°, 1°, 2° and 3° degrees. The scale bars correspond to 1 μm. The micrographs are adapted from Ref. [223].

In this work, two different etch recipes were used for exposing (111)B facets of (001) substrates. For InP, solution of C₆H₈O₇ powder and H₃PO₄:H₂O₂:H₂O in ratio of 4:3:8, where 0.45 g of powder corresponds to 1 ml of water, results in etch rate of ~ 0.5 μm/min at room temperature. The facet selectivity is ideal and V-shaped grooves can be etched both along [110] and [1 $\bar{1}$ 0] directions, exposing (111)B and (111)A facets respectively. The same solution yields different results on InAs substrates. The etch profile has an undercut along the [110] direction and the (111)B facets are not accessible, as apparent in Fig. 4.4 (a). The v-shaped (111) faceted grooves are etched only along the [1 $\bar{1}$ 0] as shown in Fig. (b). Even though it was possible to grow NWs on the etched (111)A facets, the growth direction configuration was not ideal for synthesis of NW crosses. Fortunately, the (111)B facets can be exposed on InAs, by changing the solution to H₂SO₄:H₂O₂:H₂O with ratio of 1:8:8000* corresponding to etch rate of 1 μm per 28 minutes at room temperature. Even though the concentration of the active agents is very low, it is possible to expose the (111) facets along both [110] and [1 $\bar{1}$ 0] orientations, as shown in Fig. 4.4 (c) and (d), where the inset illustrates the cross-sectional etch profiles.

It is important to achieve homogeneous spinning of resist and consistent EBL feature size, in order to attempt growth of NW with the same morphology from complex catalyst patterning on the v-groove side-facets. This is not straightforward for ridges with depth on the order of multiple micrometers. The depth is related to the area of the sidefacets which needs to be sufficient for defining arrays consisting of multiple Au nanoparticles. As mentioned above, for structured surfaces the resist was spun by gradually increasing spinning speed up to 4000 RPM, which was maintained for 45 seconds. Despite variation of resist thickness over the sample, as illustrated in Fig.4.5 (a), it is possible to achieve

*Developed by Martin Aagesen from Niels Bohr Institute under University of Copenhagen.

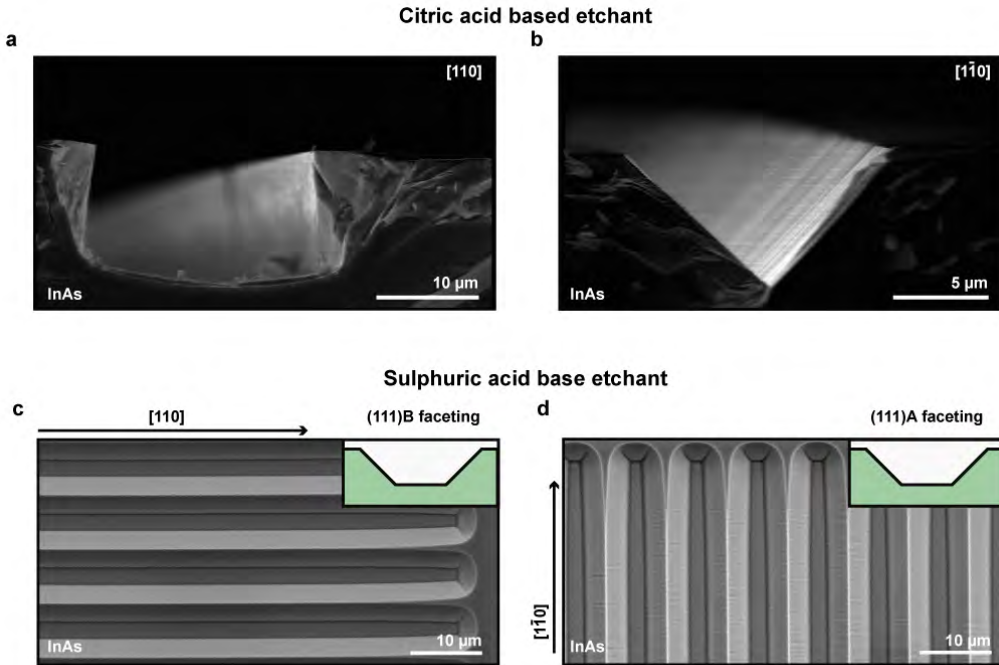


Figure 4.4: (a) and (b) Side-view SEM cross-sectional micrographs of trenches etched into InAs (001) substrates by citric acid based etchant, oriented along $[110]$ and $[1\bar{1}0]$, respectively. (c) and (d) Top-view SEM micrographs of trenches etched into InAs (001) substrates by sulphuric acid based etchant, oriented along $[110]$ and $[1\bar{1}0]$ respectively. The sketch in the insets shows the etch profile with (111)B and (111)A exposed facets.

complete liftoff after metal deposition. Even though the substrate can be fully covered by polymer, it is difficult to achieve reproducible feature size, due to resist inhomogeneity around edges and defocussing of the on the tilted side facets, as illustrated in Fig.4.5 (b). This results in difficult lift-off at the trench edges and also gradual decrease of the catalyst droplet size towards the bottom of the v-groove as shown in Fig.4.5 (c). These undesirable effects can be avoided by implementing the gradual spinning speed together with overexposing by defocused beam, as was described in section 4.1.1. The size of exposed features is not controlled in the CAD design, but by defocus of the beam. That allows to use saturated beam currents (complete overexposure) in combination with one shot exposure, to reduce the effect of resist thickness on the size distribution of the exposed dots. The small gradient in dot size is then introduced by angle profile of the trench facets and resulting difference in height of the exposed surface. For $10\ \mu\text{m}$ deep trench with (111)B facets this difference is roughly between 0 and 20 nm depending on the position

on the facet. That is much less than for standard exposure where feature size is defined in the CAD design shown in Fig.4.5 (c), where no dots were exposed at all in the deeper parts of the trench. Examples of successful v-groove facet patterning are shown in Fig.4.5 (d) and Fig.4.5 (e).

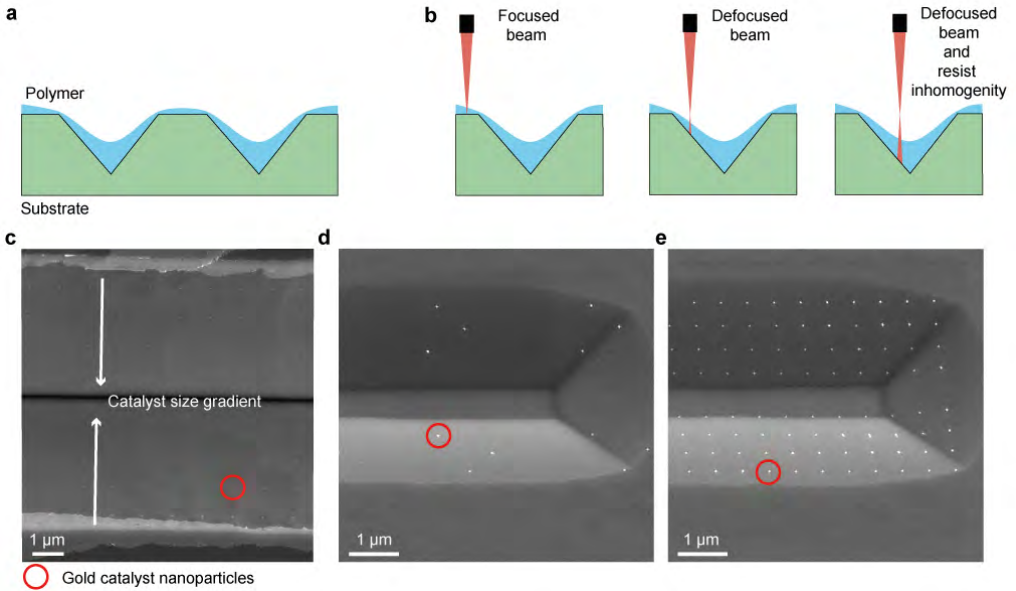


Figure 4.5: (a) Illustration of the profile of standard e-beam resist, which is a result of spinning on a pre-etched substrate with a depth of $7\ \mu\text{m}$. (b) Illustration of natural beam defocusing, which is caused by height differences over the pre-etched substrate. (c) Top-view SEM micrographs of catalyst particles positioned on (111)B facets of a trench etched into InAs (001) substrate, where standard EBL and spinning were used during the EBL step. (d) and (e) Top-view SEM micrographs of catalyst particles positioned on (111)B facets of a trench etched into InAs (001) substrate, where the beam defocusing (presented in Fig. 4.1) and gradual spinning were used during the EBL step.

As was shown in the outlook of Chapter 2, these substrates yielded promising results in inclined NW and nanocross growth.

4.3 Oxide masked substrates

Masking the growth substrates is of great importance in the case of SAG NWs, but can also be advantageously applied in the growth of VLS NWs. The simplest materials that can be used for masking are oxides with low crystallinity and high melting point. The oxide deposition can be done using various approaches such as thermal oxidation, plasma

enhanced chemical vapor deposition (PECVD), e-gun evaporation, atomic layer deposition (ALD) etc., which have different limitations, depending on application. If polymer masks have to be used prior to oxide deposition, the growth temperature can not exceed the melting point of the polymer. Depending on the material, this can make thermal oxidation and PECVD growth impossible. Another limitation arises, when low melting point substrates (i.e. III-V semiconductors are used), which makes thermal oxidation of many mask materials difficult. For InAs and GaAs, where As starts to desorb $\sim 300^\circ\text{C}$, thermal oxidation of Si is not possible, before melting the substrate. SiO_x is well established in a variety of industrial application and it has a high melting point, which makes it compatible with MBE growth and a relevant choice for this work.

The mask preparation is relatively simple and standard EBL process can be implemented in order to print arbitrary patterns on the substrates after or prior to oxide deposition. If the oxide thickness is on the order of 10th of nanometers, the EBL base dose is not strongly affected and the lithography process is the same as on non-masked substrates.

As was shown in Chapter 3, variety of oxides were tested for achieving selectivity during SAG NW growth. Also different techniques were implemented in order to produce thin features (sub 100 nm) and minimize the edge roughness after mask fabrication. The selectivity was tested on ALD Al_2O_x , HfO_x and SiO_x , where the aluminum and hafnium oxides were deposited in-house, whereas SiO_x was deposited at Microsoft-Finland in Iespoo. Other test were carried on thermally evaporated, e-gun evaporated and PECVD grown SiO_x and SiN. The PECVD growth* was done at the Danish Technical University by Robert McNeil and Karthik Jambunathan from Center for Quantum devices. For the VLS growth, where achieving growth selectivity is not necessary, the substrates were masked either with ALD Al_2O_x or e-gun evaporated grown SiO_x .

Wet etching was used for most of the masks, due to the simplicity of the process and successful growth results. The SiO_x , SiN and HfO_x were wet-etched by buffered HF, where MMA resist was used for lithography, since PMMA did strip and crack during longer etch times. Prior to etching the exposed substrates were annealed at 121°C , in order to reflow the MMA resist and smoothen its sidewalls. Right before the buffered HF etch, the wafer was dipped into isopropanol in order to wet the surface, transferred to H_2O without drying and then directly to buffered HF and H_2O after etching. The etch rates used for reproducible removal of the mask material are as follows: 10 nm per 3 s for SiO_x , 10 nm per 11 s for SiN and 10nm per 45s for HfO_x in non-diluted buffered HF at room temperature. Note that the etch rates can depend on the exact dielectric growth recipe (given in appendix A) of the oxides, but provide a good starting point for specific etch

*The growth was done in SPTS Multiplex PECVD system at 300°C .

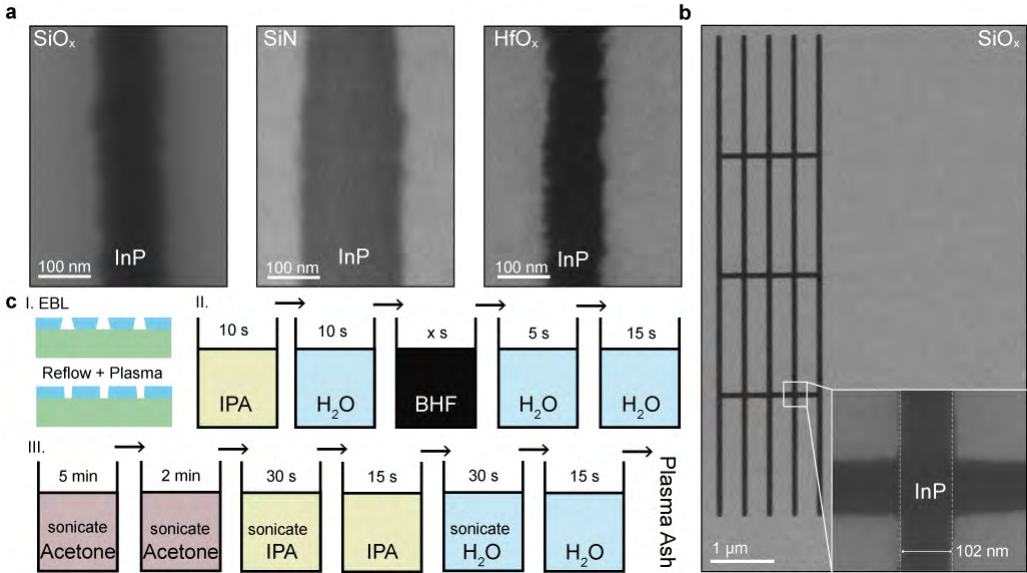


Figure 4.6: (a) Results of un-diluted buffered HF etching of SiO_x, SiN and HfO_x. (b) A network pattern etched into SiO_x mask on InP. (c) Schematics of the masked substrate pre-growth preparation process.

tests. Since the oxide thickness used for NW growth was between 10-30 nm, the short etch times lead to inconsistencies in terms of over-etching. It is difficult to achieve after-etch line width below 60 nm with wet etching, even though the limit of our lithography process is around 20 nm without cold development. The minimal observed over-etch is then ~ 40 nm for 10 nm thick oxide at given rates. Dilution of the buffered HF slows the etch rate, but results in increased etched profile roughness. The TEM results presented in Chapter 3 also indicate that the buffered HF is not 100% selective to the III-V semiconductors and the process can roughen the substrate surface.

The Al₂O₃ masks, which were successfully used in VLS NW growth, were etched in Transene D aluminum etchant at 50°C. The etch rate was ~ 10 nm a minute with over-etch of ~ 50 nm for 10 nm thick oxide mask. For VLS growth on SiO_x masks, e-gun evaporated oxide was used, with fast etch rates by buffered HF similar to the PECVD oxide described above. The results are shown in Fig. 4.6 for (a) SiO_x, (b) SiN and (c) HfO_x for 70 nm line-width before etching. Figure 4.6 (d) shows a network pattern fabricated in PECVD SiO_x, where the inset shows details of one of the junctions.

In typical MBE routine, processed substrates are cleaned in HF or other solution prior to loading into the MBE system. This is not an option for wafer masked with thin

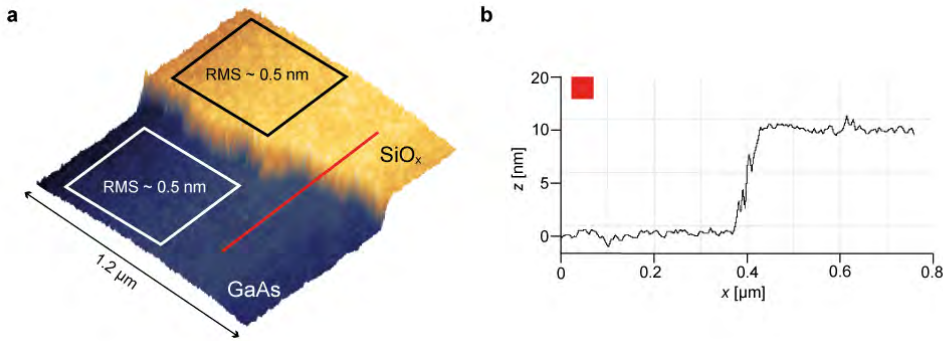


Figure 4.7: (a) 3-D AFM profile of an edge between 10 nm thick wet-etched SiO_x mask and GaAs substrate, where RMS roughness ~ 0.5 nm on both surfaces. (b) A height line cut taken from (a).

oxide layer, because roughening or local removal of the mask caused by mask etching could reduce the growth selectivity window. Therefore a special care needs to be taken in order to maintain clean samples. Our whole mask preparation process is sketched in Fig. 4.6 (c). First the oxide masked substrate is patterned by EBL, cleaned in oxygen plasma and annealed in order to reduce resist undercut (I). After, the surface is wetted in IPA, IPA is removed in H₂O, the mask is etched in buffered HF and finally then cleaned in two separate beakers with H₂O (II.). In the last step, the resist is lifted off while sonicating in acetone, sonicated in new clean acetone, sonicated in IPA, rinsed in new clean IPA, sonicated in H₂O, rinsed in new clean H₂O and finally cleaned in oxygen plasma after drying by nitrogen (III). It is also crucial to sonicate the tweezer in the relevant chemical during each sub-step. This process can consistently provide clean samples, where no contamination is apparent on the surface after growth.

The edge roughness and overetching, are natural for wet etch processes (as can be clearly seen from AFM scan* in Fig. 4.7). In a simple manner, they can be overcome by reactive ion etching, if available. The disadvantage of reactive ion etching comes from controlling of the selectivity, which can damage the substrate surface. The etch process interaction with surface can be fully avoided by depositing the mask on pre-patterned substrate and subsequent mask lift-off. Figure 4.8 summarizes two approaches that can be used in order to reduce line thickness and edge roughness of the features within SAG mask. In (a), a standard EBL and wet etch procedure is used to prepare the mask. Subsequently, another EBL step is used in order to reduce the line width and edge roughness, by second oxide deposition over the first mask. Advantage of this method is a very easy and consistent lift-off of the mask.

* AFM scan was performed by Joachim Sestoft, see Pub. 4 for affiliations.

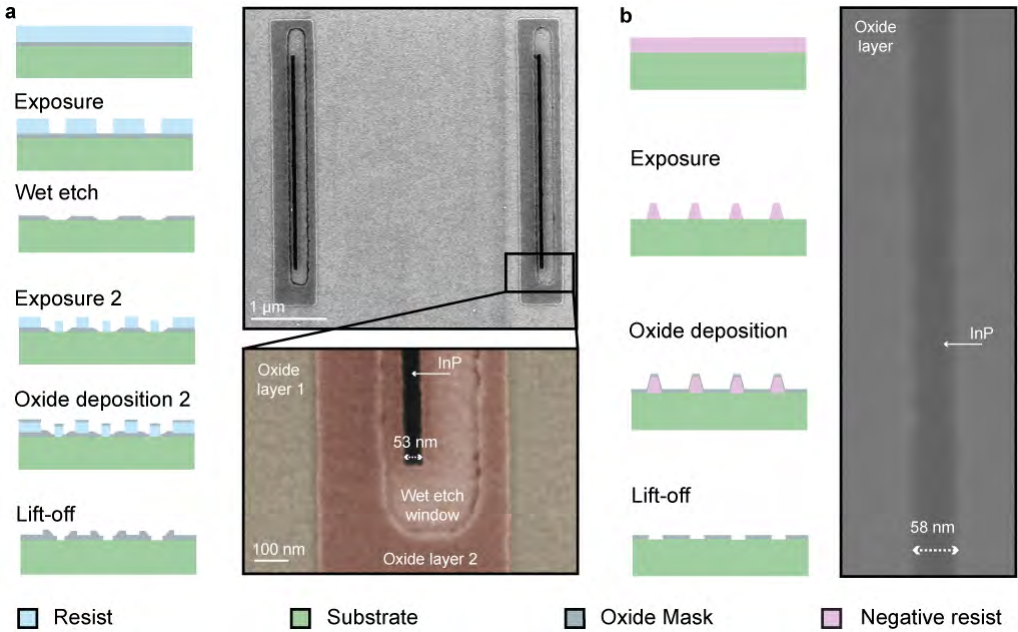


Figure 4.8: (a) Scheme of a double oxide deposition fabrication procedure, which uses positive resist to reduce edge roughness and line thickness, together with SEM micrograph of a resulting mask. (b) Schematics of mask lift-off fabrication procedure, which uses negative resist to reduce edge roughness and line thickness, together with SEM micrograph of a resulting mask.

An alternative is shown in Fig. 4.8 (b). In this case, negative resist is used before single oxide mask deposition. The absence of undercut, makes lift-off very difficult. Sonication prior and after an overnight lift-off is necessary to achieve consistent results. This method can be used to reduce the line thickness down to 25 nm while maintaining the reduced edge roughness. The biggest advantage is that the surface of the substrate is not exposed to any etchant and its quality maintained.

Unfortunately, these methods are not compatible with PECVD, due to exposure of resist to high oxide growth temperatures. The mask quality is of great importance and can clearly affect the resulting structure of the grown NWs. In addition the growth parameter selectivity window can be related to the oxide surface roughness and amount of crystallinity, which affect the growth species incorporation, desorption lifetime and diffusion on the mask surface. These methods still remain to be tested for growth and may become of importance once the SAG field progresses towards optimization of high carrier mobility NWs.

4.4 VLS Nanowire deposition

Fabrication of simple free-standing VLS nanowire devices can be achieved by using simple NW deposition methods, e.g. dry deposition or dispersion in solutions⁵⁸. As a simple example, the NWs can be picked up by gently wiping the growth sample with an edge of clean-room wipe and then shaken off to a blank Si/SiO_x chip. Such randomly deposited can be contacted and measured. Many other options for controlled NW deposition of large amounts of NWs were previously reported, eg. dielectrophoresis techniques,¹⁶¹ nanoscale combing¹⁶² and magnetic aligning of NWs.¹⁶³

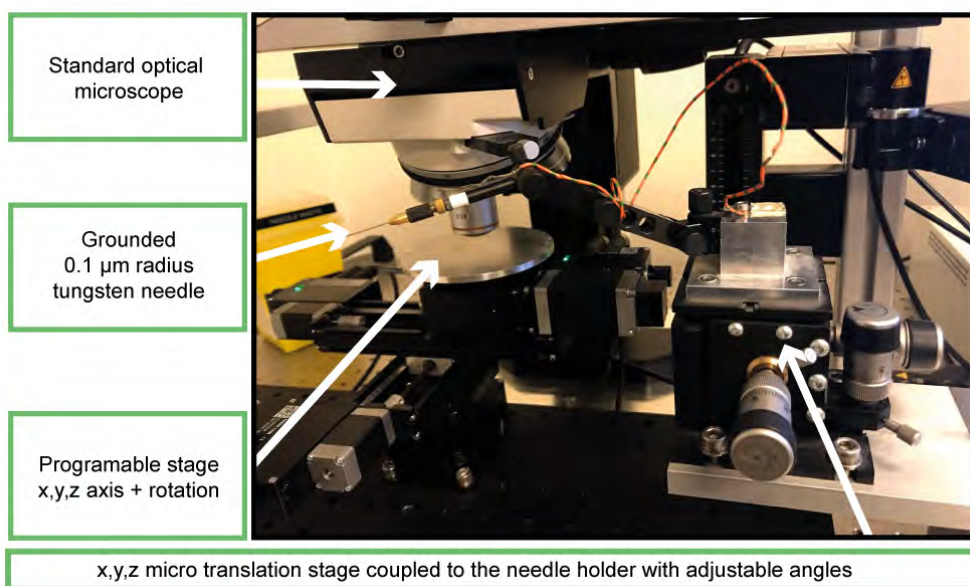


Figure 4.9: Photograph of the micromanipulator setup, with labels on the essential parts. The setup was set and maintained by Anders Kringhøj and Karl Petersson from Center for Quantum Devices.

The situation is different when specific NWs need to be selected, as can be common while growing on pre-patterned substrates. In this work an optical mechanical micromanipulator was used in combination with SEM. SEM allows for selection of a specific structure on the growth chip, which can be easily located in optical microscope if there are enough alignment marks available. A simple setup that was used for purposes of this work is shown in Fig. 4.9. The setup is built on a suspended optical table. A programmable sample stage that allows x,y,z translation and stage rotation is used to secure precise and simple refocusing from the growth substrate to either a blank chip or TEM grid. An optical microscope with 5x, 10x and 100x magnification is located above the substrate. Next to the

sample stage, another x, y, z micro translational stage is coupled to a needle holder. The holder allows to control the angle of the needle tip with respect to the substrate but also arbitrary rotation of the needle arm. In this work $0.1\ \mu\text{m}$ tungsten needles were used with the highest success rate*. Most successful and consistent depositions were then achieved if the target substrate was pre-ashed in oxygen plasma. This step changes the electrostatic charge on the chip or TEM grid surface and helps to remove the NW from the tip of the needle during transfer.

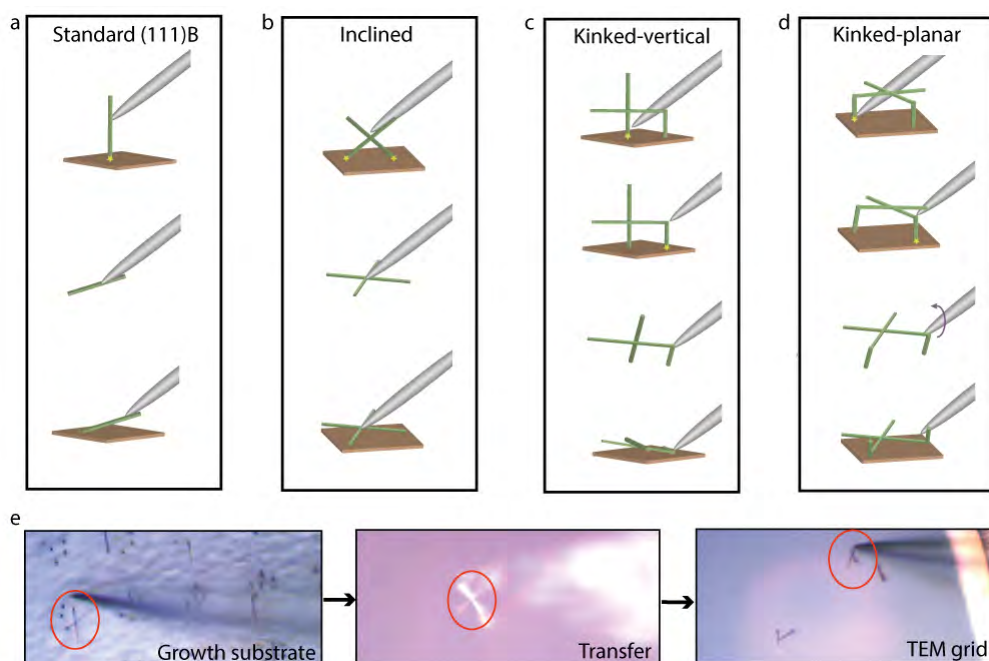


Figure 4.10: Schematics of micro-manipulator transfer of (a) Standard (111)B NWs, (b) inclined nanocrosses, (c) kinked vertical nanocrosses and (d) kinked planar nanocrosses. (e) Optical images of kinked planar nanocross onto a TEM grid.

A simple schematics of standard (111)B NW transfer is shown in Fig. 4.10 (a). The NW is gently broken off growth substrate and sticks to the needle by electrostatic forces. Subsequently, the loose end of the NW is dragged on the target substrate surface, until it sticks to the surface. As the end of the NW is dragged around by the needle, the area of contact with the substrates increases, i.e. more electrostatic force attracts the NW until loosens from the needle. If more precise placement is required, it is possible to use the needle to push the NW around on substrate. That is because the area of contact with

*The needles were purchased from American Probe and Technologies, Inc.

the substrate is now much larger than with the needle, making it almost impossible to pick it up again. A similar simple transfer can be used for inclined nanocrosses, where by pushing with the needle close to the junction, the nanocross can be picked up and placed as shown in Fig. 4.10 (b). The situation is more complicated while transferring the kinked vertical nanocrosses. First the vertical NW needs to be broken off first at the stem. After the structure is picked up by pushing on the kink which ensures smooth transfer, as depicted in Fig. 4.10 (c). Similar can be used for kinked planar nanocrosses, but the structure needs to be flipped by 180° and placed on the target substrate with stems pointing upwards, as illustrated in Fig. 4.10 (d). The three basic stages of the transfer are shown in optical images in Fig. 4.10 (e), where a kinked planar nanocross is picked up from the growth substrate and transferred to a TEM grid.

As already mentioned, the selective NW transfer is crucial for transport characterization of low growth yield NW structures. On the other hand it is obvious, that for their potential industrial applications, more complex and faster transfer methods need to be developed.

4.5 Device fabrication on VLS nanocrosses

Transport characterization of grown structures is a necessary tool, which allows to assess their potential in variety of experiments. That means, that reproducible device fabrication is crucial. In this work the NWs were transferred onto doped Si substrates with 200 nm of thermal oxide (5x5 mm chip size), by method described above.

The wafers were pre-patterned with Au leads, alignment marks, bonding pads and the backside was covered by thin layer of Au as can be seen in Fig. 4.11 (a)*. The doping and gold back-side provides an easy contact, if a global backgate needs to be used in the experiment. The 200 nm oxide serves as the backgate dielectric layer and no leakage was encountered after NW transfer. The larger outer patterns were prepared by UV lithography, but the fine alignment marks were patterned by EBL. This procedure significantly reduces the exposure time and allows for 2 inch wafer exposures within reasonable times.

Since the structures are deposited by the manipulator their precise position needs to be correlated to the CAD design before contact exposure. SEM imaging on Raith E-line SEM/EBL hybrid system can be precisely aligned to the blank chip design. Therefore, positioned images can be taken at specific sites, which can be roughly estimated from optical images. In addition the fine alignment marks are designed to fit within $25 \times 25 \mu\text{m}$ writing field. The resulting SEM image then contains the selected structure and four

*The blank chips were prepared by Shivendra Upadhyay from Center for Quantum Devices.

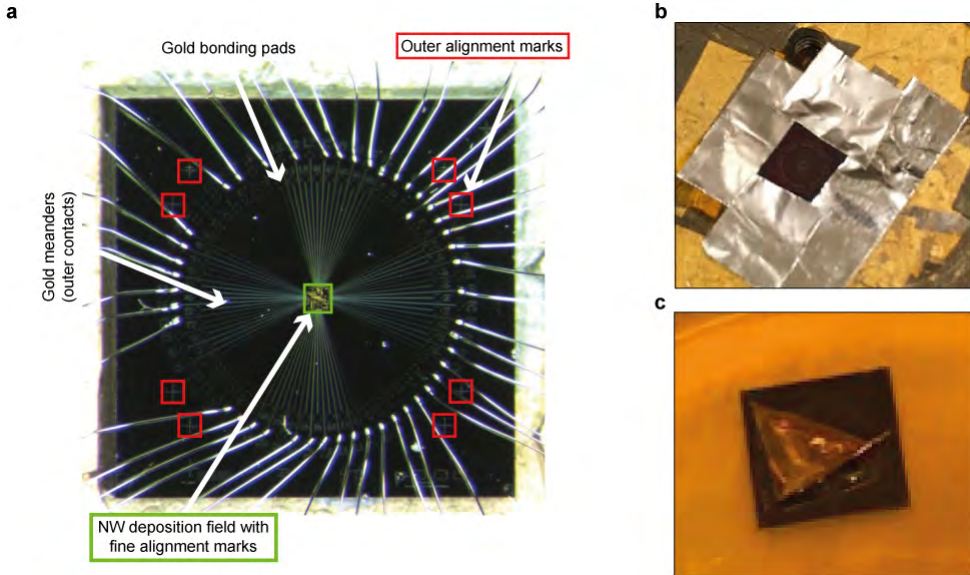


Figure 4.11: (a) Optical image of a bonded blank chip after measurement. (b) A photograph of a simple Al foil mask used before metalization. (c) A photograph of the peeled of gold after lift-off.

alignment marks. That allows for overlaying the device CAD design, with a real SEM image and for device fabrication with sub 20 nm precision.

The fabrication recipe for simple structures and devices can be summarized into following steps:

- Blank chip preparation
- NW transfer
- Taking positioned SEM images
- Design preparation
- Resist spinning
- Resist bake
- EBL exposure
- Resist development
- Oxygen plasma ashing
- In-situ Argon RF milling
- Ti sticking layer deposition
- Au contact deposition
- Lift-off

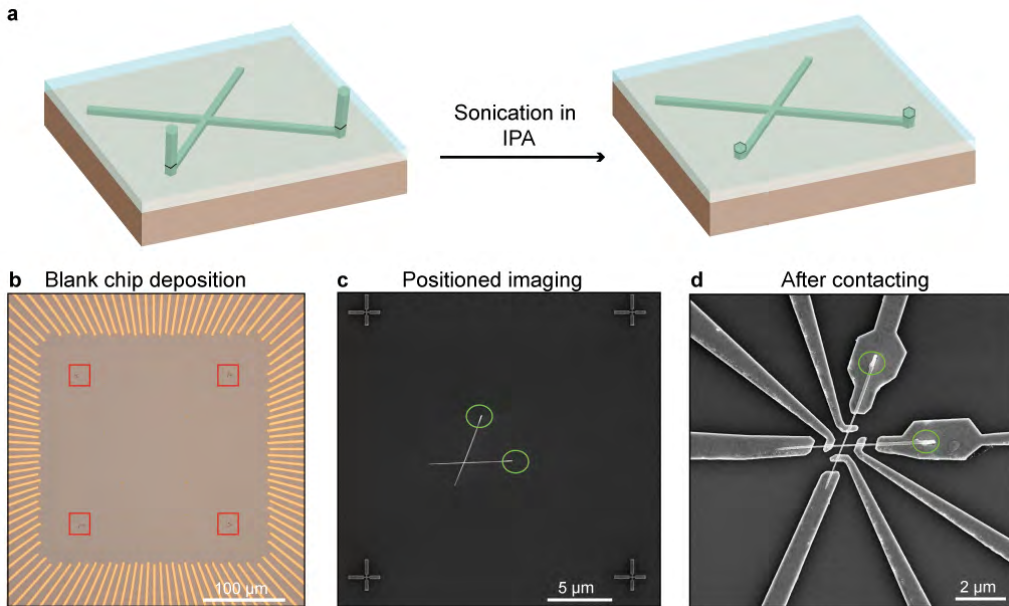


Figure 4.12: (a) Illustration of the process of breaking the kinked planar nanocross stems, by sonication in IPA after resist spinning. (b) An optical microscope image of a blank chip with 4 precisely placed kinked planar nanocrosses (red). (c) A positioned SEM micrograph of kinked planar nanocross after transfer, with the stems pointing up (green). (d) An SEM image of the same kinked planar nanocross, where the stems were broken off before device fabrication.

The step that requires the most attention is the in-situ Argon RF milling of the native oxide, which ensures good contact to the device. This step is absolutely crucial for optimization of the device performance. Details of the fabrication recipe can be found in Appendix C.

Special treatment is required during the kinked planar NW device fabrication. Since the nanocrosses are deposited with stems pointing up, as was shown in Fig. 4.10 (d), they easily break during lift-off. Therefore, they need to be broken off before device fabrication, as is shown in Fig. 4.12. Sonication in IPA after resist spinning easily breaks the stems off without putting stress onto the kinked parts of the NWs, which are of interest for the measurements.

Additional steps may be necessary for fabrication on the specific types of nanocrosses. In all cases, a very gentle lift-off is needed to avoid damaging the structures. A simple way to achieve that is to cover sides of the chips before metal deposition. This can be done

by using ultra-high vacuum compatible tape and aluminum foil as shown in Fig. 4.11 (b). That prevents the metal from sticking to the sides of the chip and the whole metal layer lifts-off as a single flake, without any necessity of additional rinsing or sonicating, as can be seen in Fig. 4.11 (c) after 15 minute lift-off in 50° acetone. A gentle lift-off is crucial and improves the fabrication yield of devices based on all three discussed nanocross types.

If the global back-gate is not sufficient for the experiment, precision of the lithography allow for use of effective side-gates, which can be put on during the same step as contacts. Another, and usually more effective possibility is to use ALD dielectric layer and fabricate top-gated devices. The top-gated device fabrication will be discussed in more detail in next section. The nanocross device fabrication on pre-patterned blank chips is very consistent (as can be once more seen in Fig. 4.13) and using unified chip designs makes it easy to the chips to boards and characterize the transport.

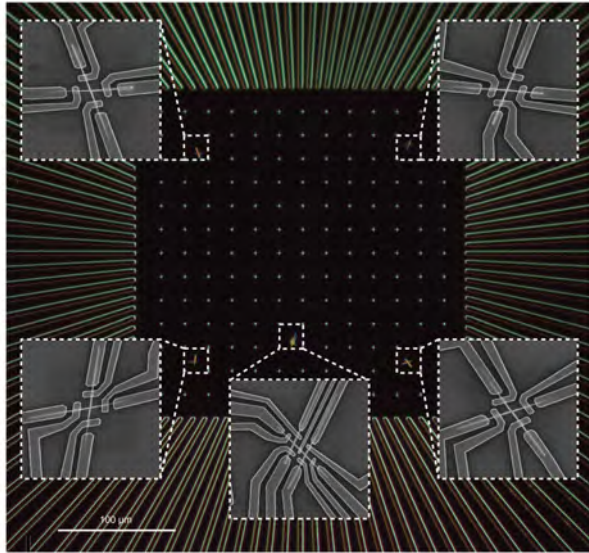


Figure 4.13: Dark field optical microscope image of a blank chip with 5 selectively deposited nanocrosses. The insets show SEM images of the same structures after device fabrication.

At first, contact needle probes were used to measure the VLS NW devices without bonding. That led to many problems, because thorough measurement of multi-terminal devices required multiple probe configurations. That led to scratching of the bond pads, electrostatic discharges if the system is not perfectly grounded and ultimately to melting of the structures. Therefore, the chips were glued and bonded onto daughterboards and connected to the measurement setups as shown in Fig. 4.14, in order to give the

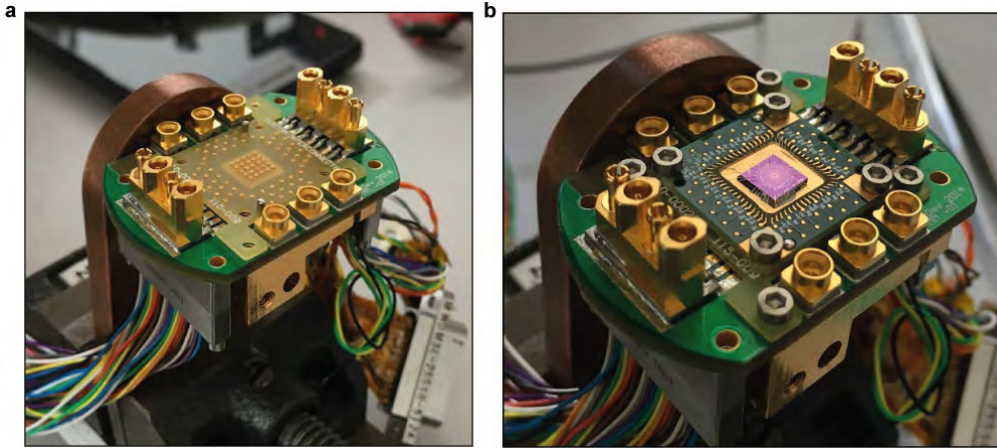


Figure 4.14: Photographs of (a) motherboard with an interposer and (b) a daughter board with a bonded chip.

measurement more stability. The boards are compatible with various setups in the group including a 4K probestation, 300 mK cryostat and 20 mK cryostat with magnet, which allows for the chips to be reused in multiple experiments.

In general, all the presented nanocrosses are easily blown up by electrostatic discharges. Therefore proper grounding needs to be used in all stages of the experiment. The used boards offer 50 normal lines, which allows for comfortable measurement of multiple devices. The whole fabrication process is significantly easier for SAG NWs, where the arbitrary designs and easy scalability offers the possibility of using unified fabrication schemes and large scale fabrication in the same manner for multiple growths.

4.6 Device fabrication on SAG NWs

As discussed in previous chapter, the SAG NWs can be grown directly on semi-insulating substrates, which offer the possibility to make devices directly on the growth chip, as-grown. The possibility to grow arbitrarily patterned chips, which can already contain alignment marks makes it advantageous to design the mask and whole device chip at once. The same mask can be used for growth of different materials and heterostructures (if the substrate crystal orientation is maintained). This is especially important for direct comparison between crystal structure and transport properties in different growths.

Figure 4.15 (a) shows an SEM micrograph of a unit chip, which was cut from a

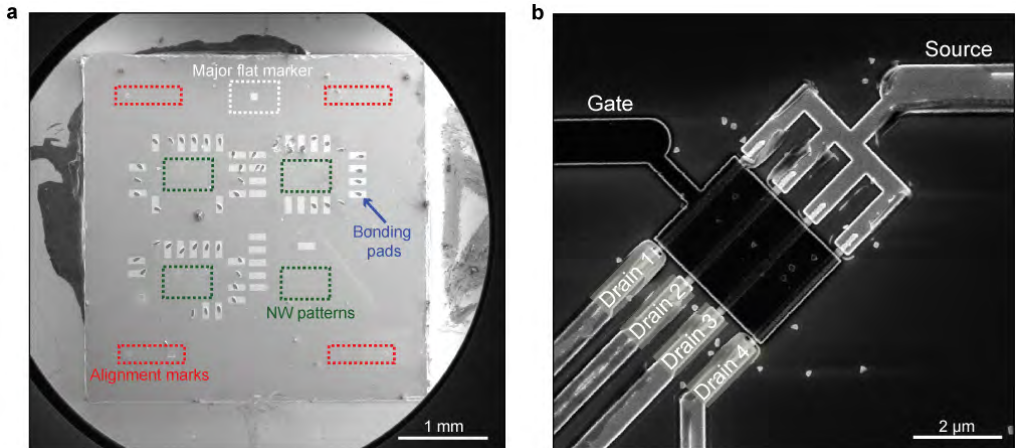


Figure 4.15: (a) SEM micrograph of a SAG chip after growth, device fabrication and bonding (bonds were ripped out before imaging). (b) SEM image of SAG device consisting of 4 NWs which have mutual source, gate and separate drains.

single growth. The chip was imaged after growth, device fabrication and measurement, but all the components (mask, alignment marks, contacts and gates) were designed in a single step. One disadvantage of the semi-insulating or insulating substrates is that it is not straightforward to implement back-gating schemes. That requires development of buffer layers, which would prevent leakage between the substrate and the SAG NW, even for high gate voltages. Therefore side-gated or top-gated devices need to be used. The fabrication is in principle the same as described for VLS NWs in previous section, but there is no need for positioned imaging and blank chip fabrication. The alignment marks can be grown in the same growth as the SAG NWs and are sufficient for very precise EBL alignment.

An important advantage is that one growth can be cleaved into many chips with same NW geometries and material properties. Also the NW diameter can be controlled not only by growth time, but width of the mask opening, which allows for characterization of multiple devices at once. That is illustrated on a simple geometry of a device with multiple NWs sharing the same source and top-gate. An example of such a SAG device is shown in Fig. 4.15 (b)*.

The top-gated device schemes require high quality dielectric layers, which would prevent leakage to the gate, while enabling for strong electrostatic coupling between the gate and the NW, but also and minimize disorder in electrostatic potential. In this work

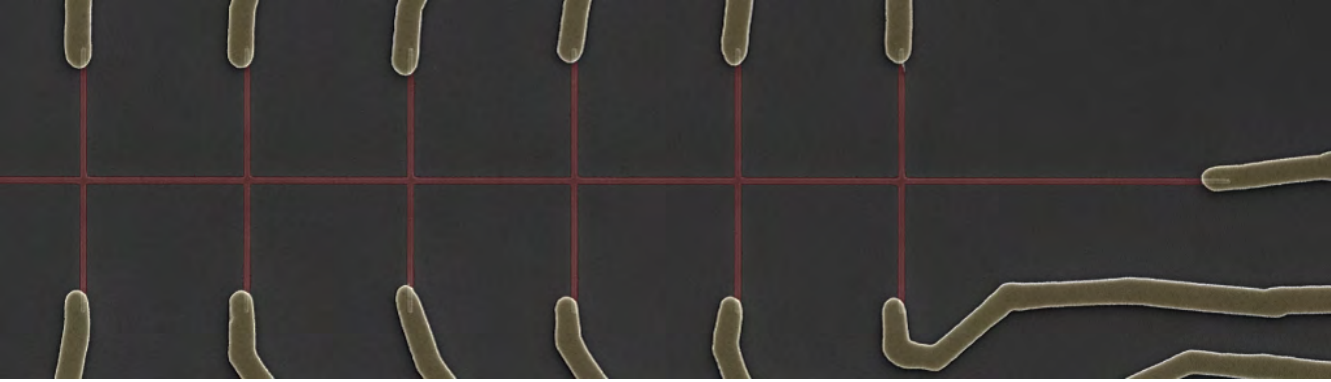
*The device was designed by Lucas Casparis and fabricated by Marina Hesselberg.

7-10 nm thick layers of HfO_x were grown by ALD at 90°C . Previous experiments in the group, have shown that multiple hour degassing in the ALD system at 90°C is beneficial for the dielectric quality and result in more reproducible device response to field effect gating. Therefore, the same 10 hour degassing step annealing step was used for the SAG NWs.

Interestingly, when InAs/Al hybrid NWs are grown, most of the substrate surface is coated with thin ~ 7 nm thick layer of Al. If this Al is patterned and selectively etched by Transene D, it can serve as an in-situ grown contact to the NW without the necessity to remove native oxide. We have demonstrated coherent electron transport in a loop device contacted in this manner in Pub. 5. In addition, there is an easy access to superconducting leads in low temperature experiments.

4.7 Conclusion

To my best knowledge, the growth on pre-patterned substrates is the most critical aspect of synthesis of NW networks. Designing the proper substrate requires innovative approach to fabrication methods, deep considerations of NW growth directions and crystal structure and most importantly, perfect alignment of the designs with respect to the substrate crystal symmetry. As the NW growth evolves to the limit, where the transport is not affected by the NW morphology and/or interface quality any more, the crystal purity will start to play a major role in the transport limitations. Therefore special attention needs to be given to substrate preparation process reproducibility and control.



5. Conclusion

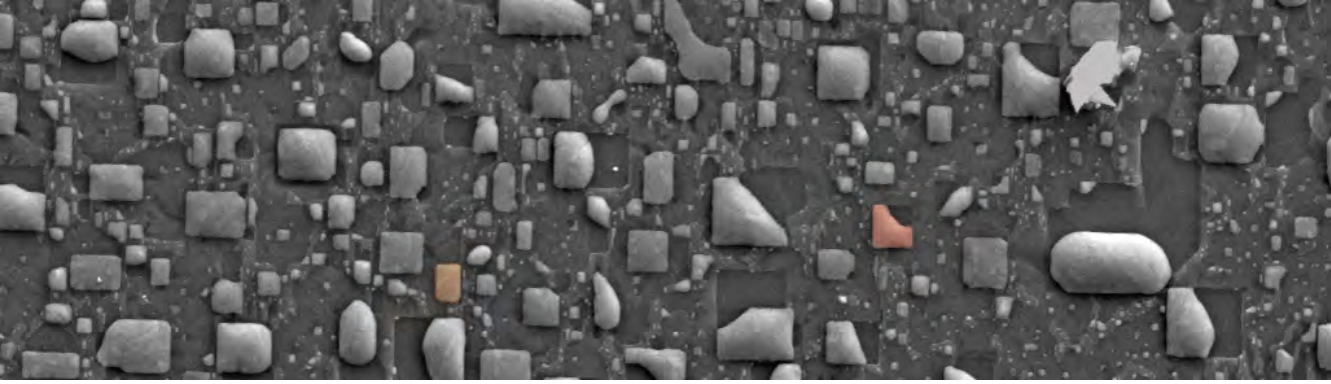
Multiple novel approaches and related phenomena in in-situ growth of InAs NW based networks by MBE, were demonstrated in this work. At first, the variability of vapor-liquid-solid growth mechanism was combined together with complex substrate preparation in order to form three distinct types of nanocrosses.

The first type was synthesized based on understanding of inclined NW growth on (001) substrates and consists from a multi-terminal WZ structure with well defined ZB segment embedded within the junction. This atypical crystal structure, provides an interesting multi-terminal platform for crystal phase alteration based quantum transport experiments. The applicability of the method is extended by showing its potential in tuning of the crystal structure within the junction by changing the energetics of the reported recrystallization processes.

The formation of two other types of presented single crystalline VLS grown nanocrosses is enabled by in-situ flux change induced modification of the NW growth direction. Given growth parameters combined with reproducible substrate fabrication also provide precise control over the kinking process. That gives the method a perspective of merging the kinked NWs into larger networks. The feasibility of the structures for transport experiments was demonstrated by characterization of the electronic transparency of the junctions.

The scalability issues related to the VLS growth methods were overcome by development of InAs SAG NW networks on semi-insulating substrates. The growth results were discussed in detail, mainly in relation to the NW/substrate interface, which was shown to have crucial impact on chemical potential tunability by electrostatic field effect gating. The transport properties of the NWs were improved by implementation of GaAs(Sb) buffer layer, which improves the interface quality and therefore also the response to gating and electron mobility. The potential of the SAG NWs in electron transport experiments was demonstrated by compatibility with as-grown fabrication and measurements directly on the growth chip.

The promising properties of the SAG buffered NW networks were further confirmed by showing efficient chemical potential tunability, long electron coherence length, strong spin-orbit coupling and compatibility with semiconductor/superconductor hybrid epitaxy, which are comparable to typically used single VLS NWs. These properties combined with the scalability of the SAG growth method satisfy the basic requirements for utilization of the material in state of the art Majorana fermion based transport experiments. That makes SAG NW networks a promising candidate for the main material supporting the quest for realization of topological quantum computing.



A. Substrate fabrication recipes

Summary of growth substrate fabrication recipes, which yielded successful results.

A.1 Au pre-patterned (001) InAs and InP substrates with SiO_x mask

Wafer

- (001) undoped (Un) InAs or InP, single side polished (SS), 500 μm thickness, WaferTech LTD
- Cleaved into quarters of a 2" wafer for processing

Mask deposition

- E-gun evaporation of SiO_x : 70 nm thickness at rate of 4 $\text{\AA}/\text{s}$

EBL exposure - Elionix ELS-7000

- Resist: MMA \sim 180 nm + PMMA \sim 60 nm
- Spinning: 4000 RPM for 45 s
- Baking: 1 min at 115°C for MMA + 2 min at 185°C after PPMA
- Exposure: based on single shot/dot exposure (constant 5 nm dot size)
 - Design - Raith Eline software
 - Write field size: 60 000 dots, 300 μm
 - Current: 500 pA
 - Aperture: 40 μm
 - Alignment to quarter edge - see chapter 4
 - Dose time: from 10 to 250 $\mu\text{s}/\text{dot}$

- Area dose: 20000 to 500000 $\mu\text{C}/\text{cm}^2$
- Manual beam defocus: 0, 15, 30 μm
- Resulting dot diameter: ~ 40 to 300 nm (See chapter 4 for details)
- Development: 60 s 1:3 MIBK:IPA, 15 s IPA
- Oxygen plasma ashing

Mask wet etch

- 1:1 HF:H₂O, 8 s

Metalization - AJA evaporation system

- RF milling: 25 W, 6 mTorr Ar pressure, 8 min
- Au evaporation: 6 nm at rate of 1 $\text{\AA}/\text{s}$
- Lift-off: 1 hour in 50°C acetone, 15 s acetone, 15 s IPA, 15+15 s H₂O
- Oxygen plasma ashing

A.2 Au pre-patterned (111)B InAs substrates Al₂O_x mask

Wafer

- (111)B undoped (Un) InAs, single side polished (SS), 500 μm thickness, WaferTech LTD.
- Cleaved into single quarters of a 2" wafer for processing

Mask deposition

- ALD Al₂O_x growth
 - Temperature: 200°C
 - Cycle time: 3 s
 - Number of cycles: 100

EBL exposure - Elionix ELS-7000

- Resist: MMA \sim 180 nm + PMMA \sim 60 nm
- Spinning: 4000 RPM for 45 s
- Baking: 1 min at 115°C for MMA + 2 min at 185°C after PPMA
- Exposure: based on single shot/dot exposure (constant 5 nm dot size)
 - Design - Raith Eline software
 - Write field size: 60000 dots / 300 μm
 - Current: 500 pA
 - Aperture: 40 μm
 - Alignment to quarter edge
 - Dose time: from 10 to 250 $\mu\text{s/dot}$
 - Area dose: 20000 to 500000 $\mu\text{s/cm}^2$
 - Manual beam defocus: 0, 15, 30 μm
 - Resulting dot diameter: \sim 40 to 300 nm
- Development: 60 s 1:3 MIBK:IPA, 15 s IPA
- Oxygen plasma ashing

Mask wet etch

- 160 s, 50° Transene D, 5 s 50°C H₂O, 15+15 s H₂O

Metalization - AJA evaporation system

- RF milling: 15 W, 18 mTorr Ar pressure, 2 min (note: the growth did not significantly depend on this step)
- Au evaporation: 10 nm at rate of 1 \AA/s
- Lift-off: 1 hour in 50°C acetone, 15 s acetone, 15 s IPA, 15+15 s H₂O

- Oxygen plasma ashing

A.3 SAG substrate fabrication

Wafer

- (001) FE-doped InP or (001) undoped (GaAs), single side polished (SS), 500 μm thickness, InP from Semiconductor Wafer, Inc. and GaAs from WaferTech LTD.
- 2" wafer processing

Mask deposition

- PECVD growth in SPTS Multiples system - done at Danish Technical University by Karthik Jambunathan and Robert McNeil.
 - Recipe: Standard HF SiO_2
 - Temperature: 300°C
 - Thickness: 10 nm

EBL exposure - Elionix ELS-7000

- Resist: MMA \sim 300 nm
- Spinning: 4000 RPM for 45 s
- Baking: 2 min at 185°C
- Exposure, fine features: nanowires, alignment marks etc.
 - Design - proximity error correction used in BEAMER software²²²
 - Write field size: 60000 dots / 300 μm
 - Current: 500 pA
 - Aperture: 40 μm
 - Alignment to major flat
 - Dose time: 0.19 $\mu\text{s}/\text{dot}$
 - Area dose: 380 $\mu\text{C}/\text{cm}^2$
- Exposure, rough features: cleave markers, orientation markers etc.
 - Design - proximity error correction used in BEAMER software²²²
 - Write field size: 20000 dots / 600 μm
 - Current: 20 nA
 - Aperture: 120 μm
 - Dose time: 0.27 $\mu\text{s}/\text{dot}$
 - Area dose: 600 $\mu\text{C}/\text{cm}^2$
- Development: 45 s 1:3 MIBK:IPA, 30 s IPA
- Oxygen plasma ashing

Mask wet etch

- Resist reflow: 121°C for 30 s

- Predip: 5 s IPA, 10 s H₂O drag up and down to clear the visible IPA from surface
- 3 s without transfer in buffered HF (ammonium fluoride and HF solution)
- Afterdip: 10 s + 20 s H₂O and straight to acetone without drying

Cleaning procedure

- acetone for 5 min after etching step
- Sonication: 20 s, 80 Hz, 30% power
- transfer to clean acetone and repeat sonication step (sonicate tweezer in acetone)
- rinse for 15 s in IPA
- transfer to clean IPA and repeat sonication step (sonicate tweezer in IPA)
- rinse for 15 s in H₂O
- transfer to clean H₂O and repeat sonication step (sonicate tweezer in H₂O)
- wash surfec under flowing H₂O
- Oxygen plasma ashing

Cleave of 2" wafer into quarters



B. Growth recipes

Summary of growth recipes, which yielded successful results. The given temperatures correspond to pyrometer measurements with 0.68 emissivity.

B.1 Growth recipe for inclined nanocrosses

Wafer

- prepared as summarized in A.1

Loading

- 5 s dip in 1:20 mixture of HF:H₂O
- 2 hours at 200°C in on trolley load-lock
- 1 hours at 250°C oh heated station in buffer chamber

Growth: Varian GEN II MBE with 10 RPM substrate rotation

- Anneal
 - 490°C for 2 minutes under 10^{-5} Torr As₂ overpressure for 2 minutes
 - ramp down
 - 475°C for 8 minutes under 10^{-5} Torr As₂ overpressure for 8 minutes
 - Cooldown to growth temperature
- Growth
 - Substrate temperature: 410°C
 - Typical growth time: 30 minutes with growth rate spread from 0 to 400 nm/min
 - In flux: $4.3 \cdot 10^{18}$ atoms/m²

- As₂ flux: $8.5 \cdot 10^{19}$ atoms/m²
- V/III ratio: ~ 20
- Corresponding planar growth rate: $\sim 0.7 \mu/h$
- Cooldown under As flux
- Unloading

B.2 Growth recipe for kinked nanocrosses

Wafer - prepared as summarized in A.2

Loading

- 2 s dip in 1:20 mixture of HF:H₂O
- 2 hours at 200°C in on trolley load-lock
- 1 hours at 250°C oh heated station in buffer chamber

Growth: Varian GEN II MBE with 10 RPM substrate rotation

- Anneal
 - 540°C for 10 minutes under 10^{-5} Torr As₄ overpressure for 2 minutes
 - ramp down
 - Cooldown to growth temperature
- Stem growth
 - Substrate temperature: 420°C
 - NW growth rate: 200 nm/min for 100 nm catalyst diameter
 - In flux: $4.3 \cdot 10^{18}$ atoms/m²
 - As₄ flux: $2 \cdot 10^{19}$ atoms/m²
 - V/III ratio ~ 10
 - Corresponding planar growth rate $\sim 0.7 \mu\text{/h}$
- Pause: 2 minutes
- Kinking step
 - Substrate temperature: 420°C
 - Time: 5 - 15 s
 - Ga flux: $4.1 \cdot 10^{18}$ atoms/m²
 - As₄ flux: $2 \cdot 10^{19}$ atoms/m²
 - V/III ratio ~ 5
 - Corresponding planar growth rate: $\sim 0.16 \text{ nm/s}$
- Pause: 1 minute
- Kink growth
 - Substrate temperature: 420°C
 - NW growth rate: $\sim 330 \text{ nm/min}$ - catalyst diameter between 100 and 200 nm
 - In flux: linear reduction from $4.3 \cdot 10^{18}$ to $3.6 \cdot 10^{18}$ atoms/m² per 5 minutes
 - As₄ flux: linear reduction from 2 to $1.75 \cdot 10^{19}$ atoms/m²
 - V/III ratio ~ 5
 - Corresponding planar growth rate: ~ 0.7 linearly reduced to $0.6 \mu\text{m/h}$
- Cooldown under As flux

B.3 Growth recipe for SAG on InP wafers

Wafer

- prepared as summarized in A.3

Loading

- 2 hours at 200°C in on trolley load-lock
- 1 hours at 250°C oh heated station in buffer chamber

Growth: Varian GEN II MBE with 10 RPM substrate rotation

- Anneal
 - 530°C for 3 minutes under 10^{-5} Torr As₂ overpressure for 2 minutes
 - ramp down
 - Cooldown to growth temperature
- InAs SAG growth
 - Substrate temperature: 510°C
 - Time: typically 20 minutes for presented results
 - In flux: $6.3 \cdot 10^{17}$ atoms/m²
 - As₂ flux: $6.7 \cdot 10^{18}$ atoms/m²
 - V/III ratio: ~ 10
 - Corresponding planar growth rate: $\sim 0.1 \mu/h$
- Cooldown under As overpressure
- Al deposition - no rotation, no As overpressure
 - Substrate temperature: -37°C (thermocouple)
 - Time: 100 seconds
 - Al flux: $1.3 \cdot 10^{19}$ atoms/m²
 - Corresponding Al thickness: ~ 4 nm planar and 7 nm on NW facet due to deposition geometry
- Unloading from the system without warming up
- Exposure to atmosphere
- Drying and removal of condensed watter by nitrogen blow off

B.4 Growth recipe for buffered SAG on GaAs wafers

Wafer

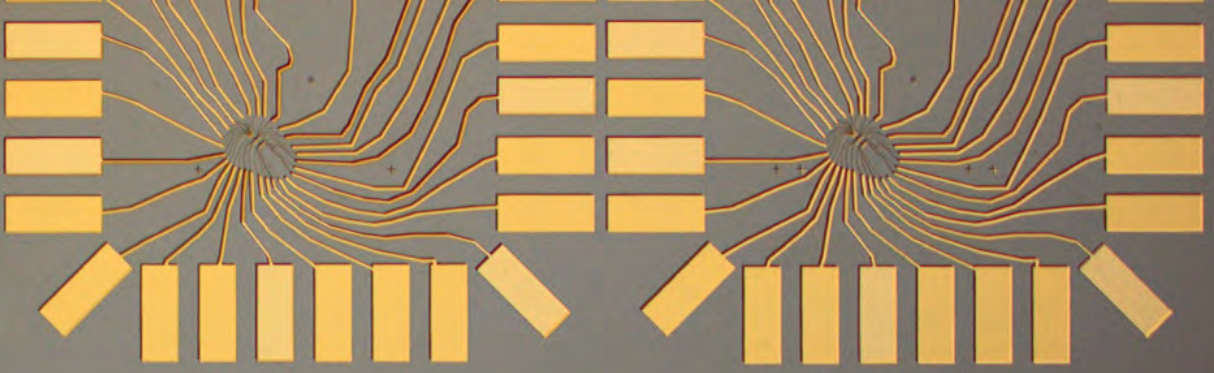
- prepared as summarized in A.3

Loading

- 2 hours at 200°C in on trolley load-lock
- 1 hours at 250°C oh heated station in buffer chamber

Growth: Varian GEN II MBE with 10 RPM substrate rotation

- Anneal
 - 630°C for 1 minutes under 10^{-5} Torr As_2 overpressure for 2 minutes
 - ramp down
 - Cooldown to growth temperature
- GaAs(Sb) buffer growth
 - Substrate temperature: 615°C
 - Time: typically 30 minutes for presented results
 - Ga flux: $8.2 \cdot 10^{17}$ atoms/m²
 - As_2 flux: $1.4 \cdot 10^{19}$ atoms/m²
 - Sb_{2+4} flux: $2.7 \cdot 10^{18}$ atoms/m²
 - V/III ratio: ~ 20
 - $\text{As}_2/\text{Sb}_{2+4}$ ratio: ~ 7
 - Corresponding planar growth rate: $\sim 0.1 \mu/\text{h}$
- Cooldown under As overpressure to InAs growth temperature: 3 minutes
- InAs SAG growth
 - Substrate temperature: 510°C
 - Time: typically 30 minutes for presented results
 - In flux: $6.3 \cdot 10^{17}$ atoms/m²
 - As_2 flux: $8.3 \cdot 10^{18}$ atoms/m²
 - V/III ratio: ~ 10
 - Corresponding planar growth rate: $\sim 0.1 \mu/\text{h}$
- Cooldown under As overpressure



C. Device fabrication

A general device fabrication recipe for contacting InAs SAG and VLS NWs.

Chip

- VLS nanowires
 - Material: 5 mm x 5 mm piece of Si with 200 nm of thermal SiO₂
 - Pre-patterned with Au/Ti bonding pads, meanders, large outer alignment marks (for exposure alignment) and small inner alignment marks (for taking positioned images, explained bellow)
- SAG nanowires
 - The growth chip itself is cleaved into 4 mm x 4 mm chips which are suitable for low-temperature measurements
 - Alignment marks are pre-patterned before growth and are grown together with NWs
 - Bonding pads, meanders and secondary sets of Au/Ti alignment marks are exposed together with contacts and gates

Nanowire transfer and positioned imaging only for VLS nanowires

- Oxygen plasma ashing of the blank chip
- NW transfer by optical mechanical micromanipulator on blank chips (shown in Chapter 4)
- Positioned imaging of transferred NWs using Raith Elne SEM: taken images include inner alignment marks on the blank chip, which are designed to fit into 25x25 μm field of view and located around the NWs.
- Overlaying of the positioned SEM imaging to the design

- Designing of the devices

EBL exposure: contact step - Elionix ELS-7000

- Resist: PMMA \sim 420 nm
- Spinning: 4000 RPM for 45 s
- Baking: 2 min at 185°C
- Exposure: fine features, e.g. inner parts of the contacts, side gates fine alignment marks
 - Design: proximity error correction used in BEAMER software²²²
 - Write field size: 60000 dots / 300 μ m
 - Current: 500 pA
 - Aperture: 40 μ m
 - Alignment
 - Dose time VLS: 0.525 μ s
 - Area dose VLS: 1050 μ C/cm²
 - Dose time SAG: 0.39 μ s
 - Area dose SAG: 780 μ C/cm²
- Exposure: rough features, e.g. outer parts of contacts, various markers, bonding pads
 - Design: proximity error correction used in BEAMER software²²²
 - Write field size: 20000 dots / 600 μ m
 - Current: 20 nA
 - Aperture: 120 μ m
 - Alignment
 - Dose time VLS: 0.472 μ s
 - Area dose VLS: 1050 μ C/cm²
 - Dose time SAG: 0.351 μ s
 - Area dose SAG: 780 μ C/cm²
- Development: 45 s 1:3 MIBK:IPA, 15 s IPA
- Oxygen plasma ashing

Metalization: contacts - AJA evaporation system

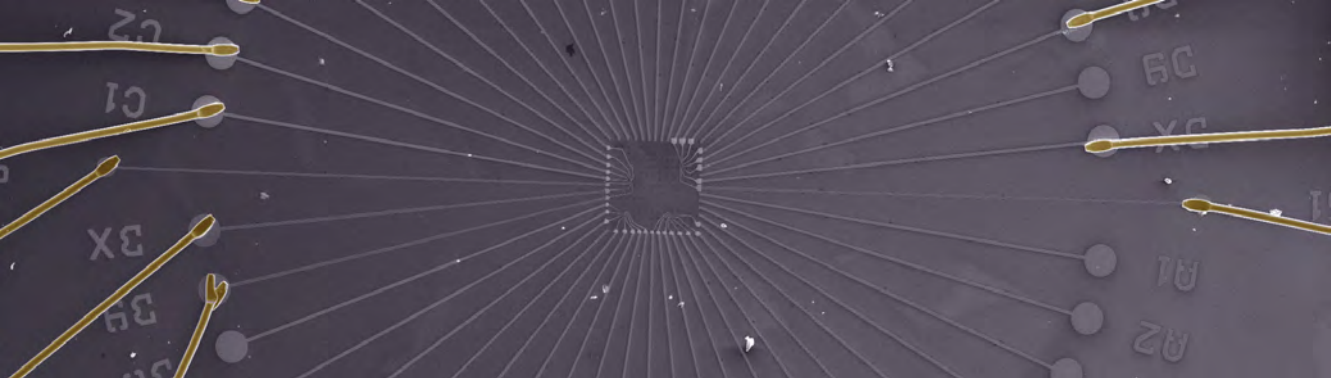
- Covering chip edges with Al foil before loading
- RF milling for native oxide removal: 15 W, 8 mTorr Ar pressure, 5 minutes
- Ti sticking layer evaporation: 5 nm at rate of 0.5 \AA /s
- Au evaporation: 180 nm for SAG and 300 nm for VLS at rate of 4 \AA /s
- Lift-off: 30 minutes in 50°C acetone, 15 s acetone, 15 sec IPA, 15+15 sec H₂O
- Oxygen plasma ashing

Top-gate fabrication when required

- ALD HfO_x growth
 - Temperature: 90°C
 - Cycle time: 180 s
 - Number of cycles: 70
 - Note: bonding to bonding pads is unaffected by the presence of the ALD layer on the whole chip.
- EBL exposure: gates
 - same as for contacts with dose increase of 10%
 - Repeat whole metalization step, but skip RF milling during metalization process

Bond to board

Load and measure: special attention needs to be given to keep chip grounding while handling VLS nanocrosses



List of Figures

1.1	Schematics of a Majorana braiding experiment	23
1.2	Schematics of a Varian GEN II MBE chamber	26
1.3	Group V flux calibration	28
1.4	Thermodynamical phases in MBE growth	30
1.5	Kinetic state transitions	31
1.6	Wulff construction	33
1.7	Growth modes in MBE	34
1.8	Schematics of VLS NW growth	39
1.9	Overview of phase transitions occurring during VLS growth	40
1.10	ZB and WZ structure models	42
1.11	TEM micrograph of stacking faults in WZ VLS nanowire	43
1.12	SEM micrograph of a pre-patterned substrate and growth on the same substrate	44

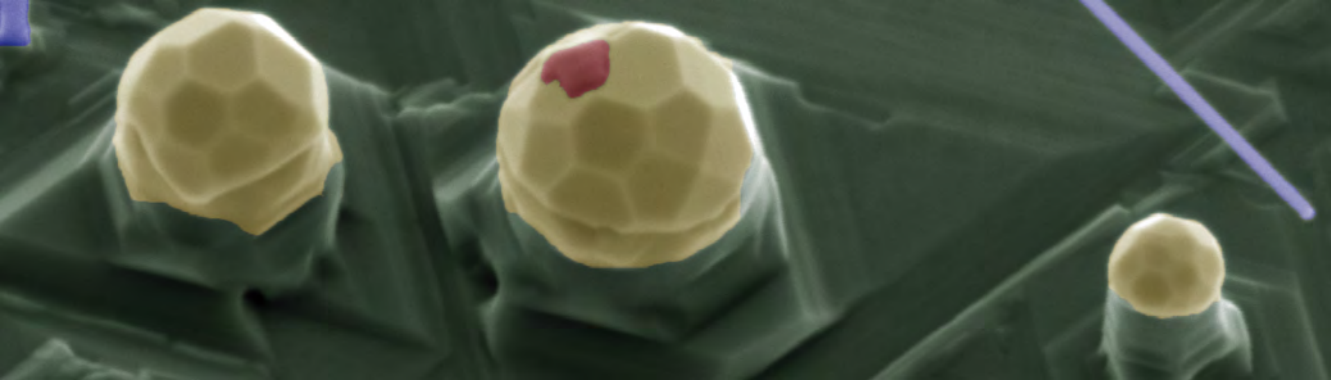
1.13	SEM overview of impact of catalyst volume on VLS NW growth	45
1.14	SEM micrograph of two different NW families grown on (100) substrate . . .	47
1.15	SEM micrograph of SAG NWs	47
1.16	Schematics of branched NW growth methods reported by Dick. et al.	49
1.17	Schematics of NW growth method reported by Dalacu et al.	50
1.18	Schematics of directional superconductor epitaxy	52
2.1	VLS nanocrosses	54
2.2	Schematics of standard VLS NW preparation process	55
2.3	Masked substrate preparation for VLS NW growth	56
2.4	Nanocross based device schematics	59
2.5	Overview of NW nucleation on (001 substrates)	61
2.6	AFM analysis of patterned (001) InAs substrate after oxide annealing step . .	62
2.7	Surface evolution during growth on (001) InAs	63
2.8	Nanoparticle migration during growth on (001) InAs	64
2.9	Catalyst pitch dependent growth on (001) substrates	65
2.10	Catalyst pitch dependent growth on (001) substrates	67
2.11	Growth of inclined nanocrosses on InP (001) substrates	69
2.12	Kinking the NW growth direction	71
2.13	Kinking the NW growth at the same height	72
2.14	Structure of the kinked NWs	73
2.15	Kinked planar nanocrosses	74
2.16	Kinked vertical nanocrosses	75
2.17	Crystal structure of inclined nanocross junctions	77
2.18	High temperature grown InAs inclined nanocrosses	78

2.19	Crystal structure of kinked planar nanocross junctions	80
2.20	Crystal structure of kinked vertical nanocross junctions	80
2.21	Transparency of nanocross junctions	82
2.22	Crystal phase quantum dots within inclined nanocrosses	84
2.23	Scaling up kinked NWs into NW networks	86
2.24	Shadowing of SU/SE hybrid NWs	87
2.25	Controlled growth of inclined nanocrosses	89
3.1	SAG symmetries and buffered growth	92
3.2	Schematics of SAG sample processing	93
3.3	Schematics of SAG four-probe device	97
3.4	Geometry of the SAG device capacitance model	98
3.5	Field effect mobility fit	99
3.6	Growth mask selectivity	102
3.7	Single SAG non-buffered NWs SEM	103
3.8	Dependency of SAG growth on substrate orientation	104
3.9	Nanowire symmetries on (001) substrate	104
3.10	Crosssection of non-buffered [100] NW.	105
3.11	Undergrown and overgrown non-buffered SAG NWs	106
3.12	SEM micrographs of SAG NW networks	107
3.13	SEM micrographs of GaAs(Sb) buffer growth with and without Sb	109
3.14	Overgrowth and top-facet deposition of InAs on the SAG buffer NWs	110
3.15	TEM characterization of SAG NW grown on top of GaAs buffer layer	111
3.16	Initial growth stage of buffered SAG NWs	113
3.17	Formation of buffered SAG NW junctions	115

3.18	Cross-sections of buffered NWs	117
3.19	InAs/InP interface	118
3.20	InAs/GaAs(Sb) interface	119
3.21	Field effect mobility device	120
3.22	Gating of non-buffered and buffered NWs	121
3.23	Gating of non-buffered and buffered NWs	122
3.24	SAG loop devices and AB oscillations	124
3.25	Analysis of AB oscillations	125
3.26	Analysis WAL	126
3.27	Superconductor deposition on SAG NWs	127
3.28	Hybrid NW shadowing for SAG substrates	130
4.1	Scheme of defocused exposure in EBL system	133
4.2	Scheme of alignment of pattern and design during EBL	134
4.3	Dependency of wet etch profile based on crystal misalignment reported by Wang et al.	135
4.4	Wet etching of (111)B facets on InAs substrates	136
4.5	EBL process on substrates with wet etched structures	137
4.6	SEM of result and scheme of fabrication process of substrates for SAG	139
4.7	AFM analysis of SAG mask roughness	140
4.8	Methods to improve line thickness and edge roughening in SAG substrate fabrication	141
4.9	Micromanipulator for VLS NW deposition	142
4.10	Deposition of VLS nanocrosses	143
4.11	Blank chips and gentle lift-off method	145
4.12	Fabrication on kinked planar nanocrosses	146

4.13	Controlled VLS nanocross transfer	147
4.14	Loading of bonded chip into measurement system	148
4.15	Fabrication on SAG NWs	149

*



Bibliography

1. Balasubramanian, G. *Advances in Nanomaterials* (2018) (cit. on p. 17).
2. Del Alamo, J. A. Nanometre-scale electronics with III–V compound semiconductors. *Nature* **479**, 317 (2011) (cit. on pp. 17, 18).
3. Moore, G. E. *Lithography and the future of Moore's law in Integrated Circuit Metrology, Inspection, and Process Control IX* **2439** (1995), 2–18 (cit. on p. 17).
4. Feynman, R. P. Quantum mechanical computers. *Foundations of physics* **16**, 507–531 (1986) (cit. on p. 17).
5. DiVincenzo, D. P. The physical implementation of quantum computation. *Fortschritte der Physik: Progress of Physics* **48**, 771–783 (2000) (cit. on p. 17).
6. Harrow, A. W. & Montanaro, A. Quantum computational supremacy. *Nature* **549**, 203 (2017) (cit. on p. 17).
7. Aspuru-Guzik, A., Dutoi, A. D., Love, P. J. & Head-Gordon, M. Simulated quantum computation of molecular energies. *Science* **309**, 1704–1707 (2005) (cit. on p. 17).
8. Bernstein, D. J. in *Post-quantum cryptography* 1–14 (Springer, 2009) (cit. on p. 17).
9. Kahn, J. IBM Taps Samsung, JP Morgan, Daimler in Quantum Computing Push. *Bloomberg Technology* (2017) (cit. on p. 17).
10. Waters, R. Microsoft and Google prepare for big leaps in quantum computing. *Financial Times* (2018) (cit. on p. 17).

11. O'Brien, J. L. Optical quantum computing. *Science* **318**, 1567–1570 (2007) (cit. on p. 17).
12. Neill, C *et al.* A blueprint for demonstrating quantum supremacy with superconducting qubits. *Science* **360**, 195–199 (2018) (cit. on p. 17).
13. Larsen, T. W. *et al.* Semiconductor-nanowire-based superconducting qubit. *Physical review letters* **115**, 127001 (2015) (cit. on pp. 17, 53, 86).
14. Veldhorst, M, Eenink, H., Yang, C. & Dzurak, A. Silicon CMOS architecture for a spin-based quantum computer. *Nature communications* **8**, 1766 (2017) (cit. on p. 17).
15. Stern, A. & Lindner, N. H. Topological quantum computation—from basic concepts to first experiments. *Science* **339**, 1179–1184 (2013) (cit. on p. 17).
16. Sarma, S. D., Freedman, M. & Nayak, C. Majorana zero modes and topological quantum computation. *npj Quantum Information* **1**, 15001 (2015) (cit. on p. 18).
17. Lutchyn, R. *et al.* Majorana zero modes in superconductor–semiconductor heterostructures. *Nature Reviews Materials*, 1 (2018) (cit. on p. 18).
18. Wagner, R. & Ellis, W. Vapor-liquid-solid mechanism of single crystal growth. *Applied Physics Letters* **4**, 89–90 (1964) (cit. on pp. 18, 38, 59).
19. Joyce, B. D. & Bradley, J. A. *Nature (London)* **195** (1962) (cit. on pp. 18, 47, 91).
20. Shaw, D. W. Effects of vapor composition on the growth rates of faceted gallium arsenide hole deposits. *Journal of The Electrochemical Society* **115**, 777–780 (1968) (cit. on p. 18).
21. Cui, Y., Lauhon, L. J., Gudiksen, M. S., Wang, J. & Lieber, C. M. Diameter-controlled synthesis of single-crystal silicon nanowires. *Applied Physics Letters* **78**, 2214–2216 (2001) (cit. on p. 18).
22. Cui, J. Zinc oxide nanowires. *Materials Characterization* **64**, 43–52 (2012) (cit. on p. 18).
23. Yu, H *et al.* in *Semiconductor Nanowires* 29–69 (Elsevier, 2015) (cit. on p. 18).
24. Hsiao, C. *et al.* Quaternary ZnCdSeTe Nanowires. *Journal of nanoscience and nanotechnology* **10**, 798–802 (2010) (cit. on p. 18).
25. Royo, M., De Luca, M., Rurali, R. & Zardo, I. A review on III–V core–multishell nanowires: growth, properties, and applications. *Journal of Physics D: Applied Physics* **50**, 143001 (2017) (cit. on p. 18).
26. Lu, W. & Lieber, C. M. Semiconductor nanowires. *Journal of Physics D: Applied Physics* **39**, R387 (2006) (cit. on p. 18).

27. Dasgupta, N. P. *et al.* 25th anniversary article: semiconductor nanowires—synthesis, characterization, and applications. *Advanced materials* **26**, 2137–2184 (2014) (cit. on p. 18).
28. Patolsky, F. & Lieber, C. M. Nanowire nanosensors. *Materials today* **8**, 20–28 (2005) (cit. on p. 18).
29. Eaton, S. W., Fu, A., Wong, A. B., Ning, C.-Z. & Yang, P. Semiconductor nanowire lasers. *Nature Reviews Materials* **1**, 16028 (2016) (cit. on p. 18).
30. Krogstrup, P. *et al.* Single-nanowire solar cells beyond the Shockley–Queisser limit. *Nature Photonics* **7**, 306 (2013) (cit. on p. 18).
31. Yao, J. *et al.* Nanowire nanocomputer as a finite-state machine. *Proceedings of the National Academy of Sciences* **111**, 2431–2435 (2014) (cit. on p. 18).
32. Dayeh, S. A. *et al.* High electron mobility InAs nanowire field-effect transistors. *Small* **3**, 326–332 (2007) (cit. on p. 18).
33. Gül, Ö. *et al.* Towards high mobility InSb nanowire devices. *Nanotechnology* **26**, 215202 (2015) (cit. on pp. 18, 49, 98).
34. Furthmeier, S. *et al.* Enhanced spin–orbit coupling in core/shell nanowires. *Nature communications* **7**, 12413 (2016) (cit. on p. 18).
35. Hernández, S. E. *et al.* Spin-orbit coupling and phase coherence in InAs nanowires. *Physical Review B* **82**, 235303 (2010) (cit. on pp. 18, 21, 127).
36. Takase, K, Ashikawa, Y, Zhang, G, Tateno, K & Sasaki, S. Highly gate-tuneable Rashba spin-orbit interaction in a gate-all-around InAs nanowire metal-oxide-semiconductor field-effect transistor. *Scientific Reports* **7**, 930 (2017) (cit. on p. 18).
37. Mourik, V. *et al.* Signatures of Majorana fermions in hybrid superconductor-semiconductor nanowire devices. *Science* **336**, 1003–1007 (2012) (cit. on pp. 18, 21, 22, 49, 51, 53).
38. Casparis, L. *et al.* Gate-mon benchmarking and two-qubit operations. *Physical review letters* **116**, 150505 (2016) (cit. on pp. 18, 128).
39. Kitaev, A. Y. Unpaired Majorana fermions in quantum wires. *Physics-Uspekhi* **44**, 131 (2001) (cit. on pp. 18, 21, 22).
40. Lutchyn, R. M., Sau, J. D. & Sarma, S. D. Majorana fermions and a topological phase transition in semiconductor-superconductor heterostructures. *Physical review letters* **105**, 077001 (2010) (cit. on pp. 18, 22).
41. Oreg, Y., Refael, G. & von Oppen, F. Helical liquids and Majorana bound states in quantum wires. *Physical review letters* **105**, 177002 (2010) (cit. on pp. 18, 22).

42. Aasen, D. *et al.* Milestones toward Majorana-based quantum computing. *Physical Review X* **6**, 031016 (2016) (cit. on pp. 18, 22, 23, 83).
43. Thelander, C. *et al.* Electron transport in InAs nanowires and heterostructure nanowire devices. *Solid State Communications* **131**, 573–579 (2004) (cit. on pp. 21, 53).
44. Hu, Y. *et al.* A Ge/Si heterostructure nanowire-based double quantum dot with integrated charge sensor. *Nature nanotechnology* **2**, 622 (2007) (cit. on p. 21).
45. Kretinin, A. V. *et al.* Spin -1/2 Kondo effect in an InAs nanowire quantum dot: Unitary limit, conductance scaling, and Zeeman splitting. *Physical Review B* **84**, 245316 (2011) (cit. on p. 21).
46. Pfund, A, Shorubalko, I, Leturcq, R & Ensslin, K. Top-gate defined double quantum dots in InAs nanowires. *Applied physics letters* **89**, 252106 (2006) (cit. on p. 21).
47. Nilsson, H. A. *et al.* Giant, level-dependent g factors in InSb nanowire quantum dots. *Nano letters* **9**, 3151–3156 (2009) (cit. on p. 21).
48. Fauth, C., Fuhrer, A., Samuelson, L., Golovach, V. N. & Loss, D. Direct measurement of the spin-orbit interaction in a two-electron InAs nanowire quantum dot. *Physical review letters* **98**, 266801 (2007) (cit. on p. 21).
49. Nadj-Perge, S, Frolov, S., Bakkers, E. & Kouwenhoven, L. P. Spin–orbit qubit in a semiconductor nanowire. *Nature* **468**, 1084 (2010) (cit. on p. 21).
50. Majorana, E. Teoria simmetrica dell’elettrone e del positrone. *Il Nuovo Cimento (1924-1942)* **14**, 171 (1937) (cit. on p. 21).
51. Dirac, P. A. *The quantum theory of the electron* in *Proc. R. Soc. Lond. A* **117** (1928), 610–624 (cit. on p. 21).
52. Alicea, J., Oreg, Y., Refael, G., Von Oppen, F. & Fisher, M. P. Non-Abelian statistics and topological quantum information processing in 1D wire networks. *Nature Physics* **7**, 412 (2011) (cit. on pp. 22, 23).
53. Krogstrup, P *et al.* Epitaxy of semiconductor–superconductor nanowires. *Nature materials* **14**, 400 (2015) (cit. on pp. 22, 51, 86, 127, 129).
54. Chang, W *et al.* Hard gap in epitaxial semiconductor–superconductor nanowires. *Nature nanotechnology* **10**, 232 (2015) (cit. on pp. 22, 51, 128).
55. Gul, O. *et al.* Hard superconducting gap in InSb nanowires. *Nano letters* **17**, 2690–2696 (2017) (cit. on p. 22).
56. Deng, M. *et al.* Anomalous zero-bias conductance peak in a Nb–InSb nanowire–Nb hybrid device. *Nano letters* **12**, 6414–6419 (2012) (cit. on p. 22).

57. Deng, M. *et al.* Majorana bound state in a coupled quantum-dot hybrid-nanowire system. *Science* **354**, 1557–1562 (2016) (cit. on pp. 22, 49, 53, 86).
58. Albrecht, S. M. *et al.* Exponential protection of zero modes in Majorana islands. *Nature* **531**, 206 (2016) (cit. on pp. 22, 86, 128, 142).
59. Gül, Ö. *et al.* Ballistic Majorana nanowire devices. *Nature nanotechnology*, 1 (2018) (cit. on p. 22).
60. Clarke, D. J., Sau, J. D. & Tewari, S. Majorana fermion exchange in quasi-one-dimensional networks. *Physical Review B* **84**, 035120 (2011) (cit. on p. 23).
61. Sau, J. D., Clarke, D. J. & Tewari, S. Controlling non-Abelian statistics of Majorana fermions in semiconductor nanowires. *Physical Review B* **84**, 094505 (2011) (cit. on p. 23).
62. Karzig, T. *et al.* Scalable designs for quasiparticle-poisoning-protected topological quantum computation with Majorana zero modes. *Physical Review B* **95**, 235305 (2017) (cit. on pp. 23, 85).
63. Rudolph, P & Jurisch, M. Bulk growth of GaAs: An overview. *Journal of crystal growth* **198**, 325–335 (1999) (cit. on p. 24).
64. Greenaway, A. L., Boucher, J. W., Oener, S. Z., Funch, C. J. & Boettcher, S. W. Low-Cost Approaches to III–V Semiconductor Growth for Photovoltaic Applications. *ACS Energy Letters* **2**, 2270–2282 (2017) (cit. on p. 24).
65. Ihn, T. *Semiconductor Nanostructures: Quantum states and electronic transport* (Oxford University Press, 2010) (cit. on pp. 25, 83, 123, 125).
66. Webpage: faebianbastiman.files.wordpress.com (17.3.2018) (cit. on p. 26).
67. Sugaya, T., Nakagawa, T., Sugiyama, Y., Tanuma, Y. & Yonei, K. Difference in Diffusion Length of Ga Atoms under As₂ and As₄ Flux in Molecular Beam Epitaxy. *Japanese journal of applied physics* **36**, 5670 (1997) (cit. on p. 29).
68. Gilfert, C, Pavelescu, E.-M. & Reithmaier, J. Influence of the As₂/As₄ growth modes on the formation of quantum dot-like InAs islands grown on InAlGaAs/InP (100). *Applied Physics Letters* **96**, 191903 (2010) (cit. on p. 29).
69. Holmes, D. *et al.* Differences between As₂ and As₄ in the homoepitaxial growth of GaAs (110) by molecular beam epitaxy. *Applied physics letters* **67**, 2848–2850 (1995) (cit. on p. 29).
70. Sartel, C, Dheeraj, D. L., Jabeen, F & Harmand, J.-C. Effect of arsenic species on the kinetics of GaAs nanowires growth by molecular beam epitaxy. *Journal of Crystal Growth* **312**, 2073–2077 (2010) (cit. on p. 29).

71. Kuech, T. F., Babcock, S. E. & Mawst, L. Growth far from equilibrium: Examples from III-V semiconductors. *Applied Physics Reviews* **3**, 040801 (2016) (cit. on p. 29).
72. Krogstrup, P. *et al.* Advances in the theory of III–V nanowire growth dynamics. *Journal of Physics D: Applied Physics* **46**, 313001 (2013) (cit. on pp. 29, 32, 36, 40, 73, 116).
73. Tran, R. *et al.* Surface energies of elemental crystals. *Scientific data* **3**, 160080 (2016) (cit. on p. 32).
74. Barmparis, G. D., Lodziana, Z., Lopez, N. & Remediakis, I. N. Nanoparticle shapes by using Wulff constructions and first-principles calculations. *Beilstein journal of nanotechnology* **6**, 361 (2015) (cit. on p. 32).
75. Kangawa, Y., Akiyama, T., Ito, T., Shiraishi, K. & Nakayama, T. Surface stability and growth kinetics of compound semiconductors: An ab initio-based approach. *Materials* **6**, 3309–3360 (2013) (cit. on pp. 32, 33).
76. Tellier, C., Huve, G & Leblois, T. Anisotropic Chemical Etching of III—V Crystals Dissolution Slowness Surface and Application to GaAs. *Active and passive electronic components* **27**, 133–154 (2004) (cit. on p. 32).
77. Ranke, W & Jacobi, K. Structure and reactivity of GaAs surfaces. *Progress in Surface Science* **10**, 1–52 (1981) (cit. on p. 32).
78. Sun, Q., Yerino, C. D., Leung, B., Han, J. & Coltrin, M. E. Understanding and controlling heteroepitaxy with the kinetic Wulff plot: A case study with GaN. *Journal of Applied Physics* **110**, 053517 (2011) (cit. on p. 33).
79. Tsao, J. Y. *Materials fundamentals of molecular beam epitaxy* (Academic Press, 2012) (cit. on p. 34).
80. Grabow, M. H. & Gilmer, G. H. Thin film growth modes, wetting and cluster nucleation. *Surface science* **194**, 333–346 (1988) (cit. on p. 34).
81. Frank, F. & Van der Merwe, J. One-dimensional dislocations. II. Misfitting monolayers and oriented overgrowth. *Proc. R. Soc. Lond. A* **198**, 216–225 (1949) (cit. on p. 34).
82. Priester, C. & Lannoo, M. Growth aspects of quantum dots. *Current Opinion in Solid State and Materials Science* **2**, 716–721 (1997) (cit. on p. 34).
83. Stranski, I. N. Zur theorie des kristallwachstums. *Zeitschrift für physikalische Chemie* **136**, 259–278 (1928) (cit. on p. 35).
84. Kossel, W. Zur theorie des kristallwachstums. *Nachrichten von der Gesellschaft der Wissenschaften zu Göttingen, Mathematisch-Physikalische Klasse* **1927**, 135–143 (1927) (cit. on p. 35).

85. Jackson, K. A. *Kinetic Processes: crystal growth, diffusion, and phase transformations in materials* (John Wiley & Sons, 2006) (cit. on pp. 35, 36).
86. Wen, C.-Y., Tersoff, J., Reuter, M., Stach, E. & Ross, F. Step-flow kinetics in nanowire growth. *Physical review letters* **105**, 195502 (2010) (cit. on p. 36).
87. Balluffi, R. W., Allen, S. & Carter, W. C. *Kinetics of materials* (John Wiley & Sons, 2005) (cit. on p. 36).
88. Madsen, M. H. *et al.* Experimental determination of adatom diffusion lengths for growth of InAs nanowires. *Journal of Crystal Growth* **364**, 16–22 (2013) (cit. on pp. 37, 44, 71).
89. Glas, F., Harmand, J.-C. & Patriarche, G. Why does wurtzite form in nanowires of III-V zinc blende semiconductors? *Physical review letters* **99**, 146101 (2007) (cit. on pp. 37, 38, 41, 59, 83).
90. Johansson, J., Svensson, C. P. T., Mårtensson, T., Samuelson, L. & Seifert, W. Mass transport model for semiconductor nanowire growth. *The Journal of Physical Chemistry B* **109**, 13567–13571 (2005) (cit. on pp. 37, 40).
91. Kolasinski, K. W. Catalytic growth of nanowires: vapor–liquid–solid, vapor–solid–solid, solution–liquid–solid and solid–liquid–solid growth. *Current Opinion in Solid State and Materials Science* **10**, 182–191 (2006) (cit. on p. 38).
92. Wojtowicz, T *et al.* MBE growth and properties of ZnTe- and CdTe-based nanowires. *Journal of the Korean Physical Society* **53**, 3055–3063 (2008) (cit. on p. 38).
93. Chou, Y.-C. *et al.* Atomic-scale variability and control of III-V nanowire growth kinetics. *Science* **343**, 281–284 (2014) (cit. on p. 38).
94. Dick, K. A. A review of nanowire growth promoted by alloys and non-alloying elements with emphasis on Au-assisted III–V nanowires. *Progress in Crystal Growth and Characterization of Materials* **54**, 138–173 (2008) (cit. on p. 38).
95. Tersoff, J. Stable self-catalyzed growth of III–V nanowires. *Nano letters* **15**, 6609–6613 (2015) (cit. on p. 38).
96. Krogstrup, P. *et al.* Impact of the liquid phase shape on the structure of III-V nanowires. *Physical review letters* **106**, 125505 (2011) (cit. on pp. 38, 41).
97. Krogstrup, P. *et al.* Junctions in axial III- V heterostructure nanowires obtained via an interchange of group III elements. *Nano letters* **9**, 3689–3693 (2009) (cit. on pp. 39, 46, 53).
98. Aagesen, M. *et al.* Molecular beam epitaxy growth of free-standing plane-parallel InAs nanoplates. *Nature nanotechnology* **2**, 761 (2007) (cit. on pp. 40, 61, 66).
99. Johansson, J. & Dick, K. A. Recent advances in semiconductor nanowire heterostructures. *CrystEngComm* **13**, 7175–7184 (2011) (cit. on p. 41).

100. Zamani, R. R., Ghalamestani, S. G., Niu, J., Sköld, N. & Dick, K. A. Polarity and growth directions in Sn-seeded GaSb nanowires. *Nanoscale* **9**, 3159–3168 (2017) (cit. on p. 41).
101. Lindberg, C. *et al.* Silver as Seed-Particle Material for GaAs Nanowires Dictating Crystal Phase and Growth Direction by Substrate Orientation. *Nano letters* **16**, 2181–2188 (2016) (cit. on p. 41).
102. Xu, H. *et al.* Defect-free <110> zinc-blende structured InAs nanowires catalyzed by palladium. *Nano letters* **12**, 5744–5749 (2012) (cit. on p. 41).
103. Wang, Y., Schmidt, V., Senz, S. & Gösele, U. Epitaxial growth of silicon nanowires using an aluminium catalyst. *Nature nanotechnology* **1**, 186 (2006) (cit. on p. 41).
104. Kriegner, D. *et al.* Unit cell structure of crystal polytypes in InAs and InSb nanowires. *Nano letters* **11**, 1483–1489 (2011) (cit. on p. 41).
105. Koguchi, M., Kakibayashi, H., Yazawa, M., Hiruma, K. & Katsuyama, T. Crystal structure change of GaAs and InAs whiskers from zinc-blende to wurtzite type. *Japanese journal of applied physics* **31**, 2061 (1992) (cit. on p. 41).
106. Galicka, M., Bukała, M., Buczko, R & Kacman, P. Modelling the structure of GaAs and InAs nanowires. *Journal of Physics: Condensed Matter* **20**, 454226 (2008) (cit. on p. 41).
107. Bukała, M *et al.* *What determines the crystal structure of nanowires?* in *AIP Conference Proceedings* **1199** (2010), 349–350 (cit. on p. 41).
108. Kretinin, A. V. *et al.* *The Kondo effect and coherent transport in stacking-faults-free wurtzite InAs nanowires* in *AIP Conference Proceedings* **1399** (2011), 327–328 (cit. on p. 41).
109. Thelander, C., Caroff, P., Plissard, S., Dey, A. W. & Dick, K. A. Effects of crystal phase mixing on the electrical properties of InAs nanowires. *Nano letters* **11**, 2424–2429 (2011) (cit. on p. 41).
110. Shimamura, K., Yuan, Z., Shimojo, F. & Nakano, A. Effects of twins on the electronic properties of GaAs. *Applied Physics Letters* **103**, 022105 (2013) (cit. on p. 41).
111. Chen, Y. *et al.* Effect of a high density of stacking faults on the Young's modulus of GaAs nanowires. *Nano letters* **16**, 1911–1916 (2016) (cit. on p. 43).
112. Kretinin, A. V., Popovitz-Biro, R., Mahalu, D. & Shtrikman, H. Multimode Fabry-Perot conductance oscillations in suspended stacking-faults-free InAs nanowires. *Nano letters* **10**, 3439–3445 (2010) (cit. on p. 43).

113. Sourribes, M. J., Isakov, I., Panfilova, M., Liu, H. & Warburton, P. A. Mobility enhancement by Sb-mediated minimisation of stacking fault density in InAs nanowires grown on silicon. *Nano letters* **14**, 1643–1650 (2014) (cit. on p. 43).
114. Nilsson, M. *et al.* Single-electron transport in InAs nanowire quantum dots formed by crystal phase engineering. *Physical Review B* **93**, 195422 (2016) (cit. on pp. 43, 82, 83).
115. De la Mata, M., Magén, C., Caroff, P. & Arbiol, J. Atomic scale strain relaxation in axial semiconductor III–V nanowire heterostructures. *Nano letters* **14**, 6614–6620 (2014) (cit. on pp. 43, 119).
116. Uccelli, E. *et al.* Three-dimensional multiple-order twinning of self-catalyzed GaAs nanowires on Si substrates. *Nano letters* **11**, 3827–3832 (2011) (cit. on pp. 43, 72).
117. Chen, W. *et al.* Incorporation and redistribution of impurities into silicon nanowires during metal-particle-assisted growth. *Nature communications* **5**, 4134 (2014) (cit. on pp. 43, 46).
118. Gomes, U., Ercolani, D., Zannier, V., Beltram, F. & Sorba, L. Controlling the diameter distribution and density of InAs nanowires grown by Au-assisted methods. *Semiconductor Science and Technology* **30**, 115012 (2015) (cit. on p. 43).
119. Dubrovskii, V. *et al.* Length distributions of Au-catalyzed and In-catalyzed InAs nanowires. *Nanotechnology* **27**, 375602 (2016) (cit. on p. 43).
120. Kashchiev, D. Dependence of the growth rate of nanowires on the nanowire diameter. *Crystal growth & design* **6**, 1154–1156 (2006) (cit. on p. 43).
121. Perez, M. Gibbs–Thomson effects in phase transformations. *Scripta materialia* **52**, 709–712 (2005) (cit. on p. 44).
122. Dubrovskii, V. *et al.* Gibbs-Thomson and diffusion-induced contributions to the growth rate of Si, InP, and GaAs nanowires. *Physical Review B* **79**, 205316 (2009) (cit. on p. 44).
123. Li, Z.-A. *et al.* Planar-defect characteristics and cross-sections of $\langle 001 \rangle$, $\langle 111 \rangle$, and $\langle 112 \rangle$ InAs nanowires. *Journal of Applied Physics* **109**, 114320 (2011) (cit. on pp. 44, 46).
124. Dalacu, D. *et al.* Selective-area vapour–liquid–solid growth of InP nanowires. *Nanotechnology* **20**, 395602 (2009) (cit. on p. 45).
125. Zi, Y., Suslov, S. & Yang, C. Understanding Self-Catalyzed Epitaxial Growth of III–V Nanowires toward Controlled Synthesis. *Nano letters* **17**, 1167–1173 (2017) (cit. on p. 46).
126. Krogstrup, P. *et al.* Structural phase control in self-catalyzed growth of GaAs nanowires on silicon (111). *Nano letters* **10**, 4475–4482 (2010) (cit. on p. 46).

127. Gomes, U. *et al.* Nucleation and growth mechanism of self-catalyzed InAs nanowires on silicon. *Nanotechnology* **27**, 255601 (2016) (cit. on p. 46).
128. Yazawa, M, Koguchi, M, Muto, A, Ozawa, M & Hiruma, K. Effect of one monolayer of surface gold atoms on the epitaxial growth of InAs nanowhiskers. *Applied Physics Letters* **61**, 2051–2053 (1992) (cit. on p. 46).
129. Fortuna, S. A. & Li, X. Metal-catalyzed semiconductor nanowires: a review on the control of growth directions. *Semiconductor Science and Technology* **25**, 024005 (2010) (cit. on p. 46).
130. Krishnamachari, U *et al.* Defect-free InP nanowires grown in [001] direction on InP (001). *Applied Physics Letters* **85**, 2077–2079 (2004) (cit. on pp. 46, 60).
131. Campos, T., Junior, P. E. F., Gmitra, M., Sipahi, G. M. & Fabian, J. Spin-orbit coupling effects in zinc-blende InSb and wurtzite InAs nanowires: realistic calculations with multiband $\vec{k} \cdot \vec{p}$ method. *arXiv preprint arXiv:1802.06734* (2018) (cit. on p. 46).
132. Jespersen, T. *et al.* Crystal orientation dependence of the spin-orbit coupling in InAs nanowires. *Physical Review B* **97**, 041303 (2018) (cit. on pp. 46, 127).
133. Fonseka, H. A. *et al.* Nanowires grown on InP (100): growth directions, facets, crystal structures, and relative yield control. *ACS nano* **8**, 6945–6954 (2014) (cit. on p. 46).
134. Kang, J.-H. *et al.* Robust Epitaxial Al Coating of Reclined InAs Nanowires. *Nano letters* **17**, 7520–7527 (2017) (cit. on pp. 46, 86).
135. Zhang, Z., Shi, S.-X., Chen, P.-P., Lu, W. & Zou, J. Influence of substrate orientation on the structural quality of GaAs nanowires in molecular beam epitaxy. *Nanotechnology* **26**, 255601 (2015) (cit. on p. 46).
136. Wang, J. *et al.* Position-controlled [100] InP nanowire arrays. *Applied Physics Letters* **100**, 053107 (2012) (cit. on pp. 46, 61).
137. Potts, H., Morgan, N. P., Tütüncüoğlu, G., Friedl, M. & i Morral, A. F. Tuning growth direction of catalyst-free InAs (Sb) nanowires with indium droplets. *Nanotechnology* **28**, 054001 (2016) (cit. on pp. 46, 53, 70).
138. Plissard, S. R. *et al.* Formation and electronic properties of InSb nanocrosses. *Nature nanotechnology* **8**, 859 (2013) (cit. on pp. 46, 51, 53).
139. Musin, I. R. & Filler, M. A. Chemical control of semiconductor nanowire kinking and superstructure. *Nano letters* **12**, 3363–3368 (2012) (cit. on pp. 46, 53).
140. Panciera, F. *et al.* Controlling nanowire growth through electric field-induced deformation of the catalyst droplet. *Nature communications* **7**, 12271 (2016) (cit. on pp. 46, 53, 83).

141. Tian, B., Xie, P., Kempa, T. J., Bell, D. C. & Lieber, C. M. Single-crystalline kinked semiconductor nanowire superstructures. *Nature nanotechnology* **4**, 824 (2009) (cit. on pp. 46, 53).
142. Yuan, X. *et al.* Tunable polarity in a III–V nanowire by droplet wetting and surface energy engineering. *Advanced Materials* **27**, 6096–6103 (2015) (cit. on pp. 46, 53).
143. Cho, A. & Ballamy, W. GaAs planar technology by molecular beam epitaxy (MBE). *Journal of Applied Physics* **46**, 783–785 (1975) (cit. on p. 47).
144. Vodjdani, N., Lemarchand, A & Paradan, H. Parametric studies of GaAs growth by metalorganic molecular beam epitaxy. *Le Journal de Physique Colloques* **43**, C5–339 (1982) (cit. on p. 47).
145. Sugaya, T., Okada, Y. & Kawabe, M. Selective growth of GaAs by molecular beam epitaxy. *Japanese journal of applied physics* **31**, L713 (1992) (cit. on p. 47).
146. Kuroda, N., Sugou, S., Sasaki, T. & Kitamura, M. Selective growth of InGaAs/InP layers by gas source molecular beam epitaxy with atomic hydrogen irradiation. *Japanese journal of applied physics* **32**, L1627 (1993) (cit. on p. 47).
147. Okamoto, A & Ohata, K. Selective epitaxial growth of gallium arsenide by molecular beam epitaxy. *Applied physics letters* **51**, 1512–1514 (1987) (cit. on pp. 47, 48).
148. Yokoyama, S, Oogi, J, Yui, D & Kawabe, M. Low-temperature selective growth of GaAs by alternately supplying molecular beam epitaxy. *Journal of Crystal Growth* **95**, 32–34 (1989) (cit. on p. 48).
149. Allegretti, F, Inoue, M & Nishinaga, T. In-situ observation of GaAs selective epitaxy on GaAs (111) B substrates. *Journal of crystal growth* **146**, 354–358 (1995) (cit. on p. 48).
150. Lee, S., Malloy, K., Dawson, L. & Brueck, S. Selective growth and associated faceting and lateral overgrowth of GaAs on a nanoscale limited area bounded by a SiO₂ mask in molecular beam epitaxy. *Journal of applied physics* **92**, 6567–6571 (2002) (cit. on p. 48).
151. Heiß, M. *et al.* Growth mechanisms and optical properties of GaAs-based semiconductor microstructures by selective area epitaxy. *Journal of Crystal Growth* **310**, 1049–1056 (2008) (cit. on p. 48).
152. Tutuncuoglu, G. *et al.* Towards defect-free 1-D GaAs/AlGaAs heterostructures based on GaAs nanomembranes. *Nanoscale* **7**, 19453–19460 (2015) (cit. on p. 48).
153. Fahed, M, Desplanque, L, Troadec, D, Patriarche, G & Wallart, X. Selective area heteroepitaxy of GaSb on GaAs (001) for in-plane InAs nanowire achievement. *Nanotechnology* **27**, 505301 (2016) (cit. on pp. 48, 103, 115–117, 129, 133).

154. Friedl, M. *et al.* Template-assisted scalable nanowire networks. *Nano letters* (2018) (cit. on pp. 48, 49, 129).
155. Mohan, P., Nakajima, F., Akabori, M., Motohisa, J. & Fukui, T. Fabrication of semiconductor Kagome lattice structure by selective area metalorganic vapor phase epitaxy. *Applied physics letters* **83**, 689–691 (2003) (cit. on pp. 48, 49).
156. Desplanque, L. *et al.* InAs/AlGaSb Esaki tunnel diodes grown by selective area epitaxy on GaSb (001) substrate in Indium Phosphide and Related Materials (IPRM), 26th International Conference on (2014), 1–2 (cit. on pp. 48, 103, 129).
157. Desplanque, L., Bucamp, A., Troadec, D., Patriarche, G & Wallart, X. In-plane InSb nanowires grown by selective area molecular beam epitaxy on semi-insulating substrate. *Nanotechnology* **29**, 305705 (2018) (cit. on pp. 48, 113, 129).
158. Dick, K. A. *et al.* Synthesis of branched ‘nanotrees’ by controlled seeding of multiple branching events. *Nature materials* **3**, 380 (2004) (cit. on pp. 49, 50).
159. Wang, D., Qian, F., Yang, C., Zhong, Z. & Lieber, C. M. Rational growth of branched and hyperbranched nanowire structures. *Nano Letters* **4**, 871–874 (2004) (cit. on pp. 49, 50).
160. Dalacu, D., Kam, A., Austing, D. G. & Poole, P. J. Droplet dynamics in controlled InAs nanowire interconnections. *Nano letters* **13**, 2676–2681 (2013) (cit. on pp. 49, 50, 53, 116, 134).
161. Freer, E. M., Grachev, O., Duan, X., Martin, S. & Stumbo, D. P. High-yield self-limiting single-nanowire assembly with dielectrophoresis. *Nature nanotechnology* **5**, 525–530 (2010) (cit. on pp. 49, 142).
162. Yao, J., Yan, H. & Lieber, C. M. A nanoscale combing technique for the large-scale assembly of highly aligned nanowires. *Nature nanotechnology* **8**, 329–335 (2013) (cit. on pp. 49, 142).
163. Hangarter, C. M. & Myung, N. V. Magnetic alignment of nanowires. *Chemistry of Materials* **17**, 1320–1324 (2005) (cit. on pp. 49, 142).
164. Gooth, J. *et al.* Ballistic one-dimensional InAs nanowire cross-junction interconnects. *Nano letters* **17**, 2596–2602 (2017) (cit. on p. 49).
165. Dick, K. A. *et al.* Height-controlled nanowire branches on nanotrees using a polymer mask. *Nanotechnology* **18**, 035601 (2007) (cit. on pp. 50, 53).
166. Beaudry, A. L. *et al.* Directed branch growth in aligned nanowire arrays. *Nano letters* **14**, 1797–1803 (2014) (cit. on p. 50).
167. Suyatin, D. B. *et al.* Electrical properties of self-assembled branched InAs nanowire junctions. *Nano letters* **8**, 1100–1104 (2008) (cit. on p. 50).

168. Rieger, T. *et al.* Crystal phase transformation in self-assembled InAs nanowire junctions on patterned Si substrates. *Nano letters* **16**, 1933–1941 (2016) (cit. on pp. 50, 53, 76, 134).
169. Fadaly, E. M. *et al.* Observation of conductance quantization in InSb nanowire networks. *Nano letters* **17**, 6511–6515 (2017) (cit. on p. 50).
170. Gazibegovic, S. *et al.* Epitaxy of advanced nanowire quantum devices. *Nature* **548**, 434 (2017) (cit. on pp. 50, 52, 53, 85, 86, 88).
171. Kang, J.-H. *et al.* Crystal structure and transport in merged InAs nanowires MBE grown on (001) InAs. *Nano letters* **13**, 5190–5196 (2013) (cit. on pp. 51, 68, 69, 76).
172. Car, D., Wang, J., Verheijen, M. A., Bakkers, E. P. & Plissard, S. R. Rationally designed single-crystalline nanowire networks. *Advanced Materials* **26**, 4875–4879 (2014) (cit. on p. 53).
173. Momma, K. & Izumi, F. VESTA 3 for three-dimensional visualization of crystal, volumetric and morphology data. *Journal of applied crystallography* **44**, 1272–1276 (2011) (cit. on p. 57).
174. Schneider, C. A., Rasband, W. S. & Eliceiri, K. W. NIH Image to ImageJ: 25 years of image analysis. *Nature methods* **9**, 671 (2012) (cit. on p. 57).
175. Webpage: jp-minerals.org/vesta/en/ (21.5.2018) (cit. on p. 58).
176. Kelrich, A. *et al.* InP nanoflag growth from a nanowire template by in situ catalyst manipulation. *Nano letters* **16**, 2837–2844 (2016) (cit. on pp. 59, 70, 83).
177. Ghosh, S., Kruse, P & LaPierre, R. The effect of GaAs (100) surface preparation on the growth of nanowires. *Nanotechnology* **20**, 115602 (2009) (cit. on p. 60).
178. Whiticar, A. M., Mårtensson, E. K., Nygård, J., Dick, K. A. & Bolinsson, J. Annealing of Au, Ag and Au–Ag alloy nanoparticle arrays on GaAs (100) and (111) B. *Nanotechnology* **28**, 205702 (2017) (cit. on p. 60).
179. Curiotto, S., Leroy, F., Cheynis, F. & Müller, P. Surface-dependent scenarios for dissolution-driven motion of growing droplets. *Scientific reports* **7**, 902 (2017) (cit. on p. 60).
180. Ye, H. *et al.* MBE growth optimization of InAs (001) homoepitaxy. *Journal of Vacuum Science & Technology B, Nanotechnology and Microelectronics: Materials, Processing, Measurement, and Phenomena* **31**, 03C135 (2013) (cit. on pp. 61, 62).
181. Ohta, K., Kojima, T. & Nakagawa, T. Anisotropic surface migration of Ga atoms on GaAs (001). *Journal of Crystal Growth* **95**, 71–74 (1989) (cit. on pp. 62, 114).

182. Fortuna, S. A., Wen, J., Chun, I. S. & Li, X. Planar GaAs nanowires on GaAs (100) substrates: self-aligned, nearly twin-defect free, and transfer-printable. *Nano Letters* **8**, 4421–4427 (2008) (cit. on p. 66).
183. Galicka, M., Buczko, R. & Kacman, P. Segregation of impurities in GaAs and InAs nanowires. *The Journal of Physical Chemistry C* **117**, 20361–20370 (2013) (cit. on p. 68).
184. Persson, A. I. *et al.* Solid-phase diffusion mechanism for GaAs nanowire growth. *Nature materials* **3**, 677 (2004) (cit. on p. 68).
185. Copel, M., Reuter, M., Kaxiras, E. & Tromp, R. Surfactants in epitaxial growth. *Physical review letters* **63**, 632 (1989) (cit. on pp. 70, 109).
186. Anyebe, E. *et al.* Surfactant effect of antimony addition to the morphology of self-catalyzed InAs 1- x Sb x nanowires. *Nano Research* **8**, 1309–1319 (2015) (cit. on pp. 70, 109).
187. Shtrikman, H. *et al.* Method for suppression of stacking faults in wurtzite III- V nanowires. *Nano letters* **9**, 1506–1510 (2009) (cit. on p. 72).
188. Kang, J.-H., Galicka, M., Kacman, P. & Shtrikman, H. Wurtzite/Zinc-Blende ‘K’-shape InAs Nanowires with Embedded Two-Dimensional Wurtzite Plates. *Nano letters* **17**, 531–537 (2016) (cit. on p. 76).
189. Dick, K. A. *et al.* Control of III–V nanowire crystal structure by growth parameter tuning. *Semiconductor Science and Technology* **25**, 024009 (2010) (cit. on p. 79).
190. Dick, K. A., Thelander, C., Samuelson, L. & Caroff, P. Crystal phase engineering in single InAs nanowires. *Nano letters* **10**, 3494–3499 (2010) (cit. on pp. 82, 83).
191. Chen, I.-J. *et al.* Conduction band offset and polarization effects in InAs nanowire polytype junctions. *Nano letters* **17**, 902–908 (2017) (cit. on pp. 82, 83).
192. Belabbes, A., Panse, C., Furthmüller, J. & Bechstedt, F. Electronic bands of III-V semiconductor polytypes and their alignment. *Physical Review B* **86**, 075208 (2012) (cit. on p. 83).
193. Nilsson, M. *et al.* Parallel-coupled quantum dots in InAs nanowires. *Nano letters* **17**, 7847–7852 (2017) (cit. on p. 83).
194. Krogstrup, P., Marcus, C. M., Jespersen, T. S. & Nygard, J. Network of nanostructures as grown on a substrate. *Patent*, CA2989727A1 (2015) (cit. on p. 85).
195. Sestoft, J. E. *et al.* Engineering hybrid epitaxial InAsSb/Al nanowires for stronger topological protection. *Physical Review Materials* **2**, 044202 (2018) (cit. on pp. 86, 99, 127).

196. Taupin, M. *et al.* InAs nanowire with epitaxial aluminum as a single-electron transistor with fixed tunnel barriers. *Physical Review Applied* **6**, 054017 (2016) (cit. on p. 86).
197. Ferry, D. K. Nanowires in nanoelectronics. *Science* **319**, 579–580 (2008) (cit. on p. 88).
198. De La Mata, M. *et al.* Polarity assignment in ZnTe, GaAs, ZnO, and GaN-AlN nanowires from direct dumbbell analysis. *Nano letters* **12**, 2579–2586 (2012) (cit. on p. 96).
199. Hytch, M. J., Snoeck, E & Kilaas, R. Quantitative measurement of displacement and strain fields from HREM micrographs. *Ultramicroscopy* **74**, 131–146 (1998) (cit. on p. 96).
200. Cottam, R. I. & Saunders, G. A. The elastic constants of GaAs from 2 K to 320 K. *Journal of Physics C: Solid State Physics* **6**, 2105 (1973) (cit. on p. 96).
201. Shur, M. S. *Handbook series on semiconductor parameters* (World Scientific, 1996) (cit. on p. 96).
202. Hansen, A., Björk, M., Fath, C., Thelander, C. & Samuelson, L. Spin relaxation in InAs nanowires studied by tunable weak antilocalization. *Physical Review B* **71**, 205328 (2005) (cit. on pp. 99, 100, 126, 127).
203. Savitzky, A. & Golay, M. J. E. Smoothing and Differentiation of Data by Simplified Least Squares Procedures. *Analytical Chemistry* **36**, 1627–1639 (1964) (cit. on p. 101).
204. Milliken, F., Washburn, S, Umbach, C., Laibowitz, R. & Webb, R. Effect of partial phase coherence on Aharonov-Bohm oscillations in metal loops. *Physical Review B* **36**, 4465 (1987) (cit. on p. 101).
205. Mikkelsen, A. E., Kotetes, P., Krogstrup, P. & Flensberg, K. Hybridization at superconductor-semiconductor interfaces in Majorana devices. *arXiv preprint arXiv:1801.03439* (2018) (cit. on p. 106).
206. Ahmad, E. *et al.* A Two-Step Growth Pathway for High Sb Incorporation in GaAsSb Nanowires in the Telecommunication Wavelength Range. *Scientific Reports* **7**, 10111 (2017) (cit. on p. 109).
207. Sarney, W. *et al.* The influence of growth temperature on Sb incorporation in InAsSb, and the temperature-dependent impact of Bi surfactants. *Journal of Crystal Growth* **406**, 8–11 (2014) (cit. on p. 109).
208. Larsson, M. W. *et al.* Strain mapping in free-standing heterostructured wurtzite InAs/InP nanowires. *Nanotechnology* **18**, 015504 (2006) (cit. on p. 119).

209. Yoshida, S., Yokogawa, T., Imai, Y., Kimura, S. & Sakata, O. Evidence of lattice tilt and slip in m-plane InGaN/GaN heterostructure. *Applied Physics Letters* **99**, 131909 (2011) (cit. on p. 119).
210. De la Mata, M. *et al.* Twin-induced InSb nanosails: a convenient high mobility quantum system. *Nano letters* **16**, 825–833 (2016) (cit. on p. 119).
211. Colinge, J.-P. & Colinge, C. A. *Physics of semiconductor devices* (Springer Science & Business Media, 2005) (cit. on pp. 120, 122).
212. Hansen, A. E., Kristensen, A., Pedersen, S, Sørensen, C. & Lindelof, P. Mesoscopic decoherence in Aharonov-Bohm rings. *Physical Review B* **64**, 045327 (2001) (cit. on p. 125).
213. Dufouleur, J. *et al.* Quasiballistic Transport of Dirac Fermions in a Bi₂Se₃ Nanowire. *Phys. Rev. Lett.* **110**, 186806 (18 2013) (cit. on p. 125).
214. Seelig, G. & Büttiker, M. Charge-fluctuation-induced dephasing in a gated mesoscopic interferometer. *Physical Review B* **64**, 245313 (2001) (cit. on p. 125).
215. Ludwig, T & Mirlin, A. Interaction-induced dephasing of Aharonov-Bohm oscillations. *Physical Review B* **69**, 193306 (2004) (cit. on p. 126).
216. Ferrier, M *et al.* Geometrical dependence of decoherence by electronic interactions in a GaAs/GaAlAs square network. *Physical review letters* **100**, 146802 (2008) (cit. on p. 127).
217. Van Weperen, I *et al.* Spin-orbit interaction in InSb nanowires. *Physical Review B* **91**, 201413 (2015) (cit. on p. 127).
218. Casparis, L. *et al.* Voltage-Controlled Superconducting Quantum Bus. *arXiv preprint arXiv:1802.01327* (2018) (cit. on p. 128).
219. Higginbotham, A. P. *et al.* Parity lifetime of bound states in a proximitized semiconductor nanowire. *Nature Physics* **11**, 1017 (2015) (cit. on p. 128).
220. Dresselhaus, G. Spin-orbit coupling effects in zinc blende structures. *Physical Review* **100**, 580 (1955) (cit. on p. 129).
221. Güsken, N. A. *et al.* MBE growth of Al/InAs and Nb/InAs superconducting hybrid nanowire structures. *Nanoscale* **9**, 16735–16741 (2017) (cit. on p. 129).
222. Webpage: www.genisys-gmbh.com/web/products/beamer.html (15.6.2018) (cit. on pp. 132, 157, 166).
223. Wang, J, Thompson, D. & Simmons, J. Wet Chemical Etching for V-grooves into InP Substrates. *Journal of the Electrochemical Society* **145**, 2931–2937 (1998) (cit. on pp. 133, 135).